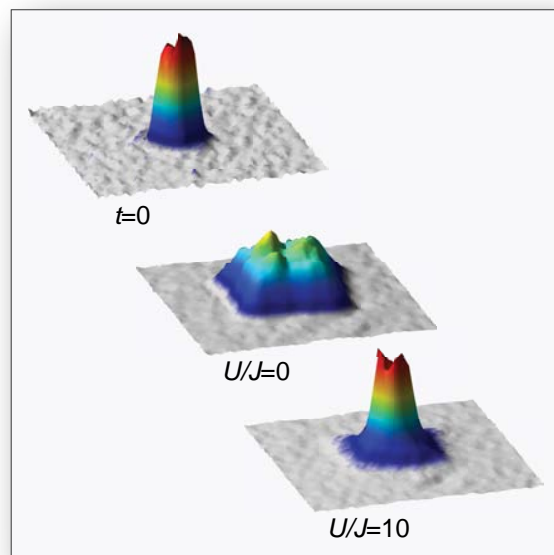


Interacting Fermionic Atoms in Optical Lattices

- A Quantum Simulator for Condensed Matter Physics

Ulrich Schneider



Dissertation zur Erlangung des Grades
"Doktor der Naturwissenschaften"
am Fachbereich Physik
der Johannes Gutenberg-Universität in Mainz

Mainz, den 9.9.2010

Abstract

This thesis reports on the creation and analysis of many-body states of interacting fermionic atoms in optical lattices. The realized system can be described by the Fermi-Hubbard hamiltonian, which is an important model for correlated electrons in modern condensed matter physics. In this way, ultra-cold atoms can be utilized as a quantum simulator to study solid state phenomena.

The use of a Feshbach resonance in combination with a blue-detuned optical lattice and a red-detuned dipole trap enables an independent control over all relevant parameters in the many-body hamiltonian. By measuring the in-situ density distribution and doublon fraction it has been possible to identify both metallic and insulating phases in the repulsive Hubbard model, including the experimental observation of the fermionic Mott insulator. In the attractive case, the appearance of strong correlations has been detected via an anomalous expansion of the cloud that is caused by the formation of non-condensed pairs. By monitoring the in-situ density distribution of initially localized atoms during the free expansion in a homogeneous optical lattice, a strong influence of interactions on the out-of-equilibrium dynamics within the Hubbard model has been found.

The reported experiments pave the way for future studies on magnetic order and fermionic superfluidity in a clean and well-controlled experimental system.

Contents

1. Introduction	7
1.1. This thesis	9
1.2. Publications	10
2. Statistical mechanics	11
2.1. Bosons	12
2.2. Fermions	13
2.2.1. Fermi-Dirac distribution	14
2.2.2. Fermionic atoms in an harmonic trap	16
2.2.3. Time-of-flight imaging	19
2.3. Ensembles	23
3. Interactions	25
3.1. Types of interactions	25
3.2. Scattering theory	27
3.2.1. Elastic scattering	28
3.2.2. Ultracold collisions	28
3.2.3. Contact interaction	29
3.3. Feshbach resonance	30
3.3.1. Losses at Feshbach resonance	31
3.3.2. Feshbach molecules	32
3.3.3. BEC-BCS crossover	34
3.4. Light assisted collisions	37
4. Optical potentials: Dipole trap and lattice	41
4.1. Dipole potential	41
4.2. Crossed dipole trap	43
4.2.1. Trap frequencies	44
4.3. Optical lattice	46
4.3.1. Implementation	46
4.3.2. Single particle eigenstates	49
5. Fermi-Hubbard model	61
5.1. Fermi-Hubbard hamiltonian	62
5.2. Conductivity and compressibility	64
5.2.1. An intuitive picture of the Mott transition	64
5.3. Two particle Hubbard model	65

Contents

5.4.	Filling factor, doublon fraction, and entropy capacity	68
5.4.1.	Doublon fraction	68
5.4.2.	Entropy capacity	70
5.5.	Phases of the three dimensional homogeneous Hubbard model	71
5.5.1.	Non-interacting	71
5.5.2.	Repulsive interaction	72
5.5.3.	Attractive interaction	74
5.5.4.	Lieb-Mattis transformation	76
5.6.	Numerical methods	77
5.7.	Inhomogeneous system	79
5.7.1.	Local density approximation	79
5.8.	Validity of the Hubbard model	81
6.	Observables: What can we measure?	83
6.1.	Momentum distribution	83
6.2.	Second order correlation functions	84
6.3.	Collective oscillations	85
6.4.	Quasi-momentum distribution: band mapping technique	86
6.5.	Density distribution: In-situ imaging	87
6.6.	Doublon fraction: Molecule creation	90
6.7.	Transport coefficients	91
6.8.	Spectroscopic techniques	91
7.	Overview over experimental cycle	93
8.	Repulsive Fermi-Hubbard model	97
8.1.	Measurement sequence	97
8.2.	Theoretical expectation	98
8.2.1.	Entropy distribution	101
8.3.	Cloud size and compressibility	102
8.3.1.	Rescaled cloud size	102
8.3.2.	Results	105
8.4.	Doublon fraction	110
8.5.	Conclusion and outlook	111
9.	Attractive Fermi-Hubbard model	113
9.1.	Temperature tracking	113
9.2.	Effects of pairing	114
9.2.1.	Two atoms in a double well - a toy model	115
9.2.2.	Zero tunneling limit	115
9.2.3.	Finite tunneling	116
9.3.	Experimental sequence	118
9.4.	Experimental results	118
9.4.1.	Influence of compression and temperature	120
9.5.	Heating during loading	121

Contents

9.6. Doublon lifetime	122
9.7. Adiabaticity timescales	123
9.8. Conclusion and outlook	124
10. Dynamics in the Fermi-Hubbard model	125
10.1. Experimental sequence	126
10.2. Non-interacting case	128
10.2.1. Canceling the harmonic confinement	132
10.3. Interacting case	133
10.3.1. Theoretical description	135
10.3.2. Core width and core expansion velocity	136
10.3.3. Dynamical U vs. -U symmetry of the Hubbard model . .	139
10.3.4. Doublon dissolution time	143
10.3.5. Width of Feshbach resonance	144
10.4. Conclusion	145
11. Challenges	147
11.1. Cooling and entropy management	147
11.2. Heating rates	149
11.3. Dynamics	149
11.4. Detection	150
12. Conclusion & Outlook	153
12.1. Outlook	154
A. Photo dissociation	157
A.1. Experimental sequence	158
A.2. Experimental results	159
A.2.1. Varying the dissociation wavelength	159
A.2.2. Dissociation rate	160
A.2.3. Influence of the magnetic field	162
B. Dynamical U vs. -U symmetry	165
C. Poly-logarithmic functions	169
Bibliography	171

1. Introduction

Although the study of ultracold atoms is a relatively new field that started with the first experimental realization of a Bose Einstein condensate in 1995 [1, 2], it has already diversified into many subbranches studying different topics ranging from the effects of disorder on non-interacting systems over collective excitations and superfluidity in weakly interacting systems to the study of strongly correlated states, molecular physics and quantum information.

Starting with the first realization of a quantum degenerate gas of fermionic atoms in 1999 [3], ultracold fermions became an important subfield, especially in the presence of strong interactions: Fermions cannot Bose condense due to the Pauli principle (cf. sec. 2.2) and superfluidity of fermionic particles therefore relies on first converting the fermions into bosonic pairs like e.g. molecules of fermionic atoms or Cooper pairs of electrons (cf. sec. 3.3.3).

There exist mainly two routes for realizing strongly interacting states of ultracold atoms: One is the use of Feshbach resonances (cf. sec. 3.3) in order to directly boost the interactions. The second route, the use of optical lattices, in contrast mostly affects the kinetic energy of the particles. In a lattice, the kinetic energy of the particles becomes confined to several distinct Bloch bands. Within a single band of a sufficiently deep lattice the kinetic energy becomes so small that the interaction energy can easily dominate over the kinetic energy. This allows the realization of strongly correlated states without the need of a Feshbach resonance, thereby avoiding the corresponding losses.

A first hallmark experiment combining ultracold atoms and optical lattices was the observation of the superfluid to Mott insulator transition with bosonic atoms in 2001 [4]. This experiment did not only demonstrate the ability to reach strongly correlated states using ultracold atoms in optical lattices but furthermore demonstrated the ability to implement Hubbard models with this technique [5, 6]. This started not only an intense research program concerning the Bose-Hubbard model [7] but also created a lot of interest in combining fermionic quantum gases with an optical lattice.

Fermionic atoms in optical lattices can be described by the fermionic Hubbard model (cf. sec. 5), which represents one of the central models in modern condensed matter physics: Due to the complexity of real materials an important goal in the study of electrons in solids is the search for the simplest models that nonetheless describe the physics of interest. In this context the Hubbard model was the first to successfully describe the Mott transition between conducting and insulating states.

1. Introduction

Optical lattices offer the possibility to study condensed matter physics using ultracold atoms and can be seen as one example of a so-called *Quantum Simulator*, which was first proposed by Richard P. Feynman in 1982 [8]. The central idea of a quantum simulation is to use one well-controlled quantum system to simulate another quantum system. This is especially appealing in the case of electrons in a solid, since many condensed matter phenomena involve a large number of electrons while exact numerical simulations are still limited to less than 20 particles due to the exponentially growing Hilbert space [9].

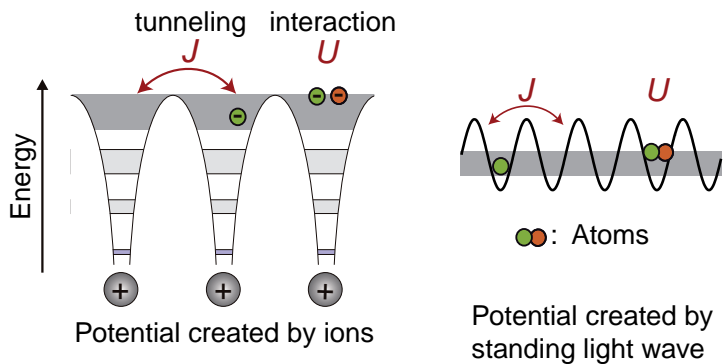


Figure 1.1.: In a tight-binding model like the Hubbard model the exact interactions and potentials are absorbed into a few coefficients. In the easiest case of a single band Hubbard model these coefficients are the hopping rate t and the on-site interaction constant U . This model can therefore be realized by such diverse systems as electrons in a solid or atoms in an optical lattice.

One major advantages of ultracold atoms in this context is that they represent a clean and simple system, which allows one to study specifically the physics at interest and nothing more: Unlike a real crystal, which always has a finite defect density, an optical lattice is a perfectly periodic potential without any defects. In addition the physics is much simpler as no additional degrees of freedom, e.g. lattice phonons, have to be considered.

The second big advantage stems from the high controllability of atomic systems. In contrast to a real solid, the strengths of all potentials can be controlled by varying the laser intensities. By the use of Feshbach resonances it in addition became possible to freely tune the interactions between the atoms, something that is impossible to achieve in a real solid, where one has to deal with the Coulomb repulsion between the electrons.

Apart from simulating condensed matter physics there are many more applications for atomic lattice systems, which form an intriguing and very rich many-body system in their own right: In a deep lattice, where tunneling can be neglected, one can think of each individual lattice site as a small "test tube" in which molecular physics of a small number of atoms can be studied in a clean and well isolated environment [10], a topic that currently sees renewed interest due to the recent production of ultracold ground state molecules [11, 12]. Using the capabilities to resolve and address individual lattice sites, which have recently been

1.1. This thesis

demonstrated [13–19], single atoms on isolated lattice sites can become an ideal candidate for a *Quantum Memory* and other *Quantum Information* applications.

1.1. This thesis

The main topic of this thesis is the experimental investigation of the equilibrium and out-of-equilibrium physics of an interacting spin mixture of ultracold fermionic atoms in optical lattices. To this end we implemented and optimized a combination of several cooling techniques in order to prepare a sufficiently degenerate sample of ultracold fermions in a crossed beam dipole trap. In order to gain full independent control over the density of atoms in the lattice, we implemented for the first time a *blue-detuned* optical lattice for ultracold atoms. In contrast to a standard red-detuned lattice, the blue-detuned case creates a repulsive potential, for which new alignment and characterization procedures had to be established.

The blue detuned lattice allowed us to create deep lattices without automatically creating a strong harmonic confinement at the same time. It therefore enabled us to control lattice depth and confinement independently, which was the key ingredient to all experiments in this thesis. In addition we adapted several measurement techniques to the fermionic case and implemented for the first time phase-contrast imaging with fermions in an optical lattice.

In the case of repulsive interactions (cf. sec. 8) the combination of varying the harmonic confinement at constant lattice depth with the measurement of the in-situ density distribution allowed us to directly measure the compressibility of the cloud and thereby to distinguish incompressible band- and Mott-insulating states from compressible metallic states.

In the case of attractive interactions (cf. sec. 9) the preparation of a low density sample enabled us to study the intriguing pseudogap regime in the attractive Hubbard model, in which fermionic atoms form pairs that do not condense due to a finite entropy.

In a last experiment, we used the possibility to change the parameters in real time to study the expansion dynamics of a Fermi gas within a deep lattice (cf. sec. 10). This experiment at the same time revealed a fascinating many body out-of-equilibrium dynamics and allowed us to gain a first glimpse at the characteristic timescales of mass transport in a Hubbard model.

During the optimization of the lattice wavelength we studied the photodissociation of Feshbach molecules by blue-detuned light in order to achieve a low enough heating rate to perform equilibrium experiments in the lattice, the results are given in the appendix (cf. sec. A).

This thesis is linked to the PhD theses of Tim Rom, Thorsten Best and Sebastian Will that were/are performed at the same experimental apparatus. They are

1. Introduction

focused on the measurement of density-density correlations of non-interacting fermions (T.R.) and experiments with Bosons and Bose-Fermi mixtures (T.B and S.W.).

1.2. Publications

The main results of this thesis are published in the following references:

- **Metallic and Insulating Phases of Repulsively Interacting Fermions in a 3D Optical Lattice**
U. Schneider, L. Hackermüller, S. Will, T. Best, I. Bloch, T. Costi, R. Helmes, D. Rasch, and A. Rosch.
[Science 322, 1520–1525 \(2008\)](#)
- **Anomalous Expansion of Attractively Interacting Fermionic Atoms in an Optical Lattice**
L. Hackermüller, U. Schneider, M. Moreno-Cardoner, T. Kitagawa, T. Best, S. Will, E. Demler, E. Altman, I. Bloch, and B. Paredes.
[Science 327, 1621–1624 \(2010\)](#)
- **Breakdown of diffusion: From collisional hydrodynamics to a continuous quantum walk in a homogeneous Hubbard model**
U. Schneider, L. Hackermüller, J. Ronzheimer, S. Will, S. Braun, T. Best, I. Bloch, E. Demler, S. Mandt, D. Rasch, and A. Rosch.
[arXiv:1005.3545v1 \[cond-mat.quant-gas\] \(2010\)](#)

The following additional references have also been published in the context of this thesis. They are covered in detail in the aforementioned PhD theses:

- **Free fermion antibunching in a degenerate atomic Fermi gas released from an optical lattice**
T. Rom, T. Best, D. van Oosten, U. Schneider, S. Fölling, B. Paredes, and I. Bloch
[Nature 444, 733–736 \(2006\)](#)
- **Role of Interactions in ^{87}Rb - ^{40}K Bose-Fermi Mixtures in a 3D Optical Lattice**
T. Best, S. Will, U. Schneider, L. Hackermüller, D. van Oosten, I. Bloch, and D.-S. Lühmann.
[Phys. Rev. Lett. 102, 30408 \(2009\)](#)
- **Time-resolved observation of coherent multi-body interactions in quantum phase revivals**
S. Will, T. Best, U. Schneider, L. Hackermüller, D.-S. Lühmann, and I. Bloch.
[Nature 465, 197 \(2010\)](#)

2. Statistical mechanics

Classical statistical physics typically deals with *distinguishable* particles: Even if two macroscopic objects would not differ by small details, they could still be distinguished by their (classical) positions and velocities. Two quantum mechanical particles in the same internal quantum state on the other hand are *indistinguishable*. If their wavefunctions overlap at some time it is later on impossible to tell which particle originated from where. This indistinguishability of the particles gives rise to fundamental differences between classical and *quantum statistics*:

In the case of two distinguishable particles (1 & 2) and two single-particle eigenstates $|a\rangle$ and $|b\rangle$ there are four possible combinations:

$$|A\rangle = |a\rangle_1 |a\rangle_2 \quad |B\rangle = |a\rangle_1 |b\rangle_2 \quad (2.1)$$

$$|C\rangle = |b\rangle_1 |a\rangle_2 \quad |D\rangle = |b\rangle_1 |b\rangle_2 \quad (2.2)$$

If the particles are indistinguishable, all physical properties (e.g. expectation values) must remain unaffected by an interchange of two particles. Formally, this can be taken into account by requiring that any physical state $|\Psi\rangle$ is an eigenstate of the permutation operator \hat{P}_{ij} which exchanges the particles i and j : $\hat{P}_{12} |\Psi\rangle = a |\Psi\rangle$, $a \in \mathbb{C}$. The possible eigenvalues a of \hat{P}_{ij} can be found by noting that (in 3D) exchanging the same pair of particles twice is equivalent to not interchanging them at all $(\hat{P}_{ij})^2 = \hat{1}$. This implies $a^2 = 1$ and leads to $a = \pm 1$, which states that the exchange of two particles can either leave the wavefunction unchanged ($a = 1$) or change its sign ($a = -1$)¹.

In the case of $a = 1$ the particles are called *bosons* and there are three possible two-particle states:

$$|\Psi_b^1\rangle = |A\rangle \quad (2.3)$$

$$|\Psi_b^2\rangle = |D\rangle \quad (2.4)$$

$$|\Psi_b^3\rangle = 1/\sqrt{2} \{ |B\rangle + |C\rangle \} \quad (2.5)$$

In the case of $a = -1$ the particles will be called *fermions* and there is only one possible state:

$$|\Psi_f\rangle = 1/\sqrt{2} \{ |B\rangle - |C\rangle \} \quad (2.6)$$

¹In the two-dimensional case the situation is more subtle and leads to the existence of so-called *Anyons*, that is particles with fractional statistics [20, 21].

2. Statistical mechanics

The above argument is known as the *Pauli principle* and can be extended to an arbitrary number of particles [22]:

- The wave function of a set of N indistinguishable particles is either completely symmetric and remains unchanged upon exchanging two arbitrary particles: In this case these particles are called bosons.
- Or it is completely antisymmetric, and thus changes its sign when two particles are exchanged: In this case the particles are called fermions.

The so-called *Spin-Statistics Theorem*, which was derived for certain cases already by Wolfgang Pauli [23], links the above distinction between bosons and fermions to the spin of the particles and states that all particles with an integer or zero spin are bosons and particles with half-integer spin are fermions.

The different symmetries of the wavefunction lead to the fundamentally different *Bose-Einstein* and *Fermi-Dirac* statistics, whose consequences can be seen perhaps most dramatically in the different Helium isotopes: Electron structure and chemical properties of ${}^3\text{He}$ and ${}^4\text{He}$ are identical, the only difference is the number of neutrons in the nucleus which leads to different nuclear spins and therefore different statistics.

Bosonic ${}^4\text{He}$ becomes superfluid below 2.17 K at atmospheric pressure while fermionic ${}^3\text{He}$ becomes superfluid only below 3 mK [24].

For simplicity only non-interacting particles are considered in this chapter. While this is a crude approximation for bosons, interactions can be safely neglected in a single component Fermi gas at ultracold temperatures (cf. sec. 3.2.2)

2.1. Bosons

As seen in the previous section, the possible many-body wavefunctions of N indistinguishable and non-interacting bosonic particles are given by all completely symmetric combinations of single-particle eigenstates. In contrast to the fermionic case, which will be discussed in the next section, the required symmetry posses no restrictions on the possible occupations of the single particle states.

The many-body ground state is therefore given by the state where all particles occupy the single-particle ground state $|\psi_0\rangle$ with energy ϵ_0 . This phenomena of a macroscopic occupation of a single quantum state is known as *Bose-Einstein condensation* (BEC). It was predicted for non-interacting particles by A. Einstein in 1925 [25], expanding work by S. N. Bose [26] and was observed in dilute gases for the first time in 1995 [1, 2].

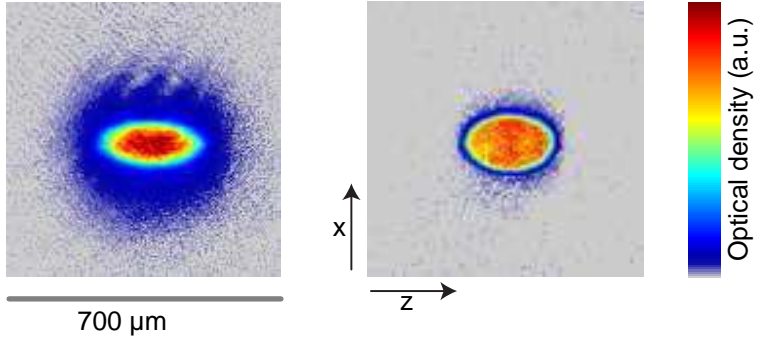


Figure 2.1.: Absorption images of a cloud of (weakly interacting) bosonic atoms after time of flight. In the left image a partial condensed cloud is shown, the right image shows a pure BEC whose central density exceeds the dynamic range of the imaging setup. X denotes a horizontal and z the vertical axis.

For finite temperatures T the occupation of the single-particle eigenstates with energy ϵ is given by the *Bose-Einstein distribution*:

$$N(\epsilon) = \frac{1}{\exp\left(\frac{\epsilon - \mu}{k_B T}\right) - 1} \quad (2.7)$$

where $\mu \leq \epsilon_0$ denotes the chemical potential (cf. sec. 2.3). There exists a critical temperature T_c below which the occupation N_0 of the single-particle ground state becomes macroscopic. In the important case of a 3D harmonic trap the *condensate fraction* N_0/N is given by [24]:

$$\frac{N_0(T)}{N} = 1 - \left(\frac{T}{T_c}\right)^3 \quad (2.8)$$

In time-of-flight images (cf. sec. 2.2.3) the onset of Bose-Einstein condensation is clearly visible in the bimodality of the cloud, which is shown in figure 2.1: The elliptical central core in the left image is the condensed atoms, while the round, Gaussian shaped background is due to the thermal component.

Most experiments so far have been carried out with weakly interacting atoms and the interactions were taken into account by use of the Gross-Pitaevskii equation and the Bogoliubov approximation. [24]. Only recently it became possible to use Feshbach resonances (cf. sec. 3.3) in order to realize systems of non-interacting bosonic atoms [27, 28].

2.2. Fermions

Fermions are particles with an half-integer spin and include the constituents of all atoms: electrons, protons and neutrons. As a consequence, any neutral atom

2. Statistical mechanics

with an uneven number of neutrons is itself fermionic. Important examples of degenerate fermionic particles include the electrons in a metal [29], neutrons in a neutron star and superfluid ^3He . In the context of laser-cooled atoms, the two most widely used fermionic species are the alkali metal isotopes Potassium ^{40}K and Lithium ^6Li . Potassium, which was also used in the experiments in this thesis, was first cooled into the quantum degenerate regime by B. DeMarco and D.S. Jin in 1999 [3].

An important consequence of the general Pauli principle for indistinguishable fermions is the so-called *Pauli exclusion principle* [22]:

Two identical fermions cannot be in the same quantum state.

This can be seen directly from the aforementioned antisymmetry of the wavefunction: The antisymmetrized wavefunction for two identical fermions in the same single-particle state $|a\rangle$ vanishes:

$$|\Psi_f\rangle = 1/\sqrt{2} \{ |a\rangle_1 |a\rangle_2 - |a\rangle_1 |a\rangle_2 \} = 0 \quad (2.9)$$

Due to this principle, N identical fermions at zero temperature will not form a BEC, where all particles would occupy the same single-particle state, but will instead form a so-called *Fermi-sea*: They will occupy the N lowest energy states by exactly one fermion per state. Important examples for this behavior are the electronic shells of atoms or the Fermi-sea of conductance electrons in a solid: Without the Pauli exclusion principle all atoms would be similar to the hydrogen atom with all electrons occupying the $1s$ energy state and (neglecting interactions) all solids would be metallic since no band-insulating state could form.

2.2.1. Fermi-Dirac distribution

For non-interacting fermions in thermal equilibrium the average occupation of a given (single-particle) eigenstate of the hamiltonian with energy ϵ is given by the *Fermi-Dirac distribution*:

$$F(\epsilon) = \frac{1}{e^{\frac{\epsilon-\mu}{k_B T}} + 1} \quad (2.10)$$

Here T denotes the temperature and μ is the chemical potential which controls the particle number (cf. sec. 2.3).

Since the exponential e^x is always positive, all occupations are less than or equal to one, as required by the Pauli exclusion principle. As a consequence, there cannot be a macroscopic occupation of any single-particle state, i.e. no BEC. In contrast to the bosonic case there is no phase transition for non-interacting fermions. Instead one finds a smooth crossover from the classical regime at high temperatures to the quantum degenerate regime at low temperatures, which makes the degeneracy much harder to detect than in the bosonic case.

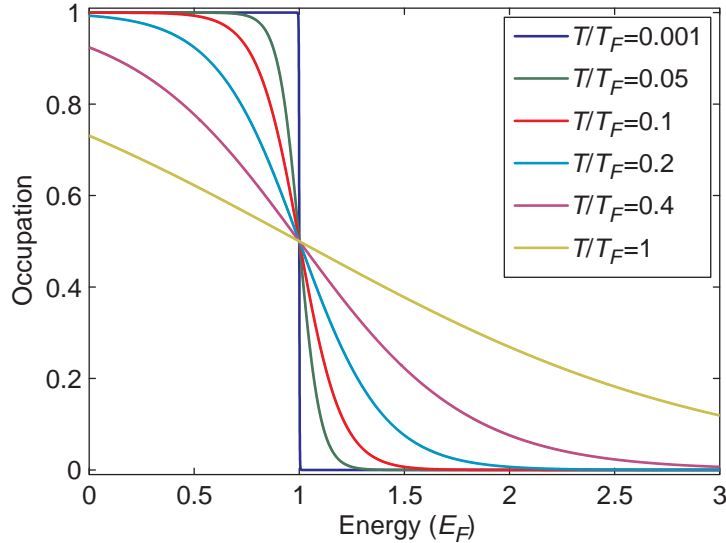


Figure 2.2.: Fermi-Dirac distribution The Fermi-Dirac distribution for several reduced temperatures T/T_F : At zero temperature the distribution reduces to a step function at the Fermi energy E_F , for small temperatures $T/T_F \ll 1$ the distribution deviates from the step function only for energies close to the Fermi energy and for large temperatures it approaches a classical Boltzmann distribution.

At zero temperature the Fermi-Dirac distribution reduces to the step function outlined in the previous paragraph: N identical particles occupy the N lowest energy states and the energy of the N th state is called the *Fermi energy* E_F :

$$F(\epsilon)_{(T=0)} = \begin{cases} 1 & \forall \epsilon \leq E_F \\ 0 & \text{other} \end{cases} \quad (2.11)$$

Accordingly, the *Fermi temperature* T_F is defined as

$$T_F = \frac{E_F - \epsilon_0}{k_B} \quad (2.12)$$

where k_B denotes Boltzmann's constant and ϵ_0 is the energy of the lowest single-particle state, which can be approximated by zero in most cases.

Fugacity

In practice, the Fermi-Dirac distribution is mostly given in a slightly different parametrization using the *fugacity* $z = e^{\frac{\mu}{k_B T}}$:

$$F(\epsilon) = \frac{1}{e^{\frac{\epsilon-\mu}{k_B T}} + 1} = \frac{1}{\frac{1}{z} e^{\frac{\epsilon}{k_B T}} + 1} \quad (2.13)$$

2. Statistical mechanics

The fugacity is a convenient parameter to express the "degree of degeneracy" as the term $1/z$ in the Fermi-Dirac distribution determines the relative weight of the e^x and the $+1$ term: In the classical regime at high temperatures $1/z$ becomes large, one can neglect the $+1$ term and the Fermi-Dirac distribution reduces to the classical Boltzmann-distribution. In the quantum degenerate regime $T/T_F \ll 1$, $1/z$ becomes very small and the $+1$ terms limits the occupations to one.

Entropy

The total entropy S of a set of identical non-interacting fermions is given by [30, 31]:

$$\frac{S}{k_B} = \frac{E - \mu N}{k_B T} + \sum_n \log \left(1 + e^{\frac{\mu - \epsilon_n}{k_B T}} \right) \quad (2.14)$$

where E denotes the total energy and the sum is taken over all single-particle states n . The entropy increases monotonically with temperature and depends on the density of single-particle states n .

2.2.2. Fermionic atoms in an harmonic trap

In the experiment the last step of evaporative cooling is performed in a crossed beam dipole trap (cf. sec. 4.2) that can be approximated by a harmonic potential:

$$V(x, y, z) = \frac{1}{2}m (\omega_x^2 x^2 + \omega_y^2 y^2 + \omega_z^2 z^2) \quad (2.15)$$

It is characterized by three trap frequencies ω_i for particles with mass m . In the experiment, the horizontal trap frequencies are approximately equal $\omega_{\perp} = \omega_x = \omega_y$ and the ratio between the vertical and the horizontal trap frequencies is the *aspect ratio* γ of the trap $\gamma = \frac{\omega_z}{\omega_{\perp}}$.

The corresponding single-particle hamiltonian \hat{H} separates into three terms $\hat{H} = \hat{H}_x + \hat{H}_y + \hat{H}_z$ which act only on a single coordinate. Consequently, the time-independent Schrödinger equation $\hat{H} |\Psi(x, y, z)\rangle = E |\Psi(x, y, z)\rangle$ can be split up into three independent equations and its solutions can be written as a product of three 1D harmonic oscillator eigenstates:

$$|\Psi(x, y, z)\rangle = |\psi_x(x)\rangle \cdot |\psi_y(y)\rangle \cdot |\psi_z(z)\rangle \quad (2.16)$$

This separability of the hamiltonian into three independent 1D hamiltonians still holds if a simple cubic lattice potential (cf. sec. 4.3) is added and enormously facilitates the solution of the problem.

Due to the separability of the problem the eigenenergies of the system are given by all possible combinations $E = E_x + E_y + E_z$ of the 1D harmonic oscillator

eigenenergies $E_i(n) = \hbar\omega_i(n + 1/2)$. The corresponding density of states can be approximated by:

$$g(\epsilon) = \frac{\epsilon^2}{2\gamma(\hbar\omega_{\perp})^3} \quad (2.17)$$

Using this density of states it is possible to give explicit formulas and relations for most thermodynamic quantities (cf. sec. C for details):

- Fermi temperature

$$T_F = \frac{E_F}{k_B} = \frac{\hbar\omega_r}{k_B}(6\gamma N)^{\frac{1}{3}} \quad (2.18)$$

- fugacity

$$\text{Li}_3(-z) = -\frac{1}{6(T/T_F)^3} \quad (2.19)$$

Here Li_3 denotes the trilogarithm (cf. sec. C) and the equation must be solved numerically.

- entropy

$$\begin{aligned} \frac{S}{k_B} &= \frac{E - \mu N}{k_B T} + \frac{1}{2\gamma\hbar^3\omega^3} \left(\frac{\mu^4}{12k_B T} + \frac{1}{6}k_B\mu^2\pi^2 T \right. \\ &\quad \left. + \frac{7}{180}k_B^3\pi^4 T^3 + 2k_B^3 T^3 \text{Li}_4(-e^{-\frac{\mu}{k_B T}}) \right) \end{aligned} \quad (2.20)$$

The most widely used parameter to measure the degeneracy is the *reduced temperature* T/T_F which is directly related to the entropy via the fugacity. For a given aspect ratio γ both temperature and Fermi energy of the cloud scale linearly with the trap frequency ω_{\perp} . Consequently, they increase even if the trap frequency ω_{\perp} is increased adiabatically.

The entropy per particle, the fugacity and the reduced temperature on the other hand stay constant and are thereby better suited as a "thermometer" than temperature itself. In addition, at constant "degeneracy", i.e. constant entropy per particle, temperature and mean energy also vary with particle number.

The emphasis on entropy per particle instead of temperature becomes especially important when adiabatically (i.e. isentropically, cf. sec. 2.3) loading into the lattice, where the density of states becomes more complex (cf. sec. 4.3.2) and does not follow a power law any more.

The measurements shown in this thesis were performed at reduced temperatures T/T_F between 0.1 and 0.15.

2. Statistical mechanics

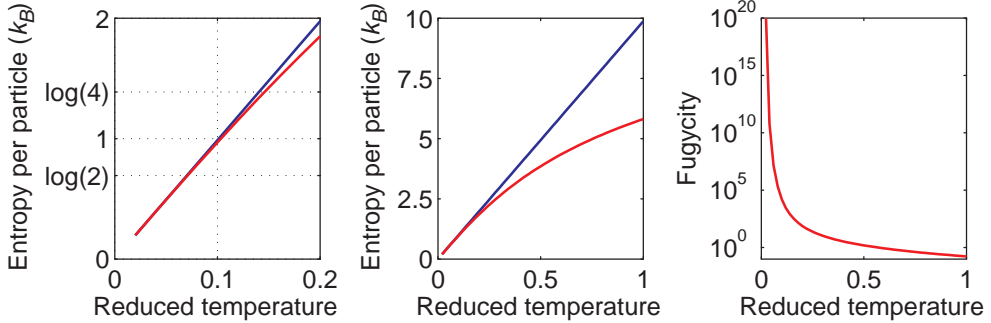


Figure 2.3.: Entropy and fugacity in an harmonic trap as a function of the reduced temperature T/T_F . Shown is the entropy according to equation 2.20 (red) and the result of a Sommerfeld expansion $\pi^2 \cdot T/T_F$ (blue), which is valid for small temperatures. The fugacity approaches zero in the classical limit at high temperatures and diverges for a vanishing temperature.

T/T_F	$S/N (k_B)$	z	$T@20\text{ Hz (nK)}$	$T@100\text{ Hz (nK)}$
0.02	0.20	$5 \cdot 10^{21}$	3	13
0.05	0.49	$4 \cdot 10^8$	6	32
0.1	0.97	16000	13	64
0.15	1.42	480	19	96
0.2	1.85	77	26	129
0.4	3.3	3.4	5	257
1	5.8	0.17	129	643
$N = 10^5 \quad \gamma = 4$				

Table 2.1.: Entropy per particle, fugacity and temperature for a cloud of non-interacting fermions in an harmonic potential. The measurements in this thesis were performed at reduced temperatures between 0.1 and 0.15.

Thomas-Fermi approximation

Since the exact eigenstates of particles in an harmonic trap are well known, both the real-space and the momentum space distributions could in principle be calculated by summing over all eigenstates.

In the limit of large particle numbers, however, it is more convenient to use a semi-classical or *Thomas-Fermi* approximation that yields analytic formulas based on a phase-space picture [32]: Every state is labeled by a position \vec{r} and a momentum \vec{p} which can be thought of to represent the center of the according wave packet. The energy of these states is given by the classical hamiltonian: $H(\vec{r}, \vec{p}) = \frac{m}{2} \omega_{\perp}^2 (x^2 + y^2 + \gamma^2 z^2) + \frac{p^2}{2m}$ and the atom distribution in phase-space is given by:

$$w(\vec{r}, \vec{p}) = \frac{1}{h^3} \frac{1}{\frac{1}{z} e^{\frac{H(\vec{r}, \vec{p})}{k_B T}} + 1} \quad (2.21)$$

The real-space density distribution can be calculated by integrating this phase-

space distribution over all momenta [33]:

$$\begin{aligned} n(\vec{r}) &= \frac{1}{(2\pi)^3} \int w(\vec{r}, \vec{p}) d^3 \vec{p} \\ &= -\frac{(k_B m T)^{3/2}}{(2\pi)^{3/2} \hbar^3} \text{Li}_{3/2} \left[-z \exp \left(-\frac{m\omega_\perp^2}{2k_B T} (x^2 + y^2 + \gamma^2 z^2) \right) \right] \end{aligned} \quad (2.22)$$

In the same way the momentum distribution can be obtained by integrating over real space:

$$\Pi(p) = -\frac{1}{(2\pi)^{3/2} \hbar^3 \gamma} \left(\frac{k_B T}{m\omega_\perp^2} \right)^{3/2} \text{Li}_{3/2} \left[-z \exp \left(-\frac{p^2}{2mk_B T} \right) \right] \quad (2.23)$$

An important observation is that in the Thomas-Fermi approximation for fermions the momentum distribution is always isotropic. As a consequence, the aspect ratio of a fermionic cloud that is suddenly released from a trap, always approaches one for sufficiently long time of flights.

2.2.3. Time-of-flight imaging

The standard way of measuring the temperature of a cloud of ultracold atoms uses so-called time-of-flight imaging, where all trapping potentials are suddenly switched off, and the cloud expands freely for some time before it is imaged. For long time-of-flights, the initial cloud size can be neglected and, in the case of non-interacting atoms, the observed density distribution is given by the initial momentum distribution and the effects of gravity:

$$x(t) = p \cdot t / m + 1/2gt^2 \quad (2.24)$$

For non-degenerate clouds the resulting distribution is a 2D Gaussian, whose width $\sigma = \sqrt{\langle p^2 \rangle t^2 / m^2}$ is a measure of temperature.

An important feature of the harmonic potential is the existence of scaling relations that lead to analytic expressions for the time evolution of an ideal gas released from an harmonic trap [34]:

$$n(x, y, z, t) = \frac{n(\frac{x}{\sqrt{1+\omega_x^2 t^2}}, \dots, 0)}{(1 + \omega_r^2 t^2) \sqrt{1 + \omega_z^2 t^2}} \quad (2.25)$$

Here ω_i denote the trap frequencies before the sudden switch-off. These scaling relations are valid for all time of flights. For ideal gases the free expansion therefore amounts to a rescaling of the spatial coordinates without altering the shape of the distribution. This shape invariance under free expansion is particular for harmonic potentials and does not hold for a general potential.

2. Statistical mechanics

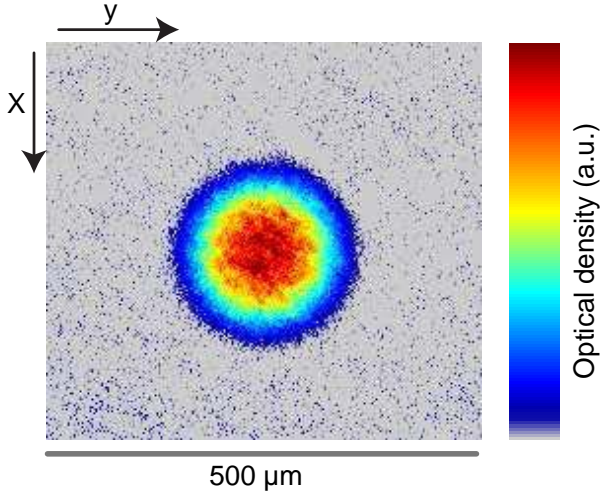


Figure 2.4.: Absorption image of a degenerate non-interacting Fermi cloud taken along the vertical direction after 10 ms time-of-flight.

Since every axes is rescaled separately, the aspect ratio of a fermionic cloud will smoothly approach one, in accordance with the momentum distribution in the Thomas-Fermi approximation (cf. eqn. 2.23).

In the case of non-interacting bosons (or a single fermionic atom) at zero temperature, however, only the single-particle ground state is occupied and the momentum distribution is anisotropic.

Extracting temperatures: Fitting procedure

The above derived equations for the density distribution after time of flight are used to extract the reduced temperature T/T_F and thereby the entropy per particle from standard absorption images (cf. e.g. app. 1 in [35]). These images record the integrated or *column density*

$$n_c(x, y) = \int n(x, y, z) dz \quad (2.26)$$

where the integration is taken along the imaging direction.

Combining the Thomas-Fermi real space density distribution (eqn. 2.22) with the above scaling relations (eqn. 2.25) and integrating along the z direction yields:

$$\begin{aligned} n_c(x, y) &= A \cdot \text{Li}_2 \left(-z \cdot e^{-\frac{x^2}{2\sigma_x^2} - \frac{y^2}{2\sigma_y^2}} \right) \\ A &= \frac{-1}{2\sqrt{1 + (\omega_\perp t)^2} \sqrt{1 + (\gamma\omega_\perp t)^2}} \frac{m(k_B T)^2}{\pi \hbar^3 \omega_\perp} \\ \sigma_i &= \frac{k_B T}{m\omega_i^2} (1 + (\omega_i t)^2) \end{aligned} \quad (2.27)$$

This distribution depends on the entropy per particle in two ways: First temperature appears directly in the prefactor and the σ_i , and it enters in form of the fugacity in the argument of the dilogarithm. Extracting the entropy per particle from the prefactor and the σ_i requires knowledge of the trap frequencies and a precise calibration of the column density in terms of the recorded optical density, which is typically limited by uncertainties due to saturation and polarization effects and optical pumping.

It is therefore common practice to use the fugacity z as a free fit parameter and then calculate the reduce temperature using (eqn. 2.19):

$$n_c^{\text{fit}}(x, y) = A \cdot \frac{\text{Li}_2\left(-z \cdot e^{-\frac{(x-x_c)^2}{2\sigma_x^2} - \frac{(y-y_c)^2}{2\sigma_y^2}}\right)}{\text{Li}_2(-z)} + b \quad (2.28)$$

In this fit function the peak density A , the center position x_c, y_c , the background b and the widths σ_x, σ_y of the Gaussian are free parameters. One can think of this distribution as a classical Gaussian that becomes deformed by the dilogarithm: In the classical limit $T \gg T_F$ the fugacity is small against one, the dilogarithm is linear and the distribution stays Gaussian. The nonlinearity of the dilogarithm, which can be seen in Fig. 2.5 becomes increasingly important for larger fugacities and leads to growing deviations from a Gaussian.

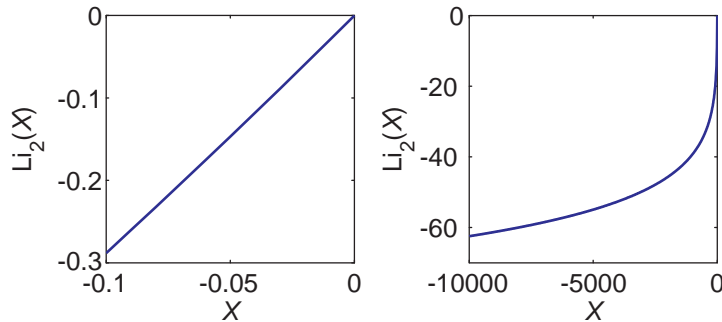


Figure 2.5.: The dilogarithm $\text{Li}_2(x)$ for different ranges of x : For small values the dilogarithm is approximately linear and the fit function of eqn. 2.28 reduces to a Gaussian. For large values the dilogarithm is highly nonlinear and reflects the deviations between Fermi-Dirac and classical statistics.

With this fit function the temperature gets extracted from the shape of the distribution, i.e. the deviations from a Gaussian distribution. This procedure requires only that the trap is harmonic and that the imaging process is linear in the atomic density. No additional calibrations are needed.

We fit the full two-dimensional distribution using a Levenberg-Marquardt algorithm [36, 37] implemented in MATLAB. In order to speed up the calculation of the dilogarithm we use a look-up table with 10^6 entries on a logarithmic grid together with a linear interpolation scheme. In addition, all fit functions are written in such

2. Statistical mechanics

a way that they can handle all points of an image in a single call, thereby massively reducing the overhead associated with function calls and loops. In order to ensure reproducible starting conditions for the Fermi-Dirac fit we perform a pre-fit using a Gaussian distribution and initialize the Fermi-Dirac fit with $z = 10^{-5}$ and the results of the pre-fit.

As the fugacity diverges for small reduced temperatures (cf. fig. 2.3) we alternatively use the logarithm of the fugacity as free fit parameter. Due to the different convergence characteristics of the two methods their results start to differ at our coldest clouds.

The results of these fitting procedures can be seen in figure 2.6. As expected for a degenerate Fermi gas, the distribution cannot be fitted with a Gaussian anymore. The black and green lines show the results of the two varieties of Fermi-Dirac fits, which are barely discernible, although the resulting temperatures differ by almost a factor of two.

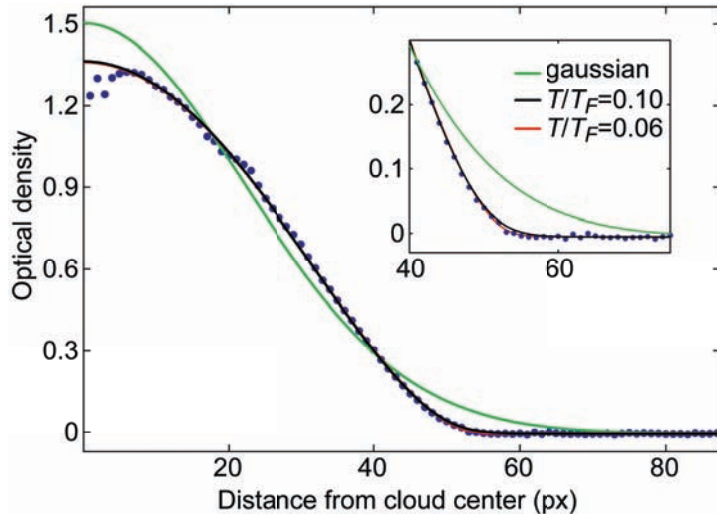


Figure 2.6.: Azimuthally averaged cloud together with several fits: Blue dots represent the measured data and the line indicates the best Gaussian fit. The black and green lines show the result of the two Fermi-Dirac fitting procedures described in the text. The fits were performed on the full two-dimensional distribution before the azimuthally averaging.

Figure 2.7 shows the result of Fermi-Dirac fits of the same image using various fixed fugacities. For low reduced temperatures significant differences can be seen only at the wings of the distribution around 55px away from the center of the image. The thickness of this "significance shell" shrinks rapidly with decreasing temperature. This effectively limits this fitting method to temperatures $T/T_F \gtrsim 0.1$ due to imaging noise (cf. inset in fig. 2.6). In addition anharmonic terms in the potential need to be taken into account at these cold temperatures.

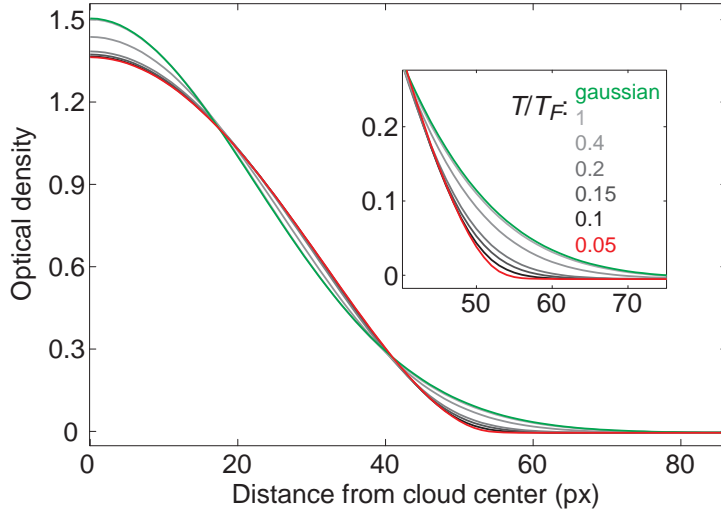


Figure 2.7.: Examples of Fermi-Dirac fits: The same image as in Fig. 2.6 was fitted for various fixed fugacities to illustrate the effect of temperature on the distribution. For low reduced temperatures the only significant difference occurs in the wings of the cloud (inset). The area with significant differences strongly decreases with temperature.

2.3. Ensembles

In statical mechanics three standard types of ensembles are used:

- A *microcanonical ensemble* is completely isolated from its environment and is characterized by a fixed particle number N and fixed total energy E .
- The *canonical ensemble* is in thermal contact with a heat reservoir, which imposes its temperature T on the ensemble. It can be described by the still fixed particle number N and the temperature.
- The *grand canonical ensemble* is coupled to a particle reservoir with chemical potential μ in addition to the heat reservoir. It is characterized by temperature T and chemical potential μ .

In the experiment the situation differs from all three ensembles:

After evaporative cooling the system is in principle isolated from the environment and is characterized by an atom number N and a fixed total entropy S .

In contrast to a microcanonical ensemble, however, several parameters (trap frequency, lattice depth, interaction strength) are controlled externally via classical parameters. Ideally, all changes of these parameters are performed slowly enough to be adiabatic and therefore conserve the entropy (isentropic processes). Thereby the total energy E and the temperature T of the system will change but atom number and entropy per particle remain constant. In the experiment, however, the chosen timescales are compromises between the adiabaticity requirements and technical heating (cf. sec. 7ff).

3. Interactions

The role of interactions in the field of degenerate quantum gases can hardly be overestimated, as any experimental study of ultracold atoms would be impossible without interactions between the atoms: Elastic collisions are one of the key requirements for evaporative cooling, since they redistribute momentum and energy between the atoms and are therefore a necessary condition for thermalization. But far beyond this "technical necessity" for interactions, they are also the key to the richness of ultracold atoms: Interactions induce correlations between the atoms and are thereby responsible for all of the intriguing many-body physics beyond the "bare" Bose-Einstein or Fermi-Dirac statistics, ranging from Bogoliubov excitations in weakly interacting Bose gases [38] to strongly interacting phases like Mott insulators (cf. sec. 5.5.2) or antiferromagnetically ordered phases (cf. sec. 5.5.2).

One of the most important features of ultracold atoms is the possibility to freely tune the effective interactions by use of Feshbach resonances (cf. sec. 3.3). In many cases, including fermionic ^{40}K in a lattice, it is possible to tune the interaction from strongly attractive over non-interacting to strongly repulsive by simply changing the magnetic field. This allows systematic tests of theoretical models as a function of interaction strength. In addition, Feshbach resonances can be used in order to produce weakly bound molecules, so-called *Feshbach molecules* (cf. sec. 3.3.2).

In the context of simulating condensed matter physics in optical lattices, the most important characteristic of the interactions between the atoms is their short-range character, which allows an easy theoretical description in terms of a contact potential (cf. sec. 3.2.3) and is well suited to implement important model hamiltonians like the Hubbard model (cf. sec. 5).

3.1. Types of interactions

The dominant character of the interaction between two atoms depends crucially on their distance. Restricting the discussion in a first step to ground state alkali atoms and neglecting all relativistic effects like spin-orbit coupling and hyperfine interactions, two regimes remain [39]:

- At long distances, where the electron clouds of the atoms are well separated, the interactions are dominated by the dipole-dipole interaction between mutually induced dipole moments, the *van der Waals* interaction,

3. Interactions

which scales as $V_{vdW} = -C_6/R^6$ in the binding case. Here R denotes the internuclear separation. The range of this potential is given by the *van der Waals length*

$$l_{vdW} = \frac{1}{2} \left(\frac{mC_6}{\hbar^2} \right)^{1/4} \quad (3.1)$$

In the case of ${}^{40}\text{K}$ the van der Waals coefficient in the electronic ground state is (in spectroscopic units) $C_6 = 0.189 \times 10^8 \text{ cm}^{-1} \text{\AA}^6$ [40] and the corresponding van der Waals length is $l_{vdw} = 65 a_0 = 3.4 \text{ nm}$.

- At short distances the electron clouds start to overlap and give rise to a quantum mechanical exchange interaction that depends crucially on the relative spin of the outer electrons and splits the electronic ground state potential into two curves, the singlet potential $X^1\Sigma_g$ and the triplet potential $a^3\Sigma_u$.

In the Born-Oppenheimer approximation [39] these interactions give rise to the *non-relativistic Born-Oppenheimer potentials*, which are shown in Figure 3.1 for the electronic ground state and the first excited state (s+p) of two potassium atoms. If one atom is in the excited state, the dominating long-range term is a resonant dipole-dipole interaction of the form $V_{dd} = \pm C_3/R^3$, which can intuitively be understood by considering each atom as being in a superposition of ground and excited state [41]. The range of this dipole-dipole interaction greatly exceeds that of the van der Waals interaction. In addition, the effects of the much weaker spin-orbit interactions can be incorporated into these potentials and become dominant at large distances, where the van der Waals potential is small. For negative total energies these potentials give rise to many bound molecular states, for positive energies the eigenstates are the scattering solutions.

The above picture of independent potentials reaches its limits, however, if one tries to include hyperfine interactions, as these couple different Born-Oppenheimer potentials and especially can couple singlet and triplet states and thereby effectively render any collision problem into a multichannel problem. The potentials essentially form a spin-dependent potential matrix, whose elements describe the (position dependent) interactions between the different spin states [42]. Following [41], one should think of the collision process as a kind of interferometer:

”A wave starts inward from long range. When the wave reaches the distance where the hyperfine and exchange interactions become comparable in size, the wave splits. One part of the wave samples the singlet potential and one part samples the triplet potential. The two parts bounce off the inner wall of their respective potentials and recombine on the way back out. Finally, the interference between the incoming wave and the outgoing wave establishes the nodal pattern of the scattering wave function.”

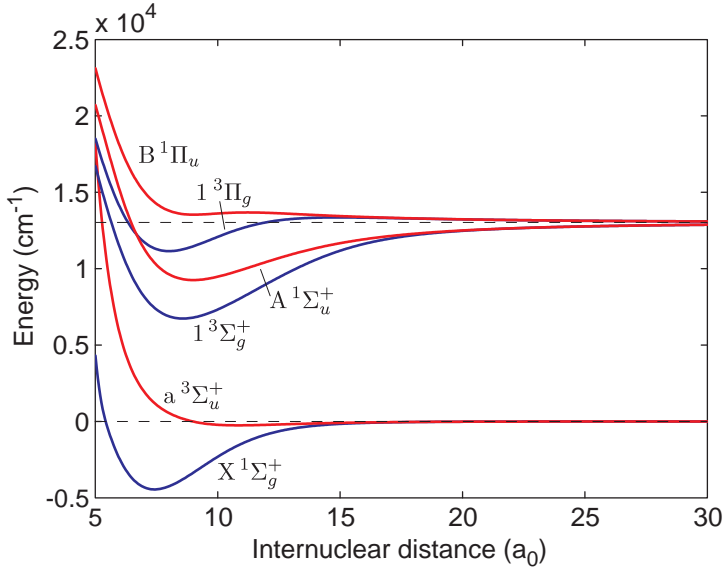


Figure 3.1.: Molecular potentials (Born-Oppenheimer potentials) between two ^{40}K atoms. Plotted are the singlet (blue) and triplet (red) potential in the electronic ground state ($X^1\Sigma_g$, $a^3\Sigma_u$) and those four excited potentials that can be reached by an (electric) dipole transition (red resp. blue). The ground state potentials are taken from reference [40] and the excited state calculations were performed by O. Dulieu (priv. comm.).

In the following the collisional channels will be labeled by the pair of atomic hyperfine states with which they coincide at large internuclear distances and small magnetic fields.

In principle, also three body interactions would need to be considered, but due to the low density of ultracold atoms and the short range of the dominant interactions, three body interactions can mostly be ignored. The only exception are inelastic three-body collisions, where a single collision can lead to the loss of three particles (cf. sec. 3.3.1).

3.2. Scattering theory

The multitude of interactions described in the previous section gives rise to a variety of elastic and inelastic collision processes, whose probabilities can be calculated using scattering theory [43].

Elastic collisions, which do not alter the relative kinetic energy, can nonetheless redistribute momentum between the atoms and are responsible for thermalization within the ensemble.

In addition, they change the many-body wavefunction and thereby give rise to the interaction energy (cf. below) and create correlations between the particles. In inelastic collisions on the other hand, internal energy gets converted into kinetic

3. Interactions

energy. Due to the large hyperfine and molecular energies involved, an inelastic collision will almost always result in a particle loss, as the typical increase in kinetic energy is much larger than the trap depth.

3.2.1. Elastic scattering

Without interactions the relative wave function of two (distinguishable) particles in the internal states $|a\rangle$ and $|b\rangle$ can be written as $\Psi_0(\vec{R}) = e^{i\vec{k}\cdot\vec{R}} |a, b\rangle$, where \vec{k} denotes their relative momentum and R the interatomic distance. Elastic scattering can now change this relative momentum and at large interparticle distances R , beyond the range of the interactions, the effects of the interactions can be incorporated into the wavefunction via

$$\Psi_{IA}(\vec{R}) \propto \left(e^{i\vec{k}\cdot\vec{R}} + \frac{e^{ik'R}}{R} f(E, \hat{k}, \hat{k}') \right) |a, b\rangle \quad (3.2)$$

where $f(E, \hat{k}, \hat{k}')$ denotes the *scattering amplitude*. Its square ($|f|^2$) describes the probability that a pair of atoms with collision energy E is scattered from relative momentum \vec{k} to relative momentum \vec{k}' [43]. Energy conservation requires $k = k'$ and the overall effect of the collision can be summarized by the *collisional cross section* $\sigma(E)$, which is defined as the integral of $|f|^2$ over all relative momenta for a given collisional energy.

The problem can be simplified tremendously by using spherical coordinates and expanding both the incoming plane wave and the scattered wave into spherical harmonics. In this expansion the scattering amplitude becomes a tensor $f_{lm'l'm'}$ and describes the probability to scatter a pair of particles from the relative angular momentum state lm to $l'm'$. In most cases one can neglect any anisotropies like e.g. dipole-dipole interactions [44] and angular momentum is conserved. As a consequence, the scattering problem decouples into independent angular momentum channels: $l = l'$, $m = m'$. The type of the collision is labeled accordingly as an *s*-wave collision for $l = 0$, *p*-wave for $l = 1$ and so on.

3.2.2. Ultracold collisions

In the case of ultracold atoms, additional simplifications arise due to the fact that at ultracold temperatures the thermal de Broglie wavelength of the relative motion is much larger than the range of the interaction. Together with the small density of ultracold gases, which ensures that also the mean distance between the atoms is large compared to the range of the interaction, this results in an inability to resolve details of the potential during the collision and leads to quantum threshold effects [43]:

3.2. Scattering theory

In the limit of small momenta k , the scattering amplitude for s -wave collisions $f_s(k)$ can be expressed by the following expansion [45]:

$$f_s(k) = -\frac{1}{a_s^{-1} + ik + k^2 r_{eff}/2 + \dots} \quad (3.3)$$

Here a_s is the (s -wave) *scattering length* and r_{eff} denotes the effective range of the interaction, which typically is on the order of the van der Waals length. A positive scattering length corresponds to a repulsive effective interaction while a negative value denotes an attractive effective interaction.

In most cases, except close to Feshbach resonances (cf. below), the scattering amplitude is dominated by the scattering length, the cross section σ_s becomes energy independent and is given for distinguishable particles by:

$$\sigma_s = 4\pi a_s^2 \quad (3.4)$$

In the case of two indistinguishable fermions, s -wave collisions are impossible since the Pauli principle prohibits the occurrence of a relative s -wave state. As a consequence, a spin mixture of two hyperfine states is needed in order to have s -wave collisions in a Fermi gas.

But even in a spin mixture the fermionic nature shows a strong influence on the interactions in a many-body system: While the effective cross section is given by the value for distinguishable particles (cf. eq. 3.4) in the classical regime ($T/T_F \gtrsim 1$) it decreases in the quantum degenerate regime and ultimately vanishes at zero temperature. This effect is referred to as *Pauli blocking* and is caused by the decreasing number of available scattering states [46].

In the case of non-vanishing angular momentum $l \geq 1$ the effective potential includes a repulsive centrifugal potential: $\hbar^2 l(l+1)/(2\mu R^2)$. This centrifugal barrier gives rise to classical turning points, which, for low enough momenta, lie outside of the interaction potential and thereby suppress these collisions. For p -wave interactions, the cross section scales as $\sigma_p(E) \propto E^2$ for low energies and p -wave collisions can be safely ignored at typical trap temperatures [47] away from p -wave Feshbach resonances (cf. next section).

3.2.3. Contact interaction

In most relevant cases the details of the potential are unimportant since both the average distance between the particles and their relative de Broglie wavelength greatly exceed the range of the interactions. As a consequence, as long as they reproduce the correct scattering lengths, easier model potentials can be used instead of the exact potentials. In the case of a smooth relative wavefunction without a singularity the complete interaction potential can be replaced by a point like contact interaction with a delta-function potential

$$V_{CI}(\vec{x} - \vec{x}') = \frac{4\pi\hbar^2 a}{2\mu} \delta^3(\vec{x} - \vec{x}') \quad (3.5)$$

3. Interactions

which reproduces the correct physics at low momenta [45].

3.3. Feshbach resonance

While a fully repulsive potential necessarily creates a positive scattering length, a typical interatomic potential can produce any real scattering length ($-\infty \leq a \leq \infty$), since it depends on the phase a pair of atoms acquires during the traverse of the interatomic potentials. Even more, for a given form of the potential the scattering length is an oscillatory function of the potential depth, as it specifically depends on the position of the last bound state in the potential [45] and more and more bound states appear for increasing potential depths.

On the one hand, this oscillatory behavior renders a theoretical ab-initio prediction of the scattering length nearly impossible, but on the other hand it opens the possibility to gain full control over the scattering length using only minuscule changes in the interactions.

The key to manipulating the scattering length stems from the coupling between different atomic states with the same spin projection $M = m_1 + m_2$ but different total magnetic moments [48]. The relative offset energies between the different states in this multichannel scattering problem can be tuned via the magnetic field, as their different magnetic moments result in relative Zeeman shifts. Typically, the atoms enter the collision in the lowest of the involved energy channels, which is often referred to as the open channel. The second involved channel at higher energy is called the closed channel, since the atoms do not possess enough energy to separate in this potential.

The relative Zeeman shifts between these two channels can be used to tune the energy of the last bound state of the multichannel potential into resonance with the kinetic energy of the atoms in the incoming hyperfine state. This results in a *Feshbach resonance* where the scattering amplitude is greatly enhanced by the resonant coupling to the molecular state. The scattering length in fact diverges at the resonance [49–53] and is given by [54]:

$$a(B) = a_{bg} \left(1 - \frac{w}{B - B_0} \right) \quad (3.6)$$

Here a_{bg} denotes the background scattering length away from the resonance, w the width of the resonance and B_0 the resonance position. The resulting scattering length is plotted in figure 3.2 for a Feshbach resonance between the two lowest hyperfine states ($|F, m_F\rangle$) $|9/2, -9/2\rangle$, $|9/2, -7/2\rangle$ in fermionic ^{40}K . This resonance was used to control the interaction in all experiments in this thesis: While the scattering length is positive for magnetic fields below the Feshbach resonance (the so-called *BEC side*), the interaction is attractive ($a < 0$) directly above the resonance (the so-called *BCS side*, cf. below). For larger fields the scattering length shows a zero crossing before it rises to the positive background scattering length.

3.3. Feshbach resonance

In ultracold gases, Feshbach resonances were first observed in 1998 by various groups [55–58] using bosonic atoms. In fermionic ^{40}K the first Feshbach resonances were predicted using a numerical coupled channels calculation in 2000 [59] followed by a first observation in 2002 by the group of D. Jin at JILA [60]¹. First experiments using a Feshbach resonance in ^{40}K in optical lattices were performed in the group of T. Esslinger at the ETHZ [62, 63]

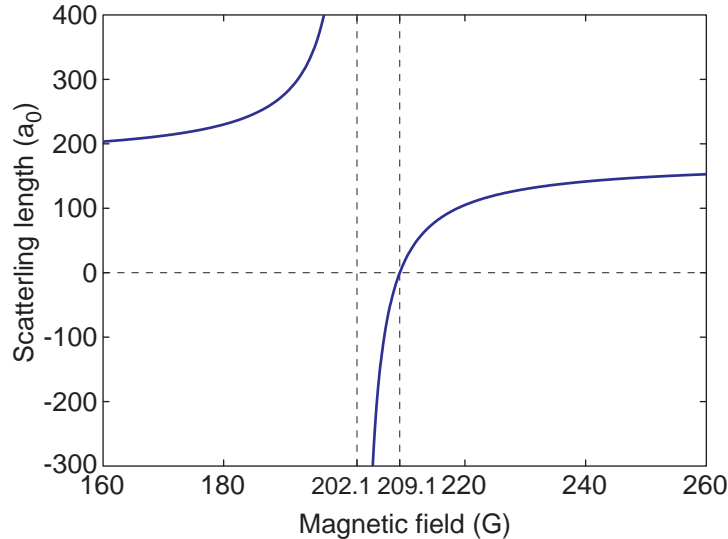


Figure 3.2.: Scattering Length between the two lowest hyperfine states ($|9/2, -9/2\rangle$, $|9/2, -7/2\rangle$) in fermionic ^{40}K . Background scattering length a_{bg} and resonance position B_0 are taken from the JILA parametrization [61], the resonance width w was taken from our measurement of the free expansion in a lattice (cf. sec. 10.3.5).

3.3.1. Losses at Feshbach resonance

In addition to the change in scattering length a Feshbach resonance also strongly enhances inelastic collisions. This magnetic field dependent losses are often used to search for Feshbach resonances. We extended this search to several new combinations of hyperfine states in ^{40}K , the results are summarized in table 3.1.

Figures 3.3 and 3.4 show two examples of these loss features obtained with a mixture of $| -7/2 \rangle$ and $| -3/2 \rangle$ atoms and a mixture of $| -9/2 \rangle$ and $| -5/2 \rangle$: In the first mixture a single s -wave resonance at 260 G can be seen, while the second mixture shows in total three resonances. The sharp feature at 224 G corresponds to the well-known s -wave resonance between the $| -9/2 \rangle$ and $| -5/2 \rangle$ atoms while the feature at 245 G is also present in a pure $| -5/2 \rangle$ sample and can therefore be ascribed to a p -wave resonance in the $| -5/2 \rangle$ channel.

¹The same group also characterized most known Feshbach resonances in ^{40}K , their results are most coherently presented in the PhD Thesis of Cindy Regal [61]

3. Interactions

open channel ($ m_F\rangle$)	l	B_0 (G)	w (G)	prev. observation
$ -9/2\rangle + -7/2\rangle$	s	202.1	7.0 ± 0.2	[60, 64–68]
$ -9/2\rangle + -5/2\rangle$	s	224.2	9.7 ± 0.6	[62, 69, 70]
$ -7/2\rangle + -5/2\rangle$	s	~ 174	~ 7	[61]
$ -7/2\rangle + -3/2\rangle$	s	168.5 ± 0.4	-	-
$ -7/2\rangle + -3/2\rangle$	s	260.3 ± 0.6	-	-
$ -7/2\rangle$	p	~ 198.8	-	[63, 64, 71]
$ -5/2\rangle$	p	245.3 ± 0.5	-	-
$ -9/2\rangle + -5/2\rangle$	p	215 ± 5	-	-

Table 3.1.: List of Feshbach resonances observed in our experiment for various hyperfine combinations in the $F = 9/2$ hyperfine ground state. Values printed in bold type are new or improved measurements, all other values are taken from [61]. The assignment of s -wave (p -wave) character to the new resonances was done according to independent numerical coupled channels calculations performed by P. Julienne and J. Bohn (private communication).

In addition to these two sharp loss features there is a very broad loss feature spanning from 200 G to 240 G. We attribute this loss process to a p -wave resonance between the $|-9/2\rangle$ and $|-5/2\rangle$ channels. In this resonance the open channel is coupled to the same channels that are also involved in the well known p -wave $|-7/2\rangle$ resonance at 199 G, which has the same total spin projection $M = -7$. The presence of this loss channel prevents us from using the, otherwise very convenient, s -wave resonance between the $|-9/2\rangle$ and $|-5/2\rangle$ atoms at 225 G. All observed features in this mixture agree well with a coupled channels calculation by Paul Julienne (private communication).

3.3.2. Feshbach molecules

Directly below the Feshbach resonance, where the scattering length is large and positive, the binding energy of the last multichannel bound state is very small and is approximately given by:

$$E_b = \frac{\hbar^2}{ma^2} \quad (3.7)$$

These *Feshbach molecules* are exceptionally large halo molecules: Their size (mean internuclear distance) is given by the scattering length $\langle r \rangle = a/2 \approx 70$ nm @201.6 G and can greatly exceed the van der Waals length ($l_{vdw} 65 a_0 = 3.4$ nm) [72]. In figure 3.5 the molecular wavefunction is plotted for different magnetic fields: While the form of the wavefunction hardly changes in the closed channel, the large outer maximum in the open channel extends to larger and larger distances upon approaching the Feshbach resonance.

These molecular states can experimentally be occupied in several ways [48]. The most widely used way to convert pairs of atoms into molecules is a Landau-Zener

3.3. Feshbach resonance

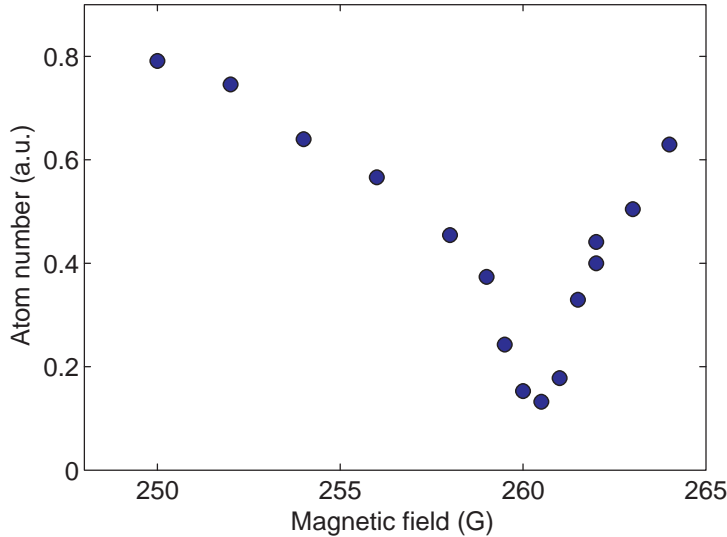


Figure 3.3.: Atom number of a $| -7/2 \rangle$ plus $| -3/2 \rangle$ spin mixture after a hold time at various magnetic fields. One sees one loss feature at 260 G that can be attributed to an s -wave Feshbach resonance in this channel.

type sweep of the magnetic field over the resonance, starting on the BCS side at $a < 0$ and ramping to the BEC side with $a > 0$ [73–75]. The efficiency of these *Feshbach sweeps* for a gas of atoms can be calculated using a simple phase-space model and can serve in the adiabatic case, where the sweep rate is sufficiently slow, as a thermometer for the weakly interacting gas in the dipole trap [76]. In order to prove that the atoms are really transferred into molecules, and not just lost from the trap, an inverse ramp is used to dissociate the molecules. The observed increase in atom number during this dissociation sweep, which is shown exemplarily in figure 3.6, is a direct proof for the creation of the molecules.

Especially in ${}^6\text{Li}$ ultracold molecules can be created by performing evaporative cooling at magnetic fields on the BEC side of the Feshbach resonance. During the final evaporative cooling the atoms are converted into molecules through three-body collisions [77]. Another method, which in addition allows to measure the binding energy of the molecules, is the use of radio-frequency pulses to convert atoms into molecules or vice versa [66, 73].

In the case of bosonic atoms, the lifetime of the resulting molecules is very short [55, 78–80], as the molecules are created in the highest rovibrationally excited state and can decay to deeper bound states by inelastic collisions with a third atom.

For fermionic atoms on the other hand, this process is highly suppressed by the Pauli principle, as it requires a close approach of two identical fermions [81, 82]. Especially in the case of ${}^6\text{Li}$, this leads to extraordinarily long lifetimes on the order of seconds [74]. In ${}^{40}\text{K}$ the achievable lifetimes depend on the magnetic field and are on the order of 1 – 100 ms [83] with the longest lifetimes being observed directly below the Feshbach resonance. In a sufficiently deep lattice with one molecule per lattice sites these collisions are suppressed and even for bosonic

3. Interactions

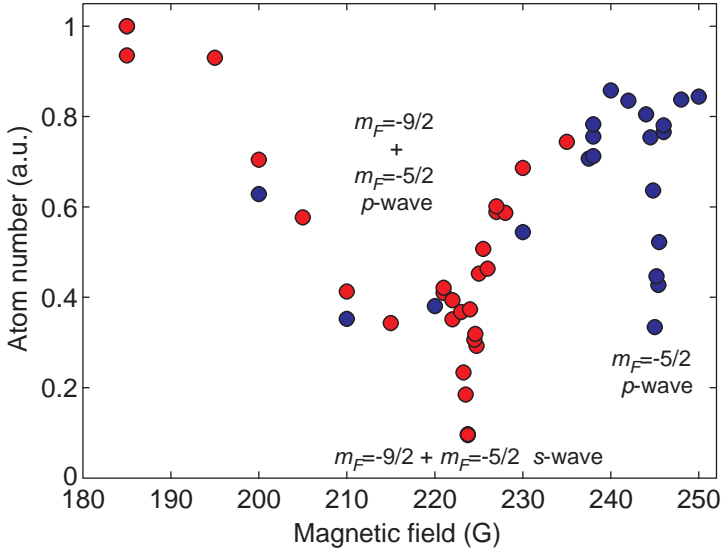


Figure 3.4.: Atom number of a $| -9/2 \rangle$ plus $| -5/2 \rangle$ spin mixture after a hold time at various magnetic fields. The colors correspond to independent experimental runs.

molecules long lifetimes up to 700 ms could be observed [84].

Feshbach molecules can be used as a starting point for the creation of ultracold ground-state molecules [11, 12], which in the case of heteronuclear molecules offer the possibility to study many-body physics in the presence of huge dipolar interactions [11].

We have used Feshbach sweeps in a deep lattice in order to convert pairs of atoms on the same lattice site into molecules and thereby detect double occupied lattice sites (cf. sec. 6.6). During the optimization of the blue-detuned lattice we studied the effects of blue-detuned light onto Feshbach molecules. The resulting photodissociation spectra are presented in the appendix (cf. sec. A) and can be used to gain direct information about the molecular wavefunction.

3.3.3. BEC-BCS crossover

The influence of Feshbach resonances on the many-body states of a fermionic spin mixture has received a lot of attention in recent years and is now commonly referred to as the BEC to BCS crossover [45]: The presence of interactions can have dramatic consequences on the many-body state of fermionic spin mixtures. Without interactions, there would be no coupling between the different spin components and the many-body ground state would consist of two independent Fermi seas. The probably most dramatic consequence of interactions is the possibility for fermions to become bound together into bosonic pairs, which then can Bose condense into a superfluid state.

3.3. Feshbach resonance

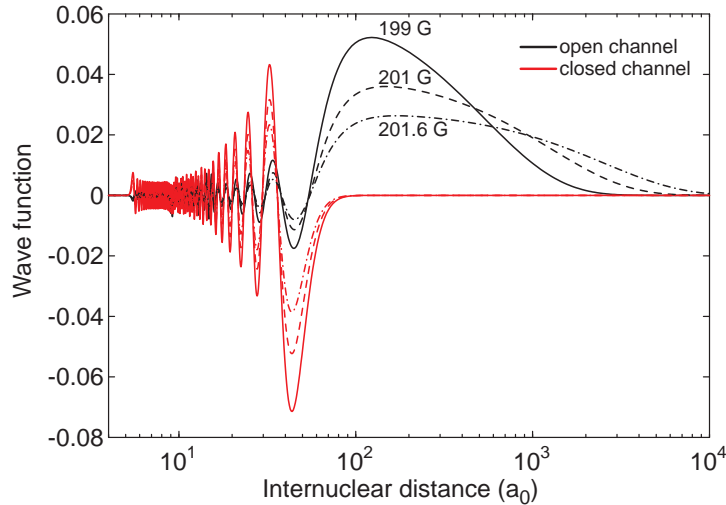


Figure 3.5.: Wavefunctions of a Feshbach molecule in the open channel/closed channel basis for the ${}^{40}\text{K}$ Feshbach resonance at 202.1 G. The open channels corresponds to a pair of atoms in the $|F=9/2, m_F=-9/2\rangle + |9/2, -7/2\rangle$ hyperfine states while the closed channel corresponds to $|9/2, -9/2\rangle + |7/2, -7/2\rangle$. Note the logarithmic scaling of the x-axis. The results were obtained by P. Julienne using a numerical coupled-channels calculation.

Far above the Feshbach resonance, where the two-body interaction is weakly attractive ($a < 0$), the many-body ground state is given by the well known BCS superfluid [24, 85, 86]. It was shown in 1957 by Bardeen, Cooper, and Schrieffer that an arbitrarily weak attractive interaction between the spin components leads to the Cooper instability: Even though there exists no two particle bound state with negative energy, the energy of a bound spin singlet state of two fermions with opposite momenta nonetheless is less than two times the Fermi energy. At sufficiently low temperatures all particles around the Fermi surface are bound into these *Cooper pairs* which condense and form a BCS superfluid. The critical temperature for superfluidity in the BCS regime is given by [45]:

$$T_{C,BCS} = 0.61e^{-\pi/(2k_F|a|)} \quad (3.8)$$

Here k_F denotes the wavevector at the Fermi momentum. The critical temperature is exponentially small for weak interactions, but rises to experimentally reachable temperatures close to the Feshbach resonance, where $1/|k_F a|$ is on the order of one.

Far below the Feshbach resonance on the other hand, there exists a weakly bound molecular state and the two particle interaction is repulsive ($a > 0$). At low temperatures the fermionic atoms form bosonic diatomic Feshbach molecules which can Bose condense, forming a superfluid BEC of molecules. In this limit the formation of pairs (molecules) and the condensation of these pairs happen at two

3. Interactions

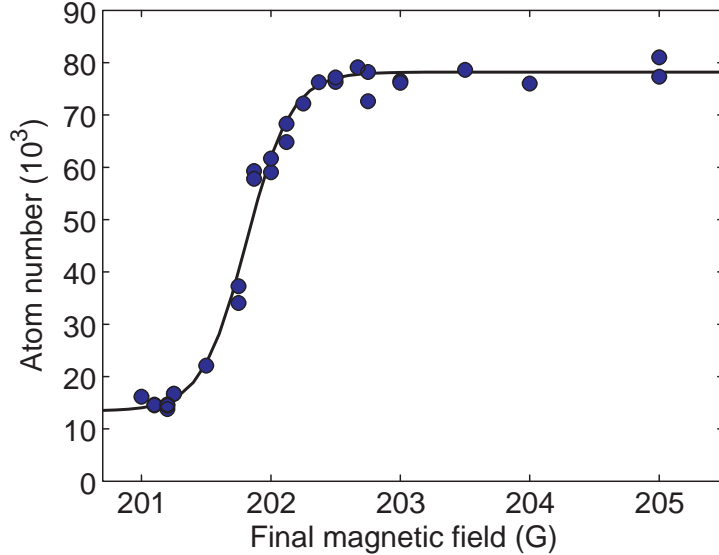


Figure 3.6.: Atom number of a $| -9/2 \rangle$ plus $| -7/2 \rangle$ spin mixture after a Feshbach ramp to 201 G followed by a dissociation ramp to a variable final value. The detected molecule fraction of $83 \pm 5\%$ is consistent with an initial temperature of $T/T_F \leq 0.15$ [76].

distinct temperatures: The pair formation happens at a temperature T^*

$$T_{BEC}^* \approx \frac{1}{3} \frac{|E_b|}{W\left(\left(\frac{\pi}{6}\right)^{\frac{1}{3}} \frac{|E_b|}{2E_F}\right)} \quad (3.9)$$

that scales with the binding energy of the molecule E_b ² [45].

Away from the resonance, where the size of the molecule is small compared to the intermolecular distance and the interaction is weak, the temperature of the superfluid transition approaches that of a non-interacting Bose gas with twice the mass and half of the density:

$$T_{C,BEC} = 0.22E_F \quad (3.10)$$

It turned out that these two limits are connected by a smooth crossover, the so-called *BEC-BCS crossover*, which is by now well studied in the dipole trap. Experiments have observed superfluidity of the gas on the BEC side of the resonance and in the strongly interacting crossover regime where $1/|k_F a| < 1$ [65, 87–94]. Upon varying the interactions, the system evolves smoothly from the BCS regime, where the pair size (the size of a Cooper pair) is large compared to the interatomic distance and its binding energy is small, through the crossover regime, where the system is strongly interacting and the pair size is comparable to the interparticle spacing, all the way to the BEC limit, where the pair size (the size of the molecule)

²Here $W(x)$ denotes the Lambert W-function, which is the solution to $x = We^W$ and can be expanded into $W(x) \approx \log(x) - \log(\log(x))$ for $x > 3$.

3.4. Light assisted collisions

is smaller than the interatomic distance and its binding energy is large compared to the Fermi energy.

But not only the superfluid phase is affected by the BEC-BCS crossover: The normal state varies from an essentially non-interacting Fermi gas of atoms to a weakly interacting Bose gas in the so-called *pseudogap regime*. In this regime, where the fermions are paired but the pairs are not condensed, bosonic excitations are more important than fermionic excitations and e.g. the spin susceptibility is strongly reduced.

Especially in the crossover region, where both bosonic and fermionic excitations are relevant, this can lead to intriguing effects, e.g. the formation of polarons in strongly imbalanced mixtures [95, 96].

3.4. Light assisted collisions

An additional type of collisions, which becomes important in the presence of strong light fields, i.e. laser fields, is termed *light assisted collisions* or *radiative collisions*. These are collisions between a ground state and an excited state atom, or, more precisely, the term describes a collision between two atoms where one atom absorbs a photon during the collision.

Due to the long-range dipole-dipole interaction between a ground states and an excited state atom (cf. sec. 3.1), the excitation results in a strong force between the atoms:

In the blue detuned case the potential is repulsive and accelerates the atoms away from each other until the excited atom returns to its electronic ground state via the spontaneous emission of a photon. Due to the high gain in kinetic energy, which is on the order of a fraction of the photon detuning, the atoms will typically be lost from the trap.

In the red-detuned case on the other hand, the atoms will be excited into a bound molecular state in the excited potentials, whose subsequent decay can also lead to a loss of the atoms.

An intuitive model for the rate of these collisions can be gained from the *Franck-Condon principle*, that is the approximation that both the position and the kinetic energy of the nuclei remain constant during the absorption of the photon. Roughly speaking, the timescale of the optical transition is fast compared to the typical timescales for the motion of the nuclei, and the photon momentum is small compared to the momenta of the nuclei.

As a consequence, for every photon energy the transition happens dominantly at the *Condon points* R_c , where the photon energy $\hbar\omega_L$ matches the difference between the potential energies:

$$\hbar\omega_L = E_{\text{es}}(R_c) - E_{\text{gs}}(R_c) \quad (3.11)$$

3. Interactions

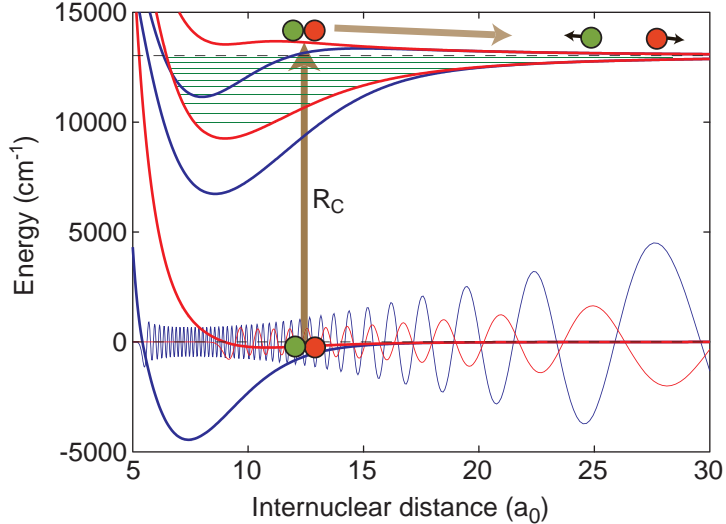


Figure 3.7.: Cartoon picture of a light assisted collision. Thick red and blue lines denote the molecular triplet and singlet potentials from fig. 3.1. Thin lines denote the resp. wavefunctions in those potentials calculated by P. Julienne using a couple channels calculation. Thin green lines denote some bound molecular states in the excited potentials (sketch). During a light assisted collisions a pair of atoms is excited at the Condon point R_C into the repulsive excited potential, where the atoms are accelerated and gain a fraction of the photon detuning as kinetic energy before they return to the ground state via a spontaneous emission.

Here E_{gs} and E_{es} denote Born-Oppenheimer potentials (cf. sec. 3.1) between two ground state atoms (E_{gs}) or one ground state and one excited atom (E_{es}). The relevant potentials in the case of two ^{40}K atoms are depicted in figure 3.7 together with a typical ground-state wavefunction.

In a quantum mechanical calculation the transition probability between two molecular states (either bound or unbound) is proportional to the *Franck-Condon factor*, which describes the overlap between the nuclear wave functions:

$$FCF(\text{gs}, \text{es}) = \left| \int \Psi_{\text{es}}^*(R) \Psi_{\text{gs}}(R) dR \right|^2 \quad (3.12)$$

Here $\Psi_{\text{gs}}, \Psi_{\text{es}}$ denotes the molecular wavefunctions in the ground and excited state and R is the internuclear distance. Typically, the strongest contribution to this integral stems from the vicinity of the Condon points [39].

In the red-detuned case, i.e. light which is red-detuned with respect to the atomic transition, the resonant absorption of a photon is only possible if the detuning of the light matches the binding energy of a molecular state in the excited potentials, as depicted in figure 3.7.

This is in stark contrast to the blue-detuned case, where unbound states in the scattering continuum are excited and a resonant absorption is possible for all blue detunings. This has important consequences for the use of red-/blue-detuned light

3.4. Light assisted collisions

(cf. sec. 4.1) in the trapping and manipulation of ultracold atoms: While in the red-detuned case light assisted collisions can be efficiently suppressed by detuning the laser from the molecular resonances [84], they are always present for blue-detuned light.

In the case of not too large detunings ($\Delta \lesssim 200 \text{ cm}^{-1}$), the Condon point lies at rather large internuclear distances $R_c \gtrsim 20 a_0$, where the derivative of the ground state van der Waals potential can be neglected in comparison to the derivative of the excited state dipole-dipole potential. In this case the *reflection approximation* shows that the Franck-Condon factor of the exciting transition in the blue-detuned case is simply proportional to the amplitude of the ground-state wave function at the Condon point [97, 98].

This was experimentally demonstrated by Vuletić *et.al.*: By use of a Feshbach resonance, they could suppress the collision rate for a given detuning by a factor of 15 by tuning the scattering length, and thereby the position of a node of the wavefunction, to the Condon point [99].

In the regime of larger detunings, like the ones used in this thesis for the creation of blue-detuned lattices (cf. sec. 4.3.1), the Condon points are located at smaller internuclear distances. There the form of the ground state wave function is fixed by the molecular potential and cannot be changed by the magnetic field.

As is shown in the appendix (cf. app. A), it is however still possible to significantly suppress light assisted collisions by use of a suitable lattice wavelength. Nonetheless, for the used parameters light assisted collisions give rise to an additional loss channel in the lattice, which selectively affects only doubly occupied lattice sites. In the non-interacting case the mean distance between two atoms occupying the same lattice site is on the order of the harmonic oscillator lengths (55 – 70 nm), which is already considerably smaller than the mean interparticle distance in a typical dipole trap. In the interacting case, however, the mean distance strongly depends on the sign and strength of the interactions. This results in a strong interaction dependence of the lifetime of doubly occupied sites (cf. sec. 9.6), which, at least for attractive interactions, creates a considerable heating rate.

Light assisted collisions are also responsible for the fast pair losses during fluorescence imaging in optical lattices, which have been observed recently [18, 19]. In addition, these collisions constituted a major limitation for the atom numbers achievable a MOT operated at low background pressure. They could eventually be circumvented by the use of *dark spot MOTs*, where most of the trapped atoms are pumped into a dark state of the cooling transition [100, 101].

4. Optical potentials: Dipole trap and lattice

4.1. Dipole potential

The interaction between atoms and light is probably the single most important tool for the creation, manipulation, and detection of ultracold atoms. The character of the interaction between a two-level atom and a monochromatic light field consists of two parts, namely the absorptive and the dispersive interaction. Their relative importance depends on the detuning $\delta = \omega - \omega_0$ between the frequency ω of the light field and the transition frequency of the atom ω_0 [102].

This chapter mainly deals with the resulting dipole potentials in the case of large detunings and describes the red-detuned dipole trap and the blue-detuned optical lattice used in the experiments.

Absorptive interaction The absorptive part of the interaction describes the scattering of photons from the incident light field by the atoms. It consists of the absorption of an incident photon followed by a spontaneous emission into another mode. If a two-level atom is continuously illuminated with a not too far detuned monochromatic light field ($\delta \gg \Gamma$, $\delta \ll \omega_0$) of intensity I , the average scattering rate is given by [103]:

$$\Gamma_{sc} = \frac{3\pi c^2}{2\hbar\omega_0^3} \left(\frac{\Gamma}{\delta}\right)^2 I \quad (4.1)$$

Here Γ denotes the natural linewidth of the emitted fluorescence light and serves as a measure for the strength of an atomic transition.

This scattering process is used in the initial laser-cooling of the atoms (cf. sec. 7) and in absorption imaging [35]. When trapping ultracold atoms, however, photon scattering needs to be avoided: Scattering a photon transfers an average momentum of $p = \sqrt{2}\hbar k$ ($k = 2\pi/\lambda$) onto an atom that was initially at rest, which would lead to a severe heating of the cloud. Furthermore, the emission of the photon would localize the atom [104] and thereby severely alter any delocalized states.

4. Optical potentials: Dipole trap and lattice

Dispersive interaction The dispersive part of the interaction can be modeled by a Raman process where an atom can (virtually) absorb a photon from the monochromatic light field and re-emit it into the light field by stimulated emission. This creates a phase shift of the light, which is used in phase contrast imaging (cf. sec. 6.5) and induces energy shifts (light shifts) of the atomic levels [102]: For a two-level atom and not too large detunings $\delta \ll \omega_0$ the energy shift of the ground state creates the so-called *dipole potential*:

$$U_{\text{dip}} = \frac{3\pi c^2}{2\hbar\omega_0^3} \frac{\Gamma}{\delta} I \quad (4.2)$$

While the scattering rate decreases as I/δ^2 with detuning, the dipole potential scales as I/δ . For a given dipole potential the scattering rate therefore scales as $1/\delta$ and in general high intensities and large detunings are used in order to achieve the needed potential strength at the lowest possible scattering rate.

By using inhomogeneous intensity distributions $I(r)$ it is possible to create a wide variety of conservative potentials $U(r)$ in order to trap and manipulate atoms. The sign of the potential is given by the detuning of the light field:

- If the frequency of the light is smaller than the transition frequency of the atom ($\delta < 0$), the potential is called *red detuned* and negative. The potential minima coincide with the intensity maxima and ground state atoms experience a force towards high intensities, e.g. the center of a Gaussian beam.
- In the *blue-detuned* case ($\delta > 0$) the potential is positive and the atoms feel a force towards the intensity minima.

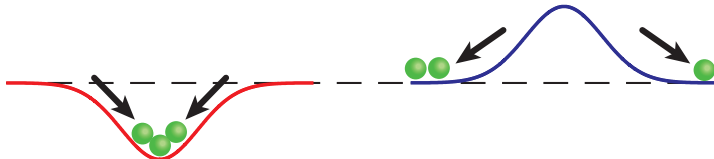


Figure 4.1.: Dipole potential due to a red (blue) -detuned Gaussian beam. The red detuned beam attracts the atoms while the blue-detuned beam repels them.

In the experiment a red-detuned dipole trap at $\lambda = 1030$ nm is used together with a blue-detuned optical lattice at $\lambda = 738$ nm.

Compared to equation 4.2, at these wavelengths two additional effects need to be taken into account: The lattice wavelength is close enough to the D lines of Potassium ($4s \rightarrow 4p$) and Rubidium ($5s \rightarrow 5p$) such that the spin-orbit coupling in the excited state and the resulting fine structure splitting into the D_1 and D_2 lines needs to be considered. The detuning of the dipole trap wavelength on the other hand is so large that an additional term proportional to $1/(\omega + \omega_0)$ becomes relevant. The resulting potential for linear polarized light is given by [103]:

$$U_{\text{dip}}(r) = \frac{\pi c^2}{2} \frac{\Gamma}{\omega_0} \left(\frac{1}{\omega - \omega_{D_1}} + \frac{1}{\omega + \omega_{D_1}} + \frac{2}{\omega - \omega_{D_2}} + \frac{2}{\omega + \omega_{D_2}} \right) \quad (4.3)$$

4.2. Crossed dipole trap

where Γ and ω_0 are averaged over the D_1 and D_2 lines.

One major advantage of optical potentials compared to magnetic potentials is their possibility to affect all spin states in the same way, provided that the detunings are large and linear polarizations are used. This opens the possibility to realize spin mixtures without differential potentials between the components and to access magnetic Feshbach resonances at arbitrary magnetic fields. In addition the strength of the potentials, and thereby the trap depth, can easily be controlled by varying the light intensity.

4.2. Crossed dipole trap

The dipole trap used in the experiment consists of two beams¹ traveling in the horizontal plane and intersecting each other at right angles (cf. fig. 4.2). The elliptical foci ($w_{0,\text{hor}}^x = 140 \mu\text{m}$, $w_{0,\text{vert}}^x = 30 \mu\text{m}$ and $w_{0,\text{hor}}^y = 170 \mu\text{m}$, $w_{0,\text{vert}}^y = 70 \mu\text{m}$) overlap and create an oblate (“pancake-shaped”) trap. In order to prevent unwanted interference effects, the two beams have orthogonal polarizations and a frequency offset of 160 MHz .

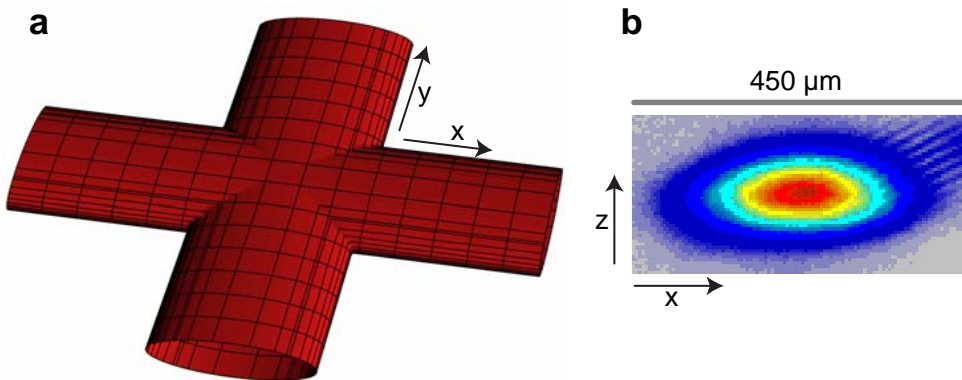


Figure 4.2.: left: The two dipole trap beams are focused to overlapping elliptical foci. right: The intensity distribution in one of the foci, the stripe pattern in the upper right corner is an artifact of interferences in the imaging path.

The resulting trapping potential is shown in figure 4.3 and consists of the sum of the two dipole potentials and gravity. As one can see in the left image, the trap is in general not isotropic in the horizontal directions. In most relevant cases, however, the atoms are confined to the central part of the trap, which can be well approximated by a harmonic potential.

In the vertical direction the influence of gravity shifts the potential minimum away from the beam center (“gravitational sag”). This shift becomes larger for weaker dipole traps until the so-called *trap bottom* is reached. Below the trap bottom the

¹The light for the dipole trap is created by a diode-pumped single-frequency Yb:YAG disc laser (Versadisc by ELS, now Sahajanand) that creates 18 W output power at $\lambda = 1030 \text{ nm}$.

4. Optical potentials: Dipole trap and lattice

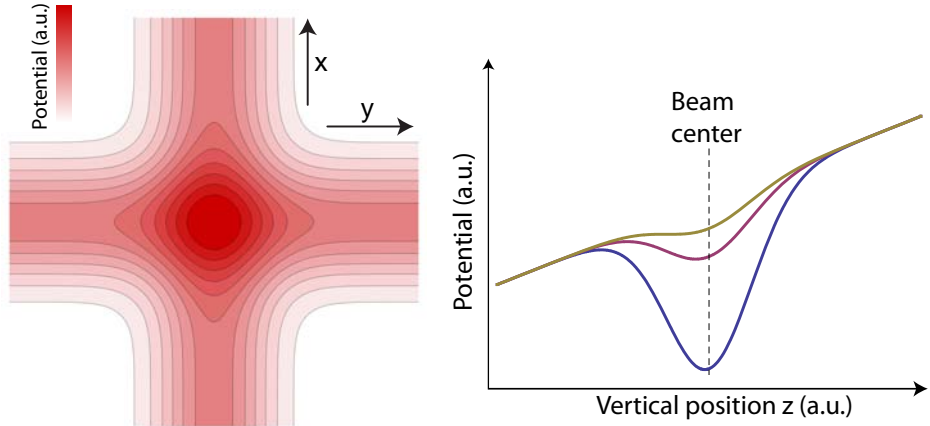


Figure 4.3.: Crossed dipole trap potential. left: Equipotential lines of the crossed dipole trap in the horizontal plane. In the center, the trap is isotropic in the horizontal plane. right: Trapping potentials along the vertical direction, consisting of the sum of dipole potentials of various strengths and gravity. Due to the influence of gravity the minimum position is shifted away from the center of the dipole beams (dashed line).

dipole potential cannot hold the atoms against gravity anymore.

In the case of a mixture of Rubidium and Potassium atoms this shift is especially important: The detuning of the dipole trap is large compared to the difference between the resonance frequencies, and the linewidths of the transitions are almost equal. This leads to approximately equal dipole potentials for both species while their masses differ by more than a factor of two. The resulting difference in the gravitational sags could diminish the spatial overlap between the species and thereby hinder sympathetic cooling, which relies on collisions between ^{40}K and ^{87}Rb atoms (cf. sec. 7).

The chosen oblate trap geometry minimizes gravitational sags due to the tight vertical confinement and thereby allows an efficient sympathetic cooling.

4.2.1. Trap frequencies

In most relevant cases, the atoms occupy only the central part of the trapping potential, which can be approximated by a harmonic potential. The strength of the trap can then be parameterized by three trap frequencies ω_i (cf. sec. 2.2.2), which are measured in the experiment by exciting dipole oscillations of the cloud in the trap ("sloshing") and recording the center of mass momentum using time of flight imaging. The oscillations are excited by vertically displacing the trap center using a sudden change of the dipole trap power. This sudden change of the gravitational sag induces a vertical center of mass motion. The excitation will spread over all three axes and induce harmonic center of mass oscillations at the trap frequency, as can be seen in figure 4.4.

4.2. Crossed dipole trap

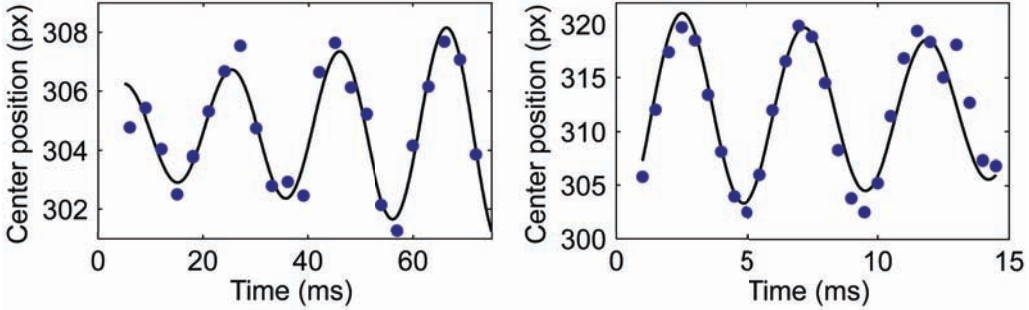


Figure 4.4.: Measured and fitted trap frequencies: The left (right) image shows an example of the horizontal (vertical) center of mass motion. The amplitude of the slower ($\omega = 2\pi \times 50$ Hz) horizontal oscillation increases while the faster ($\omega = 2\pi \times 210$ Hz) vertical motion is damped.

In figure 4.5 the measured trap frequencies are shown for various dipole trap powers. The horizontal trap frequencies are equal $\omega_x = \omega_y = \omega_{\perp}$ and scale, as expected, like the square root of the power ($\omega_{\perp}^2 \propto p$) in the dipole beams. In the vertical direction gravity alters the power-law scaling of the trap frequencies: The trap bottom, that is the power where the vertical trap frequency vanishes, occurs when the steepest gradient of the dipole potential just compensates gravity. Away from this point, the aspect ratio γ of the trap, which is given by the ratio between the vertical and horizontal trap frequencies $\gamma = \omega_z/\omega_{\perp}$ approaches $\gamma = 4$.

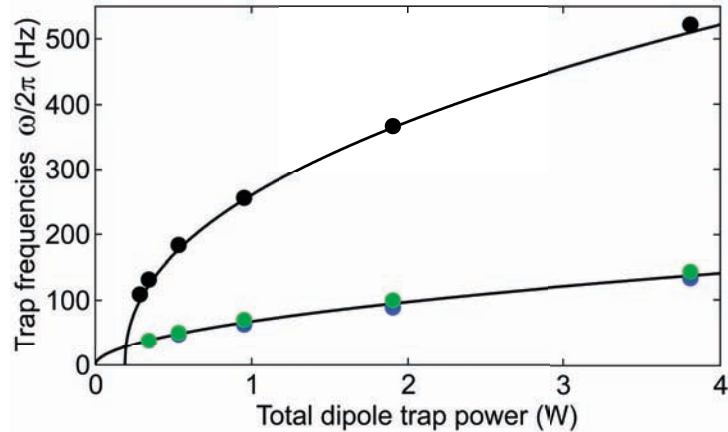


Figure 4.5.: Measured trap frequencies in the dipole trap as a function of total dipole trap power together with power-law fits. Blue and green points denote the measured trap frequencies in the two horizontal directions, the vertical frequencies are shown in black. The measured exponents of approx. 1/2 coincide with the expected behavior of $\omega^2 \propto I_{\max} \propto p$.

4. Optical potentials: Dipole trap and lattice

4.3. Optical lattice

The term *optical lattice* describes a spatially periodic dipole potential, which acts on ultracold atoms in a similar way like the coulomb potential of the ions in a crystalline solid acts on the electrons: The periodic potential modifies the dispersion relation of the atoms, leading to a *band structure* in which the allowed energy bands are separated by band gaps. In the case of non-interacting fermionic atoms (or electrons in a solid) this band structure can generate metallic states that are similar to the Fermi sea in a pure dipole trap but in addition the existence of the band gaps can give rise to band-insulating many-body states.

In the limit of a very deep optical lattice every lattice site can be seen as an individual microtrap in which e.g. very clear and precise experiments concerning few-body physics and molecular dynamics are possible [10].

In this chapter a brief description of the experimental implementation of the lattice and the used calibration methods is given together with a description of the single-particle eigenstates in homogeneous and inhomogeneous lattices.

A review of the physics of optical lattices and previous experiments can be found in [7, 105].

4.3.1. Implementation

Spatially periodic intensity distributions can be created by a number of methods ranging from imaging a periodic intensity mask to exploiting interference effects between several beams. The method used in these experiments consists of retroreflecting linear polarized monochromatic laser beams back onto themselves:

The superposition of two running plane waves with wave vectors \vec{k} ($k = 2\pi/\lambda$) and $-\vec{k}$ creates a standing wave with a periodic intensity distribution $I(\vec{r}) \propto \cos(\vec{k}\vec{r})^2$, which gives rise to a 1D lattice potential with a periodicity of $d = \lambda/2$:

$$V(z) = V_0 \cdot \cos(kz)^2 = V_0 \frac{1}{2} (1 + \cos(2kz)) \quad \text{Figure: A sinusoidal wave pattern representing the 1D lattice potential.} \quad (4.4)$$

The *lattice depth* V_0 is typically given in units of the *recoil energy* E_r , which denotes the change in kinetic energy associated with the emission or absorption of a photon with momentum $\hbar k$:

$$E_r = \frac{\hbar^2 k^2}{2m} \quad (4.5)$$

By superimposing more laser beams a variety of higher dimensional periodic potentials can be created. In the experiment three mutually orthogonal beam pairs are used to create a simple cubic (sc) periodic potential. Cross interferences between the different beam pairs are minimized by choosing mutually orthogonal linear polarizations and are additionally averaged out due to frequency offsets between them [106].

Blue vs. red-detuned lattice

The form of the potential in equation 4.4 is identical for both blue- and red-detuned laser light, the only difference is the sign of V_0 :

In a red-detuned lattice the potential minima correspond to the intensity maxima, while in a blue-detuned lattice the atoms are located at the nodes of the light field. This difference becomes important in the case of Gaussian beams instead of plane waves, since in this case the intensity does not only depend on the longitudinal ($\parallel \vec{k}$) but also the transversal ($\perp \vec{k}$) position within the beams.

In a red-detuned lattice the atoms are located around the intensity maxima and therefore experience a Gaussian shaped dipole potential in the transverse direction, which has the same width w_0 and amplitude V_0 as the lattice potential (cf. fig. 4.6).

For a typical beam waist of $w_0 = 150 \mu\text{m}$ and lattice depth of $8 E_r$ at a red-detuned wavelength of $\lambda = 830 \text{ nm}$ this creates an additional confining potential with a trap frequency of

$$\omega_c = \sqrt{2} \sqrt{\frac{4V_0}{mw_0^2}} = 2\pi \times 72 \text{ Hz}. \quad (4.6)$$

Here the factor $\sqrt{2}$ is due to the fact that for every axes the transversal confinements by two lattice axes need to be added.

In the case of a blue-detuned lattice, as used in this thesis, the atoms are located near the intensity minima, where the (repulsive) transverse dipole potential vanishes in the ideal case. It is proportional only to the intensity difference between the incoming and retro-reflected lattice beam.

Since in both cases the lattice depth depends on the transverse position within the beams, another contribution to the effective transverse potential arises from the on-site ground state energy, i.e. the energy of the single-particle ground state of a single lattice site in 1D. In the harmonic approximation, which becomes exact for deep lattices, the on-site ground state energy is given by $\frac{1}{2}\hbar\omega_{\text{on-site}}$ where the trap frequency due to the lattice potential is given by

$$\omega_{\text{on-site}} = \sqrt{\frac{2V_0 k^2}{m}} \quad \begin{array}{c} \text{---} \\ \text{---} \\ \text{---} \\ \text{---} \\ \text{---} \end{array} \quad (4.7)$$

and depends via $\omega_{\text{on-site}}(x) \propto \sqrt{V_0(x)}$ also on the transversal position. This dependence leads to a Gaussian shaped anticonfining potential with a width of $\sqrt{2}w_0$ in both cases. In the harmonic approximation this yields

$$\omega_{\text{ac}} = \frac{\sqrt{2}\hbar}{mw_0\lambda} \left(\frac{V_0}{E_r} \right)^{\frac{1}{4}}, \quad (4.8)$$

4. Optical potentials: Dipole trap and lattice

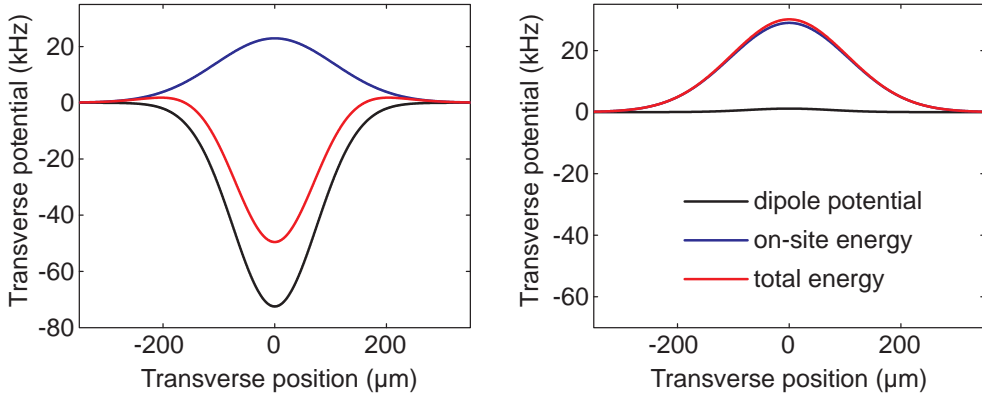


Figure 4.6.: Transverse potential in a red (left, $\lambda = 830 \text{ nm}$) and blue (right, $\lambda = 738 \text{ nm}$) detuned 1D optical lattice with a central lattice depth of $V_0 = 10 E_r$ and a beam waist of $w_0 = 150 \mu\text{m}$. The black lines denote transverse cuts through the dipole potential at a longitudinal potential minimum (red $\rightarrow I = I_{\max}$, blue $\rightarrow I = I_{\min}$). The indicated small dipole potential in the blue case is due to an assumed imperfect reflection of the lattice beam. The blue line indicates the spatial dependence of the on-site energy, and the red line shows the sum of the two terms.

which results in anticonfining trap frequencies of $\omega_{\text{ac}} = 2\pi \times 30 \text{ Hz}$ for the above red-detuned case and $\omega_{\text{ac}} = 2\pi \times 34 \text{ Hz}$ for a blue-detuned lattice at $\lambda = 738 \text{ nm}$ and otherwise equal parameters.

For a red-detuned lattice the quadratic sum of both contributions amounts to an additional confinement of $\omega_c = 2\pi \times 65 \text{ Hz}$, which fundamentally limits the usable dynamic range of the setup, since no weaker confinements can be reached in the lattice without the use of additional potentials.

For a blue-detuned lattice, as used in this experiments², both contributions are anticonfining and can easily be compensated by the red-detuned dipole trap. This results in a huge range of possible confinements that is independent of the lattice depth and is a key ingredient for the experiments presented in this thesis. Especially it allows experiments with high atom numbers (and therefore strong signals) in the interesting regime of deep lattices but low to medium filling factors. The expansion experiments presented in chapter 10 specifically exploit the possibility to realize a homogeneous lattice without any additional potential (cf. fig. 10.6).

The anticonfining trap frequencies can be measured (Fig. 4.7) for every pair of lattice beams individually by adapting the method used for the pure dipole trap. To this means, the 1D lattice is ramped up to the desired lattice depth and the two trap frequencies in the transversal directions are measured as before. The anticonfining trap frequency is then given by $\omega_{\text{ac}} = \sqrt{\omega^2 - \omega_0^2}$, where ω is the measured trap frequency with lattice and ω_0 is the trap frequency measured without the lattice.

²The lattice light is produced by a single-frequency Ti:Sa solid state laser (Coherent MBR) which produces up to 3 W power at $\lambda = 738 \text{ nm}$ and is optically pumped by an 18 W, $\lambda = 532 \text{ nm}$ diode pumped ND:YVO₄ solid state laser (Coherent, Verdi V18).

4.3. Optical lattice

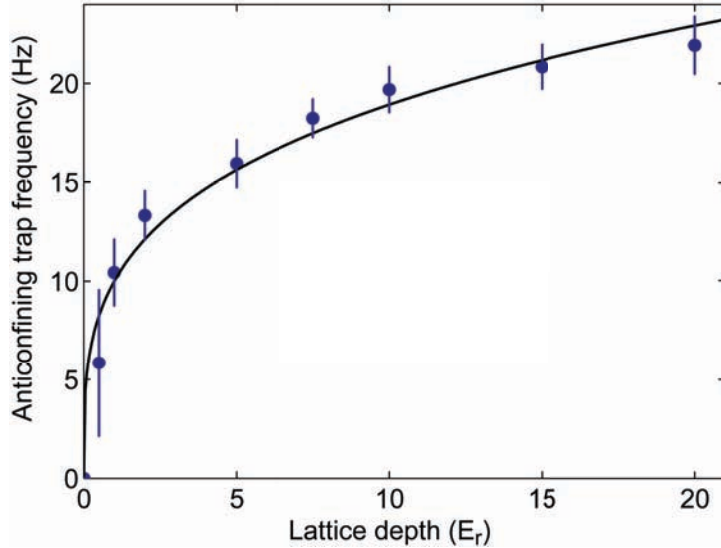


Figure 4.7.: Measured anticonfining trap frequencies of the vertical lattice as a function of lattice depth together with a powerlaw fit. The fitted exponent of 0.28 ± 0.03 agrees well with the expected $V_0^{1/4}$ behaviour.

4.3.2. Single particle eigenstates

In this chapter a description of the single-particle eigenstates in homogeneous and inhomogeneous lattices is given.

Together with the Fermi Dirac statistics, the resulting band structure is already sufficient to describe many aspects of electrons in solids, e.g. the existence of metallic and band-insulating states. In the experiment, these non-interacting systems can be simulated using a single component Fermi gas or by using the zero crossing of the scattering length near a Feshbach resonance.

The introduced notations will also be used in the following chapter, where interacting fermions will be discussed.

Bloch waves

In order to describe the dynamics of a single particle in a strictly periodic potential like a homogeneous lattice, the *Bloch theorem* is a good starting point. It states that all single particle eigenstates of a periodic potential can be written as periodically modulated plane waves, that is as products of a plane wave $e^{i\vec{q}\cdot\vec{r}}$ times a periodic function $u_{\vec{q}}^n(\vec{r})$ with lattice periodicity:

$$\phi_{\vec{q}}^n(\vec{r}) = e^{i\vec{q}\cdot\vec{r}} u_{\vec{q}}^n(\vec{r}) \quad (4.9)$$

These solutions are the well-known *Bloch waves* and are delocalized eigenstates for non-interacting particles in a homogeneous lattice [107, 108]. The index n is called the band index and denotes the fact that for every *quasi-momentum* \vec{q} there

4. Optical potentials: Dipole trap and lattice

exist infinitely many orthogonal solutions with different eigenenergies. The following discussion will mostly be restricted to the lowest band of the one-dimensional case, and the index n and the vector notation will be dropped.

Due to the $2kz$ periodicity of the lattice potential in equation 4.4, the function $u_q(z)$ in equation 4.9 can be written as a discrete Fourier sum

$$u_q(z) = \sum_l c_{l,q} e^{il2kz} \quad l \in \mathbb{Z}, \quad (4.10)$$

which leads to the following expression for the Bloch waves:

$$\phi_q(z) = \sum_l c_{l,q} e^{i(q+l2k)z} \quad (4.11)$$

A Bloch wave can therefore also be regarded as a superposition of plane waves with wavevectors $q + l \cdot 2k$, where $l \cdot 2k$ are the *reciprocal lattice vectors* [29].

This description, which was derived solely from the periodicity of the potential, can also be explained using the photon picture of the light field: As mentioned above (cf. sec. 4.1), the homogeneous dipole potential of a plane wave arises due to Raman processes where an atom absorbs a photon from the plane wave followed by a stimulated emission back into the plane wave.

A standing wave consists of two counterpropagating plane waves and gives rise to an additional type of Raman process: An atom can absorb a photon from one beam with wavevector \vec{k} and re-emit it into the second beam with wavevector $-\vec{k}$. These Raman processes change the momentum of the atom by $2\hbar k$ and thereby couple the momenta p and $p \pm 2\hbar k$. This naturally leads to eigenstates in the form of equation 4.11, i.e. Bloch waves.

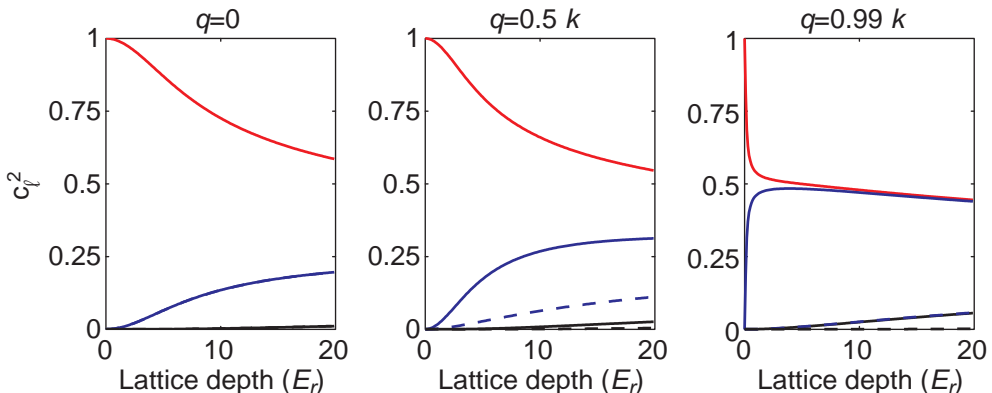


Figure 4.8.: Composition of Bloch waves: for three different quasi-momenta $\hbar q$ the weight of the corresponding plane waves is shown as a function of lattice depth. The red lines denote the real space momentum $p = \hbar q$, blue (black) denote $p = \hbar(q + 2k)$, ($p = \hbar(q + 4k)$) and the dashed lines denote $p = \hbar(q - 2k)$, ($p = \hbar(q - 4k)$). At zero lattice depth the Bloch waves are identical to plane waves with momentum $p = \hbar q$.

4.3. Optical lattice

By inserting expression 4.11 into the Schrödinger equation with a potential given by equation 4.4 and numerically diagonalizing the resulting matrix (cf. e.g. [106]), the coefficients $c_{l,q}$ and the eigenenergies can be calculated³.

Figure 4.8 shows the composition of various Bloch waves in the lowest band as a function of the lattice depth. At zero lattice depth the Bloch wave coincides with a plane wave of momentum $p = \hbar q$ and for increasing lattice depth the admixtures of higher momenta $p = \hbar(q \pm 2k)$ become important.

Band structure In figure 4.9 the four lowest eigenenergies are shown as a function of the quasi-momentum (or *lattice momentum*) $\hbar q$ for various lattice depths. In the case of zero lattice depth (upper left) the dispersion relation is given by the free space parabola, but is periodic in q with a periodicity of $2k$. This periodicity in quasi-momentum is a consequence of the discrete translational symmetry of the lattice. Intuitively speaking, the argument $\vec{q} \cdot \vec{r}$ of the plane wave in equation 4.9 measures the phase difference between adjacent lattice sites and is 2π -periodic. It is therefore sufficient to restrict the values of q to the the *first Brillouin zone*, i.e. the interval $\hbar q \in]-\hbar k, \hbar k]$.

With increasing lattice depth the dispersion relations differ more and more from the free-space parabola and form distinct *bands* separated by *band gaps*, which are energy intervals without any eigenstates. As shown in figure 4.10 there is a band gap separating the lowest from the first excited band for every finite lattice depth in 1D.

In the separable case of simple cubic lattices all 3D eigenstates can be written as products of three 1D eigenstates (cf. eqn. 2.16). If the lattice depth is equal along the three directions, the first excited band is threefold degenerate and consist of products of two lowest band 1D eigenstates and one eigenstate of the first excited 1D band. In 3D, the band gap only opens for lattice depths larger than $V_0 \approx 2.2 E_r$.

All experiments in this thesis focus on the physics within the lowest band and we consequently try to avoid any populations of higher bands. For experiments on the dynamics in higher bands see e.g. [109]. While the band gap is large at deep lattices, where the final measurements were performed, care has to be taken during the initial ramp of the lattice. In order to avoid atoms populating the first excited band, the Fermi energy in the dipole trap prior to the loading should be smaller than the recoil energy $E_F < E_r$.

The width of the allowed energy bands, the *band width*, decreases approximately exponentially for increasing lattice depths and vanishes for infinitely deep lattices. In this limit the harmonic approximation of equation 4.7 becomes exact and the energies in the n th Bloch band are given by $(n - 1/2)\hbar\omega_{\text{on-site}}$.

³By introducing a cutoff in the index l , a finite size matrix can be obtained. In order to calculate the two lowest bands at the relevant lattice depths, already $|l| < 5$ is sufficient.

4. Optical potentials: Dipole trap and lattice

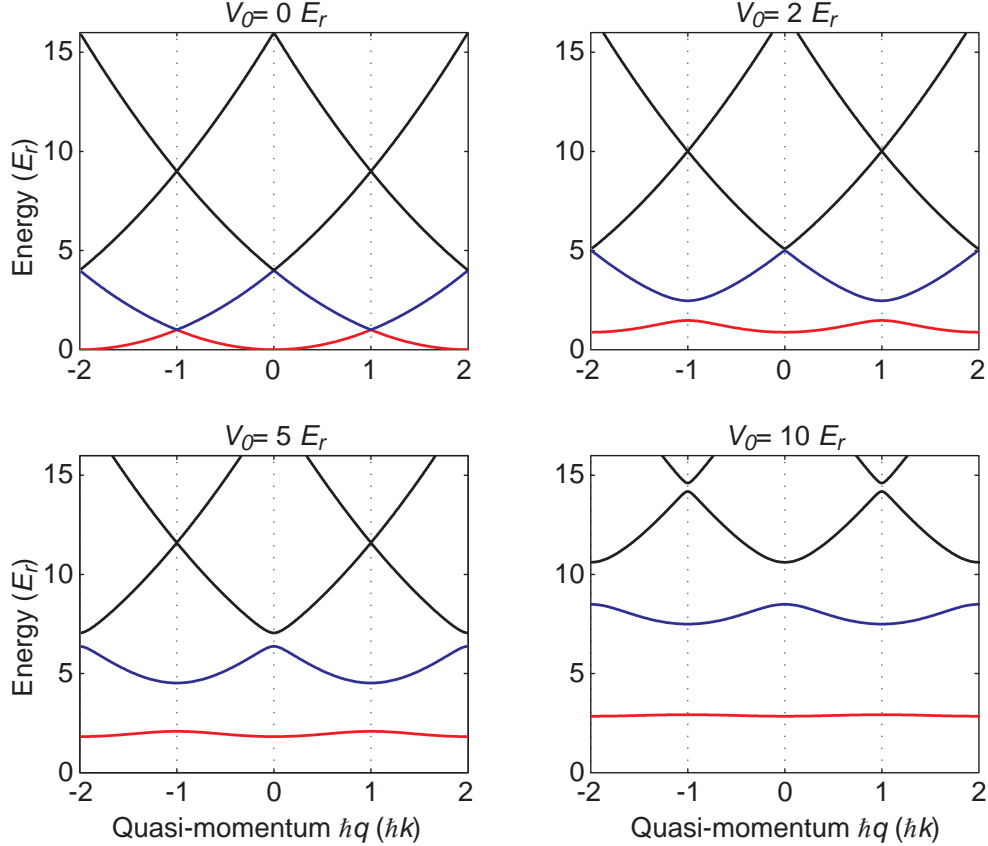


Figure 4.9.: Energies of Bloch waves for various lattice depths. The lowest band is shown in red, the first excited band in blue and higher bands in black.

This strong decrease of the kinetic energy for deeper lattices promotes the relative strength of the interactions and creates the possibility to reach the strongly correlated regime without the use of Feshbach resonances. On the down side, however, it renders the system more susceptible to all sorts of imperfections in the potentials.

Lattice depth calibration Spectroscopic measurements of the transition frequencies from the lowest band to the first excited band have been used to measure the lattice depths. To this means, transitions were induced in a 1D lattice by modulating the frequency of the lattice light using an Acousto Optical Modulator. At the position of the atoms, this frequency modulation translates into an oscillation of the potential minima position. The number of atoms remaining in the lowest band was measured as a function of the modulation frequency using a band-mapping technique (cf. sec. 6.4). As can be seen in figure 4.11, there exists a rather sharp upper edge of the resulting minimum, which corresponds to the maximal energy difference between Bloch-waves in the lowest band and the first excited band, i.e. $hf_{\text{edge}} = E_1(q = 0) - E_0(q = 0)$. By comparing this frequency to the result of a numerical band structure calculation (cf. fig. 4.10), the lattice depth can be

4.3. Optical lattice

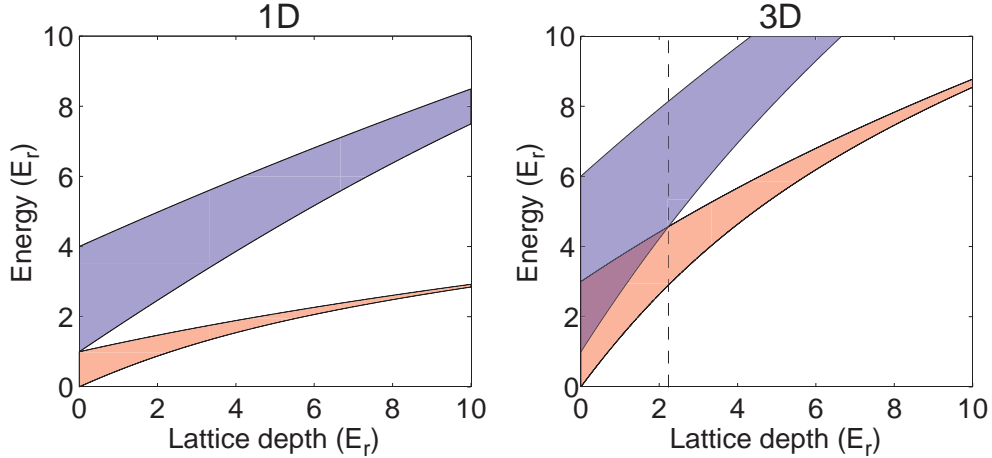


Figure 4.10.: Band structure as a function of lattice depth. Shown are the lowest and the first excited band in a 1D (left) and 3D (right) homogeneous lattice. The vertical dashed line in the 3D case denotes a lattice depth of $V_0 \approx 2.2 E_r$, where the band gap opens.

extracted with an uncertainty of less than 5%. Due to the weak confinement used in this measurement the large cloud samples a rather large fraction of the lattice beam. This leads to an asymmetric broadening of the excitation towards smaller frequencies due to the inhomogeneous lattice depth.

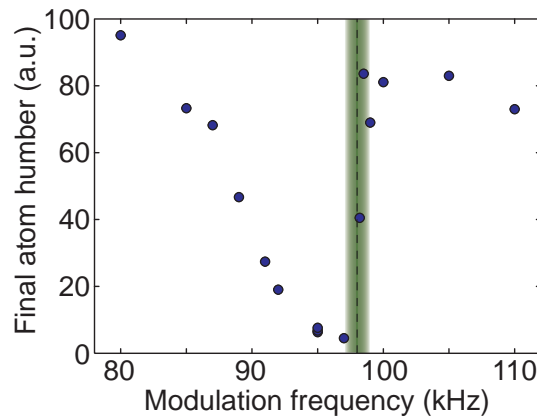


Figure 4.11.: Calibrating the lattice depth by lattice modulation spectroscopy. The picture shows the remaining atom number in the lowest band as a function of the modulation frequency. The measured position of the upper flank (98 ± 1 kHz) results in a lattice depth calibration of $V_0 = 34.8 \pm 0.7 E_r$

Wannier states

Even though the Bloch waves are the correct eigenstates for non-interacting particles in a homogeneous lattice, it is convenient to introduce the localized *Wannier functions* as a second basis to describe atoms in a lattice. They are localized

4. Optical potentials: Dipole trap and lattice

around individual lattice sites z_i and form an orthonormal basis that is well suited to incorporate the effects of inhomogeneous potentials or short-range interactions. Wannier functions can be defined as Fourier transforms of the Bloch waves

$$w(z - z_i) = \frac{1}{\sqrt{N}} \sum_q e^{iqz_i} \phi_q(z), \quad (4.12)$$

where N is the number of lattice sites⁴.

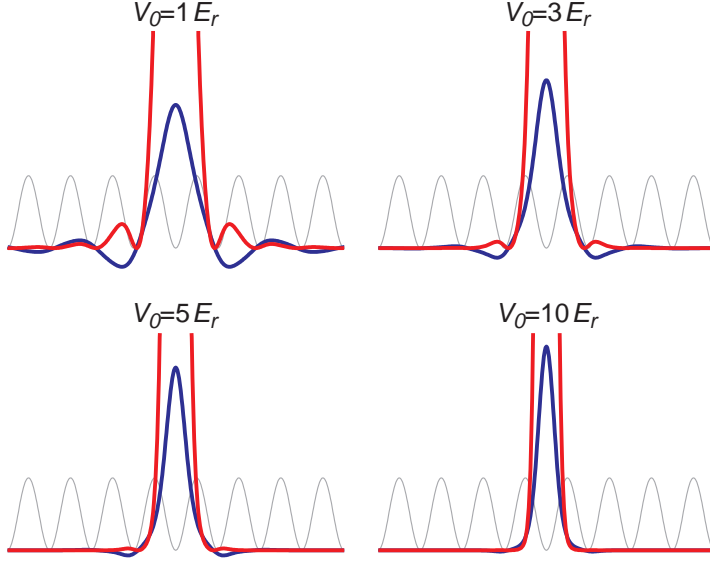


Figure 4.12.: Wannier functions for different lattice depths. The Wannier functions w are plotted in blue together with the resulting density $|w|^2$ in red. The lattice potential is schematically shown in gray.

Using the Wannier basis, the hamiltonian of a single particle in a possibly inhomogeneous lattice can be written as:

$$H_{ij} = \begin{cases} \epsilon_i & i = j \\ J_{ij} & i \neq j \end{cases} \quad (4.13)$$

Here ϵ_i denotes the on-site energy of an atom localized on site i , which can be divided into two parts:

$$\epsilon_i = E_i^{\text{on-site}} + \int w^*(z - z_i) V_{\text{ext}}(z) w(z - z_i) dV \quad (4.14)$$

The first part $E_i^{\text{on-site}}$ is the on-site energy due to the lattice potential and the second part is the potential energy associated with an additional potential $V_{\text{ext}}(\vec{r})$.

The J_{ij} denote the *tunneling matrix elements* between sites i and j and are given by

$$J_{ij} = \int w(z - z_i) \left(-\frac{\hbar^2}{2m} \frac{\partial^2}{\partial z^2} + V_{\text{lat}}(z) \right) w(z - z_j) dz \quad (4.15)$$

⁴In a finite 1D system of N sites there exist only N discrete allowed quasi-momenta in the first Brillouin zone, in an infinite system the sum is replaced by an integral.

4.3. Optical lattice

In a homogeneous lattice all ϵ_i are equal and can be set to zero, thereby choosing the energy of a localized atom as reference point. Furthermore, the tunneling matrix elements (or tunneling rates) J_{ij} only depend on the distance between the sites ($J_{ij} = J_{|i-j|}$).

The additional potential $V_{\text{ext}}(\vec{r})$ is assumed to be only slowly varying such that it does not alter the tunneling matrix elements J_{ij} . Although there exist approximate formulas for the tunneling element at deep lattices [7], they need to be calculated numerically in the relevant regime.

Tight-binding regime

All experiments are performed in the *tight-binding regime* where (in the lowest band) only tunneling between neighboring sites $j = i \pm 1$ needs to be taken into account ($J \equiv J_1$). In this regime, which is reached for lattice depths larger than approximately $5 E_r$, the bandwidth of the lowest band becomes $4J$ and the dispersion relation is given by [7]

$$E(q) = -2J \cos(qd), \quad (4.16)$$

where $d = \pi/k$ denotes the lattice constant. Figure 4.13 shows how the dispersion relation evolves from a free space parabola into a cosine function in the tight-binding regime.

The term tight-binding regime refers to the fact that in solid-state physics the same cosine-shaped band can be derived by the Linear Combination of Atomic Orbitals (LCAO) method using s-orbitals: In this method one starts from the tightly bound limit where every electron occupies an atomic orbital of a single atom and incorporates the potentials due to all other atoms in the solid using perturbation theory [29].

Kinetic energy and group velocity

An important difference between free space and the lowest band of a lattice model stems from the fact that kinetic energies are bounded in the lattice case: While all positive kinetic energies are possible in free space, only kinetic energies within the bandwidth $l4J$ can occur in a tight-binding band. Here l denotes the number of dimensions. Furthermore, the possible kinetic energies are distributed symmetrically around the energy of a localized atom ($E = 0$), i.e. they range from $-6J$ to $6J$ in the three-dimensional case. This reflects the fact that, as a consequence of Heisenberg's uncertainty relation, a localized atom can actually lower its kinetic energy by delocalizing over several lattice sites.

The group velocity of an atom in a Bloch wave with quasi-momentum $\hbar q$ is in general given by

$$v_{\text{gr}}(q) = \frac{1}{\hbar} \frac{\partial E(q)}{\partial q}, \quad (4.17)$$

4. Optical potentials: Dipole trap and lattice

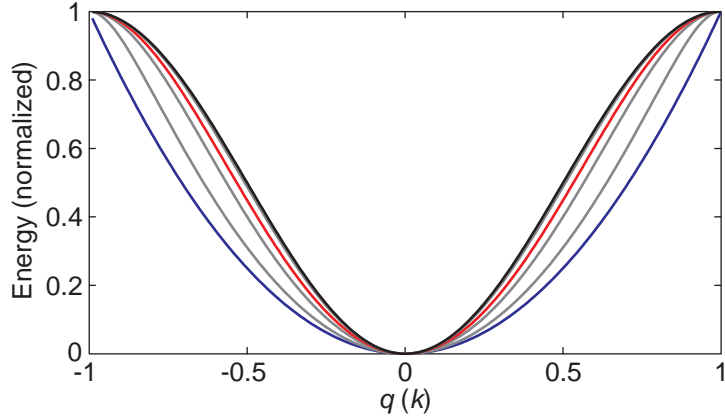


Figure 4.13.: Normalized dispersion relation in the lowest band for various lattice depths. The shape of the dispersion relation changes from a free space parabola at zero lattice depth (blue) into a cosine band in the tight-binding regime, which starts around a lattice depth of $5 E_r$ (red). The black line corresponds to $100 E_r$ and additional gray lines to 1,3, and $10 E_r$ lattice depths.

where $E(q)$ denotes the dispersion relation. In the tight-binding case of $E(q) = -2J \cos(qd)$ (cf. eqn. 4.16) this becomes

$$v_{\text{gr}}(q) = \frac{2Jd}{\hbar} \sin(qd). \quad (4.18)$$

If we define the *tunneling time* τ to be

$$\tau \equiv \frac{\hbar}{J}, \quad (4.19)$$

the spread of possible group velocities is given by $-2d/\tau \leq v_{\text{gr}} \leq 2d/\tau$.

This group velocity distribution, which is plotted in figure 4.14, shows several important features: In sharp contrast to free space, where a higher kinetic energy always results in higher velocities, in a tight-binding band the maximum group velocities appear at zero energy in the center of the band, i.e. for quasi-momenta $\hbar q = \pm \hbar \frac{k}{2} = \pm \hbar \frac{\pi}{2d}$. For both higher and lower kinetic energies the group velocities decrease symmetrically and vanish at the upper and lower band edges, i.e. at $\hbar q = 0$ and $\hbar q = \pm \hbar k = \pm \hbar \pi/d$

This at first glance counterintuitive behavior can be understood by considering the relative phase factor e^{iqd} between neighboring lattice sites (cf. sec. 4.3.2): In the case of a quasi-momentum at the edge of the Brillouin zone ($\hbar q \pm \hbar \pi/d$), the relative phase between neighboring lattice sites is $\pm\pi$. Due to the 2π -periodicity of the phase, these two cases correspond to the same state. As a consequence the velocity in the two cases must be equal, i.e. $v = -v$, and therefore vanish.

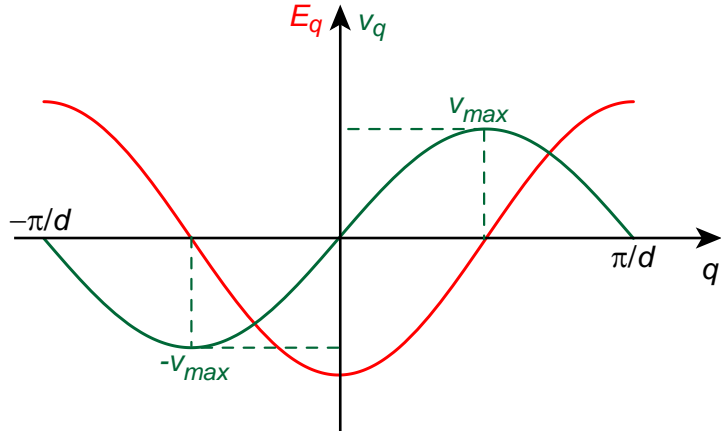


Figure 4.14.: Single particle energy E_q and corresponding group velocity v_q in a tight-binding band.

Combined potential

In the experiment the atoms are subjected to the combined potential of a three-dimensional blue-detuned optical lattice in the tight-binding regime and a red-detuned dipole trap. In this situation the periodicity of the lattice potential is broken and the Bloch waves are no eigenstates anymore [110–112].

For typical dimensions of the atomic cloud in the lattice ($R < 60 d$, cf. sec. 6.5), the variation in lattice depth over the cloud is less than 5%, which results in an approximately constant tunneling rate J . Using the Wannier basis, the resulting 1D hamiltonian (eqn. 4.13) for the lowest band can be written in second quantization:

$$\hat{H} = -J \sum_{\langle i,j \rangle} \hat{c}_i^\dagger \hat{c}_j + \sum_i \epsilon_i \hat{n}_i \quad (4.20)$$

The operators \hat{c}_i^\dagger , \hat{c}_i denote the creation and annihilation operators of a particle on site i and obey fermionic anticommutator relations, i.e. $(\hat{c}_i^\dagger)^2 = 0$. This ensures that two identical fermions cannot occupy the same lattice site, as required by the Pauli exclusion principle (cf. sec. 2). The number operator at site i is denoted by $\hat{n}_i = \hat{c}_i^\dagger \hat{c}_i$.

Neglecting the on-site energy of lattice sites in the trap center, but retaining the anticonfining effects (cf. eqn. 4.8), the total confining potential is assumed to be harmonic:

$$\epsilon_i = V_t i^2 \quad (4.21)$$

The trap center is at $i = 0$ and the prefactor V_t is given by the trapping frequency ω and the distance d between adjacent lattice sites:

$$V_t = \frac{1}{2} m \omega^2 d^2 \quad (4.22)$$

4. Optical potentials: Dipole trap and lattice

For finite system sizes this hamiltonian can be diagonalized numerically⁵, examples of the eigenstates are shown in figure 4.15. Typically, the eigenstates are extended over several lattice sites and can be characterized by a density distribution both in real space and in quasi-momentum space (cf. fig. 4.16).

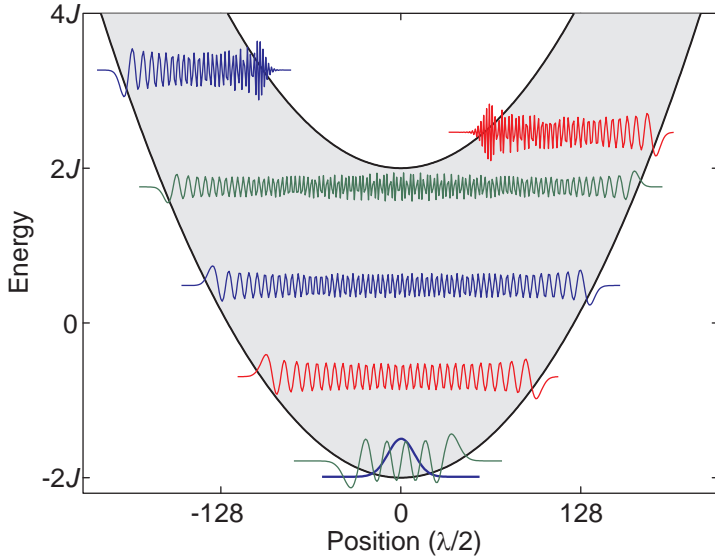


Figure 4.15.: Selected eigenstates of the combined potential. The gray shaded area depicts the spatially varying lowest energy band (see text).

The lowest lying eigenstates look like harmonic oscillator eigenstates: In this regime the relevant quasi-momenta are small and the cosine-shaped dispersion relation can be approximated by a parabola. The system can then be described by a particle in a purely harmonic trap but with an *effective mass* that is determined by the lattice potential [105].

For higher-lying eigenstates the involved kinetic energies and quasi-momenta increase, the differences between a parabola and the cosine-shaped dispersion relation become important, and the eigenstates deviate from harmonic oscillator states.

When the total eigenenergy equals the bandwidth $4J$, the maximum quasi-momentum $\hbar q = \hbar k$ is reached in the trap center and the matterwave will be *Bragg reflected*. As a consequence, states with an eigenenergy above $4J$ cannot extend to the trap center but are localized to either the right or the left wing of the harmonic potential.

If the external potential is varying slowly enough, its effects can be visualized as a curved Bloch band: At every point in space \vec{r} one can think of a $4J$ (or $12J$ in 3D) thick energy band which is offset from zero by the potential $V_{\text{ext}}(\vec{r})$. In a semi-classical picture a particle in this potential would be represented by a wave

⁵In order to avoid degeneracies, the trap center can be offset by a fraction of a lattice site.

4.3. Optical lattice

packet localized at a certain position and with a certain energy (a certain quasi-momentum). The wave packet would travel until it reaches either the lower or the upper edge of the band. Reaching the lower edge results in a reflection due to the potential, as in a harmonic oscillator, reaching the upper edge results in a Bragg reflection.

This is a general feature of the combination of a periodic potential with a slowly varying potential. In the easiest case of a linear potential (Wannier-Stark system) this leads to *Bloch oscillations* [113], where non-interacting particles perform periodic oscillations without a net travel [27, 28, 114, 115]. The amplitude A of these oscillations is given by the ratio between half the bandwidth and the potential gradient F :

$$A = \frac{2J}{F} \quad (4.23)$$

The typical extension of an eigenstate in the combined potential of lattice and dipole trap can intuitively be understood in two ways: In the limit of very weak lattices, the eigenstates can be well approximated by harmonic oscillator eigenstates and the effect of the lattice can be approximated using the effective mass of the particles. A deeper lattice leads to a higher effective mass and thereby to a smaller harmonic oscillator length. In the case of weak harmonic traps this results in a pronounced shrinking of the cloud during the loading into the lattice.

Starting in the limit of an infinitely deep lattice, where the tunneling vanishes ($J \rightarrow 0$), the particles are localized to individual lattice sites. For decreasing lattice depths tunneling increases and will lead to a larger extension of the eigenstates.

These two limits are smoothly connected and, for a constant external potential, a deeper lattice will generally lead to more localized eigenstates, as expected by the above picture of a curved Bloch band.

4. Optical potentials: Dipole trap and lattice

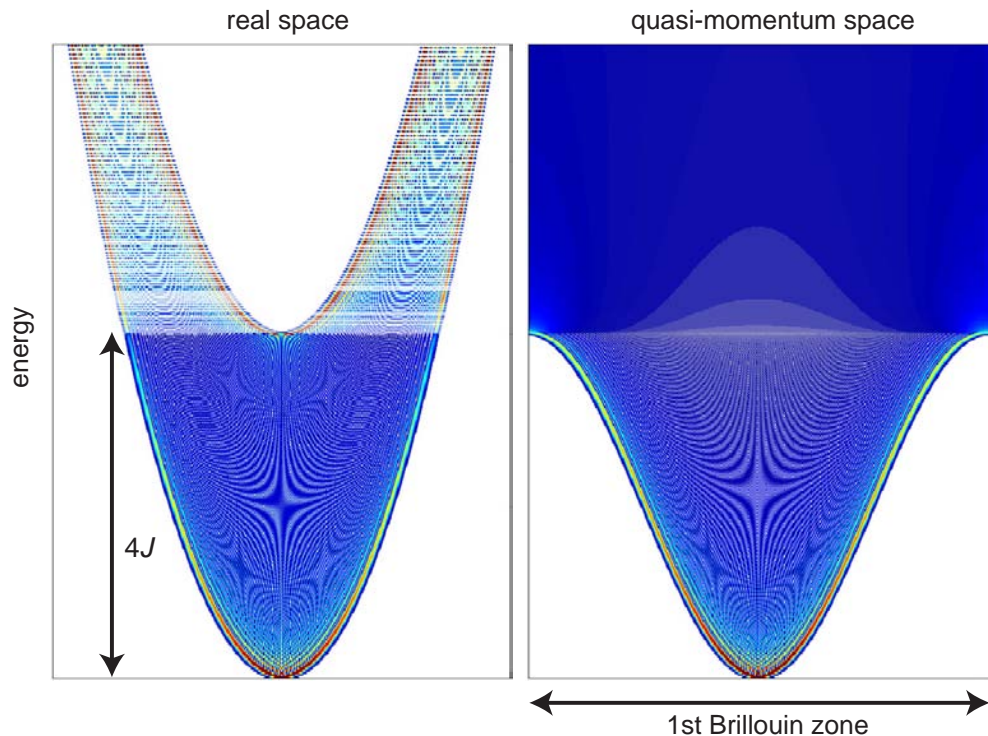


Figure 4.16.: 1D eigenstates of a combined potential of lattice and harmonic confinement. The vertical axis denotes the eigenenergies and every line depicts the color coded density distribution of a single eigenstate in real space and quasi-momentum space. For eigenenergies higher than the bandwidth $4J$, the eigenstate is localized in either the left or the right wing of the harmonic potential. The alternation between the wings leads to the characteristic stripe pattern.

5. Fermi-Hubbard model

Due to the sheer number of electrons and ion cores in a solid, all interacting via long-range Coulomb interactions, the problem of calculating the many-body state of the electrons in a solid is in general not solvable without massive approximations.

An important theme in the study of electrons in solids is therefore the search for the simplest models that nonetheless describe the physics of interest.

Historically, these models did fall into two distinct classes:

- In order to capture the transport behavior of many metallic and band-insulating solids, the electrons are described by delocalized states. In these models, the easiest one being the free electron model by A. Sommerfeld [108], correlations between the electrons are typically neglected [29]. The many-body state can be described by using only Fermi-Dirac statistics (cf. sec. 2.2.1) and the Bloch wave picture described in the previous chapter.
In these models a solid is metallic (conducting) if there is a partially filled band, and insulating if all bands are either completely filled or empty.
- A second independent class of models used localized electrons in order to explain magnetic phenomena. Examples of these ordering phenomena of localized spins include the paramagnetic to (anti) ferromagnetic transition in the Heisenberg model [116] or other spin models.

Already in the late 1930s it became clear, however, that the band models used to predict whether a material should be metallic or insulating were not sufficient, as many transition-metal oxides like NiO were found to be insulators or bad conductors, although they possess partially filled d -electron bands [117, 118].

These insulators are referred to as *Mott Insulators* [119–121] and it was believed that their insulating behavior was caused by interactions between the electrons. A new model, which incorporated possible correlations between the electrons, was needed in order to describe the interaction-driven transition from a metal to Mott-insulating states.

One of the most important models used to study these effects is the so-called *Hubbard model*, which was first proposed by J. Hubbard in 1963 [122]. Historically, the Hubbard model was the first theoretical model to successfully describe the Mott transition [123] by correlation effects in a band picture (cf. below). It has served as a prototype model for strongly-correlated states in solid state physics, and many other models like the t-J model [124, 125] can be derived from it in certain regimes.

5. Fermi-Hubbard model

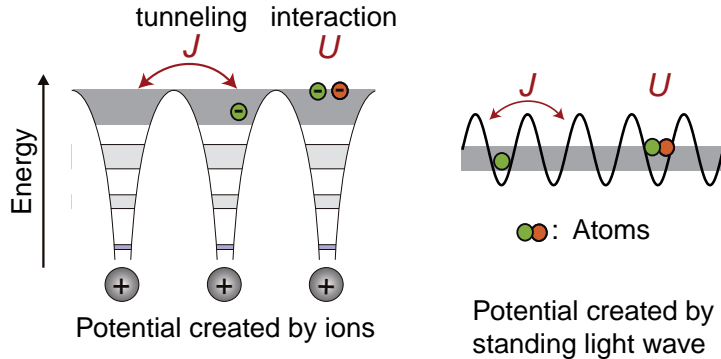


Figure 5.1.: In a single band tight-binding model like the Hubbard model the effects of the actual potential and interactions are approximated by a few matrix elements J, U .

During the last 20 years, the 2D Hubbard model received renewed interest in solid state physics due to the appearance of high-temperature superconductivity in the copper-oxide layers of cuprates [126, 127] and it still is an object of active debate to which degree this phenomenon can be explained in terms of a Hubbard like model [128, 129].

Despite its conceptual simplicity, already the homogeneous Hubbard model is not analytically solvable in two- and three-dimensional situations apart from special cases.

In the context of atomic physics, a Hubbard type model was first introduced for bosonic atoms in optical lattices [5, 6] and proved very successful in describing all experiments up-to-date [7].

The following sections will first present the Fermi-Hubbard hamiltonian together with some simple results on certain aspects of the homogeneous Hubbard model in order to build an intuition of what to expect. This is followed by an overview over some of the expected and observed phases of the Hubbard model and a brief summary of common numerical techniques. The last section of this chapter presents a generalization to trapped systems together with some remarks on dynamics and the applicability of the Hubbard model for cold atoms.

5.1. Fermi-Hubbard hamiltonian

In the Hubbard model the hamiltonian is written using the Wannier basis (4.12) and is given by the sum of three terms. In addition to the tunneling term and the offset potential, that were already present in the single-particle hamiltonian of equation 4.20, the many-body Hubbard model also contains an interaction term:

5.1. Fermi-Hubbard hamiltonian

Tunneling In the Hubbard model tunneling is mostly restricted to nearest neighbor tunneling (cf. sec. 4.3.2), whose strength is given by the hopping amplitude J (cf. eqn. 4.15), which leads to the following kinetic energy operator in second quantization:

$$T = -J \sum_{\langle i,j \rangle, \sigma} \hat{c}_{i,\sigma}^\dagger \hat{c}_{j,\sigma} \quad (5.1)$$

For electrons, the index $\sigma \in \{\downarrow, \uparrow\}$ denotes the spin for a given quantization axes, while for fermionic atoms it denotes two different hyperfine states. In the case of higher dimensions the indices i, j are vectors (3D: $i = (i_x, i_y, i_z)$) and the brackets $\langle i, j \rangle$ denote that the sum only runs over nearest neighbors. In the solid state literature the hopping (or tunneling) amplitude is typically denoted by t , while J would refer to the exchange coupling (cf. sec. 5.5.2), which is denoted by J_{ex} in this thesis.

Interaction One of the main approximations in the Hubbard model is the fact that interactions are treated as local interactions between particles on the same lattice site. This is an excellent approximation in the case of ultracold atoms, where the typical range of the interactions is given by the van der Waals length (cf. sec. 3.1), and is much shorter than the lattice constant.

Assuming only s -wave interactions and using the pseudopotential approximation (cf. sec. 3.2.3), the effective interaction between two atoms in the same Wannier state becomes:

$$U = \frac{4\pi\hbar^2 a}{m} \int |w(\vec{r})|^4 dV \quad (5.2)$$

With this effective interaction the total interaction energy W becomes:

$$W = U \sum_i \hat{n}_{i,\downarrow} \hat{n}_{i,\uparrow} \quad (5.3)$$

Here $\hat{n}_{i,\sigma} = \hat{c}_{i,\sigma}^\dagger \hat{c}_{i,\sigma}$ measures the number of particles with spin σ on site i .

Although electrons in a solid interact primarily via the long-range Coulomb interaction, the high density of additional electrons in other orbitals leads to strong shielding effects that can reduce the interaction between electrons in a given band to effective short-range interactions [121].

External potential The third term in the Hubbard model is the offset energy due to additional slowly varying potentials (cf. sec. 4.21):

$$V = \sum_i \epsilon_i (\hat{n}_{i,\downarrow} + \hat{n}_{i,\uparrow}) \quad (5.4)$$

5. Fermi-Hubbard model

By combining these terms the *Fermi-Hubbard hamiltonian* can be written as:

$$\hat{H} = -J \sum_{\langle i,j \rangle, \sigma} \hat{c}_{i,\sigma}^\dagger \hat{c}_{j,\sigma} + U \sum_i \hat{n}_{i,\downarrow} \hat{n}_{i,\uparrow} + \sum_i \epsilon_i (\hat{n}_{i,\downarrow} + \hat{n}_{i,\uparrow}), \quad (5.5)$$

This model can easily be extended to include several bands as well as additional hopping and interaction terms, e.g. next-to-nearest neighbor hopping, nearest-neighbor interactions or density-induced hoppings [121].

5.2. Conductivity and compressibility

While the electronic conductivity is one of the standard observables in solid state physics it turned out that the compressibility is easier to measure in trapped cold atom setup (cf. sec. 6.5, 8.3, [130]). The question whether a given solid is conducting or insulating is directly related to the question whether the many-body state of the electrons in this material is compressible or not. This *electronic compressibility* [131–133] is defined as the derivative of the electron density with respect to the chemical potential $\kappa_e = \frac{\partial n}{\partial \mu}$.

At zero temperature both the electronic compressibility and the conductance are proportional to the single-particle density of states at the Fermi energy:

If there are unoccupied states available at the Fermi energy, the electron density will increase with an infinitesimal increase of the chemical potential, i.e. the state is compressible. Applying a voltage across the solid excites electrons into these states which results in a current, i.e. the material in question is a conductor.

If there is an energy gap between the highest occupied and the lowest empty single particle states, any change in chemical potential or any applied voltage needs to overcome this gap before it can create any excitation. This results in an incompressible and insulating state.

5.2.1. An intuitive picture of the Mott transition

An intuitive picture of how the interaction between the particles leads to correlation effects and insulating behavior can already be given using only two fermions with different spin (\downarrow, \uparrow) in a double well: At zero temperature and without interactions both particles will occupy the same (not normalized) single-particle ground state:

$$|\Psi_0\rangle = (|l\rangle + |r\rangle)_\downarrow (|l\rangle + |r\rangle)_\uparrow = |l_\downarrow l_\uparrow\rangle + |l_\downarrow r_\uparrow\rangle + |r_\downarrow l_\uparrow\rangle + |r_\downarrow r_\uparrow\rangle \quad (5.6)$$

In this state both particles are uncorrelated (i.e. the wave function factorizes) and delocalized over both wells.

One straightforward idea to incorporate the effects of a repulsive on-site interaction between the particles into this wavefunction originates from the study of

5.3. Two particle Hubbard model

molecular hydrogen and was introduced to the field of correlated electrons by M.C. Gutzwiller [121, 134]:

Since a repulsive interaction raises the energy of all configurations in which both particles occupy the same site, it will consequently decrease their weight in the ground state. In the strongly interacting limit this yields:

$$|\Psi_U\rangle = |l_\downarrow r_\uparrow\rangle + |r_\downarrow l_\uparrow\rangle \quad (5.7)$$

This wavefunction describes a strongly correlated or entangled [135] state: The position of one particle depends on the position of the other and the wavefunction cannot be written as a product of two individual wavefunctions for the two particles.

Generalized to an infinite system, the single-particle eigenstates are Bloch waves (cf. sec. 4.3.2) and the non-interacting many-body state corresponds to a half filled Brillouin zone. As the energy difference between subsequent Bloch waves vanishes in the thermodynamic limit, this describes a compressible metallic state.

In the strongly interacting limit on the other hand, the cost of adding another particle is on the order of U in the half-filled case, since it necessarily includes the creation of double occupation, independent of the system size. The opening of this energy gap, the so-called Mott gap for an exactly half-filled band drives the transition from a compressible and conducting metal to an incompressible Mott insulator.

5.3. Two particle Hubbard model

Analogous to the BEC-BCS crossover in free space (cf. sec. 3.3.3), the existence of a two-particle bound state will also in the Hubbard model have a profound influence on the many-body physics.

In order to study the existence of these bound states, a homogeneous lattice containing only one atom per spin state will be analyzed in this section.

The two-particle wavefunction can be written in center-of-mass \vec{R} and relative coordinates \vec{r} [136, 137]:

$$\vec{R} = \frac{1}{2} \cdot (\vec{r}_1 + \vec{r}_2) \quad \vec{r} = \vec{r}_1 - \vec{r}_2 \quad (5.8)$$

$$\vec{Q} = \vec{q}_1 + \vec{q}_2 \quad \vec{q} = \frac{1}{2}(\vec{q}_1 - \vec{q}_2) \quad (5.9)$$

The tunneling term separates into center-of-mass and relative terms and the interaction depends only the relative coordinate. Thus the total wavefunction can be written as a product of the center-of-mass motion, which is a Bloch wave, and the relative motion:

$$\Psi(\vec{r}_1, \vec{r}_2) = e^{i\vec{Q}\cdot\vec{R}} \psi_{\vec{Q}}(\vec{r}) \quad (5.10)$$

5. Fermi-Hubbard model

The remaining hamiltonian for the relative motion is:

$$\hat{H}_{\vec{Q}}^{\text{rel}} = \sum_l \left(-J_{Q_l} \sum_{i_l} (\hat{c}_{i_l,r}^\dagger \hat{c}_{i_l+1,r} + \text{h.c.}) \right) + U \prod_l \delta_{i_l,0} \quad (5.11)$$

Here the sum (product) over l denotes the sum (product) over the different dimensions.

This hamiltonian is equivalent to a single particle Hubbard model with an additional potential at the central lattice site. Due to the cosine shaped dispersion relation in the Hubbard model, the effective tunneling for the relative motion depends on the center-of-mass momentum [136]

$$J_{Q_l} = 2J \cos \left(Q_l \frac{d}{2} \right) \quad (5.12)$$

In the non-interacting case the solution is again a Bloch wave with quasi-momentum \vec{q} and all eigenenergies are given by¹:

$$E_{\vec{Q},\vec{q}} = E_{\vec{q}_1} + E_{\vec{q}_2} = -4J \sum_l \cos(Q_l d/2) \cos(q_l d) \quad (5.13)$$

In the interacting case the above hamiltonian (eqn. 5.11) can be solved numerically using exact diagonalization. Its spectrum consists of the band of two particle scattering states with energies ranging from $-4Jl$ to $4Jl$ and a possible bound state:

While in 1D and 2D a bound state exists for all non-vanishing interactions, it appears only above a critical interaction of $|U/J| = 7.9136$ [7] in the three dimensional case.

Similar to the case of a Feshbach resonance in free space (cf. sec. 3.3), the appearance of a bound state causes a scattering resonance [138, 139], which leads to a BEC-BCS crossover in the many-body case.

The appearance of this bound state and the corresponding scattering resonance are a generic Hubbard model effect that is independent of the (molecular) Feshbach resonance studied in free space. The scattering resonance can be addressed either by changing the lattice depth at constant magnetic field (i.e. constant free space scattering length), or by changing the free space scattering length using a (molecular) Feshbach resonance. But also in the latter case the resonance in the Hubbard model is reached at some finite scattering length.

Moreover, the spectrum of eigenenergies, which is shown in figure 5.2, illustrates another peculiar aspect of all single-band Hubbard models: In the tight-binding regime (cf. sec. 4.3.2) the possible kinetic energies are distributed symmetrically around the energy of a localized particle and are bounded from below and above.

¹The allowed values for q_l depend on the value of Q_l via $|q_l| \leq k - |Q_l/2|$

5.3. Two particle Hubbard model

This is in stark contrast to free-space, where the kinetic energy is only bounded from below, it needs to be positive but can be infinitely large.

One important consequence of this symmetry is the existence of repulsively bound states: In the case of $U/J > 8$ the highest energy state is separated from the continuum of scattering states in an exactly symmetric way to the lowest energy state for $U/J < -8$. Due to the energy gap to the scattering continuum, two particles in this repulsively bound state cannot decay into a scattering state and are therefore bound together due their repulsive interaction. These states, which were first observed for bosonic atoms [140], can determine the time constants with which the system responds to parameter changes, as will be seen in the expansion measurements in chapter 10.

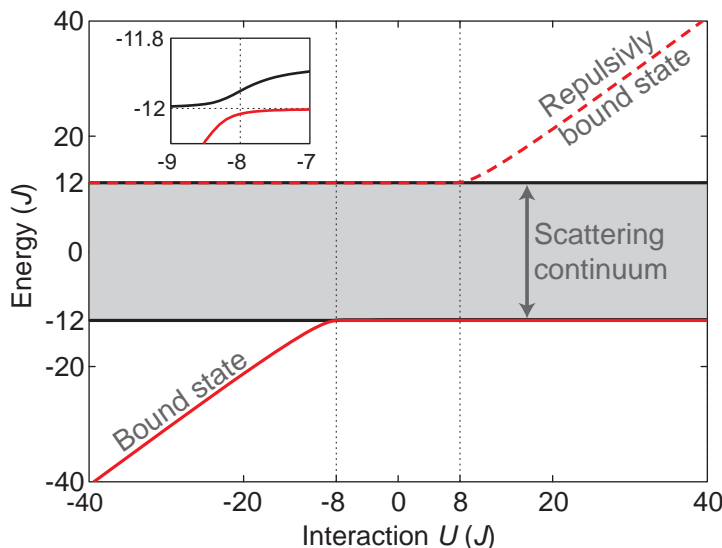


Figure 5.2.: Eigenenergies of the relative hamiltonian of the 3D two-particle Hubbard model for $\vec{Q} = \vec{0}$. The spectrum consists of a band of scattering states with energies ranging from $-12J$ to $12J$. For interactions larger than $|U/J| = 7.9136$ an additional bound state appears. The inset shows the two lowest eigenenergies around the critical interaction (calculated for a finite lattice size).

The character of the bound states can also be seen from figure 5.3, where the probability to find both particles on the same lattice site is plotted together with the extension of the two lowest lying eigenstates: For $|U/J| < 8$ both states are scattering states and their sizes are on the order of the simulated system size. For $|U/J| > 8$ the lowest (highest) lying state is a bound state and its size decreases for stronger interactions, while the second state remains a scattering state. In the limit of dominating interactions $|U/t| \gtrsim 20$ the probability of finding both particles on the same site approaches one and the energy of the bound state is approximately U . In this case the two fermionic particles can be described as one composite boson, similar to a Feshbach molecule.

In the many-body case (cf. below) the hamiltonian can then be mapped onto a Hubbard model for hard-core bosons [141].

5. Fermi-Hubbard model

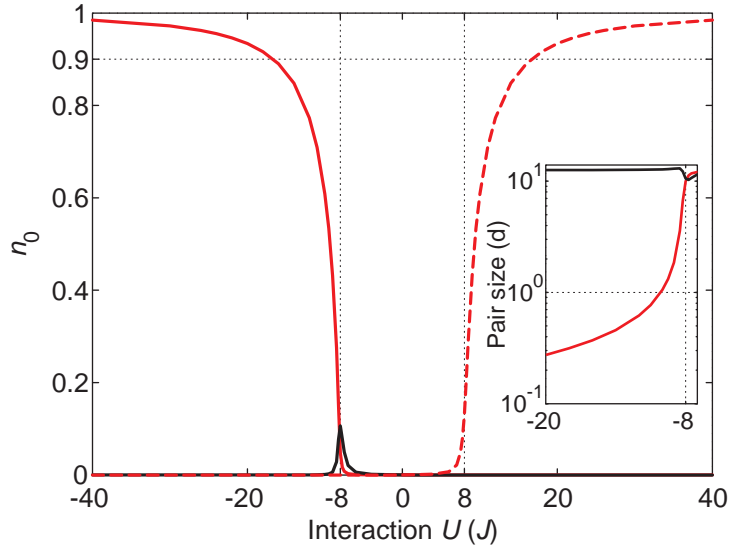


Figure 5.3.: Probability of finding the two particles in the 3D two-particle Hubbard model on the same lattice site. The solid lines denote this probability for the two lowest lying states, the dashed line for the highest energy state. The inset shows the root-mean-square extension of the two lowest lying states (calculated for a finite lattice size).

5.4. Filling factor, doublon fraction, and entropy capacity

In order to characterize the many-body states of interest, several important parameters, i.e. filling factor, doublon fraction, and entropy capacity, will be defined below together with their values in some limiting cases.

A first important parameter to characterize a state in the homogeneous Hubbard model is the filling factor n , that is the expectation value of the number operator $n_\sigma = \langle \hat{n}_\sigma \rangle$, i.e. the average particle number per lattice site of a given spin state. In the experimentally studied case of an even spin mixture in the trap the filling factor is independent of the spin $n = n_\uparrow = n_\downarrow$ but depends on the position in the trap $n = n(\vec{r})$ (cf. ref. 5.7). The filling factor can range from zero to one, where unity filling denotes two atoms per lattice site and half-filling denotes the important case of on average one atom per lattice site.

5.4.1. Doublon fraction

One important observable in the experiment is the doublon fraction, that is the fraction of atoms on doubly occupied lattice sites. It strongly depends on the interaction, the temperature, and the filling factor and can be calculated exactly for certain limiting cases:

5.4. Filling factor, doublon fraction, and entropy capacity

Assuming a homogeneous lattice and an even spin mixture with filling factors $n = n_\sigma$ we define the doublon fraction D as:

$$D = \frac{2N_{pair}}{N_{atoms}} = \frac{2 \langle \hat{n}_\downarrow \cdot \hat{n}_\uparrow \rangle}{\langle \hat{n}_\uparrow \rangle + \langle \hat{n}_\downarrow \rangle} = \frac{\langle \hat{n}_\downarrow \cdot \hat{n}_\uparrow \rangle}{n} \quad (5.14)$$

Non-Interacting Without interactions there are no correlations between the different spin states and the doublon fraction simplifies to:

$$D_{\text{non-IA}} = \frac{\langle \hat{n}_\downarrow \cdot \hat{n}_\uparrow \rangle}{n} = \frac{\langle \hat{n}_\downarrow \rangle \cdot \langle \hat{n}_\uparrow \rangle}{n} = \frac{n \cdot n}{n} = n \quad (5.15)$$

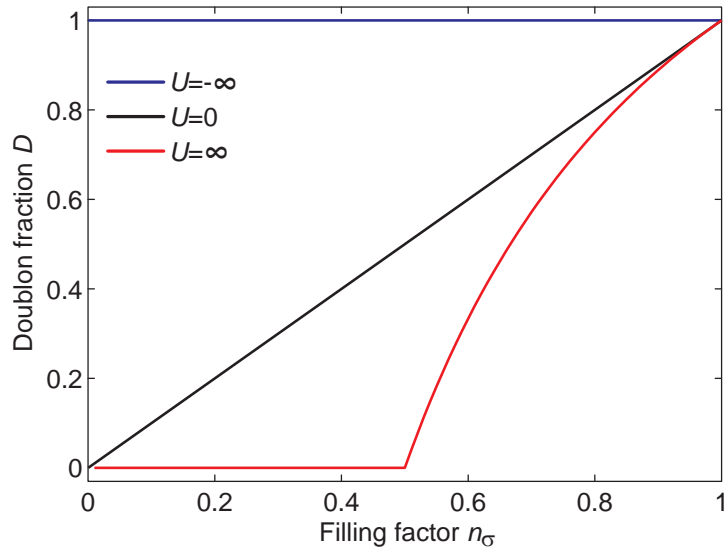


Figure 5.4.: Doublon fraction as a function of filling in the non-interacting case and the limits of strong interaction $|U| \gg J, k_B T$. In the strongly attractive and repulsive case up to half filling, the doublon fraction is constant and yields no information about the filling. It therefore cannot distinguish between a Mott insulator (cf. sec. 5.5.2) at $n = 0.5$ and a complex metal with $n < 0.5$.

Strong repulsive interaction In the limit of dominating repulsive interactions $U \gg 12J$ and $U \gg k_B T$ the energy cost U of two atoms on the same lattice site is the biggest energy scale in the problem and the doublon fraction is as small as possible for the given filling factors. Below half filling there are more lattice sites than atoms and the doublon fraction is zero. Above half filling the number of atoms is bigger than the number of available lattice sites and a fraction $2n - 1$ of lattice sites must be occupied by two atoms, which leads to the following doublon fraction

$$D_{\text{rep-IA}} = \frac{2N_{pair}}{N_{atoms}} = \begin{cases} 0 & n \leq 0.5 \\ \frac{2(2n-1)}{2n} = 2 - \frac{1}{n} & n > 0.5 \end{cases} \quad (5.16)$$

5. Fermi-Hubbard model

Strong attractive interaction In the case of $-U \gg 12J$ and $-U \gg k_B T$ all atoms will form pairs: $D = 1$

5.4.2. Entropy capacity

Another relevant quantity in the Hubbard model is the entropy capacity S_{\max} per lattice site, which depends on both the filling and the interaction and can be calculated using $S = -k_B \text{tr}(\rho \log(\rho))$ [142]. In the high temperature limit the density matrix for a single lattice site is diagonal

$$\begin{aligned} \rho = h &|0_\downarrow, 0_\uparrow\rangle\langle 0_\uparrow, 0_\downarrow| + sd |1_\downarrow, 0_\uparrow\rangle\langle 0_\uparrow, 1_\downarrow| \\ &+ su |0_\downarrow, 1_\uparrow\rangle\langle 1_\uparrow, 0_\downarrow| + d |1_\downarrow, 1_\uparrow\rangle\langle 1_\uparrow, 1_\downarrow| \end{aligned} \quad (5.17)$$

in the Fock basis. The coefficients h, sd, su, d denote the probability for zero, single, and double occupation. They are determined by maximizing the entropy under the requirements of an equal spin mixture ($sd = su$), the desired filling factor ($sd + d = n$), normalization ($h + sd + su + d = 1$) and the doublon fractions calculated in the previous section (5.4.1). The resulting entropy capacity is plotted in figure 5.5.

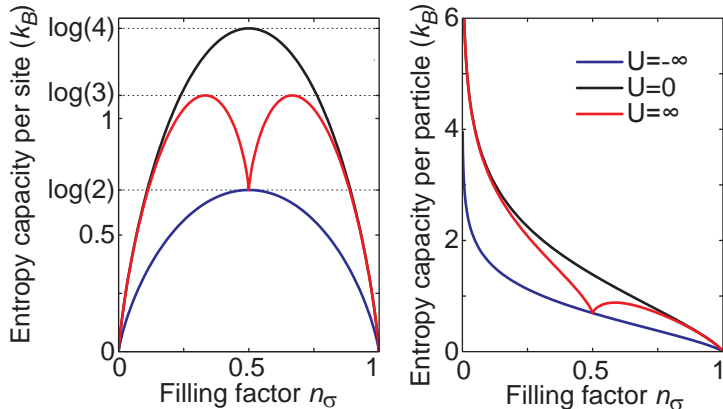


Figure 5.5.: Entropy capacity of a homogeneous Hubbard model. left: Maximum entropy per lattice site in the non-interacting and strongly-interacting limits. right: Corresponding entropy capacity per particle.

As the local (single-site) Hilbert space is four dimensional, the maximum entropy capacity is bounded by $k_B \log(4)$, which is reached for a non-interacting cloud at half filling, where all four possible configurations have the same probability. In the limit of strong interactions the effective dimensionality of the local Hilbert space is reduced to two in the attractive case ($sd = su = 0$) resp. three in the repulsive case ($n \leq 0.5 \rightarrow d = 0$ and $n \geq 0.5 \rightarrow h = 0$). This leads to a corresponding reduction of the entropy capacity: At half filling the entropy capacity in the repulsive case, i.e. the Mott Insulator (cf. sec. 5.5.2), is given by $k_B \log 2$, as there are both no holes and no doublons ($h = d = 0$).

5.5. Phases of the three dimensional homogeneous Hubbard model

The maximum entropy per particle, which is plotted in the right panel of figure 5.5, scales as S_{\max}/n and diverges for low fillings similar to the number of available lattice sites per particle. For high fillings on the other hand, the maximum entropy per particle vanishes. For a given entropy density, this limits the achievable densities and gives rise to incompressible band insulating states at all temperatures (cf. sec. 5.5.1).

The average entropy per particle that can be reached experimentally (cf. table 2.1) is on the order of $1 - 1.5 k_B$ and is above the entropy capacity of a half-filled Hubbard model in the strongly interacting case. This regime can nonetheless be realized experimentally by exploiting the inhomogeneity given by the trapping potential: As will be detailed in chapter 8.2.1, most of the entropy will be stored in the low filling regions (cf. fig. 8.5), where large entropies per par particle are possible.

5.5. Phases of the three dimensional homogeneous Hubbard model

This section gives a brief overview over the phase diagram of the homogeneous Hubbard model. As there exists no analytical solution for the Fermi-Hubbard model, except from special cases, the phase diagram is not completely known and many details of the various published phase diagrams [143–149] depend on the approximations made in the calculations resp. the chosen numerical method.

The phase diagram of the homogeneous model is discussed as a function of filling n and temperature T , the connection to the trapped case will be given in section 5.7. In the experiment the total particle number N and total entropy S (c.f. sec. 2.3) are conserved and limit the accessible regimes. Unity filling for instance cannot be reached at finite entropies in the homogeneous system, as the entropy capacity of the Hubbard model vanishes in this limit (cf. sec. 5.4.2).

5.5.1. Non-interacting

In the non-interacting case there are no correlations between particles with different spins and all many-body states can be described using only Fermi-Dirac statistics and the single-particles eigenstates, the Bloch waves. Every particle is delocalized over the whole lattice and there exist two zero temperature regimes, a band-insulating state at unity filling and a metallic state for all other fillings.

The metallic state is conducting and compressible (cf. sec. 5.2): Adding another particle changes the Fermi energy by an amount on the order of the bandwidth divided by the number of lattice sites ($\Delta E_F \sim 12J/N_{\text{lat}}$), which vanishes in the thermodynamic limit.

The band insulating state is incompressible since an additional particle would need

5. Fermi-Hubbard model

to occupy a higher band and would thereby increase the Fermi energy by the band gap.

Due to the decreasing entropy capacity of the Hubbard model above half filling (cf. fig. 5.5), this incompressible band insulating phase exists for all entropies: For every entropy per particle there exists a maximum filling, above which the given entropy would exceed the entropy capacity of the single band Hubbard model.

5.5.2. Repulsive interaction

The inclusion of repulsive interactions leads to modifications both in the charge and in the spin distribution. If spin ordering is neglected, the system displays metallic and band-insulating phases at weak interactions, similar to the non-interacting case. For strong interactions in addition the incompressible *Mott insulator* phase appears at half filling:

In the Mott insulator every particle is localized due to the mutual repulsion between the particles (cf. sec. 5.2.1), and the addition of another particle would change the Fermi energy by a finite amount of order U . This energy gap, the *Mott gap*, gives rise to the incompressible and insulating behavior of this phase.

In the absence of magnetic order there is a first order phase transition at a critical interaction $U_c/12J = 1.26$ [150] from metallic to insulating behavior for low temperatures. Above a critical temperature [121] the phase transition turns into a smooth crossover. In DMFT calculations (cf. sec. 5.6) the phase transition shows up as a discontinuous jump in the doublon fraction [151]. In the Mott phase the doublon fraction is exponentially suppressed in U and vanishes in the limit of strong repulsive interactions ($U \rightarrow \infty$), where the system reduces to a set of uncoupled micro-traps with one particle per site.

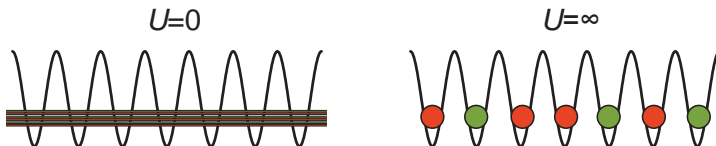


Figure 5.6.: left: In a non-interacting metal every atom is in a delocalized Bloch state. right: In the Mott insulating phase the atoms are localized due to the mutual repulsion and at $U = \infty$ every particle occupies a Wannier state.

Including the possibility of magnetic ordering, however, the ground state at half filling shows antiferromagnetic long-range order for all interactions due to a perfect nesting of the Fermi surface [152].

At finite temperatures the antiferromagnetic order parameter, which is given by the sublattice magnetization or staggered magnetization, is reduced by thermal fluctuations and vanishes at the *Néel temperature*, where a transition into the paramagnetic regime occurs. Quantum Monte Carlo calculations (cf. sec. 5.6) have shown that the Néel temperature in a 3D simple cubic lattice at U_c lies well above

5.5. Phases of the three dimensional homogeneous Hubbard model

the critical temperature of the Mott transition [152], so that only a crossover from a correlated metal to a Mott insulator can be observed. At small interactions the critical temperature decreases exponentially with U [153].

In the spin-balanced case ($N_\uparrow = N_\downarrow$) the staggered magnetization can point in every direction. In the spin-imbalanced case ($N_\uparrow \neq N_\downarrow$), however, the system will form a *canted antiferromagnet*, where the magnetization is the sum of a constant component along the z -direction and a staggered magnetization in the x, y -plane.

Away from half filling, where the atoms are not localized, the system is expected to become ferromagnetic for large interactions due to the Stoner instability [154, 155]. In the inhomogeneous trapped case the spin-imbalance can locally vary and the system will show complex spin textures [155].

Strong repulsive interactions

In order to analyze the regime of finite but strong repulsive interactions ($U \gg 12J, k_B T$), the Hubbard model can be approximated using perturbation theory: Starting in the limit of uncoupled lattice sites, where the hamiltonian consists only of the interaction term of the Hubbard model, tunneling between the sites is treated as a perturbation. At half filling the first order contribution, which describes uncorrelated single particle tunneling, can be neglected, as it is detuned by the large on-site interaction U . The behavior of the system is dominated by two second order contributions that are analogues to two-photon Raman processes in light fields:

The first one consists of a particle virtually hopping to the next site and back, where the intermediate state is again detuned by U . This process creates a coherent admixture of the adjacent site to the eigenstate and thereby lowers its energy by $\sim J^2/U$.

The second process is superexchange tunneling [156], in which two adjacent fermions interchange their positions in a correlated second order hopping.

In the half filled case, where all particles are localized due to the repulsive interaction, the Hubbard hamiltonian reduces to a *Heisenberg hamiltonian* [108] for the remaining spin degree of freedom:

$$H_{\text{heis}} = J_{\text{ex}} \sum_{\langle i,j \rangle} \vec{S}_i \cdot \vec{S}_j \quad (5.18)$$

The isospin operators \vec{S}_i can be expressed in terms of the Pauli matrices σ^j

$$\hat{S}_i^j = \frac{1}{2} \sum_{\sigma, \sigma'} \hat{c}_{i,\sigma} \sigma_{\sigma, \sigma'}^j \hat{c}_{i,\sigma'}^\dagger \quad (5.19)$$

and the coupling between the spins is given by the *exchange coupling* $J_{\text{ex}} = 4J^2/U$, which favors an antiferromagnetic ordering of the spins.

5. Fermi-Hubbard model

This tendency towards an antiferromagnetic state can be understood by observing that the first process lowers the energy of the localized particles but is only possible for adjacent particles with opposite spins, as the intermediate state is otherwise Pauli forbidden.

In the case of a balanced spin mixture the ground state of this Heisenberg model is indeed an antiferromagnetic insulator, whose Néel temperature again scales as J^2/U while the critical entropy per particle approaches $S/N = 0.34 k_B$ [157]. Similar critical entropy densities have also been reported for the full Hubbard model at $U/J = 8$ [158]

In the case of spin-imbalanced mixtures the ground state can also show superfluid counterflow [159]. Away from half filling the system can be described by the $t-J$ model [124, 125], in which t describes the uncorrelated models of the defects (holes or doublons) and J refers to the exchange coupling of the Heisenberg model.

Superconducting phases

Since there exists no analytic solution for the Hubbard model (or even the $t-J$ model) in two and three dimensions, one has to rely on numerical and approximative methods, e.g. renormalization group methods [160], which predict rich phase diagrams [147]. One important question, especially in the 2D repulsive Hubbard model, is the existence of superconducting eigenstates that could be used to model the cuprate high- T_c superconductors [129].

Superfluid eigenstates of the suitable d symmetry have indeed been found in various approximative treatments of the 2D Hubbard model and its extensions [161–165], but a rigorous proof of their existence is still missing, which makes an experimental observation of these states very desirable [166]. In the case of an extended Hubbard model with next-to-nearest neighbor tunneling, the ground state is expected to show superfluidity also in the weakly interacting limit [167].

5.5.3. Attractive interaction

In the spin balanced case the ground state for weak attractive interactions is a BCS like superfluid state, consisting of very loosely bound pairs of spin up and spin down particles [168]. This is completely analogous to classical superconductors, where the BCS pairing is a genuine many-body effect in the absence of two-particle bound states [24] in the 3D case.

If the interaction becomes stronger than a critical interaction ($|U_c/J| \approx 8$), a two-particle bound state appears (cf. sec. 5.3) in the attractive Hubbard model and causes a scattering resonance that is similar to a Feshbach resonance in free space (cf. sec. 3.3). This gives rise to a BEC-BCS crossover, which has been extensively studied in free space (cf. [45] and references therein). At stronger interactions

5.5. Phases of the three dimensional homogeneous Hubbard model

the fermionic particles form tightly bound pairs, whose size decreases to a single lattice site for strong interactions (cf. sec. 5.3)².

Without spin imbalance the ground state of the attractive 3D Hubbard model is a superfluid for all interactions and all fillings. At half filling the superconducting state is degenerate with a charge density ordered state [144] (cf. sec. 5.5.4). For weak interactions, the critical temperature T_c of the superfluid transition grows exponentially with increasing interactions similar to free space, and reaches a maximum at intermediate interactions in the vicinity of the geometric resonance. In contrast to free space, where the critical temperature approaches that of the non-interacting Bose gas in the BEC limit, it decreases as $J^2/|U|$ (cf. below) in the 3D lattice [143–145]. At half filling, the critical entropies for the superfluid phase equal those of the antiferromagnetically ordered phase of the corresponding repulsive Hubbard model, as can be seen from the Lieb Mattis transformation discussed below (cf. sec. 5.5.4).

In a 2D system the superfluid is reached through a Berezinskii-Kosterlitz-Thouless transition whose critical entropy per particle has been calculated using quantum Monte Carlo methods [170] and yielded entropies below $S/N < 0.2 k_B$, which is considerably colder than the entropies currently reached in the experiment (cf. sec. 2.2.2).

Even richer phase diagrams can be obtained in the spin imbalanced situation where additional phases, e.g. the FFLO phase [148, 171–173] become relevant.

Strong attractive interactions: Hard core bosons

An important difference between the lattice and free space on the BEC side of the geometric resp. Feshbach resonance is the quantum statistics of the tightly bound pairs:

In free space the bound state is a chemically bound molecule that can be treated as a bosonic object at all experimentally relevant densities. The fermionic nature of the atoms becomes relevant only in calculating the interaction strength and life times of the molecules [82] (cf. sec. 3.3.2). Consequently, the many body ground state in free space is a superfluid for all interaction strengths [45].

In the first band of the lattice on the other hand, the Pauli principle forbids the occupation of a single lattice site by more than two fermions. As a consequence, the bound states –or pairs– can be described as *hard core bosons*, as no lattice site can be occupied by more than one pair.

²Due to the high symmetry of the tight-binding dispersion, exactly the same physics appears also in the high energy (small negative temperature) limit of the repulsive Hubbard model [169]. This can be seen by observing that for every eigenstate with energy E of a hamiltonian H there exists an eigenstate with opposite energy $-E$ for the hamiltonian $-H$. As described in chapter 10.3.3, for the Hubbard hamiltonian the transformation $H \leftrightarrow -H$ consists of the transformations $U \leftrightarrow -U$ and $J \leftrightarrow -J$, where the latter is equivalent to π -boost in quasi-momentum space (cf. sec. 10.3.3). As a consequence, a BEC-BCS crossover exists for states centered around $\vec{q} = (\pi/d, \pi/d, \pi/d)$ in the repulsive Hubbard model.

5. Fermi-Hubbard model

In the strongly interacting case ($|U| \gg 12J, k_B T$) the binding energy of the pairs approaches $|U|$ (cf. sec. 5.3) and all particles will be paired. Similar to the repulsive case, an effective hamiltonian can be derived for the pairs using second order perturbation theory [174]:

$$H_{\text{eff}} = - \sum_{\langle i,j \rangle} J_{\text{pair}} \hat{b}_i^\dagger \hat{b}_j + \sum_{\langle i,j \rangle} J_{\text{pair}} \hat{n}_{b_i} \hat{n}_{b_j} \quad (5.20)$$

where $\hat{b}_i = \hat{c}_{i,\downarrow} \hat{c}_{i,\uparrow}$, $\hat{b}_i^\dagger = \hat{c}_{i,\downarrow}^\dagger \hat{c}_{i,\uparrow}^\dagger$, $\hat{n}_{b_i} = \hat{b}_i^\dagger \hat{b}_i$ are the annihilation, creation and number operators of the pairs and $J_{\text{pair}} = 2J^2/|U|$. These pair operators indeed describe hard core bosons, as can be seen from $\hat{b}_i \hat{b}_i = \hat{c}_{i,\downarrow} \hat{c}_{i,\uparrow} \hat{c}_{i,\downarrow} \hat{c}_{i,\uparrow} = \hat{c}_{i,\downarrow} \hat{c}_{i,\downarrow} \hat{c}_{i,\uparrow} \hat{c}_{i,\uparrow} = 0$, since the Pauli principle requires $\hat{c}_{i,\uparrow} \hat{c}_{i,\uparrow} = 0$.

The first term in the above hamiltonian describes the correlated hopping of a pair from one site to the next, while the second part describes a nearest neighbor repulsion between the pairs. This second term stems from the same principle as the antiferromagnetic tendency in the repulsive case: If the neighboring site is unoccupied, a localized pair can lower its energy via virtual hopping of one fermion to the neighboring site and back.

Pseudogap regime

The occurrence of pairing has dramatic consequences on the many-body state also above T_c : In the pseudogap -or preformed pair- regime the particles are bound into pairs, but the pairs are not condensed yet [145, 146, 175]. This formation of uncondensed pairs e.g. dramatically alters the thermodynamics of the system, as shown in chapter 9.

This regime is related to the Pseudogap regime in the cuprate based high-temperature superconductors, where the formation of preformed pairs is one possible explanation for the observed gap in the electronic excitation spectrum [24, 176]. This gap opens below a crossover temperature $T^* > T_C$ and manifests itself in e.g. the decrease of the spin-susceptibility, the specific heat and the in-plane d.c. resistivity in the underdoped regime [177].

In the BCS regime of the Hubbard model the crossover temperature into the pseudogap regime $T^* > T_C$ almost coincides with the critical temperature, but starts to deviate from it in the BEC-BCS crossover regime. In the BEC (large $|U|$) limit, where T_c decreases again as $J^2/|U|$, T^* scales like the pair binding energy, which approaches $|U|$ (cf. fig. 5.2).

5.5.4. Lieb-Mattis transformation

The Hubbard model is a highly symmetric model and incorporates many useful symmetries between e.g. particle and hole state or U and $-U$ dynamical properties

(cf. sec. 10.3.3).

The *Lieb-Mattis transformation* is a particular particle-hole transformation that can be formulated for any bipartite lattice and relates the phases of the repulsive Hubbard model to those of the attractive Hubbard model. It consists of a particle-hole transformation together with an additional phase shift for one spin state, while leaving the other spin state unchanged [173, 178]:

$$\hat{c}_{i,\downarrow} \rightarrow (-1)^{i_x+i_y+i_z} \hat{c}_{i,\downarrow}^\dagger \quad (5.21)$$

$$\hat{c}_{i,\uparrow} \rightarrow \hat{c}_{i,\uparrow} \quad (5.22)$$

Due to the choice of the phase shift, which corresponds to an additional phase of π on all lattice sites belonging to one sublattice, the kinetic energy operator (cf. eqn. 5.1) remains unchanged, while the number operator of the spin down particles changes into $\hat{n}_{i,\downarrow} = 1 - \hat{n}_{i,\uparrow}$. This change in the number operator effectively flips the sign of the interaction energy³ ($U \rightarrow -U$) and furthermore exchanges the roles of imbalance ($n_{i\downarrow} - n_{i\uparrow}$) and doping ($n_{i\downarrow} + n_{i\uparrow} - 1$).

As localized single atoms in the repulsive Hubbard model are transformed into either empty lattice sites (spin down), or doublons (spin up), a paramagnetic Mott insulator becomes a disordered charge density wave of doublons, i.e. a state in which doublons are localized to random lattice sites.

Any magnetic order in the repulsive Hubbard model is related to a paired or density ordered state on the attractive side [173]: Antiferromagnetic order for instance is mapped onto either an ordered charge density wave, where all sites belonging to one sublattice are occupied by a doublon, or a superfluid state, depending on the direction of the staggered magnetization: Its z -component corresponds to the ordered charge density wave while the x - and y -components are mapped onto the real and imaginary part of the superfluid order parameter [178].

As was pointed out in [178], this mapping creates the possibility to experimentally prove the existence of a d -wave superfluid in the doped repulsive 2D Hubbard model by observing the corresponding phase (a d -wave antiferromagnetic phase) in the attractive Hubbard model. One major advantage in this case is the possibility to effectively control the doping of the repulsive model by controlling the spin imbalance in the attractive case.

5.6. Numerical methods

In 1D the Fermi-Hubbard model has been solved analytically by E. Lieb and F.-Y. Wu in 1968 and a Mott Insulator was found for any positive U at half filling [179],

³In addition an unimportant constant energy offset (UN_\uparrow) is added, which will be neglected in the following. To avoid this offset it is convenient to write the interaction term in symmetrized densities, where the density difference to half filling is measured: $W = U \sum_i (\hat{n}_{i\downarrow} - 1/2)(\hat{n}_{i\uparrow} - 1/2)$.

5. Fermi-Hubbard model

while a conducting ground state was found for $U=0$ and away from half filling. In higher dimensions the Hubbard model cannot be solved analytically, and one has to rely on numerical methods or analytic approximations.

Exact diagonalization In some cases the exact many-body eigenstates can be found by numerically diagonalizing the hamiltonian in a suitable basis. The computational costs and the memory requirements of this method scale exponentially with the number of particles and therefore limit this method to less than 20 particles on less than 25 lattice sites, even if modern supercomputers are used [9]. Although the exponential scaling renders an application in 3D impossible, exact diagonalization of small model systems with only two particles or on a few lattice sights still provides valuable insight and many effects can be modeled at least qualitatively, several examples of which are given in this thesis. In addition, the non-interacting problem can be solved exactly and efficiently with this method for realistic system sizes and a lot of trap varieties. This can be used e.g. in order to check the validity of the local density approximation (LDA) (cf. sec. 5.7.1).

Dynamical mean field theory Another important numerical method is *dynamical mean field theory* (DMFT), in which the many-site problem is reduced to a single site problem in the presence of an effective bath, which represents the remaining system [180]. This method has been used by R.W. Helmes, T.A. Costi and Prof. A. Rosch at the University of Cologne and the Research Center Jülich in order to model the metal to Mott insulator transition in the presence of an harmonic trap [150]. In chapter 8 their results are presented in more detail and are compared to the experimental results. In addition, this method has also been used to study the attractive Hubbard model [144] and has been extended to the three species repulsive Hubbard model [181].

Further methods In the context of ultracold atoms in optical lattices, two further numerical methods are in common use: The density matrix renormalization group (DMRG) method [182] is very successful in 1D and is currently expanded to 2D. In addition there exist several quantum Monte Carlo methods, which are very powerful in the bosonic case, but are notoriously plagued by the so-called sign problem when applied to repulsive fermions. It could indeed be shown that the sign problem lies in the complexity class of nondeterministic polynomial (NP) hard problems [183], which almost certainly excludes the existence of an efficient algorithm.

Nonetheless, they could be applied to the attractive Hubbard model in order to predict the critical entropies of various superfluid phases in 2D [170], and 3D [173]. In addition they could predict the onset of antiferromagnetic order in the exactly half filled repulsive Hubbard model [152, 184], where the sign problem is also absent.

5.7. Inhomogeneous system

The presence of the harmonic trap destroys the translational symmetry of the lattice and could in principle change the physics of the problem completely. While the inhomogeneity can easily be incorporated into a numerical calculation for non-interacting particles (cf. sec. 4.3.2), it poses a severe complication in the general case.

Fortunately, it turns out that, for typical experimental parameters, the length scale of the additional potential is sufficiently large compared to the lattice constant such that the system can locally be approximated by a homogeneous system, as detailed in this section.

By combining the general Fermi-Hubbard hamiltonian (cf. eq. 5.5) with the three dimensional harmonic trapping potential (cf. eq. 4.21) with aspect ratio γ one arrives at:

$$\hat{H} = -J \sum_{\langle i,j \rangle, \sigma} \hat{c}_{i,\sigma}^\dagger \hat{c}_{j,\sigma} + U \sum_i \hat{n}_{i,\downarrow} \hat{n}_{i,\uparrow} + V_t \sum_i i^2 (\hat{n}_{i,\downarrow} + \hat{n}_{i,\uparrow}) \quad (5.23)$$

where the horizontal trap frequency ω_\perp is used in the strength of the harmonic trap V_t (cf. eqn. 4.22) and i^2 is a short hand notation for $i^2 = i_x^2 + i_y^2 + \gamma^2 i_z^2$.

5.7.1. Local density approximation

If the external potential varies slowly enough, the description of the inhomogeneous Hubbard model can be simplified substantially by use of the *local density approximation* (LDA), in which the inhomogeneous system is locally approximated by a homogeneous Hubbard model. The effects of the external potential are then incorporated by local shifts in the chemical potential:

$$\mu(\vec{r}) = \mu_0 - \epsilon_{\vec{r}} \quad (5.24)$$

All local quantities, e.g. the filling factor $n(\vec{r})$ or the entropy density $s(\vec{r})$ are approximated by the corresponding quantities of the homogeneous system:

$$n(\vec{r}) = n(\mu_0 - \epsilon_{\vec{r}}, T) \quad (5.25)$$

In order to compare the results of such calculations to experimental data, the central chemical potential μ_0 and the temperature T are adjusted such that the resulting total atom number and entropy match the experimental values:

$$N = 2 \int n(\mu_0 - \epsilon_{\vec{r}}, T) dV \quad (5.26)$$

$$S = \int s(\mu_0 - \epsilon_{\vec{r}}, T) dV \quad (5.27)$$

5. Fermi-Hubbard model

The validity of the LDA for calculating thermodynamic properties and the real- and momentum-space density (cf. sec. 6) of the repulsive Hubbard model could be shown by a direct comparison with numerical results obtained for the full inhomogeneous system [150, 185].

Characteristic trap energy

For a given set of hamiltonian parameters (tunneling J , interaction U , and trap frequency ω_\perp, γ), any thermal state in the trapped system is determined by the chemical potential μ_0 and the temperature T , which encode its total atom number N and entropy S .

These six parameters are, however, not independent of each other: The number of independent degrees of freedom is for instance reduced by the freedom to choose a global energy scale, i.e. to express all parameters in units of the bandwidth $12J$. In the case of a typical harmonic trapping potential (cf. sec. 4.3.2) the validity of the LDA implies an additional scaling relation connecting the trap frequencies and the total atom number at constant chemical potential. This can be seen by imagining the inhomogeneous system as a sequence of boxes with constant chemical potentials (μ_0, μ_1, \dots). As illustrated in figure 5.7, a change in the trapping frequency ω amounts to a rescaling of the volume of the boxes $V_{\text{box}} \propto 1/\omega$ (3D: $V_{\text{box}} \propto 1/\omega_\perp^3$). If all extensive parameters (E, N, S) are scaled accordingly to the change of the box volume, the local physics and all intensive parameters (n, s, μ, T) remain unchanged.

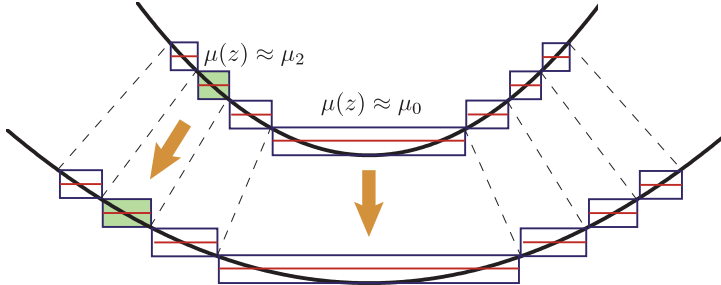


Figure 5.7.: Illustration of the scaling relation in LDA. If one approximates the inhomogeneous system by a sequence of boxes with constant chemical potential, a change in the trap frequency leads to a rescaling of the box volume. In LDA, the physics in each box is approximated by the (infinite) homogeneous system and remains unchanged by the rescaling.

A convenient parameter to exploit this scaling relation is the Fermi energy in the limit of vanishing interactions and zero tunneling $E_F(J = 0, U = 0)$. In this limit the eigenstates coincide with the Wannier states and the N_σ lowest energy eigenstates correspond to the Wannier states on all lattice sites within an ellipsoid of volume $N_\sigma/(\lambda/2)^3$ around the trap center:

$$V_{\text{ellip}} = \frac{4\pi}{3} \frac{r_\perp^3}{\gamma} \approx N_\sigma/(\lambda/2)^3 \quad (5.28)$$

5.8. Validity of the Hubbard model

Here N_σ denotes the total atom number *per spin state*. The Fermi energy is then given by the confining potential at the edge of the cloud

$$r_\perp = \left(\frac{\gamma N_\sigma}{4\pi/3} \right)^{\frac{1}{3}} \frac{\lambda}{2} \quad (5.29)$$

and is denoted as the *characteristic trap energy* E_t :

$$E_t = V_t \left(\frac{\gamma N_\sigma}{4\pi/3} \right)^{\frac{2}{3}} \quad (5.30)$$

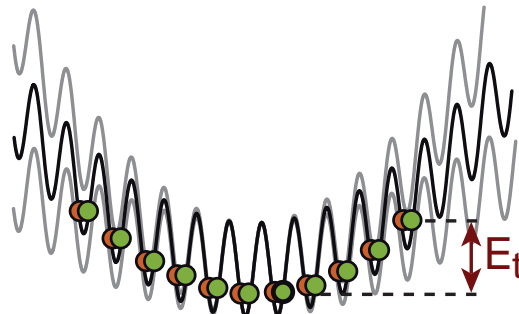


Figure 5.8.: Illustration of the characteristic trap energy E_t . It depends on both the total atom number and the trap frequencies and can intuitively be understood as the Fermi energy in the limit of zero tunneling and vanishing interaction.

Together with the entropy per particle S/N and the strength of the interaction $U/12J$, the characteristic trap energy $E_t/12J$ completely determines the many-body state up to the aforementioned rescaling.

The ratio of characteristic trap energy to bandwidth $E_t/12J$, which is also referred to as the *compression*, is equivalent to another widely used parameter, namely the characteristic density [62, 130]: $\rho_c \propto (E_t/12J)^{3/2}$. The main advantage of the characteristic trap energy is its dimensionality, which allows an intuitive comparison to other energies, e.g. the bandwidth $12J$ or interaction strength U .

5.8. Validity of the Hubbard model

In the context of solid state physics, the Hubbard model really needs to be seen as a model, i.e. a highly idealized system that neglects many aspects of the real system, e.g. disorder, impurities, or phonons. With respect to ultracold atoms, the Hubbard model is a much more precise description. Nonetheless, several assumptions of the Hubbard model are not fulfilled in all cases and need to be checked in any given situation:

5. Fermi-Hubbard model

- In the Hubbard hamiltonian (cf. eqn. 5.5) only nearest neighbor tunneling is included. This limits its applicability to the tight-binding regime of sufficiently deep lattices ($V_0 > 5E_r$, cf. sec. 4.3.2).
- An additional approximation is the use of Wannier functions as on-site wavefunctions. While this is perfectly justified for non-interacting particles, the form of the on-site wavefunction generally depends on the interactions and the number of particles. This was shown for bosonic systems and Bose-Fermi mixtures in the following publications [186–188] and will be discussed in detail in the PhD theses of Thorsten Best and Sebastian Will.
- For not too strong interactions, the change in the on-site wavefunction can be accounted for by a renormalization of the Hubbard parameters J and U . In the presence of strong interactions, however, more complicated interaction terms, e.g. density assisted hopping, need to be included [189].
- In order for the single band approximation to be valid, the band gap needs to be large compared to all other energy scales, esp. the interaction energy U and the Fermi energy E_F . While this is typically a good approximation in a relatively deep lattice, care has to be taken during the ramp up of the lattice in order to avoid occupation of the second band (cf. sec. 4.3.2)

6. Observables: What can we measure?

The fast progress in ultracold atoms in recent years is directly linked to technical progress, as new technologies enable new experiments that enlarge our knowledge about these systems.

The technical advancement in the field of ultracold atoms is threefold: It includes better cooling techniques, which allow us realize colder samples with less entropy. Also more advanced tools to manipulate and engineer many-body states, such as optical lattices or Feshbach resonances, have enabled us to prepare new quantum states.

Additionally there is a continuous effort to develop new observables that allow us to probe and identify these states.

This chapter gives a brief introduction into several standard observables and discusses their potential in the context of the fermionic Hubbard model.

6.1. Momentum distribution

The classical probe to analyze ultracold atoms is the study of their momentum distribution using *time-of-flight imaging*. In this method, which was already used in the first BEC experiments [1, 2], all trapping potentials are switched off instantaneously and the cloud is allowed to expand freely under the influence of gravity for a certain time, the *time-of-flight*, before its density distribution is recorded by e.g. absorptive imaging. For sufficiently long times-of-flight the recorded density distribution directly reflects the initial velocity distribution of the atoms (cf. sec. 2.2.3), provided that interactions during the expansion can be neglected.

In lattice experiments this method was used e.g. in the case of bosonic atoms to detect the transition from a superfluid to a Mott insulating state [4], which is signaled by a dramatic change in the contrast or visibility of the peaks in the momentum distribution [190], as is shown in figure 6.1.

Although the quantitative interpretation of these images can be quite involved [191], this method has proven to give useful information on the phase coherence between different lattice sites in the system [192] and is still one of the key observables in the study of bosonic systems.

For fermions in a lattice on the other hand, simple time-of-flight imaging is less useful, as there does not exist any long-range phase coherence. Nonetheless,

6. Observables: What can we measure?

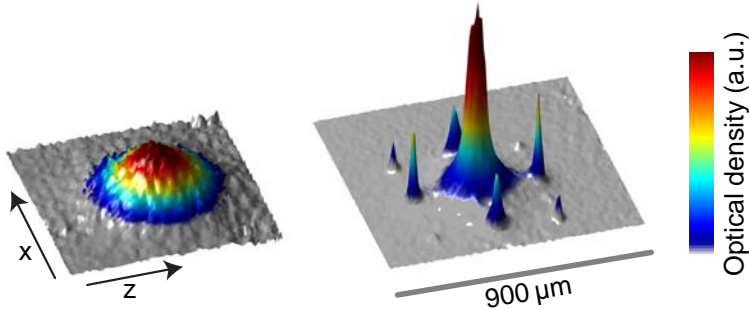


Figure 6.1.: left: Momentum distribution of a Mott insulator of bosonic ^{87}Rb monitored using absorption imaging after time-of-flight. right: Momentum distribution after a slow ramp-down of the lattice depth across the transition back into a superfluid.

important information about the system can be extracted from the density-density correlations within these images (cf. next section).

In the context of this thesis, measurements of the momentum distribution were primarily used to determine the temperature of the fermionic cloud in the dipole trap (cf. sec. 2.2.3).

It was, however, the prime observable in the related PhD thesis of Thorsten Best, where the influence of the interaction between bosons and fermions on the superfluid to Mott insulator transition of the bosonic atoms was studied in detail [186]. It was also used in the related work on quantum phase diffusion in purely bosonic systems [188], where Sebastian Will was the main investigator.

6.2. Second order correlation functions

An important extension of the above method is the analysis of second order density-density correlations in time-of-flight images, as described in detail in the PhD thesis of Tim Rom:

Although a bosonic Mott insulator with one atom per site and a spin polarized fermionic band insulator have the same average momentum distribution at zero temperature, they can be distinguished by looking at density-density correlations in the measured column density distributions $n(\vec{x})$:

$$C(\vec{d}) = \frac{\int \langle n(\vec{x} - \vec{d}/2)n(\vec{x} + \vec{d}/2) \rangle d^2x}{\int \langle n(\vec{x} - \vec{d}/2) \rangle \langle n(\vec{x} + \vec{d}/2) \rangle d^2x}$$

While bosonic atoms show positive density-density correlations at distances that correspond to reciprocal lattice vectors [193], fermionic atoms show anticorrelations (dips) at the same positions [194], as can be seen in figure 6.2.

6.3. Collective oscillations

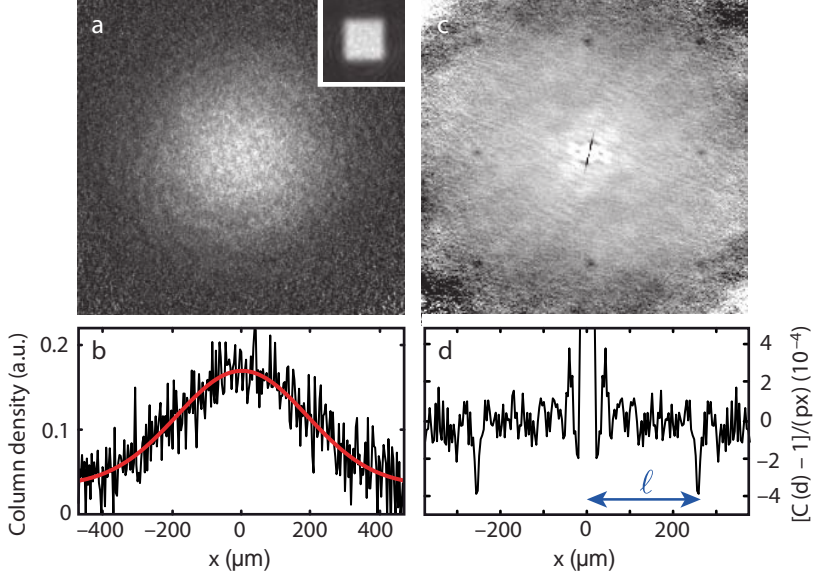


Figure 6.2.: a: Single shot absorption image of a single species fermionic band-insulator (inset: quasi-momentum distribution, see below), b: cut through (a) together with Gaussian fit, c: second order correlation function of 158 images and d: high-pass filtered cut through (c). The position of the dips corresponds to the first reciprocal lattice vector $\ell = 2\hbar k t_{\text{tof}}/m$. The image is taken from T. Rom *et.al.* [194].

As the position ℓ of these dips corresponds to the periodicity of the initial density distribution, this method offers great potential to unambiguously detect ordered states of fermionic atoms in an optical lattice. In an antiferromagnetically ordered state for instance the unit cell is doubled, which leads to extra dips in the noise correlation signal at exactly half of the original distance [195, 196], as could already be demonstrated by artificially creating a density wave for bosonic atoms using a superlattice [197]. More generally, this method should allow the detection of all periodically ordered states in both spin and charge sector and the measurements of their period [198].

By focusing on $\vec{k}, -\vec{k}$ correlations between the different spin states, noise correlation measurements should be able to directly detect pairing between fermions, as was already demonstrated for the case of weakly bound molecules in a dipole trap [199]. In principle, noise correlations between the two spin components can not only detect superfluidity in the lattice but distinguish between BCS and FFLO states [200].

6.3. Collective oscillations

In a trapped system collective modes are a convenient way to probe low lying excitations of the system. The typically used modes include dipole oscillations,

6. Observables: What can we measure?

quadrupole oscillations and breathing modes [45]. They can be excited by sudden changes of the trapping frequency or the trap center and can be monitored either in real space or by monitoring the momentum distribution using time-of-flight measurements. In pure dipole traps they were used to measure e.g. the viscosity of a strongly interacting fermionic gas [201] and the effective mass of fermionic polarons [96]. Oscillation experiments were also the first experiments to show beyond-meanfield effects in these systems [202].

In a lattice context it was shown that, at least in 1D, the metal to Mott insulator transition can in principle also be detected by observing the dipole and breathing modes [203].

In this thesis dipole oscillations were used to measure the trap frequencies (cf. sec. 4.2.1) and the anticonfinement produced by the lattice (cf. sec. 4.3.1).

6.4. Quasi-momentum distribution: band mapping technique

Another related method is the use of *band mapping* techniques, where the lattice potential is not switched off instantaneously but on a timescale that is fast compared to the tunneling timescale in the lowest band of the lattice but adiabatic with respect to interband transitions [204, 205]. In this method a Bloch wave is adiabatically transferred into a plane wave and the initial quasi-momentum distribution in the lowest band becomes the final (free-space) momentum distribution. In addition this method allows the unambiguous detection of population in higher bands, as they are mapped onto higher momenta corresponding to higher Brillouin zones [109].

In the case of non-interacting fermions this method can in principle be used to distinguish metallic and band-insulating states, as was first shown experimentally by the group of T. Esslinger [62]. The situation is complicated, however, by the inhomogeneity of the harmonic trap, as the observed quasi-momentum distribution is the sum over the whole trap.

While this method does return valuable information about the quasi-momentum distribution of the many-body state, it can only yield the relative population of the different quasi-momenta, and not the absolute populations. This is because without any in-situ density measurement, the in-trap cloud size, and therefore the number of quasi-momentum states, is not known.

On its own the Brillouin zone mapping cannot distinguish a band-insulating state from e.g. a Mott insulator, as any collection of localized atoms, irrespective of its temperature, has the same relative quasi-momentum distribution like a zero temperature band insulator.

6.5. Density distribution: In-situ imaging

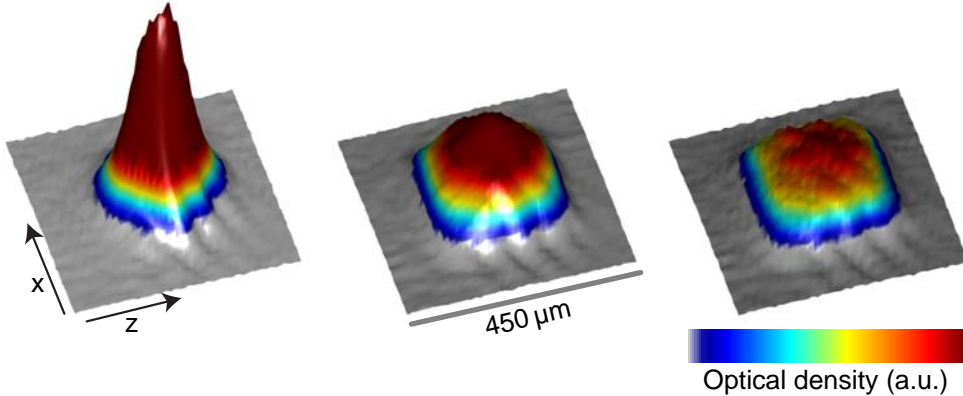


Figure 6.3.: Quasi-momentum distribution for non-interacting fermions in a $8 E_r$ deep lattice. The harmonic confinement was increased from the left to the right image, leading to many-body states ranging from purely metallic (left) to mostly band-insulating (right). The band-insulating character was tested by use of in-situ imaging, as detailed in chapter 8.

6.5. Density distribution: In-situ imaging

The main observable used in this thesis is the in-situ real space density distribution of the atoms in the combined potential of optical lattice and dipole trap. Within the local density approximation this is equivalent to measuring the density as a function of chemical potential for a given temperature (cf. sec. 5.7.1).

In 3D any in-situ imaging method cannot directly measure the density, but only the *column density*, that is the density integrated along the line-of-sight, which is given by the beam path of the imaging laser. There exist several numerical methods to extract the real density distribution from the recorded column densities by exploiting symmetries of the trapping potential [206]. A second approach, which is used here, is to integrate the corresponding theoretical data as well and to directly compare the resulting column densities.

In combination with the blue-detuned optical lattice, which offers the possibility to change the harmonic confinement at a constant lattice depth, the in-situ density distribution allows a direct measurement of the global compressibility of the cloud and can thereby distinguish conducting from insulating many-body states (cf. sec. 5.2).

The high column densities of the in-situ atom distribution typically result in optical densities that greatly exceed the dynamic range of standard, non-saturated absorption imaging. This can be circumvented for example by the use of saturated absorption imaging [207] or fluorescence imaging [208].

In this thesis a different approach was used, namely *phase contrast imaging*, a method that is well known in microscopy, where it is used to image almost transparent objects, like living cells, without the need to stain them [209].

Phase contrast imaging does not rely on the absorption of photons but instead

6. Observables: What can we measure?

uses the dispersive interaction between atoms and non-resonant light. It is a non-destructive imaging method that offers the possibility to record several images of the same cloud [210, 211].

In the experiment, both the in-situ density distribution and the quasi-momentum distribution of the same cloud were recorded by using phase contrast imaging followed by a band mapping technique (cf. sec. 6.4).

At typical detunings of several hundred MHz absorption of the probe light can be neglected and only the phase shift due to the dispersive interaction has to be taken into account:

Assuming that the light enters and leaves the cloud at the same transversal position, which corresponds to the thin lens approximation in optics, the phase shift Φ is proportional to the column density at these transverse coordinates $\Phi(x, y) \propto n_c(x, y)$. Accordingly, an incident plane monochromatic wave $E_i(x, y, z, t) = E_0 \sin(kz - \omega t)$ acquires a position-dependent additional phase:

$$E_{at}(x, y, z, t) = E_0 \sin(kz - \omega t + \Phi(x, y)) \quad (6.1)$$

This field can be decomposed into an attenuated reference field with the original phase, and an additional quadrature component with a $\pi/2$ phase difference compared to the original field¹:

$$\begin{aligned} E_{at}(x, y, z, t) &= E_{ref} + E_{add} \\ &= E_0 \sin(kz - \omega t) \cos(\Phi(x, y)) \\ &\quad + E_0 \cos(kz - \omega t) \sin(\Phi(x, y)) \end{aligned} \quad (6.2)$$

Imaged onto a CCD chip, however, the phase shift alone would not alter the recorded intensity distribution. Phase contrast imaging relies on a homodyne-like interference between the two quadrature components, which is created by introducing an additional phase shift P of $\pm\pi/2$ on the reference field:

$$\begin{aligned} E_{pci}(x, y, z, t) &= P(E_{ref}) + E_{add} \\ &= E_0 \cos(kz - \omega t) [\pm \cos(\Phi(x, y)) + \sin(\Phi(x, y))] \end{aligned} \quad (6.3)$$

The total field can thus be described as an amplitude-modulated wave, whose mean intensity is given by:

$$\begin{aligned} I_{PCI} &= I_0 [\pm \cos(\Phi(x, y)) + \sin(\Phi(x, y))]^2 \\ &= I_0 [\cos^2(\Phi(x, y)) \pm 2 \cos(\Phi(x, y)) \sin(\Phi(x, y)) + \sin^2(\Phi(x, y))] \\ &= I_0 [1 \pm \sin(2\Phi(x, y))] \end{aligned} \quad (6.4)$$

For small phases Φ the intensity can be approximated by

$$I_{pci}(x, y) \approx I_0 [1 \pm 2\Phi(x, y)], \quad (6.5)$$

¹ $\sin(x + y) = \sin(x) \cos(y) + \cos(x) \sin(y)$

6.5. Density distribution: In-situ imaging

where, according to $\Phi(x, y) \propto n_c(x, y)$, the intensity modulation is linear in the column density. In this limit, phase contrast images can be interpreted in a straightforward way, as the intensity modulation directly reflects the atomic column density. It is a very versatile method, suitable for a large range of column densities, as the desired dynamic range can be controlled by the detuning. Without the small phase approximation the dynamic range is even larger, at least for smooth density distributions, as the intensity modulation is periodic in the column density.

Technically, the necessary extra phase shift of the reference field is created by a phase plate, that is a glass plate with a small dip in the center, which produces a relative phase shift of $\pi/2$ for light that passes through this central phase spot. The phase plate is positioned in a focus of the unscattered light. In the idealized situation of figure 6.4, this position matches the Fourier plane of the imaging system, where the light scattered by the atoms resembles the (extended) Fourier transform of the column density distribution. Ideally the phase spot affects the unscattered reference wave only, while it leaves the unfocused scattered light unchanged.

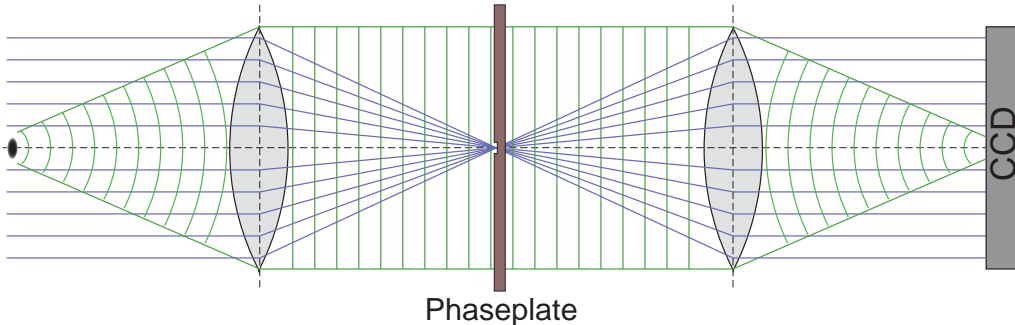


Figure 6.4.: Schematic phase contrast imaging setup. The incident plane wave is shown as blue rays and illuminates the atomic cloud indicated on the left. The scattered light, which is indicated by green phase fronts, is imaged via a telescope onto a CCD camera (right), where it interferes with the unscattered reference light. The reference light is phase-shifted by $\pi/2$ due to the phase plate in between the telescope lenses.

In reality, however, a small part of the scattered light passes through the phase spot as well and acquires the same phase shift as the reference wave. This leads to several imaging artifacts like halos and shade-off effects that are symptomatic for phase-contrast imaging [212], and, together with the thin lens approximation, form the fundamental limitations of this method.

In the experiment, the total imaging setup consists of two telescopes with a total magnification of ≈ 3.3 , where the phase plate (phase spot diameter $300\ \mu\text{m}$ resp. $170\ \mu\text{m}$) was positioned in the second telescope. Due to technical problems with unwanted interferences in the imaging setup, we used a slightly focused probe beam instead of a plane wave. Therefore the position of the phase plate, which was positioned in the focus of the probe beam, did not correspond to a Fourier

6. Observables: What can we measure?

plane of the imaging system.

Nonetheless, the above mentioned aberrations are especially noticeable for the largest clouds studied during expansion measurements (cf. sec. 10), as these clouds show a higher spectral weight at small spatial frequencies compared to the small in-situ clouds.

A more detailed description of the used phase contrast setup will be found in the PhD Thesis of Sebastian Will. The in-situ images are taken along the vertical axis, which exploits a second advantage of the chosen oblate trap geometry as the imaging integrates over less atoms than with a spherical trap. In addition, any change in the volume of the cloud corresponds to a more pronounced change in the horizontal directions.

6.6. Doublon fraction: Molecule creation

A third main observable used in this work is the so-called *doublon fraction*, that is the fraction of atoms sitting on doubly occupied lattice sites. As was detailed already in section 5.4.1, interaction effects manifest themselves also in the doublon fraction and can lead either to a suppression of doubly occupied sites for repulsive interactions or to a strong enhancement of the doublon fraction in the attractive case.

In the experiment, the doublon fraction is measured by first increasing the lattice depth to typically $V_0 = 20 E_r$ in $200 \mu\text{s}$, a timescale that is adiabatic with respect to interband transitions but fast compared to tunneling in the lowest band. Once in the deep lattice, where tunneling can be neglected ($J = 23 \text{ Hz}$), pairs of atoms sitting on the same lattice site are converted into molecules using a magnetic Feshbach sweep (cf. sec. 3.3.2)². The ramp parameters were chosen such that all molecules were photodissociated by the lattice light (cf. sec. 3.4, A) before the end of the ramp. The kinetic energy imposed on the dissociated atoms is on the order of half the detuning of the lattice light ($\Delta = 15 \text{ THz}$) and leads to a fast escape of these atoms from the trap.

By measuring either the total atom number (time-of-flight) or the density distribution (in-situ) of the cloud both with and without the Feshbach sweep we can infer either the total doublon fraction or the spatial doublon distribution.

During the hold time needed for the Feshbach ramps, doubly occupied sites can already be lost due to light assisted collisions (cf. sec. 3.4). This process selectively affects only doubly occupied sites and therefore leads to an underestimation of the measured doublon fraction p , for which the experimental data has to be corrected. The measured doublon lifetimes in a deep lattice ($V_{\text{lat}} = 24 E_r$) are strongly interaction dependent and range from below $< 40 \text{ ms}$ for attractive interactions

²The programmed ramp speed was 5 G/ms and the final programmed field was 190 G . Owing to the high inductance of the used coils, however, the real field showed a considerable lag compared to the programmed values.

6.7. Transport coefficients

($a = -200 a_0$) over 70(10) ms in the non-interacting case to 310(70) ms for repulsive interactions ($a = 150 a_0$).

Due to the necessity to calculate the doublon fraction from atom numbers obtained in different shots, this method is less accurate than alternative methods that rely on dissociating the formed molecules using radio-frequency pulses and subsequently separating the different spin states using the Stern-Gerlach effect during time-of-flight [70]. However, the potential to observe the spatial doublon distribution is a big advantage of the used method.

6.7. Transport coefficients

One of the most prominent observables in real condensed matter systems are transport properties, i.e. the current induced by an applied bias. Depending on the applied bias, the current can either be an electric current, carried by the electric charge of the electrons, or a thermal (magnetic) current carried by the energy (spin) of the electrons.

In ultracold atoms, the observable corresponding to an electric current is the mass flow, which can either be measured directly in-situ or through a measurement of the momentum distribution. Due to the perfect periodicity of an optical lattice, which is by construction defect-free, directly applying a potential gradient does not lead to a net flow of atoms but instead creates Bloch oscillations [27, 28, 115]. In order to avoid these oscillations we studied transport properties in a homogeneous optical lattice where the net flow of atoms was driven by initial gradients in the chemical potential, as will be discussed in section 10.

6.8. Spectroscopic techniques

In condensed matter experiments many different spectroscopic techniques are used e.g. to study the dispersion relations of various quasiparticles like phonons or excitons.

An important example is angle-resolved photoemission spectroscopy (ARPES), which is one of the most powerful techniques to probe the energy and momentum distribution of the electrons in a material [213]. In the context of cuprate superconductivity, ARPES measurements e.g. provided important information about the superconducting gap, the pseudogap and enabled a direct measurement of the Fermi surface [214].

Similar methods have been implemented in ultracold atom systems using radio frequency photons in order to spin-flip atoms out of a (possibly strongly-interacting) many-body state into non- or weakly interacting states [215].

In the interpretation of these measurements an additional complication arises due

6. Observables: What can we measure?

to the inhomogeneity of the trap [216, 217]. While these methods have recently been extended to momentum resolved detection [218] or to spatially resolving the origin of the spin-flipped atoms [219], it was, however, so far not possible to combine spatial and momentum resolution into a single method.

Another important observable in condensed matter systems is the dynamical structure factor [220], which can be measured by inelastic neutron scattering [107] and contains information e.g. about the phonon and magnon spectrum of the material. In ultracold atom systems, an analogous probe is the use of stimulated two-photon *Bragg scattering*, where both the momentum and energy transfer are given by the differences in momentum and energy of the two photons involved.

This method was first used to measure the real momentum width of a BEC [221] and was recently applied to study the momentum resolved excitation spectrum of non-interacting and interacting bosons in an optical lattice [222].

An important special case is the use of Bragg spectroscopy with vanishing momentum in the lattice, where the excitation can be provided by amplitude modulating the potential depth without the need of additional beams [223]. In interacting fermionic systems in optical lattices, this spectroscopy method can be combined with a measurement of the doublon fraction [70, 224]. While this procedure does provide a direct measurement of the on-site interaction energy, it cannot provide a general measure of possible many-particle gaps due to the restriction to zero quasi-momentum transfer.

In this thesis a variation of this spectroscopy, which is colloquially referred to as *shaking spectroscopy*, i.e. frequency modulation of the lattice light, was used to calibrate the lattice depths by measuring the band gap between the lowest and the first excited band (cf. sec. 4.3.2).

7. Overview over experimental cycle

This chapter gives a brief overview over the experimental sequence and the applied cooling techniques. The used methods, laser-cooling and evaporative as well as sympathetic cooling, are nowadays standard techniques and will only be recalled briefly. The experimental setup and the first part of the cooling sequence are presented in more detail in the PhD thesis of Tim Rom.

The experimental cycle starts with a two-species magneto optical trap (MOT) [225] in which first several 10^7 ^{40}K atoms are trapped and laser-cooled. During the last few seconds of the Potassium MOT the Rubidium MOT lasers are added and several 10^9 ^{87}Rb atoms are laser-cooled in the MOT as well. Together with a small offset in the positions of the clouds, which is created by slightly imbalanced light intensities, this sequence minimizes the overlap between ^{40}K and ^{87}Rb during the presence of the near-resonant MOT light, and thereby minimizes losses due to light-assisted collisions. The MOT phase is followed by a short optical molasses [225] by which primarily ^{87}Rb is further cooled. After an optical pumping stage both ^{40}K and ^{87}Rb are recaptured in a quadrupole trap and magnetically transported within 2 s over 40 cm into a UHV glass cell [226]. This two-chamber design offers two advantages: First, it allows the MOT to operate at a background pressure of around 5×10^{-10} mbar, while keeping the pressure in the glass cell, where the evaporative cooling takes place, below 10^{-11} mbar. Second, the optical access to the glass cell is improved, as no MOT optics need to be integrated into the lattice, dipole trap, and imaging setup.

After the magnetic transport the atoms are loaded into an optically plugged quadrupole trap [2], where a first evaporative cooling stage takes place. This part of the experimental cycle is described in more detail in the PhD thesis of Thorsten Best. ^{87}Rb is actively cooled using a standard radio frequency sweep while ^{40}K is sympathetically cooled by collisions with ^{87}Rb . In order to prevent Majorana losses at the magnetic field zero [35], we focus a tapered amplifier laser at $\lambda = 760$ nm and a waist of $20\ \mu\text{m}$ to the center of the quadrupole trap and plug the "Majorana hole" using its repulsive dipole potential (see Fig. 7.1,7.2).

In this manner we can reach 10×10^6 Rb at $2\ \mu\text{K}$ in thermal equilibrium with 2×10^6 ^{40}K after 9 s of evaporation. During the last 170 ms of this radio frequency sweep we start to overlap the quadrupole trap with a crossed dipole trap, which is described in detail in section 4.2. By decreasing the current in the upper quadrupole coil and applying additional offset fields, the quadrupole field is adiabatically transformed into a homogeneous offset field. During this field ramp

7. Overview over experimental cycle

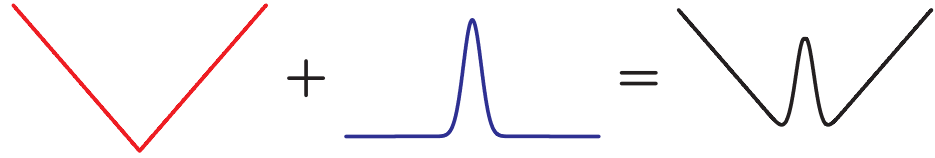


Figure 7.1.: left: Magnetic potential of a quadrupole trap. In the center the magnetic field vanishes, which leads to Majorana losses. middle: Repulsive potential of a tightly focused blue-detuned laser in the transverse direction. right: Combined potential of quadrupole trap and optical plug.

the magnetic field zero is moved along the plug beam in order to avoid losses and depolarization.

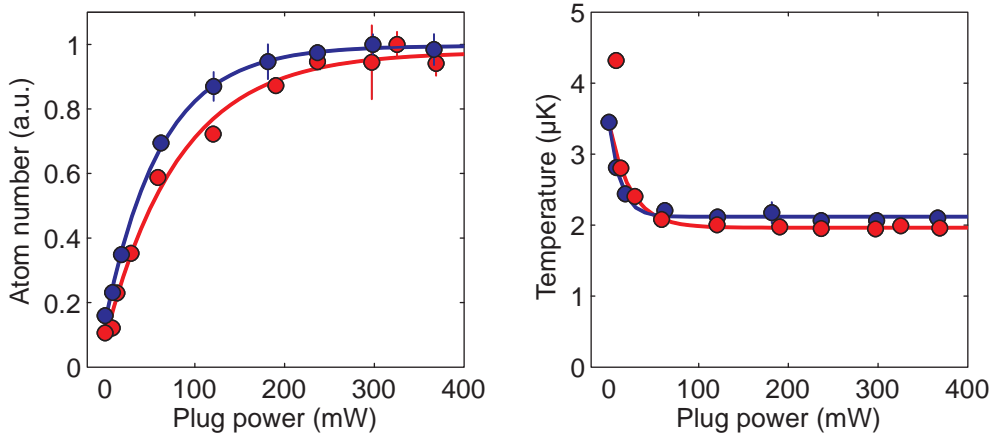


Figure 7.2.: left: Atom numbers of ^{40}K (red) and ^{87}Rb (blue) after the radio-frequency forced evaporation in the plugged quadrupole trap as a function of the plug power. right: The corresponding temperatures show that ^{40}K and ^{87}Rb are in good thermal contact, as they reach the same temperature although only ^{87}Rb is actively cooled.

Once in a pure dipole trap, both species are transferred into their hyperfine ground states (^{87}Rb $|F=1, m_F=1\rangle$; ^{40}K $|F=9/2, m_F=-9/2\rangle$) by use of adiabatic radio-frequency and microwave sweeps (rapid adiabatic passage, RAP). Subsequently, a second stage of evaporative cooling is performed by reducing the dipole trap depth. After 3 – 4 s of cooling we can reach an almost pure BEC of ^{87}Rb together with a quantum degenerate spin-polarized Fermi gas at $T/T_F = 0.16 – 0.18$. Images of such clouds are shown in figures 2.1 and 2.4.

In order to create a degenerate spin mixture of ^{40}K we use an additional RAP pulse on the $|F=9/2, m_F=-9/2\rangle$ to $|F=9/2, m_F=-7/2\rangle$ transition. By lowering the RF power in this sweep we can reduce its transfer efficiency to 50% and thereby create a superposition of both hyperfine states.

Subsequent collisions and inhomogeneities of the magnetic field lead to dephasing of this superposition [227] and transform it into an incoherent spin mixture. It turned out to be beneficial to perform the mixing sweep rather early during the

cooling sequence, where the entropy is still high, as this process creates additional entropy.

By lowering the dipole power below the trap bottom for ^{87}Rb , all bosons are evaporated away and the resulting purely fermionic spin mixture can be further cooled. After total evaporation times of $6 - 7$ s in the dipole trap we can reach reduced temperatures on the order of $T/T_F \gtrsim 0.10$, which is at the limit of the used fitting method (cf. sec. 2.2.3).

A typical experiment then consists of setting the desired dipole trap strength and magnetic field and subsequently ramping up the optical lattice before probing the resulting state using one of the observables described in section 6.

Most theoretical calculations relevant for this thesis are performed using the grand canonical ensemble, which yields the desired observables (e.g. density) as a function of chemical potential and temperature. In order to compare theoretical and experimental results, these parameters are adjusted such that the calculated distributions reproduce the measured atom number and entropy per particle (cf. sec. 8). While the atom number can be extracted from images taken in the lattice, the entropy per particle is typically extracted from dedicated time-of-flight images taken in the dipole trap.

One experimental issue in using this entropy as a parameter in the lattice system is the presence of technical heating due to e.g. scattering of photons, technical noise, and collisions with background gas atoms. As a consequence, the experimentally chosen timescales for changing parameters like the lattice depth are always a compromise between both technical and non-adiabatic heating. Up to now, the relevant adiabaticity timescales for inhomogeneous, strongly interacting fermionic systems are not known in general (cf. sec. 11.3), but the dynamic expansion measurements presented in chapter 10 and other recent experiments [228] suggest that these timescales can become surprisingly long for large interactions.

8. Repulsive Fermi-Hubbard model

This chapter presents the first main result of this thesis, the observation and experimental distinction of metallic and insulating states of the Fermi-Hubbard model, including the fermionic Mott insulator. The main parts of this chapter are published in [229] and [131].

After presenting the used measurement sequence, the theoretically expected results are discussed and then compared to the experimental data.

8.1. Measurement sequence

In order to probe the different regimes of the repulsive Fermi-Hubbard model we created quantum degenerate spin mixtures of the two lowest hyperfine states of fermionic potassium and transferred them into a combination of a blue-detuned optical lattice and a red-detuned dipole trap. At the end of the cooling sequence described in chapter 7 the dipole trap depth was slightly increased in order to prevent further evaporation and the experiment started with $N = 1.5 - 2.5 \times 10^5$ atoms at a reduced temperature of $T/T_F = 0.15(3)$.

In this experiment, where large repulsive interactions were needed, the final cooling was performed either at $B = 220$ G above the $(-9/2, -7/2)$ Feshbach resonance (cf. fig. 3.2) or at $B = 165$ G below the resonance. While the former field allowed to access interactions ranging from non-interacting up to scattering lengths of $a = 150 a_0$, the latter allowed us to additionally access higher values up to $a = 300 a_0$ ($B = 191.3$ G) without the need to cross the resonance. In principle, even higher values could be achieved by a closer approach to the resonance position at $B_0 = 202.1$ G in practice, however, this was hindered by enhanced losses and heating in the lattice.

The desired interaction was chosen by adjusting the magnetic field once the evaporative cooling was completed and the final optical potentials were approached in the following sequence: First, the optical lattice was increased to a depth of $1 E_r$ during a linear 7 ms "preramp", followed by a linear 100 ms ramp to the desired dipole power before finally the lattice depth was linearly increased to its final value of $8 E_r$ in 50 ms.

In the typically assumed limit of an adiabatic/isentropic evolution (cf. sec. 2.3), the final state in the lattice is completely determined by the entropy per particle S/N together with the final compression $E_t/12J$ and interaction U/J (cf. sec. 5.7.1), and is independent of the specific phase-space path. In other words, the final state

8. Repulsive Fermi-Hubbard model

in the lattice would only depend on the end point of the chosen sequence, but not on the specific ramp. Note, however, that the ramp time needed to ensure adiabaticity does depend on the chosen path in phase-space.

In the presence of technical heating rates (cf. sec. 11.2), it is therefore of paramount importance to use a ramp sequence that is optimized with respect to the sum of technical heating and non-adiabaticities. Empirically we found that the best strategy is to first set the trapping frequency and the scattering length in a very weak lattice, where tunneling is still fast and the system is only weakly interacting, before ramping up the lattice to its final value. In the Hubbard regime even moderate interactions, on the order of half the bandwidth or less, can substantially hinder mass transport, as studied in later experiments (cf. sec. 10).

After a hold time of 12 ms the in-situ density distribution was measured using phase-contrast-imaging (cf. sec. 6.5) followed by a measurement of the quasi-momentum distribution using a band mapping technique (cf. sec. 6.4) in the same experimental run. Alternatively, the fraction of doubly occupied lattice sites (doublons) was measured using Feshbach sweeps in order to convert atoms on doubly occupied lattice sites into Feshbach molecules (cf. sec. 6.6).

8.2. Theoretical expectation

All measurements are compared to DMFT (cf. sec. 5.6) calculations engineered in the group of Prof. Achim Rosch at the University of Cologne and performed in the John von Neumann Institute for Computing Jülich. Details of the numerical implementation can be found in [131].

At the experimentally realizable entropies magnetic order and the low temperature phases of the Hubbard model can be neglected and only three regimes are relevant in the homogeneous case:

For weak interactions there exist the compressible and conducting metallic phase of delocalized atoms and the incompressible band insulator at maximum filling. While the maximum filling at zero temperature is exactly two atoms per lattice site, it becomes reduced at finite entropies due to the density dependent entropy capacity (cf. fig. 5.5). For strong repulsive interactions and low enough entropy densities, the Mott insulator appears in addition to the metallic and band insulating regimes at precisely half filling.

Due to the inhomogeneity of the trap the filling factor is position dependent and always decays from a maximum at the trap center to zero at the edge of the cloud. As a consequence, several phases can coexist in different areas of the trap. Even in the limiting cases of figure 8.1 the density always drops below unity filling near the edge of the cloud, leading to a metallic outer shell: The cloud can be either purely metallic (A), or contain a Mott insulating (B) or band insulating (C) core. Away from these limits an even more complex scenario can arise, where a band insulating core is surrounded by a first metallic shell above half filling, followed

8.2. Theoretical expectation

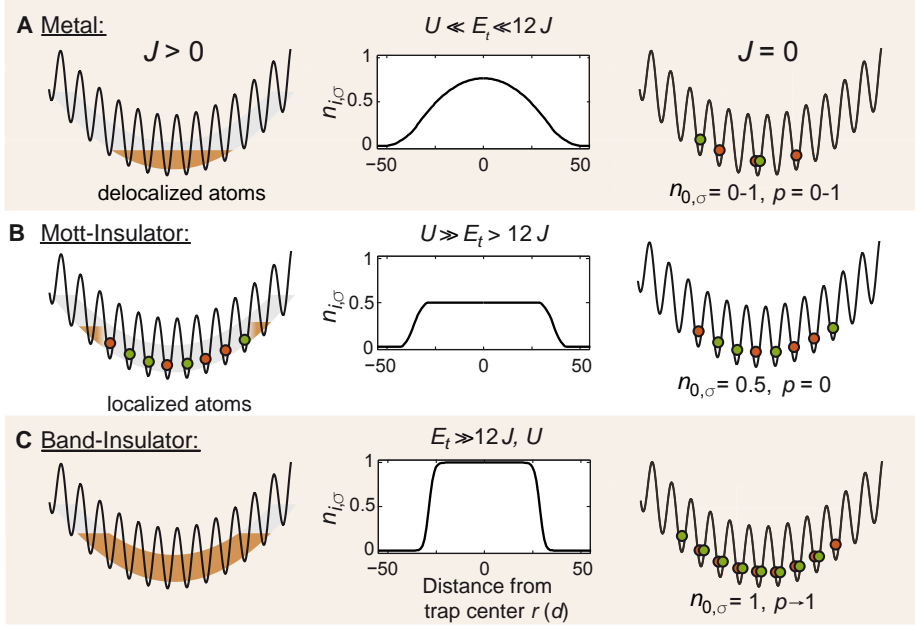


Figure 8.1.: Illustration of the eigenstates of the trapped system in the limits of dominating kinetic (A), interaction (B) or trap energy (C). (right) Resulting atom distribution after a fast ramp into a deep lattice - as used in measuring the doublon fraction (cf. sec. 6.6).

by a Mott insulating shell at unity filling and finally a second metallic shell at lower density.

The expected density distributions were calculated as a function of the characteristic trap energy (compression) $E_t/12J$ for various interactions strengths $U/12J$ and several average entropies per particle. Figure 8.2 shows the resulting density distributions for an average entropy per particle of $S/N \approx \log(2) k_B$, where magnetic ordering may become important in an harmonically trapped system.

For low compressions ($E_t/12J \lesssim 0.25$) the whole cloud is metallic for all interactions, while for sufficiently strong compressions a band insulating core is formed. Beginning with $U/12J \approx 1$ a Mott insulating core is formed for compressions above $E_t/12J \gtrsim 0.25$. Above $E_t \approx U/2$, the central density rises above unity and the Mott insulating core becomes a Mott insulating shell.

The experimentally relevant case of $S/N \approx \log(4) k_B$ (cf. fig. 8.3) exhibits the same qualitative behavior.

8. Repulsive Fermi-Hubbard model

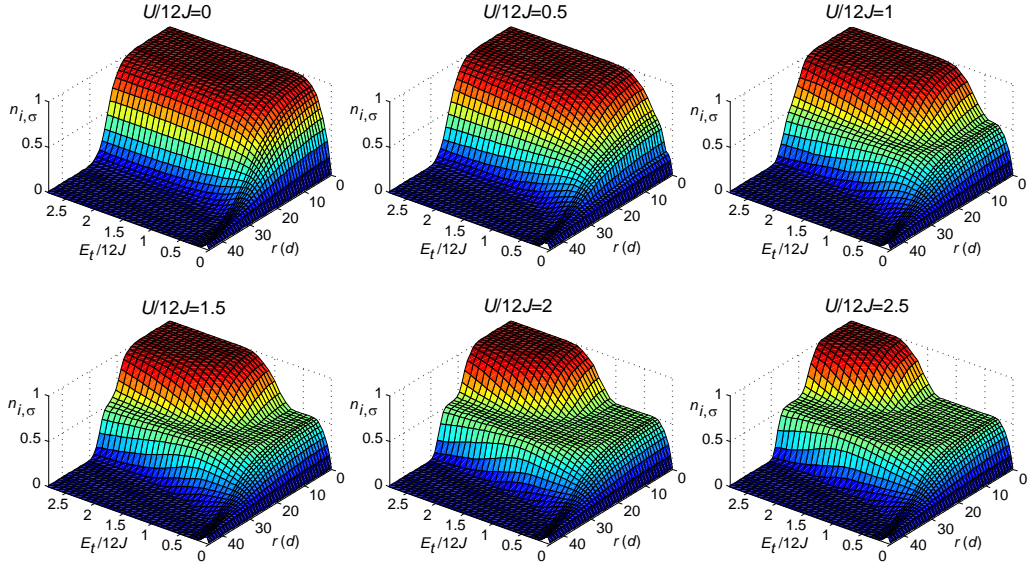


Figure 8.2.: Calculated density distributions for various interactions and an average entropy per particle of $S/N \approx \log(2) k_B$, which corresponds to an initial temperature of $T/T_F = 0.07$ in the dipole trap. The Mott insulating plateau is clearly visible for $U/12J \geq 1$. (Data taken from [131])

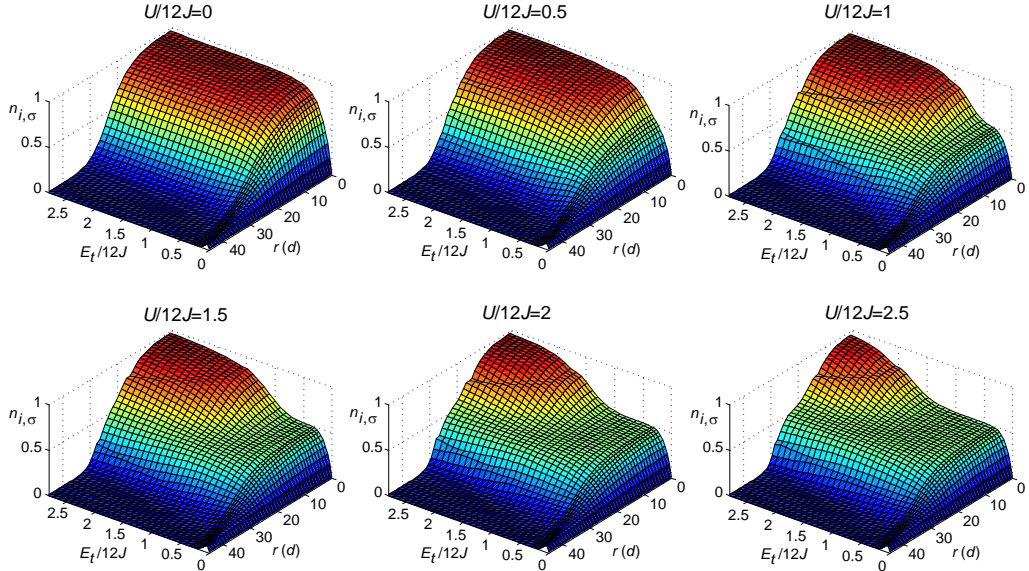


Figure 8.3.: Calculated density distributions for an average entropy per particle of $S/N \approx \log(4) k_B$, which corresponds to an initial temperature of $T/T_F = 0.15$ in the dipole trap. Due to the higher entropy the density distribution is washed out compared to low temperatures but the Mott insulating plateau remains clearly visible. The small structures at higher fillings are numerical artifacts. (Data taken from [131])

8.2. Theoretical expectation

The incompressibility of the Mott insulating phase can for instance be seen in the central density, which is plotted in figure 8.4. For low temperatures the central density remains at half filling over a large range of compressions. This indicates a vanishing electronic compressibility $\partial n / \partial \mu$ (cf. sec. 5.2), as the central chemical potential varies with the compression. Due to the compressibility of the surrounding metallic shell, however, the global compressibility of the cloud stays finite in all cases (cf. fig. 8.9).

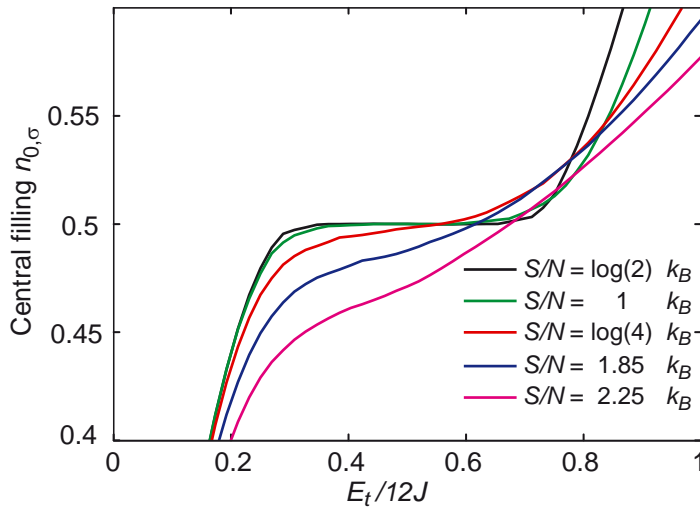


Figure 8.4.: Calculated central density for $U/12J = 1.5$. The average entropies correspond to $T/T_F = 0.07, 0.10, 0.15, 0.20, 0.25$ in the dipole trap. (Data taken from [131])

Together with these density distributions the DMFT calculations also yield the doublon distribution, which are presented in section 8.4 together with the experimental data.

8.2.1. Entropy distribution

As shown in the previous section the DMFT calculations predict a fermionic Mott insulator in an inhomogeneous system at an average entropy per particle of $S/N \approx \log(4) k_B$. This is in stark contrast to the homogeneous system, where the maximum entropy per particle in the Mott phase is given by $S/N = \log(2) k_B$ (cf. sec. 5.4.2).

The reason for this difference lies in the density dependent entropy capacity of the Hubbard model (cf. sec. 5.4.2): Even though the entropy capacity per lattice site vanishes for small filling factors, the *entropy capacity per particle* in fact diverges (cf. fig. 5.5). Intuitively speaking, the number of lattice sites an atom can choose from diverges in the low density limit, leading to a diverging entropy capacity per particle. As a consequence, atoms at the cloud edge carry much more entropy (cf. fig. 8.5) than atoms at the center. This entropy redistribution enables the formation

8. Repulsive Fermi-Hubbard model

of Mott insulating regions with entropy densities below $\log(2) k_B$ in the trap at high average entropies. Furthermore, this redistribution of entropy towards the low density regions can be used to implement further cooling schemes (cf. sec. 11.1).

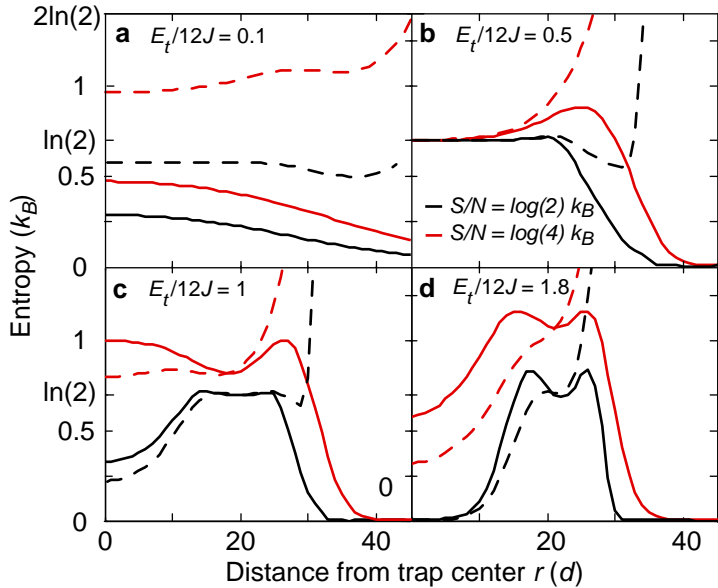


Figure 8.5.: Entropy distribution for $U/12J = 1.5$ and two average entropies. The solid lines denote the average entropy per lattice site and the slashed lines denote the average entropy per particle. (Data taken from [131])

8.3. Cloud size and compressibility

Within the local density approximation (cf. sec. 5.7.1), the in-situ density distribution allows one to measure the functional dependence of the density on the chemical potential in a single shot (cf. sec. 6.5). As shown in figure 8.6 (column A), the existence of the Mott insulating plateau (A2) or a Mott insulating shell (A3) could in principle be directly deduced from an inspection of the density profiles. In the experiment, however, only the column density can be recorded (cf. sec. 6.5) and the visible signatures of the Mott insulator are washed out by the integration along the line of sight. As a consequence, a quantitative comparison between the numerically calculated distributions (B) and the experimentally recorded ones (C) is needed in order to reliably identify the different phases.

8.3.1. Rescaled cloud size

The comparison between numerical and experimental density distributions was performed using the *cloud size* R , which denotes the expectation value of the

8.3. Cloud size and compressibility

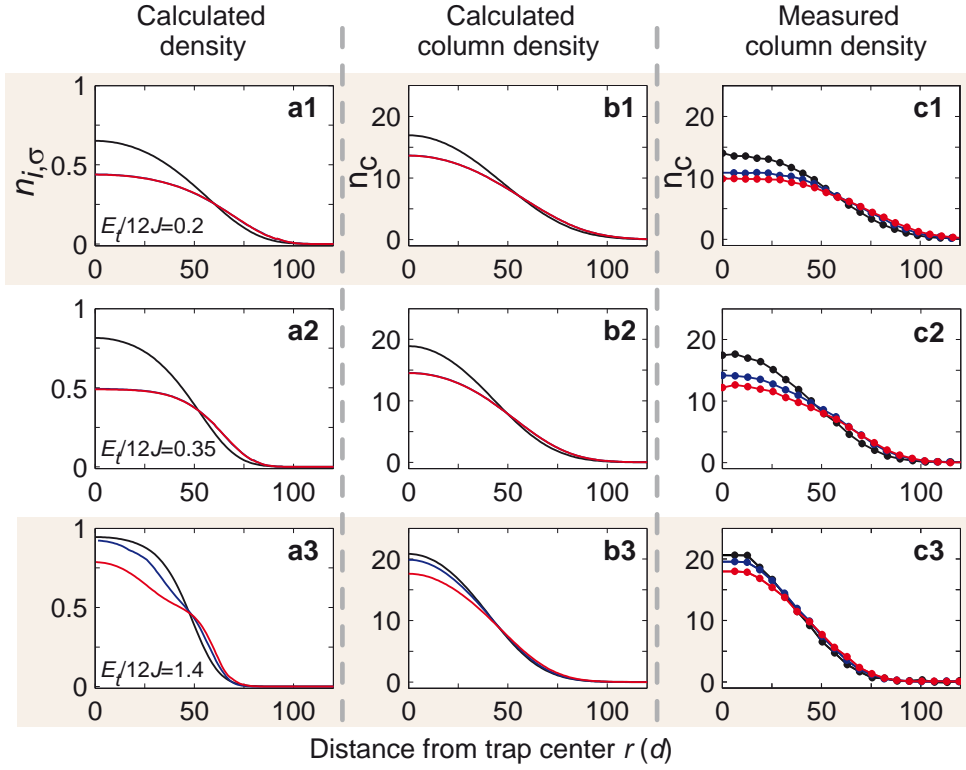


Figure 8.6.: Comparison of in-trap density profiles. Calculated radial density profiles for different harmonic confinements (compressions) $E_t/12J$ (left column), corresponding column densities obtained after integration over the vertical axis and convolution with the point spread function of our imaging system (center column), and experimental results (azimuthally averaged over more than five shots) for three different interaction strengths $U/12J = 0$ (black), $U/12J = 1$ (blue), and $U/12J = 1.5$ (red). At small compressions the calculated density profiles for $U/12J = 1$ and $U/12J = 1.5$ are indistinguishable, as in both cases double occupations are almost completely suppressed for $n_{i,\sigma} < 1/2$. (Data taken from [229])

transversal position operator $\hat{R} = \sqrt{\langle \hat{x}^2 + \hat{y}^2 \rangle}$:

$$R = \frac{\int_{\mathbb{R}^2} (x^2 + y^2) n_c(x, y) dA}{\int_{\mathbb{R}^2} n_c(x, y) dA} \quad (8.1)$$

where $n_c(x, y)$ denotes the column density. Typically the cloud size is given in rescaled units:

$$R_{sc} = R / (\gamma N_\sigma)^{1/3} \quad (8.2)$$

Here N_σ denotes the atom number per spin state and $\gamma = \omega_v/\omega_\perp \approx 4$ is the aspect ratio of the trap (cf. sec. 4.2.1).

In thermal equilibrium the rescaled cloud size depends only on the compression $E_t/12J$, the strength of the interaction $U/12J$ and the entropy per particle, which

8. Repulsive Fermi-Hubbard model

is given by the initial temperature in the pure harmonic trap T/T_F . Within the local density approximation (cf. sec. 5.7.1) there remains no dependence of these rescaled units (R_{sc} vs. E_t) on the atom number. The use of these units therefore allowed us to greatly reduce the experimental noise, as the main noise source are shot-to-shot fluctuations in the atom number.

In contrast to the numerical data, where the cloud size R was extracted by direct integration of equation 8.1, imaging noise at large distances would add considerable noise in the case of experimental data. In order to avoid this problem, the phase-contrast images were first fitted using the following adapted Fermi-Fit function:

$$F(x, y) = a \operatorname{Li}_2 \left(-100 e^{-\frac{(x-x_c)^2}{2\sigma_x^2} - \frac{(y-y_c)^2}{2\sigma_y^2}} \right) + b + c \sqrt{\frac{(x-x_c)^2}{\sigma_x^2} + \frac{(y-y_c)^2}{\sigma_y^2}} \quad (8.3)$$

Here Li_2 denotes the di-logarithm, $x_c, y_c, \sigma_x, \sigma_y, a, b, c$ are free fit parameters and the last term models a broad funnel-shaped background, which is an artifact of phase-contrast imaging (cf. sec. 6.5). As can be seen in figure 8.7, this function describes the measured distributions much better than a Gaussian. Indeed the adapted Fermi-Fits yield on average 8% (non-interacting cloud) and 23% (interacting cloud with $U/12J = 1.5$) smaller squared residuals compared to a Gaussian fit function including the last background term. Performing the integral of eqn. 8.1 over the fit function results in the imaged cloud size being given by:

$$R = \sqrt{1.264^2 (\sigma_x^2 + \sigma_y^2) - \eta^2} \quad (8.4)$$

Here η denotes the imaging resolution (radius of Airy disc $< 3 \mu\text{m}$) of the imaging setup, which is well below one third of the smallest used cloud size.

The resulting cloud sizes are plotted in figure 8.10 together with the theoretical prediction (cf. fig. 8.8). In order to perform the rescaling and to determine the compression, several parameters need to be known precisely: While trap frequencies and lattice depth were calibrated independently (cf. sec. 4.2.1, 4.3.1 and 4.3.2), this turned out to be impossible in the case of the absolute atom number. Although relative atom numbers can easily be deduced from fits to absorption images, a precise calibration of the column density in terms of the recorded optical density is limited by uncertainties due to saturation, polarization effects and optical pumping. Within their uncertainty, the resulting atom numbers nonetheless agree with an independent calibration using the in-situ cloud size of non-interacting atoms in the pure harmonic trap.

It turned out, however, that for both calibrations the resulting uncertainty ($\approx 15\%$) is larger than the scatter of the rescaled in-situ cloud sizes in the lattice: While the cloud size in the harmonic trap scales as $R \propto N^{1/6}$ [38] for non-interacting fermions, the restriction to the lowest band dictates $R \propto N^{1/3}$ in the lattice, rendering this cloud size much more sensitive to the total atom number. Accordingly, the precise adjustment of the atom number calibration was performed using the

8.3. Cloud size and compressibility

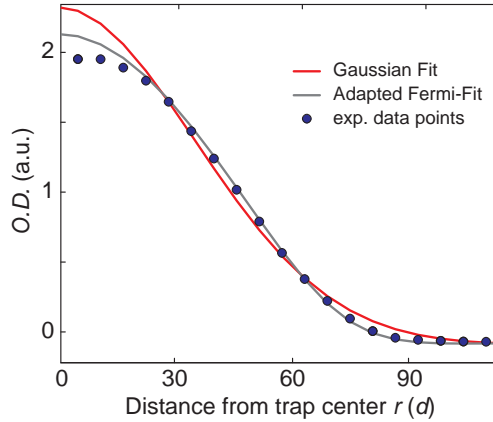


Figure 8.7.: Comparison of different fit functions. The azimuthally averaged data (dots) is shown together with a fitted Gaussian (red line) and an adapted Fermi-fit (black line). Both fits were performed on the full 2D distribution before averaging. The influence of the small deviation at the trap center on the resulting atom number (cloud size) is below 1% (0.1%), as the statistical weight of each averaged data point increases linearly with the distance from the cloud center.

non-interacting cloud sizes in the lattice at medium high compressions, where the cloud is mostly band-insulating and the cloud size becomes independent of the compression.

8.3.2. Results

The theoretically expected cloud size is plotted in figure 8.8 for the experimentally relevant initial temperature of $T/T_F = 0.15$. In the limit of small compressions the cloud is very extended and the central density becomes very low, resulting in metallic states for all interactions.

Focusing first on the lower black line, which denotes the non-interacting case, one sees that the cloud size decreases monotonically, approaching a limiting value for strong compressions. This limit is due to the formation of an incompressible band insulator, where the maximum density is limited by the Pauli principle. It is a direct consequence of the fermionic nature of the atoms combined with the restriction to the lowest band of the lattice. In a pure harmonic trap there exists no minimum cloud size as there is a gapless continuum of higher states in which the atoms can be excited. In the lattice, a further compression of the cloud is only possible if either Fermi energy or temperature are on the order of the band gap, such that atoms can be excited into higher bands.

This behavior can be described quantitatively by defining the *global compressibility* of the cloud:

$$\kappa_{R_{sc}} = -\frac{1}{R_{sc}^3} \frac{\partial R_{sc}}{\partial (E_t/12J)} \quad (8.5)$$

8. Repulsive Fermi-Hubbard model

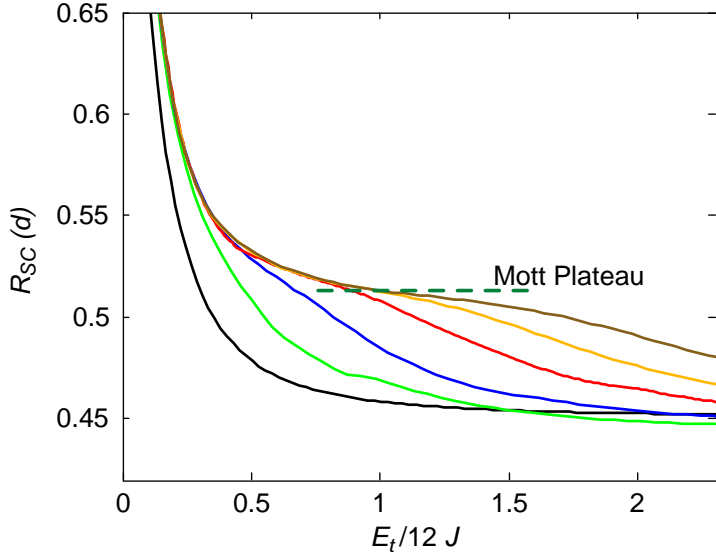


Figure 8.8.: Numerically calculated cloud sizes of the interacting spin mixture versus compression for various interactions $U/12J = 0, 0.5, \dots, 2.5$ (increasing cloud sizes) and an entropy per particle, which corresponds to a temperature of $T/T_F = 0.15$ in the harmonic trap. The dashed line indicates the Mott insulating plateau. The remaining slope at the Mott plateau is caused by the compressible metallic shells surrounding the incompressible Mott insulator. (Data taken from [131])

which is the derivative of the cloud size with respect to the compression. In the non-interacting case the compressibility, which is shown in figure 8.9, decreases monotonically with increasing confinement and vanishes in the band-insulating limit.

In the case of a repulsive interaction the resulting cloud size is larger than in the non-interacting case, indicating that repulsive interactions tend to lower the density. For strong enough interactions the formation of the Mott insulating core/shell leads to an intermediate plateau in the cloud size $R_{sc} \approx 0.52$ that is significantly larger than the band insulator at the same entropy. For stronger compressions the harmonic confinement starts to dominate over the interaction energy and the cloud size shrinks faster again, as a metallic core above unity filling is formed. For strong compressions the cloud size approaches that of the non-interacting band insulator. This formation of the Mott insulating region at intermediate compressions leads to a characteristic feature in the compressibility, namely the appearance of a local minimum. As shown in figure 8.9, this local minimum appears first for $U/12J \approx 1$, where the Mott insulator starts to form, and becomes more pronounced for stronger interactions, when the Mott insulating region becomes larger. For a given interaction strength it is most pronounced for the coldest temperatures and vanishes above a critical entropy (cf. fig. 8.11). The global compressibility is therefore an ideal observable to study the formation and melting of a fermionic Mott insulator.

8.3. Cloud size and compressibility

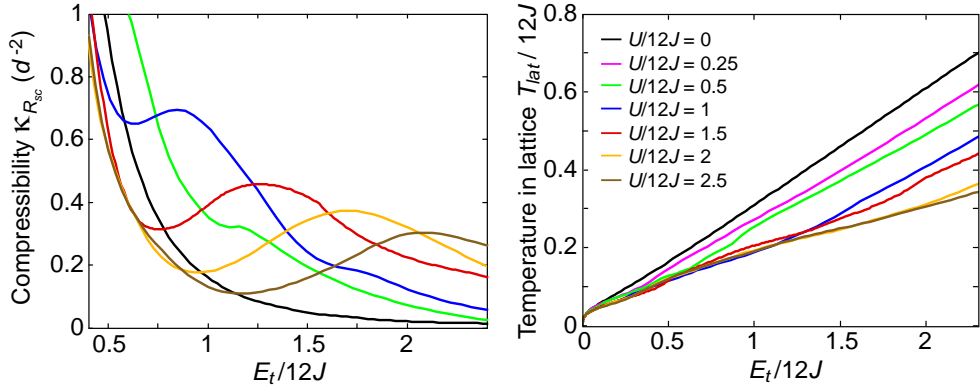


Figure 8.9.: Numerically calculated global compressibility and temperature of the interacting spin mixture versus compression for various interactions and an entropy per particle corresponding to a temperature of $T/T_F = 0.15$ in the harmonic trap. left: The formation of the Mott insulator manifests itself as a local minimum in the global compressibility. right: The repulsive interaction leads to a stronger localization of the particles and therefore increases their spin entropy, which leads to a decrease in temperature. (Data taken from [131])

For high compressions a second interesting effect can appear: At constant entropy and medium interaction strengths the cloud size can become slightly smaller than in the non-interacting case due to the Pomeranchuk effect [230, 231]: Repulsive interactions lead to more localized particles. This increases their spin entropy or—at constant entropy—leads to a colder temperature in the lattice [189], as can be seen in figure 8.9.

The same behaviour can also be seen in the experimental results, which are shown in figure 8.10: The non-interacting data agrees very well with the theoretical expectation for all compressions up to $E_t/12J \approx 2$. This shows that the chosen lattice ramp is adiabatic on the one-particle level for all trap frequencies. The insets (A-E) show the simultaneously measured quasi-momentum distribution, which nicely illustrates the observed crossover from a purely metallic phase (A-C), characterized by a partly filled Brillouin zone to an almost completely band-insulating cloud (E) with an evenly filled Brillouin zone. While such an evenly filled Brillouin zone could also result from a strongly heated cloud or localized atoms, the vanishing compressibility of the experimental data (cf. fig. 8.11) is a direct proof of the formation of an incompressible (band-) insulating state.

At very high compressions ($E_t/12J \gtrsim 2$), the second Bloch band gets slightly populated during the lattice ramp-up (cf. sec. 4.3.2), which leads to smaller cloud sizes for all interactions, because a small number of atoms in a nearly empty band can carry a considerable amount of entropy and thereby lower the temperature.

In the interacting case the lines in figure 8.10 represent a direct prediction without free parameters! In general we achieved a good agreement between theory and experiment, showing all the characteristic features expected in this system: In the limit of low compressions the density becomes small and interaction effects are unimportant. For growing compressions, the interacting clouds become signifi-

8. Repulsive Fermi-Hubbard model

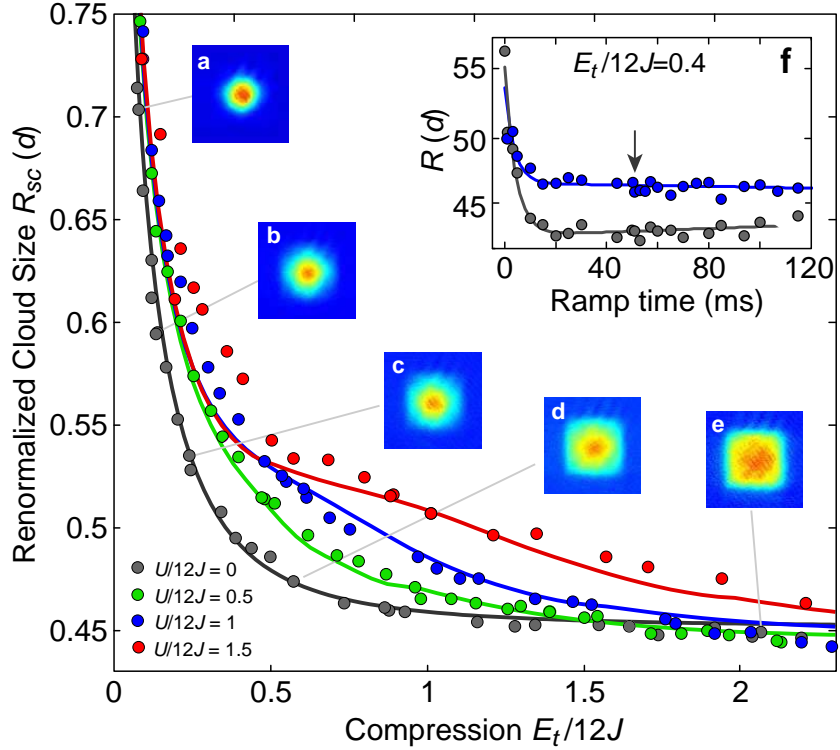


Figure 8.10.: Cloud sizes of the interacting spin mixture versus compression. Measured cloud size R_{sc} in a $V_{\text{lat}} = 8 E_r$ deep lattice as a function of the external trapping potential. Dots denote single experimental shots, lines denote the theoretical expectation from DMFT for an initial temperature $T/T_F = 0.15$. The insets (A to E) show the quasi-momentum distribution of the non-interacting clouds (averaged over several shots). F: Resulting cloud size for different lattice ramp times at $E_t/12J = 0.4$ for a non-interacting and an interacting Fermi gas. The arrow marks the ramp time of 50 ms used in the main graph. (Data taken from [229])

cantly larger than in the non-interacting case, indicating that the expected suppression of doubly occupied sites (cf. sec. 5.2.1) leads to lower densities. The size differences show a maximum around $E_t/12J \approx 0.7$, where the Mott-insulator is expected in the strongly interacting case, and then decrease again for higher compressions, where the state becomes dominated by the trapping energy. In the case of strong interactions ($U/12J = 1.5$) we find the onset of a region ($0.5 < E_t/12J < 0.7$) where the cloud size decreases only slightly with increasing harmonic confinement, whereas for stronger confinements the compressibility increases again. This is consistent with the formation of an incompressible Mott insulating core surrounded by a compressible metallic shell, as can be seen in the corresponding in-trap density profiles (cf. fig. 8.3). For higher confinements, an additional metallic core ($1/2 < n_{i,\sigma} < 1$) starts to form in the center of the trap and the cloud size decreases again.

The emergence of the Mott insulator can also be seen from the global compressibilities shown in figure 8.11, where a local minimum around $E_t/12J \approx 0.7$ can

8.3. Cloud size and compressibility

be observed in the strongly interacting case. While the shape of the minimum differs from the theoretical expectation, its position agrees very well with the largest extension of the Mott insulating phase in the numerical calculations (cf. fig. 8.3).

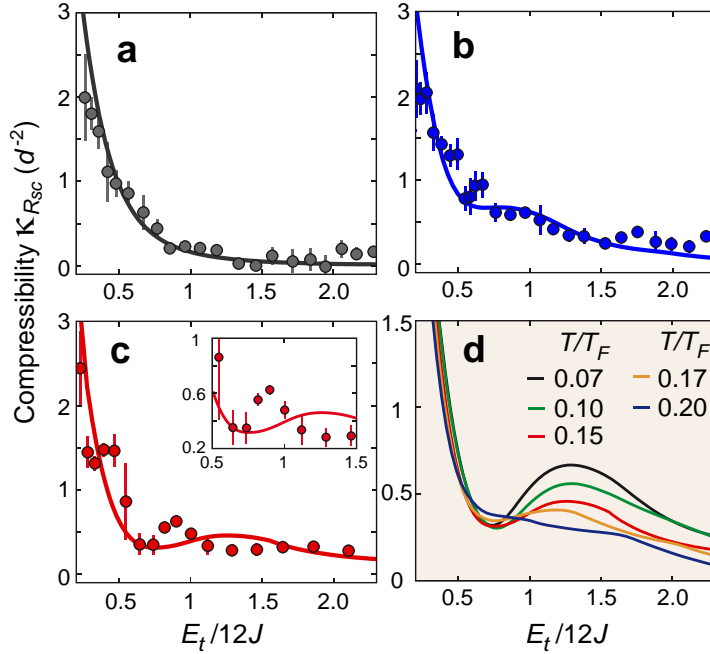


Figure 8.11.: Global compressibility $\kappa_{R_{sc}}$ of the atom cloud for various interactions [(A) $U/12J = 0$, (B) $U/12J = 1$, (C) $U/12J = 1.5$]. Dots denote the result of linear fits on the measured data and the error bars represent the fit uncertainty. Solid lines display the theoretically expected results for an initial temperature $T/T_F = 0.15$. The influence of the initial temperature on the calculated compressibility is shown in (D) for $U/12J = 1.5$. (Data taken from [131])

The only region with considerable deviations between experiment and theory lies below the Mott-insulating region at moderately weak compressions $E_t / 12J \lesssim 0.4$. While in the non-interacting case the cloud sizes show perfect agreement between theory and experiment, growing deviations appear for increasing interactions, where the observed cloud sizes are systematically larger than theoretically expected. The most probable explanation for this discrepancy are non-adiabaticities during the loading: In this compression regime, the cloud shrinks considerably during the main lattice ramp up (cf. fig. 9.4), as its kinetic energy gets strongly reduced during the loading (cf. sec. 4.3.2).

Although a variation of the used ramp time (cf. fig. 8.10(F)) seems to suggest that the resulting cloud size depends only weakly on the used ramp time, this may in fact be misleading, as the resulting cloud size incorporates the effects of both non-adiabaticities and technical heating during the ramp sequence. In the non-interacting case (gray) this results in a pronounced minimum of the resulting cloud size: While a too short ramp time increases the cloud size due to non-adiabaticities, a too long ramp time heats the cloud considerably, resulting again in a larger cloud.

8. Repulsive Fermi-Hubbard model

In the case of strong interactions (blue), both effects could partially compensate each other, leading to the observed weak dependence of the cloud size on the used ramp time, while in truth there exists a much longer adiabaticity timescale. This explanation is supported by our observation that interactions indeed dramatically increase the timescale needed for mass transport in this system, as will be shown in chapter 10. Another possible source of non-adiabaticities comes from the decay time of excess doublons, see following section.

8.4. Doublon fraction

In addition to the global compressibility measurements, the fraction of atoms on doubly occupied lattice sites (doublon fraction D) was measured for magnetic fields above the Feshbach resonance ($U/12J = 0, 0.5, 1$) by converting all atoms on doubly occupied sites into molecules using a linear magnetic field ramp (0.2 ms/G) over the Feshbach resonance (cf. sec. 6.6). The doublon fraction, which is plotted in figure 8.12 together with the theoretical expectation, gives insight into the local on-site physics of the system. In combination with the in-situ size measurements, this fraction can be compared for different interaction strengths at constant cloud size R_{sc} .

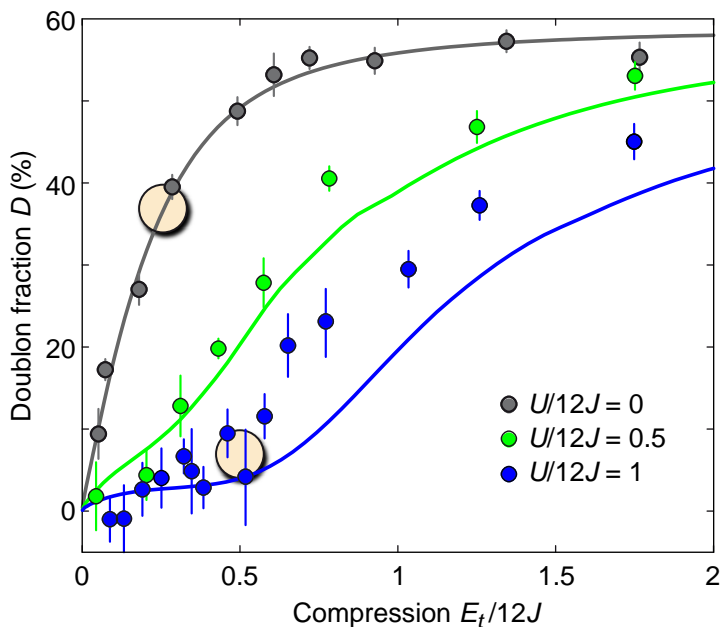


Figure 8.12.: Doublon fraction versus compression for different interaction strengths. The yellow circles indicate the doublon fraction for a constant cloud size $R_{sc} = 0.53$ (cf. fig. 8.10). Dots correspond to experimental data where the error bars denote the standard deviation of at least four measurements, while the lines are the DMFT predictions. (Data taken from [229])

8.5. Conclusion and outlook

In the limit of weak confinement densities are low and the doublon fraction D tends to zero, regardless of the strength of the repulsive interaction.

For intermediate compressions on the other hand, the doublon fraction depends crucially on the interaction. At a constant size $R_{\text{sc}} = 0.53$ the doublon fraction is around 40% for a non-interacting cloud but only around 5% for an intermediate repulsive interaction $U/12J = 1$ (yellow circles in fig. 8.12). In this regime of repulsive interactions, it is energetically favorable to reduce the number of doubly occupied sites despite the cost in potential and kinetic energy. Consequently, different compressions are needed to reach the same cloud size for different interactions (cf. fig. 8.10). The observed suppression of the doublon fraction at intermediate compressions directly shows the emergence of strong correlations in the system when the interaction energy U becomes comparable or larger than the bandwidth $12J$.

For strong compressions, where the trap dominates, the measured doublon fraction becomes comparable for all interactions, as the atom distributions are expected to contain a large band-insulating core in all cases. The pair fraction is limited to values smaller than 60% due to the finite entropy per particle, which limits the filling factor in the band-insulating state (cf. sec. 5.4.2).

Although the non-interacting and the slightly repulsively interacting curve $U/12J = 0.5$ match the DMFT results, we see deviations for stronger repulsive interactions ($U/12J = 1$). In this case, the measured pair fraction is in general $\sim 10\%$ higher than predicted by theory while the qualitative behavior agrees very well.

This can again be explained by non-adiabaticities during the loading: In the first phases of the loading, where U/J is still small, doublons will form similar to the non-interacting case. Most of these doublons should decay again later in the sequence, when U/J becomes important. Recent measurement in the group of T. Esslinger (ETHZ) have shown, however, that the decay time of excess doublons scales almost exponentially in U/J , and is at the relevant interactions on the order of the used ramp times [228, 232].

For strong repulsive interactions a suppression of the doublon fraction with respect to the non-interacting case occurs for all temperatures in the lattice below $k_B T_{\text{lat}} \approx U$, regardless of the formation of an incompressible Mott insulating phase in the inhomogeneous system. Even for a compressible purely metallic phase with $n_{i,\sigma} < 1/2$ the doublon fraction vanishes completely in the strongly interacting regime (cf. sec. 5.4.1). As a consequence, the doublon fraction alone cannot prove the formation of a Mott insulator.

8.5. Conclusion and outlook

By measuring the global compressibility and the doublon fraction of repulsively interacting fermionic atoms in an optical lattice it was possible to explore different regimes of the repulsive Fermi-Hubbard model. The global compressibil-

8. Repulsive Fermi-Hubbard model

ity allowed for a direct distinction between compressible Fermi liquid states and Mott-/band-insulating states. By comparing clouds at constant density, the suppressed doublon fraction at strong interactions directly signaled the entrance into the strongly-correlated regime.

At present, the loading into the lattice is limited by a combination of technical heating, which limits the usable ramp times, and non-adiabaticities due to the limitation of mass transport by interactions and the long decay time of excess doublons.

In order to quantify the total heating, the temperatures before loading into the lattice and after a return to the dipole trap with a reversed sequence were compared. We found a rise in temperature between $0.010(5) T/T_F$ for a non-interacting cloud and $0.05(2) T/T_F$ for a medium repulsion of $U/12J = 1$ at compressions around $E_t/12J = 0.5$. The heating increased both for very low compressions, where mass-transport limitations are more pronounced and very high compressions, where light assisted collisions become more important due to the higher density.

The good agreement between the experimental data and the numerical calculations, which assume adiabatic loading and an initial temperature of $T/T_F = 0.15$, indicates that the actual initial temperatures lie rather at the lower end of the measured temperature range $T/T_F = 0.15(3)$.

For low enough initial temperatures¹ the system is expected to enter an antiferromagnetically ordered phase. In order to realize this state experimentally, the best loading sequence would be to start at a higher trap frequency, such that the central density in the harmonic trap matches the density of the Mott insulator $n_{\text{har}} \approx 1 / (\lambda/2)^3$ and to decrease the harmonic confinement during the loading of the lattice, thereby minimizing the need for mass redistribution in the lattice.

Straightforward extensions of the measurements in this chapter include studying the effects of spin imbalance on the system and the extension to the ternary Mott insulator [181] in a mixture of three hyperfine states. In the case of one atom per lattice site three body losses should be suppressed and the atoms form a Heisenberg spin model with $SU(3)$ symmetry [234] and an enhanced entropy capacity of $S/N = \log(3)k_B$, compared to $S/N = \log(2)k_B$ in the binary case.

For a broken $SU(3)$ symmetry, that is different interaction strengths between the three components, even more complex states are expected, including color selective and paired Mott insulator states [235, 236].

Furthermore, the method of directly measuring the global compressibility can be readily extended to bosonic systems and Bose-Fermi mixtures.

¹Predictions range from $T/T_F \approx 0.035$ [157] to $T/T_F \approx 0.058$ [233] for the homogeneous system. In a trapped system the values will be considerably higher due to the inhomogeneous entropy distribution (cf. sec. 8.2.1,11.1).

9. Attractive Fermi-Hubbard model

In a second set of experiments we studied the equilibrium states of the attractive Hubbard model, using the same techniques as in the previous chapter. The attractive Fermi-Hubbard model is an intriguing many-body system, which allows one to study the effects of fermionic pairing in a lattice system in a wide parameter range: Similarly to free-space, a bound state of two particles in an otherwise empty system exists only above a certain threshold in the interaction strength ($U/J \lesssim -8$, cf. sec. 5.3). In the many-body case on the other hand, the BCS mechanism predicts Cooper pairing for all interactions. This allows one to study the so-called *BEC-BCS crossover* (cf. sec. 3.3.3) in the lattice. An important difference lies in the position of the crossover, which occurs at a finite interaction strength and not at the position of the free space Feshbach resonance, where enhanced heating and losses are observed.

Away from special commensurate situations like half-filling, the ground state is a superfluid state for all interactions, analogous to free space (cf. sec. 5.5.3). Its character changes gradually from a BCS like state for small interactions to a BEC of tightly bound pairs for strong interactions (cf. sec. 3.3.3). In stark contrast to free space, however, where the critical temperature for superfluidity in the BEC limit approaches that of non-interacting bosons [45], the effective hopping of the pairs ($J_{\text{pair}} \propto J^2/U$), and thereby the critical temperature, vanishes in the strongly interacting limit (cf. sec. 5.5.3). In addition, the pairs in the strongly interacting limit don't form a weakly interacting Bose gas, but a gas of hard-core bosons, as the Pauli principle forbids the occupation of a single lattice site by more than one pair. This highlights the differences between particles in free space and in the lowest band of a lattice.

But also above T_c the occurrence of pairing has dramatic consequences on the many-body state, e.g. the existence of the pseudogap regime (cf. sec. 5.5.3).

9.1. Temperature tracking

By measuring the cloud size at constant compression and low densities it was possible to essentially track the temperature as a function of the interaction. In a simplified picture the extension of the low-density cloud is connected to the temperature via:

$$\frac{1}{2}m_{\text{eff}}\omega^2r_{\text{max}}^2 \approx E_F + k_B T \quad (9.1)$$

9. Attractive Fermi-Hubbard model

A rising temperature, at otherwise unchanged parameters, leads to a larger cloud, as states with higher potential energies become accessible.

Tracking the temperature at constant entropy provides valuable information about the density of states, as can easily be seen from the usual relation between temperature and entropy in a canonical ensemble [22]:

$$S = -k_B \sum_i p_i \ln(p_i) \quad (9.2)$$

with $p_i = \exp(-\beta E_i)/Z$ ($\beta = 1/k_B T$) being the probability to find the system in the micro state i with energy E_i and $Z = \sum_i \exp(-\beta E_i)$ being the canonical partition function.

By introducing the density of states $\rho(E)$ of the many-body system and exchanging the sum for an integral this becomes:

$$S = -k_B \int_E \rho(E) \frac{\exp(-\beta E)}{Z} \ln \frac{\exp(-\beta E)}{Z} dE \quad (9.3)$$

In the experimentally relevant case of constant entropy (cf. sec. 2.3), equation 9.3 is an implicit formula for the temperature.

The resulting temperature of the system depends on the density of states $\rho(E)$ at all energies smaller than the sum of Fermi energy E_F and thermal energy $k_B T$: $E \lesssim N \times (E_F + k_B T)$.

This connection between the temperature and the density of states allows one in principle to observe changes in the low energy sector of the system at relatively high temperatures. As a specific example it enabled us to observe correlation effects near the BEC-BCS crossover by a rise in temperature; although our entropies were too high to observe superfluidity.

The theoretical arguments and simulations describing the effects presented in this chapter were developed by Maria Moreno-Cardoner (Mainz, Germany), Takuya Kitagawa and Eugene Demler (Harvard, USA), Ehud Altman (Rehovot, Israel) and Belén Paredes (Mainz, Germany) and the results in this chapter are published in [237].

9.2. Effects of pairing

The influence of pairing on the thermodynamics of the gas can already be seen in the maximum entropy capacity in some limiting cases:

The entropy capacity of a quantum system is directly proportional to the dimensionality $d_H = \dim(H)$ of its Hilbert space.

$$S_{\max} = \max \left(-k_B \sum_i p_i \ln(p_i) \right) = -k_B d_H \frac{1}{d_H} \ln \left(\frac{1}{d_H} \right) = k_B \ln(d_H) \quad (9.4)$$

9.2.1. Two atoms in a double well - a toy model

In the minimal model of one spin-up and one spin-down particle in a double well, which is shown in figure 9.1, the entropy capacity in the non-interacting case is $k_B \ln(4)$. In the limit of strong attractive interactions ($|U| \gg J, k_B T$), the entropy capacity is reduced by a factor of two, as only the two configurations with both particles in the same well remain energetically accessible.

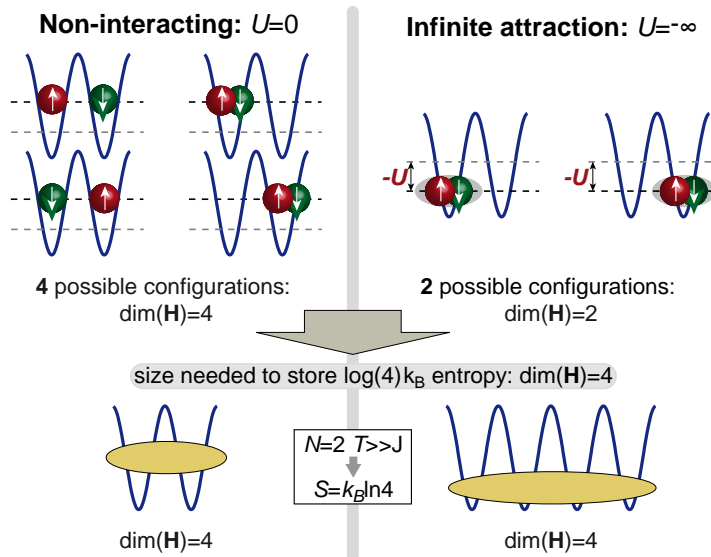


Figure 9.1.: Possible state and resulting entropy capacity of a minimal model of two fermions in a double well.

In a double well model, adiabatically increasing the interaction at a constant entropy of $k_B \ln(4)$ would result in a strong temperature rise, as the temperature must remain large compared to the interaction ($k_B T \gg |U|$). Alternatively, the system would need to expand to four lattice sites in order to store all the entropy. In the case of an harmonically trapped system at finite temperature, isentropically increasing the interactions will therefore result in a moderate temperature increase, such that higher lying lattice sites become accessible, and consequently lead to an expansion of the cloud.

9.2.2. Zero tunneling limit

In the zero tunneling limit the Hubbard hamiltonian reduces to a sum of uncoupled, local hamiltonians for each lattice site that can be solved analytically [237]. In this limit, which neglects the kinetic energy of the particles, an increasing attractive interaction progressively suppresses single occupied lattice sites and the system evolves from a non-interacting spin mixture into a gas of spinless, hard-core pairs. In a similar manner, an increasing repulsive interactions progressively

9. Attractive Fermi-Hubbard model

suppresses doubly occupied sites (cf. sec. 5.2.1, 8.4).

At zero entropy ($T = 0$) the cloud size in the non- or attractively interacting case is given by the smallest size (R_0) compatible with the Pauli principle. This maximally packed state, which consists only of doubly occupied sites minimizes both the potential energy due to the trap and the interaction energy and corresponds to a perfect band insulator. For repulsive interaction the cloud size increases due to the competition between interaction and potential energy.

At constant, finite entropy the cloud size shows a minimum for vanishing interactions and increases for both repulsive and attractive interactions due to the reduced entropy capacity. In the attractive case the strongly interacting cloud carries only half of the entropy of the non-interacting cloud [237] at the same cloud size.

9.2.3. Finite tunneling

At finite tunneling the above situation gets slightly modified due to the kinetic energy of the particles. This is illustrated in figure 9.2, where the results of an exact diagonalization calculation in a finite size one-dimensional system are shown. The simulation was performed by Maria Moreno-Cardoner and will be analyzed in detail in her PhD thesis.

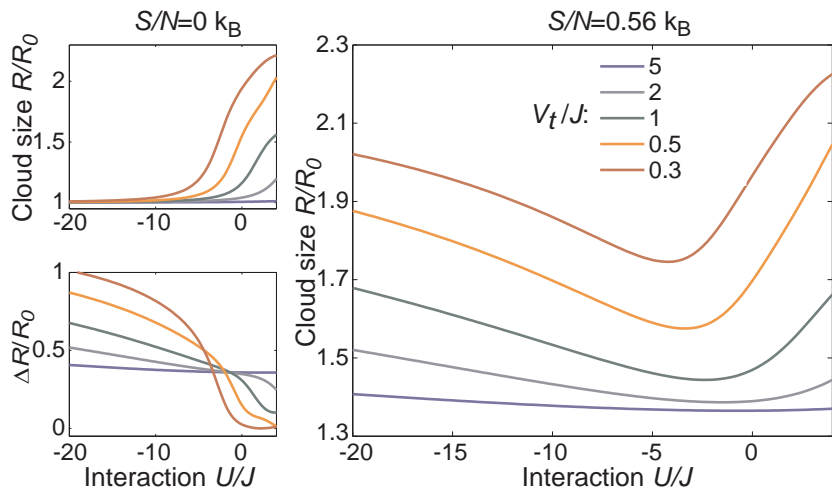


Figure 9.2.: Numeric simulation of the cloud size as a function of interaction. right: The cloud size at finite entropy $S/N = 0.56$ shows the interplay between the effect of pairing on the kinetic energy and on the entropy capacity. upper left: Ground state cloud size. lower left: Cloud size increase ΔR from $S/N = 0$ to $S/N = 0.56$. Data courtesy of Maria Moreno-Cardoner [237].

Even though there are crucial differences between 1D and 3D with respect to the existence of two-particle bound states and the density of states, nonetheless all principal effects show up in this calculation. As illustrated in the upper left panel figure 9.2, the zero temperature cloud size for finite tunneling is larger than in

9.2. Effects of pairing

the zero tunneling case, as the ground state now minimizes the sum of potential, interaction and kinetic energy. In the case of a dominating trap $V_t \gg J, |U|$, kinetic energy can be neglected and the cloud consists of a perfect band-insulator with unity filling and cloud size R_0 . For decreasing confinement, however, kinetic energy becomes important and leads to larger cloud sizes, as the band-insulator gives way to metallic states (cf. sec. 4.3.2).

For strong attractive interactions the cloud consists of tightly bound pairs, as discussed in chapter 5.3. Since their kinetic energy vanishes in the strongly interacting limit ($J_{\text{pair}} \propto J^2/U$), the cloud again approaches a perfect band-insulator. Repulsive interactions on the other hand again suppress the double occupancy of lattice sites and increase the cloud size.

At finite entropy the aforementioned decrease of the local entropy capacity again comes into play and is clearly visible in the increase of the cloud size. As shown in the lower left panel of figure 9.2, this effect depends strongly on the confinement. While the increase in cloud size is nearly independent of the interaction in the strongly confined limit, it develops a very pronounced interaction dependence in the weak confinement regime: While finite entropy results only in minor size increase in the non-interacting or repulsively interacting case, the formation of pairs leads to a large increase in cloud size for attractively interacting atoms.

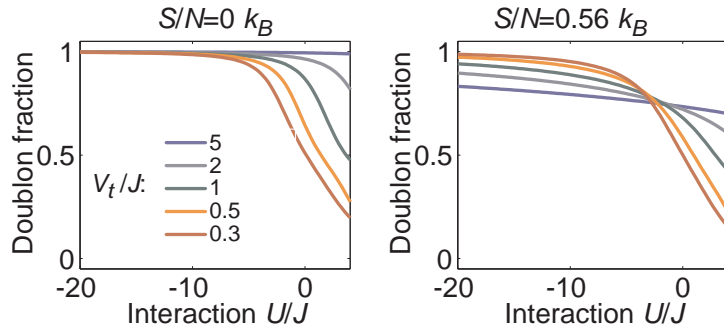


Figure 9.3.: Numeric simulation of the doublon fraction in a 1D model. left: At zero temperature an increasing confinement always increases the doublon fraction. right: At finite entropy, however, the doublon fraction *decreases* with increasing confinement for large attractive interactions. Data courtesy of Maria Moreno-Cardoner [237]

The competition between these two interaction effects, i.e. the shrinking of the zero temperature cloud size and the strong increase in the entropy effects, results in a shift of the minimum cloud size to finite attractive interactions, as can be seen in the main panel of figure 9.2.

The formation of pairs and its interplay with the entropy capacity can also be seen in the doublon fraction, which is shown in figure 9.3: In the zero temperature case (left panel), the doublon fraction increases monotonically with both increasing confinement, i.e. increasing density, and increasing attractive interactions.

9. Attractive Fermi-Hubbard model

At finite entropy, however, an increasing confinement leads to an increasing temperature (cf. fig. 8.9), which becomes comparable or larger than the interaction energy ($k_B T \sim U$). As a consequence, the effect of the interaction on the doublon fraction decreases with increasing confinement (cf. sec. 8.4). This leads to an abnormal behaviour for attractive interactions, where the doublon fraction *decreases* for increasing confinement, cf. figure 9.3, right panel.

9.3. Experimental sequence

The key ingredient to experimentally observe the aforementioned effects once again was the combination of a red-detuned dipole trap and a blue-detuned optical lattice, which allows an independent control of the confinement energy E_t and the lattice depth and thereby offers the possibility to realize low density systems with large atom numbers.

After evaporation, the dipole trap depth is ramped in 100 ms to the desired value of the external confinement ($\omega_\perp = 2\pi \times 20$ to 70 Hz) and the magnetic field is adjusted to set the scattering length (cf. sec. 3.3). In this way, negative scattering lengths up to $a \approx -400 a_0$ can be reached, before a further approach to the Feshbach resonance is hindered by enhanced losses and heating. Subsequently, the optical lattice is linearly increased to a potential depth $V_0 = 0$ to $9 E_r$ with a ramp rate of 7 ms/ E_r . We used the same adapted Fermi-Fit as in the repulsive case (cf. eqn. 8.3) to extract the cloud size from in-situ phase-contrast images taken along the short, vertical axis of the trap (cf. sec. 6.5) or measured the doublon fraction by converting atoms on doubly occupied lattice sites into molecules (cf. sec. 6.6).

9.4. Experimental results

The principal experimental result is presented in figure 9.4, where the cloud size (top) and the doublon fraction (bottom) are shown as a function of the scattering length for various lattice depths.

In the pure dipole trap (dark gray) the change in scattering length has no measurable effect on the cloud size, as the resulting interaction energies can be neglected in comparison to the Fermi energy.

This changes dramatically in the lattice, where interaction effects are strongly enhanced by the increased on-site density and, more importantly, the reduction of the kinetic energies (cf. sec. 4.3.2): As in the previous chapter (cf. fig. 8.10), increasing repulsive interactions lead to larger cloud sizes. Similarly, small attractive interactions result in slightly smaller clouds. For larger attractive interactions, however, the cloud sizes increases again. We observe the expected minimum at small

9.4. Experimental results

attractive interactions¹. The minimum becomes more pronounced and "sharper" for deeper lattices, where smaller scattering lengths are sufficient to create the same effective interaction strength U/J .

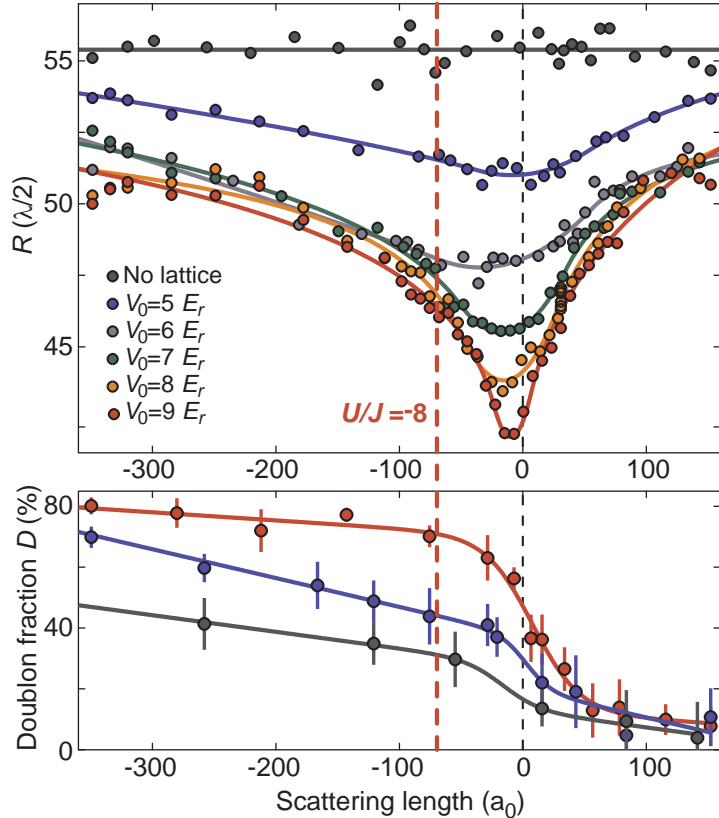


Figure 9.4.: Cloud size and doublon fraction as a function on interaction. top: Measured cloud size vs. scattering length for various lattice depths. Dots represent the running average over three experimental shots. bottom: Corresponding doublon fraction. Dots denote the average over at least five consecutive measurements, with the standard deviations shown as error bars. Lines are guides to the eye. Data were taken in a fixed external dipole trap ($\omega_{\perp} = 2\pi \times 25$ Hz, aspect ratio $\gamma \approx 4$) at a fixed entropy before loading of the lattice of $S/N = 1.42(26)$ k_B ($T/T_F = 0.15(3)$)

This at first glance counter-intuitive or anomalous expansion of the cloud for increasing attractive interactions can be understood intuitively by considering the thermodynamic arguments presented before. In order to further check this explanation, we additionally measured the doublon fraction for the same experimental parameters (cf. fig. 9.4, bottom).

In the non-interacting case there exist no correlations between the different spin

¹Compared to the plots in [237], the analysis presented here uses an updated parametrization of the Feshbach resonance. This uses a new measurement of the zero-crossing of the scattering length, which is based on the free expansion of an initially localized cloud in a homogeneous Hubbard model (cf. sec. 10.3.5).

9. Attractive Fermi-Hubbard model

components and the number of doubly occupied sites is given by the integral over the squared density (cf. sec. 5.4.1). In comparison to the non-interacting case we observe a strong increase in the doublon fraction for increasing attractive interactions. This increase directly signals the occurrence of strong correlation between the spin components, as the mean density simultaneously decreases due to the expansion. The high observed doublon fractions of up to 80% confirm the assumption that in this limit the cloud consists mostly of tightly bound on-site pairs.

The vertical, dashed red line in figure 9.4 denotes the threshold for the existence of a two-body bound state ($U/J \approx -8$, cf. sec. 5.3) in the deepest used lattice ($V_0 = 9 E_r$, red). At this interaction strength one would expect strong correlations to appear in the case of two particles in an otherwise empty system.

The fact that the observed minimum in cloud size appears for much smaller interactions hints towards a many-body origin of the pairing, as expected by the Cooper instability (cf. sec. 3.3.3). The system is in the so-called pseudogap or pre-formed pair regime where bound pairs have formed but did not condense yet (cf. sec. 5.5.3).

9.4.1. Influence of compression and temperature

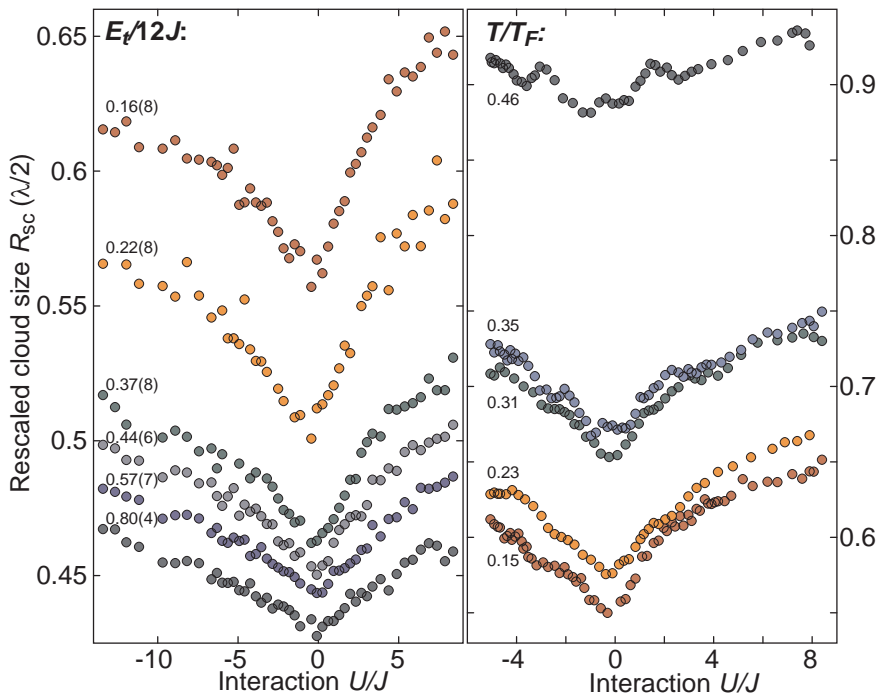


Figure 9.5.: Measured rescaled radius R_{sc} versus interaction strength U/J for different compressions $E_t/12J$ (left) and entropies (right). Dots denote running averages over four experimental shots. left: $V_0 = 7 E_r$, $S/N = 1.15(25) k_B$ ($T/T_F = 0.12(3)$), right: $V_0 = 7 E_r$, $E_t/12J = 0.16(8)$

9.5. Heating during loading

As can be seen in figure 9.5 (left), the effect on the cloud size is most pronounced for low compression ($E_t/12J$), where Fermi energy and temperature are lowest. At higher compressions, where the densities are higher, stronger interactions are needed to dominate over Fermi energy and temperature. In addition the observed heating is more pronounced at higher compressions (cf. below). This unfortunately prohibits a quantitative comparison of the experimental result with the perturbative calculation in [237], which was based on a high temperature expansion [238–240] and is only valid in the compression regime.

As can be seen in the right part of figure 9.5, an increasing entropy leads to larger clouds and decreasing interaction effects.

9.5. Heating during loading

In order to measure the amount of heating during the loading sequence, the atoms were unloaded from the lattice back into the harmonic trap by inverting the used loading sequence, followed by a hold time of 150 ms at $a = 100 a_0$. During this hold time the cloud equilibrates via elastic collisions and all previous excitations are converted into an entropy/temperature increase. The non-isentropic temperature increase during the loading is approximated by one-half of the temperature difference between measurements with and without the loading/unloading sequence and is presented in figure 9.6.

For low compressions, where the anomalous expansion effect is most pronounced, the heating during the loading is below 2% of the Fermi temperature, but rises considerably for higher compressions. In addition, the heating also depends on the interaction and increases for stronger attractive interactions.

Note that this simple evaluation assumes equal heating during both ramps [241] and implicitly assumes that the cloud remains in thermal equilibrium during the loading!

The main sources of heating expected in this system are pair losses due to light assisted collisions, inelastic three-body collisions, technical noise and non-adiabaticities of the loading sequence. Concerning non-adiabaticities, an additional possibility are unwanted reflections of the dipole trap laser stemming from the inside of the glass cell. These lead to a second, incommensurable standing wave that would act as a quasi-disorder potential [242] whose depth would increase with the compression and could hinder mass transport.

Especially non-adiabaticities during the loading will lead to non-equilibrium states in the lattice. It is, however, not clear, whether such non-adiabaticities necessarily result in a large entropy increase. Even if the state in the lattice becomes considerably altered, some of the non-adiabatic effects could be "reversed" during the unloading by processes similarly to a "freezing in" and subsequent melting of a state.

Even though later expansion experiments have shown a strong increase of the

9. Attractive Fermi-Hubbard model

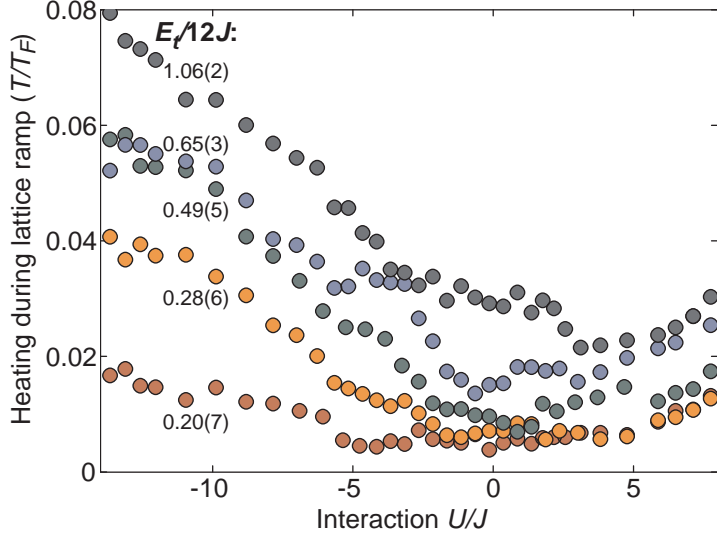


Figure 9.6.: Heating during lattice loading as a function of scattering length for various compressions and a maximum lattice depth of $7 E_r$. The plotted heating is given by $\frac{1}{2}(T_{\text{with Lat.}} - T_{\text{without Lat.}})$.

adiabaticity timescales due to interactions (cf. sec. 10), the increase was found to be symmetric for attractive and repulsive interactions. The observed heating in this experiment on the other hand is asymmetric and is stronger for attractive interactions.

While non-adiabaticities and technical heating will play a role, the dominant effect appears to be light assisted collisions, as the separately measured doublon lifetime, which is shown in the next section, strongly decreases on approaching the Feshbach resonance, matching the observed increasing heating.

9.6. Doublon lifetime

The lifetime of a doublons was directly measured by comparing the doublon fractions measured after variable hold times in a $20 E_r$ deep lattice. In such a deep lattice three-body collisions can be neglected, as they are suppressed by the Pauli principle. Binary on-site collisions, especially the light assisted collisions introduced in section 3.4 on the other hand, should increase in deep lattices. This is due to the fact that the extension of the on-site wavefunction decreases for deeper lattices, thereby increasing the wavefunction at the Condon point. The higher light intensity of a deep lattice additionally increases the collision rate (cf. sec. A.2.2).

In this measurement doublons were created by loading into a $9 E_r$ deep lattice at various attractive interactions and low compression. Subsequently, the lattice depth was increased to $20 E_r$ in $200 \mu\text{s}$, thereby creating a low density gas of

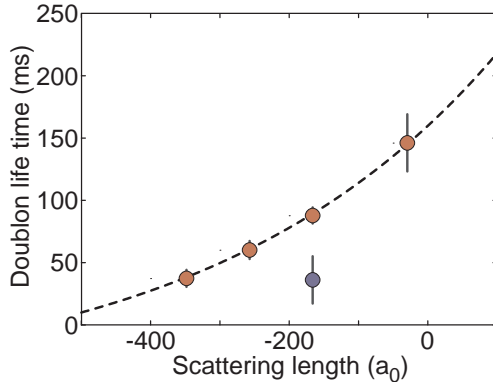


Figure 9.7.: Doublon lifetime in a $20 E_r$ deep lattice. red: loading at strong attractive interaction and low density $E_t/12J = 0.25(8)$. blue: same sequence at higher density $E_t/12J = 2.0(1)$. The dashed line is a guide to the eye.

tightly bound on-site pairs (cf. following section and fig. 9.4). The number of doublons was measured as a function of holdtime and the resulting lifetimes are plotted in figure 9.7.

The observed lifetimes are strongly interaction dependent and decrease for increasing attractive interactions. In addition the lifetime decreases for deeper lattices and higher densities. The doublon lifetime is expected to almost vanish on approaching the Feshbach resonance, as the on-site wavefunction of the two atoms approaches that of a Feshbach molecule, for which much shorter lifetimes have been measured (cf. sec. A) in the presence of the lattice light.

These relatively short doublon lifetimes render light-assisted collisions the most likely candidate for the observed non-isentropic heating. The observed compression dependence could be caused either by a direct influence of the dipole light or by additional losses due to collisions between already dissociated atoms and atoms on nearby lattice sites.

9.7. Adiabaticity timescales

In order to get a handle on the loading dynamics, and a first estimate on the relevant adiabaticity timescales in the strongly attractive regime, both cloud size and doublon fraction were measured as a function of lattice ramp time. Figure 9.8 shows that the doublon fraction saturates already for ramp times as short as 5 ms, while the ramp needed to be 20 times slower in order to reach the equilibrium cloud size in this deep lattice.

This illustrates that, in the strongly interacting limit, pair formation is a local two-particle process that is independent of global equilibrium, as long as the temperature remains much smaller than the binding energy of order U . The strong difference of more than an order of magnitude between the timescales also highlights

9. Attractive Fermi-Hubbard model

the fact that local observables, like the doublon fraction, can only yield limited information about the global equilibrium of the system.

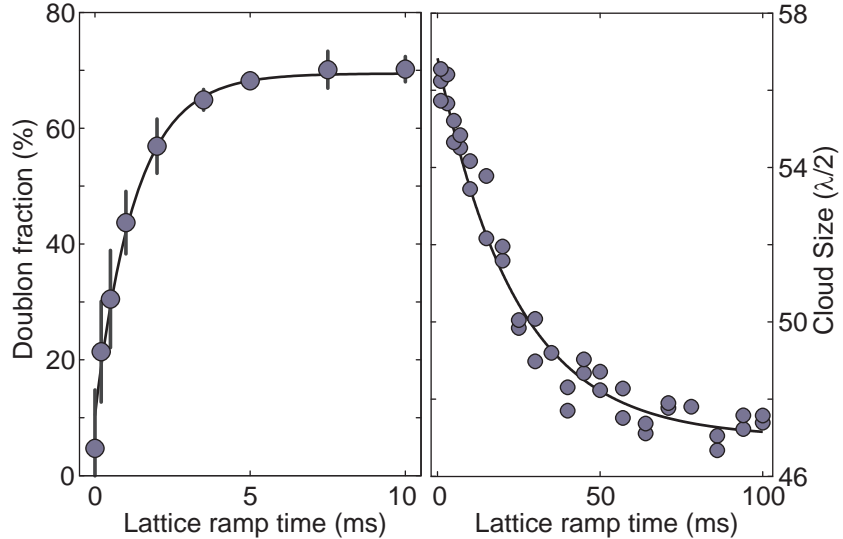


Figure 9.8.: Influence of the lattice ramp time on doublon fraction and cloud size. left: Doublon fraction at an harmonic confinement of $\omega_{\perp} = 2\pi \times 28$ Hz. right: Cloud size for a harmonic confinement of $\omega_{\perp} = 2\pi \times 40$ Hz. Both measurements were taken at $a = -75 a_0$, a final lattice depth of $15 E_r$, and utilized a $1 E_r$ pre-ramp.

9.8. Conclusion and outlook

The results presented in this chapter show how pair formation in a fermionic Hubbard model with attractive interactions gives rise to an anomalous expansion of the gas as the attraction increases. The consequences of pairing in the first band of a lattice potential are fundamentally different from the consequences of pairing in the continuum.

The realization of the so-called pseudogap or preformed pair regime, where bound pairs have formed but did not condense yet (cf. sec. 5.5.3), is an important step towards the experimental study of fermionic superfluidity in the attractive Hubbard model. The fact that the observed minimum in cloud size appears for interactions much smaller than the position of the BEC-BCS crossover hints towards a many-body origin of the pairing, as predicted by the Cooper instability (cf. sec. 3.3.3). In the future, this studies can be extended to include the effects of population imbalances, where even richer phase diagrams with additional phases (e.g. the FFLO phase) are predicted [148, 171–173].

In addition this work opens an interesting route toward the detection of quantum many-body phases at finite entropies, where a marked change in the thermodynamic behavior can serve as a footprint of the crossover between two phases exhibiting substantially different entropy densities, as observed recently for a quantum critical condensed matter system [243].

10. Dynamics in the Fermi-Hubbard model

In this last part of the experimental work we took advantage of the fact that ultracold atoms offer a full real-time control over all hamiltonian parameters by e.g. varying laser intensities or magnetic fields. In particular it is possible to instantaneously change parameters and thereby implement *quantum quenches*. This is a major advantage of ultracold atoms compared to real solids where the implementation of quantum quenches is hindered by both the lack of real-time control and the short relaxation timescales. In typical metals for example, electronic relaxation occurs on timescales on the order of $10^{-15} - 10^{-11}$ s [244] and can only be probed at surfaces by pump-probe spectroscopy using fast laser pulses.

The second important motivation for this experiment is of a more technical nature: One open, fundamental question in optical lattice experiments concerns the timescales needed to adiabatically load into the lattice (cf. previous chapters and [245–247]) or to achieve equilibrium in the lattice [228, 247]. With the exception of the one-dimensional case, where DMRG [182, 248] enables the theoretical study of dynamics in the Hubbard model at least for short time spans [249], there exists no theoretical method to calculate these timescales.

In addition it turned out that, for the inhomogeneous systems studied here, the timescales of e.g. mass transport are more involved than simple scaling arguments (e.g. $\propto 1/J$, $1/U$, $1/\omega$) would predict.

Although there have been several previous studies of out-of-equilibrium dynamics in optical lattices [27, 28, 68, 114, 115, 250–252], up to now all experiments were performed in the presence of additional potentials, either in a trap or under the influence of gravity. This had profound consequences for the dynamics already on the single particle level by e.g. inducing Bloch oscillations (cf. sec. 4.3.2).

Here it was possible to eliminate all external potentials in a two-dimensional (2D) system by compensating the anticonfining potential of the blue-detuned optical lattice (cf. sec. 4.3.1) in the horizontal directions and to study dynamics and transport properties in a homogeneous Hubbard model. This was achieved by first preparing a confined state in a combination of the optical lattice and an harmonic trap and suddenly switching off the harmonic confinement while retaining the lattice. The subsequent dynamic expansion is driven by density gradients instead of potentials and therefore does not alter the single-particle dynamics. The dynamics was probed by monitoring the evolution of the in-situ density distribution, as depicted in figure 10.1.

10. Dynamics in the Fermi-Hubbard model

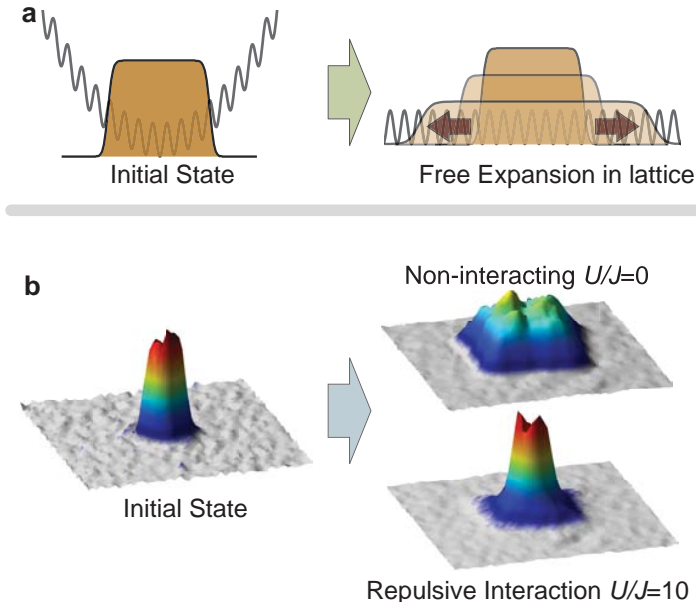


Figure 10.1.: top: Free expansion in a homogeneous lattice. First a band-insulator is created in the combination of an optical lattice and a strong harmonic trap. Subsequently the harmonic confinement is switched off and the cloud expands in a homogeneous Hubbard model. bottom: Observed in-situ density distributions. The evolution of the initial density distribution (left) crucially depends on the interaction (right).

The theoretical analysis of the resulting dynamics was performed in collaboration with the group of Prof. Achim Rosch from the university of Cologne and Prof. Eugene Demler from Harvard University. All numerical simulations of the interacting system shown in this chapter were performed by Stephan Mandt, David Rasch and Prof. Achim Rosch.

10.1. Experimental sequence

The experiment starts with the preparation of a band-insulating state of a balanced spin mixture, using a sequence similar to the one in chapter 8: Through evaporative cooling in the dipole trap a quantum degenerate mixture of the two lowest hyperfine states of potassium was reached with atom numbers of $N = 1-1.5 \times 10^5$ atoms per spin state at reduced temperatures of $T/T_F = 0.13(2)$, where T_F denotes the Fermi temperature in the harmonic trap (cf. sec. 2.2.2). The trapping frequencies of the dipole trap were then increased to approx. $2\pi \times 100$ Hz ($2\pi \times 400$ Hz) in the horizontal (vertical) directions.

Subsequently, the blue-detuned 3D optical lattice is ramped up linearly to a depth of $8E_r$ in 56 ms. During the ramp the magnetic field is held at 209.1 G, which

10.1. Experimental sequence

corresponds to vanishing interactions (cf. sec. 10.3.5). This loading procedure results in a large band-insulating core with a high doublon fraction surrounded by a metallic shell at a compression of $E_t/12J = 1.8$ (cf. fig. 8.3). In the next step, the tunneling rate J is reduced to $J = h \times 23$ Hz by linearly increasing the lattice depth to $20 E_r$ in $200 \mu\text{s}$, a timescale that is slow enough to avoid excitations into excited bands, but fast compared to tunneling within the lowest band. Due to this reduced tunneling rate the density distribution is essentially frozen out during the following 40 ms magnetic field ramp to $B_{dyn} = 206 - 260$ G, which sets the interaction for the expansion. Combined with the strong harmonic confinement this leads to a dephasing between different lattice sites and effectively localizes all particles to individual sites, similar to the effects observed in our study of coherent multi-body interactions in quantum phase revivals in bosonic ^{87}Rb [188], which will be presented in detail in the thesis of Sebastian Will.

In total, this sequence produces a cloud of localized atoms with a well-known density distribution that is independent of the interaction between the particles.

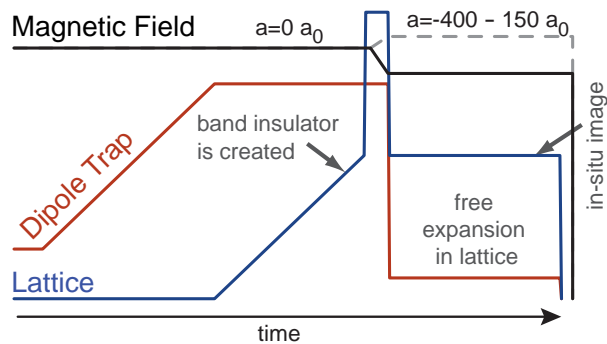


Figure 10.2.: Experimental Sequence. Starting with a degenerate Fermi gas in the dipole trap a non-interacting band insulator is created. During a freeze-out period the atoms localize to individual lattice sites and the desired interaction is set without altering the density distribution. Subsequently the harmonic confinement is switched off and the cloud expands in a homogeneous Hubbard model.

The expansion is initiated by lowering the lattice depth in $200 \mu\text{s}$ to values between $4E_r$ and $15E_r$ while simultaneously switching off the harmonic confinement. To this end, the strength of the dipole trap is reduced by more than 90%, such that for the horizontal directions the remaining dipole potential precisely compensates the anticonfinement produced by the lattice beams (cf. sec. 10.2.1). While the vertical motion is expected to be strongly suppressed by gravity-induced Bloch oscillations of amplitude $A = 2J/mg < 2\lambda/2$, cf. eq. 4.23), the atoms are exposed to a homogeneous Hubbard model without additional potentials in the horizontal directions. The evolution of the density distribution during the following expansion in this *quasi 2D* situation was monitored by in-situ imaging along the vertical axis of the cloud, thereby integrating over any vertical dynamics.

In a second set of experiments, vertical tunneling of the atoms during the expansion was suppressed by retaining the depth of the vertical lattice at $20 E_r$, thereby

10. Dynamics in the Fermi-Hubbard model

realizing several layers of independent two-dimensional Hubbard models without any influence of gravity.

10.2. Non-interacting case

In the absence of collisions and additional potentials the Hubbard hamiltonian (cf. eqn. 5.5) consists only of the hopping term. In this case quasi-momentum, and thereby also group velocity \vec{v} , is conserved and each initially localized particle expands independently with a constant velocity distribution, leading to a ballistic expansion.

The delocalized density distribution $\rho(\vec{r}, t)$ after an expansion time t of an atom, which is initially localized at the central lattice site ($\vec{r}_0 = 0$), is given by the initial velocity distribution $\rho_v(\vec{v})$,

$$\rho(\vec{r}, t) = \rho_v(\vec{r}/t) \quad (10.1)$$

which can be characterized by the *mean expansion velocity* v_{exp} :

$$v_{\text{exp}}^2 = \langle \hat{v}_x^2 + \hat{v}_y^2 \rangle = \frac{\int_{\mathbb{R}^3} (v_x^2 + v_y^2) \rho(\vec{v}) dV}{\int_{\mathbb{R}^3} \rho(\vec{v}) dV} \quad (10.2)$$

The root mean square (RMS) width $R_{\text{sp}}(t) = \sqrt{\langle \hat{x}^2 + \hat{y}^2 \rangle}$ (cf. eqn. 8.1) of the expanding particle, which will be denoted as the *single particle width*, scales linearly with expansion time and is proportional to the mean expansion velocity:

$$R_{\text{sp}} = v_{\text{exp}} \cdot t \quad (10.3)$$

The total density distribution of the whole cloud after an evolution time t is given by the convolution of the initial density distribution with the delocalized probability distribution (eqn. 10.1) of the individual atoms and its RMS width is given in the relevant cases by:

$$R(t) = \sqrt{R_0^2 + v_{\text{exp}}^2 t^2} \quad (10.4)$$

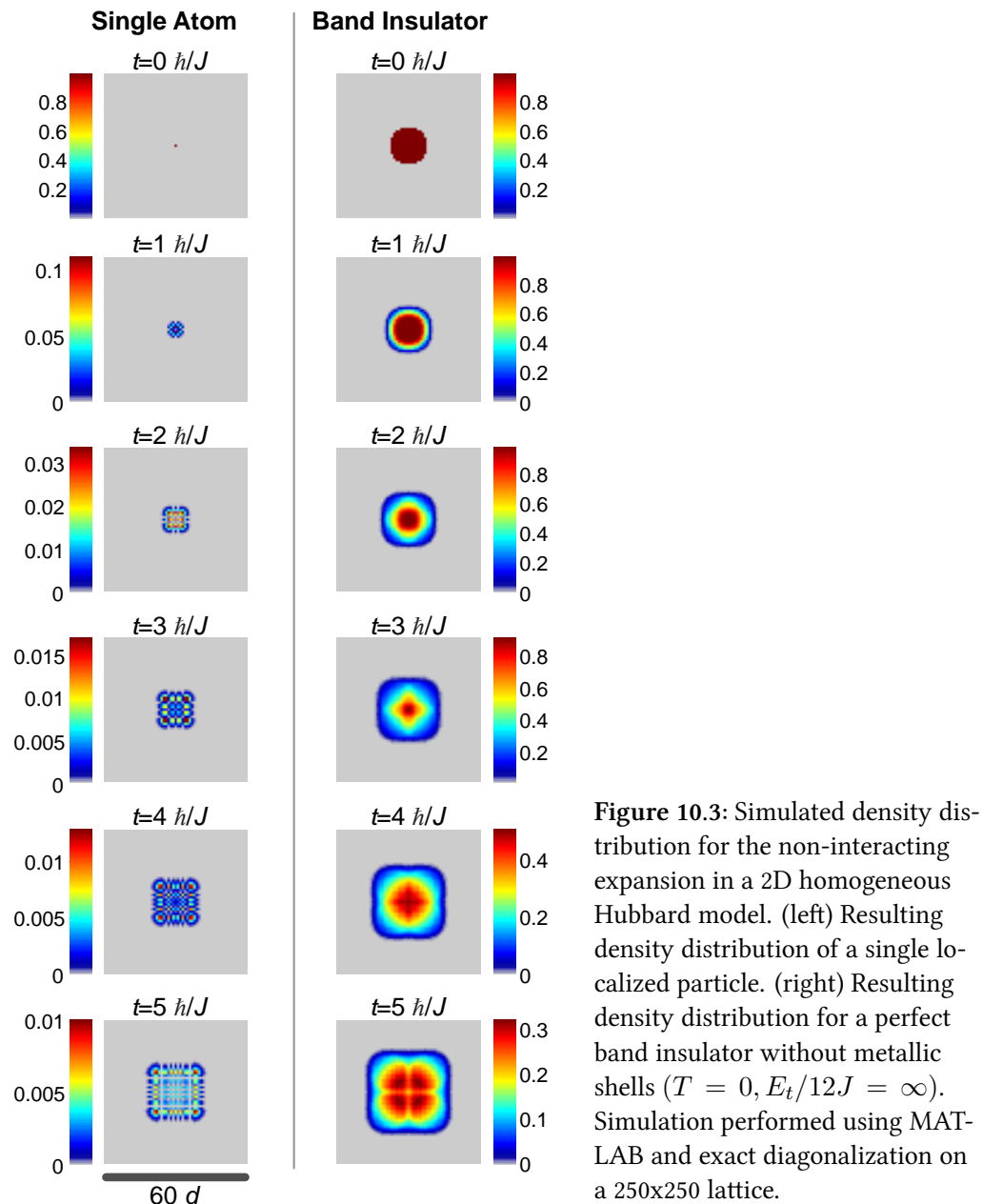
In the case of an initially localized particle its wave function is given by a single Wannier function, that is an equal superposition of all Bloch waves (cf. sec. 4.3.2). In 1D the corresponding mean expansion velocity can then be calculated by averaging the squared group velocities $v_{\text{gr}}(q) = \frac{2Jd}{\hbar} \sin(qd)$ of the Bloch waves (cf. sec. 4.3.2) over the first Brillouin zone:

$$v_{\text{exp}}^2 = \frac{d}{2\pi} \int_{-\pi/d}^{\pi/d} \left(\frac{2Jd}{\hbar} \right)^2 \sin^2(qd) dq \quad (10.5)$$

In the separable D -dimensional case this results in a mean expansion velocity of:

$$v_{\text{exp}} = \sqrt{\sum_{i=1}^D v_{\text{exp},i}^2} = \sqrt{2D} \frac{Jd}{\hbar} \quad (10.6)$$

10.2. Non-interacting case



10. Dynamics in the Fermi-Hubbard model

As is shown in the left panel of figure 10.3, the expanding density distribution of an individual non-interacting atom acquires the square symmetry of the underlying simple-cubic lattice.

As a consequence also the symmetry of the expanding cloud as a whole changes during the expansion from the rotational symmetry of the initial density distribution into a square symmetry. This can be seen both in the numerical calculation (fig. 10.3, right panel) and in the experimental data (fig. 10.4).

For very long expansion times this symmetry becomes distorted in the experiment by residual inhomogeneities in the remaining potential and in the lattice depth.

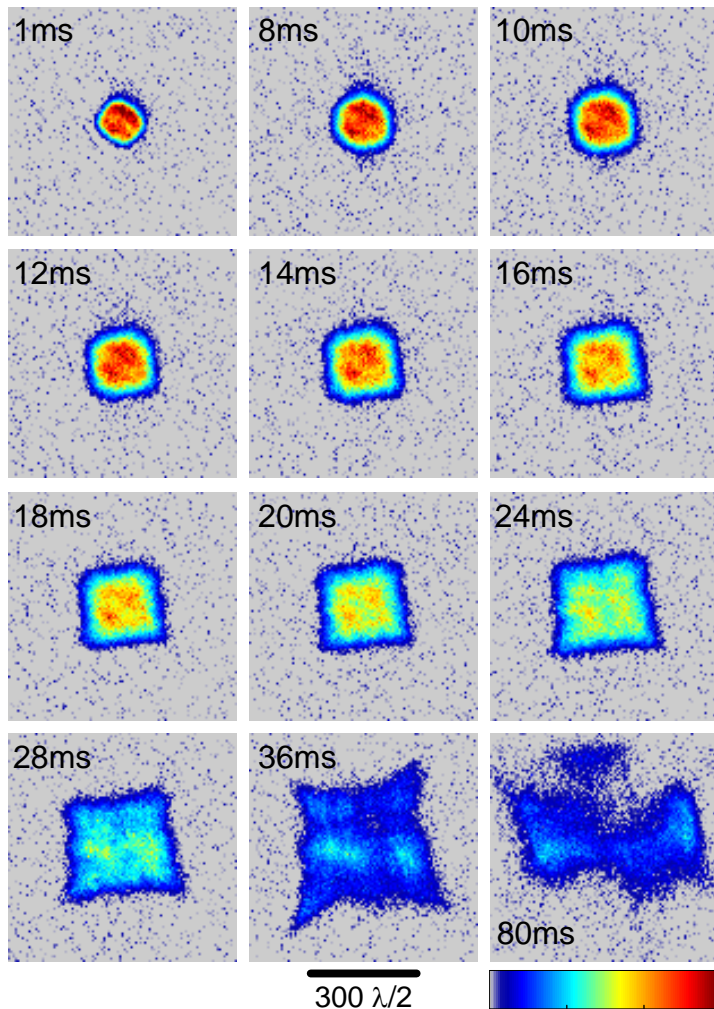


Figure 10.4.: In-situ absorption images (column density a.u.) of an expanding non-interacting ($|U/J| \lesssim 0.3$) cloud in a quasi 2D lattice with lattice depth $8 E_r$. The expansion changes the symmetry of the cloud from the rotational symmetry of the harmonic trap to the square symmetry of the lattice Brillouin zone. At long expansion times residual potentials and lattice inhomogeneities deform the cloud.

In order to experimentally measure the mean expansion velocity, the cloud size $R = \sqrt{\langle \hat{r}_\perp^2 \rangle}$ is extracted from in-situ phase-contrast images using a 2D Gaussian

10.2. Non-interacting case

fit similar to the previous chapters (cf. sec. 8.3.1)¹:

$$G(x, y) = A e^{-\frac{(x-x_c)^2}{2\sigma_x^2} - \frac{(y-y_c)^2}{2\sigma_y^2}} + b \quad (10.7)$$

Here $x_c, y_c, \sigma_x, \sigma_y, A$, and b are free fit parameters and the perpendicular cloud size is given by $R = \sqrt{\langle \hat{r}_\perp^2 \rangle} = \sqrt{\sigma_x^2 + \sigma_y^2 - w^2}$, where w denotes the imaging resolution (radius of Airy disc $w < 3\mu\text{m}$) of our imaging setup. The resulting cloud sizes $R(t)$ (fig. 10.5, orange) were fitted by the expected behaviour of eqn. 10.4, thereby yielding the desired mean expansion velocity v_{\exp} . The corresponding single-particle width $R_{sp}(t)$ is calculated by deconvolving $R(t)$ with the initial width $R(0)$: $R_{sp}(t) = \sqrt{R(t)^2 - R(0)^2}$.

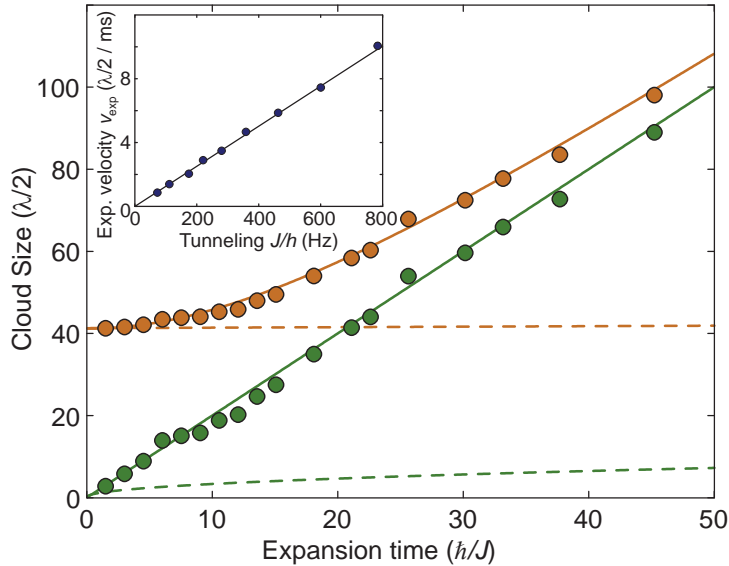


Figure 10.5.: Measured cloud size (orange) and deconvolved single-particle width (green) of an expanding non-interacting cloud in an $8 E_r$ deep lattice. Solid lines denote the quantum-mechanical prediction and dashed lines the corresponding classical random walk. The inset shows the linear scaling of the mean expansion velocity with tunneling J .

The measured widths $R(t)$ (orange dots in figure 10.5) show a very good agreement with the theoretically expected behaviour. In particular does the deconvolved single-particle width R_{sp} (green) grow linearly in time, thereby confirming the ballistic expansion. The expansion rate agrees well with the quantum-mechanical prediction of the mean expansion velocity (cf. eqn. 10.6), which is shown as solid lines in figure 10.5). Classical hopping, on the other hand, would result in a random walk where at every timestep the particle randomly hops to *one* of the neighbouring sites. A classical random walk of the same hopping rate would predict a much slower square-root expansion of the single-particle width (dashed lines). It would furthermore preserve the spherical shape of the initial cloud.

¹While the adapted Fermi-Fit of equation 8.3 is better suited to describe the initial distribution, a gaussian fit function yields better fits for the expanding clouds.

10. Dynamics in the Fermi-Hubbard model

This result directly shows that the dynamics is governed by the quantum-mechanical tunneling from lattice site to lattice site and not by classical thermal hopping, which would occur e.g. for a thermalized atom on the surface of a crystal. The ballistic expansion therefore can be viewed as a continuous quantum walk [253–255], which is also the basis of a recently proposed quantum computing algorithm [256].

10.2.1. Canceling the harmonic confinement

An important condition for the observed ballistic expansion is the absence of additional potentials, as any residual potential would change the velocity distribution during the expansion. In figure 10.6 the measured cloud sizes $R(t)$ of an expanding non-interacting cloud in an $8 E_r$ deep quasi 2D lattice are shown as a function of the dipole laser power during the expansion. The red line denotes a fit with the expected dynamics (cf. eqn. 10.4) for the homogeneous case to the first 20 ms.

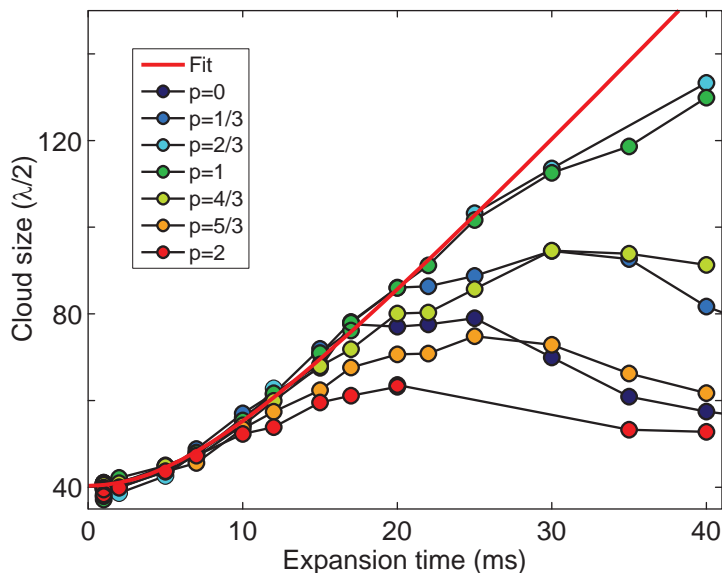


Figure 10.6.: Expansion of non-interacting atoms as a function of dipole beam power p (a.u.) in an $8E_r$ lattice.

While the initial expansion velocity depends only slightly on the residual confinement, it completely dominates the size after long expansion times. The largest cloud sizes are reached only if the confinement created by the dipole trap compensates the anticonfinement due to the lattice. This situation corresponds to dipole powers between $p = 2/3$ and $p = 1$ in figure 10.6. Both an over- and an under-compensation leads to deviations from the expected ballistic behaviour and ultimately limits the cloud size by either classical reflections or Bragg reflections of the expanding atoms (cf. sec. 4.3.2).

In the well-compensated case the dominant deviation from the homogeneous situation arises due to the finite size of the lattice beams ($w \approx 150 \mu\text{m}$), which leads

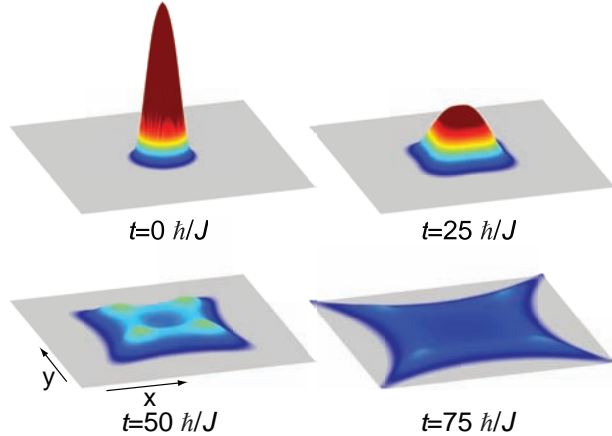


Figure 10.7.: Simulated column density distribution for the non-interacting expansion including the finite size of the lattice beams. Simulation performed in the group of Prof. A. Rosch.

to a position dependent hopping rate: The lattice depth in any given direction decreases with increasing distance to the center of the corresponding laser beam. This in turn leads to an increase in the hopping rate. Including these effects into a numerical calculation (cf. fig. 10.7) reproduces the star-like deformation visible in the lower row of figure 10.4. For very long expansion times ($\gtrsim 35$ ms) additional potentials due to imperfections in the alignment and beam shapes of the dipole and lattice beams become important and lead to further distortions of the cloud.

10.3. Interacting case

The ballistic expansion observed for non-interacting atoms is in stark contrast to the interacting case, where a qualitatively different dynamics is observed: Figure 10.8 shows in-situ absorption images taken after 25 ms of quasi 2D expansion in an $8 E_r$ deep lattice. The observed dynamics gradually changes from a purely ballistic expansion in the non-interacting case, which results in a square density distribution, into a more complex expansion for interacting atoms: For increasing interaction strengths the center of the cloud expands slower and slower and preserves the initial rotational symmetry, while a small part of the atoms nonetheless expands ballistically.

10. Dynamics in the Fermi-Hubbard model

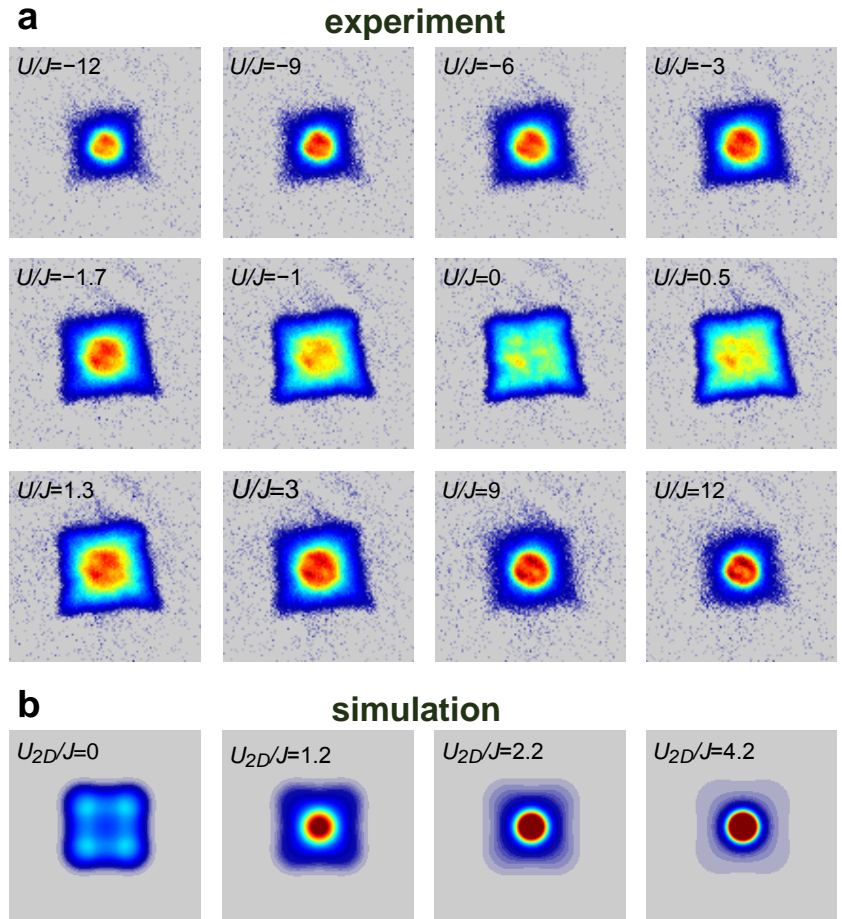


Figure 10.8.: In-situ absorption images for various interactions after 25 ms expansion in a homogeneous quasi 2D lattice. The images show a symmetric crossover from a ballistic expansion for non-interacting clouds to an interaction dominated expansion for both attractive and repulsive interactions. Images are averaged over at least five shots and all scales are identical to figure 10.4. The bottom line shows the results of a 2D simulation of the Boltzmann equation performed by St. Mandt for the same initial conditions.

10.3. Interacting case

This can be understood intuitively by observing that interactions, i.e. elastic collisions, lead to a diffusive dynamics and allow the particles to regain local thermal equilibrium [257, 258]. As a consequence, sufficiently large atomic clouds, where density gradients are small, remain close to local thermal equilibrium and their dynamics can be described by the laws of hydrodynamics. As the diffusion equation (cf. below) is rotationally invariant, the initial spherical shape is preserved for most parts of the cloud already for moderately strong interactions, cf. figures 10.1 and 10.8.

For a small fraction of atoms in the outer parts of the atomic cloud, however, the density is so small that mean free path is larger than the distance to the cloud edge, resulting in a ballistic expansion of these atoms. Therefore the tails of the cloud show the square symmetry characteristic for freely expanding particles (cf. fig. 10.8). This initial fraction of ballistically expanding atoms decreases for increasing interaction strengths. During the expansion the density gets reduced and, in the limit of infinite expansion times, all atoms are expected to become ballistic.

We observe the same behaviour irrespective of the sign of the interactions, although one would intuitively expect that repulsive (attractive) interactions lead to a positive (negative) pressure and therefore an increased (reduced) expansion rate.

This symmetry is a direct consequence of the chosen initial state, which consists only of localized atoms, and the highly symmetric dispersion relation of the Hubbard model and is further discussed in section 10.3.3.

10.3.1. Theoretical description

The resulting dynamics of interacting atoms was analyzed in collaboration with the group of Prof. Achim Rosch. Elastic collisions between the interacting atoms lead to a constant redistribution of kinetic energy and quasi-momentum and give rise to a particular kind of diffusive dynamics: As the time τ between scattering events strongly depends on the density n , the same holds for the diffusion constant $D \propto \tau$. It shows a minimum in the half filled case and diverges in the limits of an empty or completely filled band, where scattering is suppressed, as in this case no scattering partners or unoccupied final states are available:

$$D(n) \propto (n(1-n))^{-1} \quad (10.8)$$

Accordingly, the dynamics is described by a highly singular, non-linear diffusion equation [259] :

$$\partial_t n(r, t) = \nabla \cdot (D(n) \nabla n) \quad (10.9)$$

The divergence of the diffusion constant at vanishing densities $D(n) \propto 1/n$ leads to the unphysical prediction of diverging currents $j_i = D(n) \frac{\partial n}{\partial i}$ and diverging velocities.

10. Dynamics in the Fermi-Hubbard model

In reality, however, the diffusive description becomes invalid in this limit and the dynamics gradually becomes ballistic again. Intuitively speaking, the velocity limit imposed by the band structure constrains the maximal velocity and gives rise to a strong feedback from the ballistic tails on the diffuse core, as the ballistic outer regions thereby hold the diffusive part of the cloud together. Thus the bare diffusion equation becomes invalid even in relatively dense regions, where the scattering rate is high.

For a theoretical description of the expanding clouds one consequently needs an approach that can correctly describe both the diffusive and the ballistic regime. The probably simplest one is a Boltzmann equation in the relaxation time approximation [29]:

$$\partial_t f_{\mathbf{q}} + \mathbf{v}_{\mathbf{q}} \nabla_{\mathbf{r}} f_{\mathbf{q}} + \mathbf{F}(\mathbf{r}) \nabla_{\mathbf{q}} f_{\mathbf{q}} = -\frac{1}{\tau(n, e)} (f_{\mathbf{q}} - f_{\mathbf{q}}^0(n, e)) \quad (10.10)$$

It describes the evolution of the quasi-classical momentum distribution $f_{\mathbf{q}}(\mathbf{r}, t)$ as a function of position and time in the presence of a force \mathbf{F} . The transport scattering time $\tau(n)$ describes the relaxation towards an equilibrium distribution $f_{\mathbf{q}}^0$ for given energy (e) and particle densities (n).

Numerical simulations performed in the group of Prof. A. Rosch used this equation to predict the evolution of the interacting clouds. Examples of the resulting distributions are shown in the lowest row of figure 10.8, details of the calculation and the analysis can be found in [260, 261].

In two dimensions the non-linear diffusion equation predicts a universal minimal loss rate $\partial_t N \leq -4\pi\gamma$ of the total number of particles N for $D(n) = \gamma/n$ [259, 262], which describes the rate of particles reaching infinity and is completely independent of the initial distribution. This loss rate is closely related to the rate with which the diffusive part of the cloud emits ballistic particles [260, 261]. In addition, these effects have an interesting geometrical interpretation [259] due to their connection with the famous Ricci flows [263, 264], which were used e.g. in the proof of the celebrated Poincaré conjecture in three dimensions [264].

In one dimension there exists an infinite number of conservation laws that strongly restrict the possibilities for equilibration. This leads to a different behaviour that cannot be described by this hydrodynamic approach.

10.3.2. Core width and core expansion velocity

For a more quantitative analysis, the same experiment was performed in a fully two-dimensional situation. In this experiment the vertical lattice is kept at a depth of $20 E_r$ during the expansion in an otherwise identical sequence. In both cases (quasi 2D and 2D) we observe a spherical, diffusive core surrounded by ballistic tails without any qualitative differences between the cases.

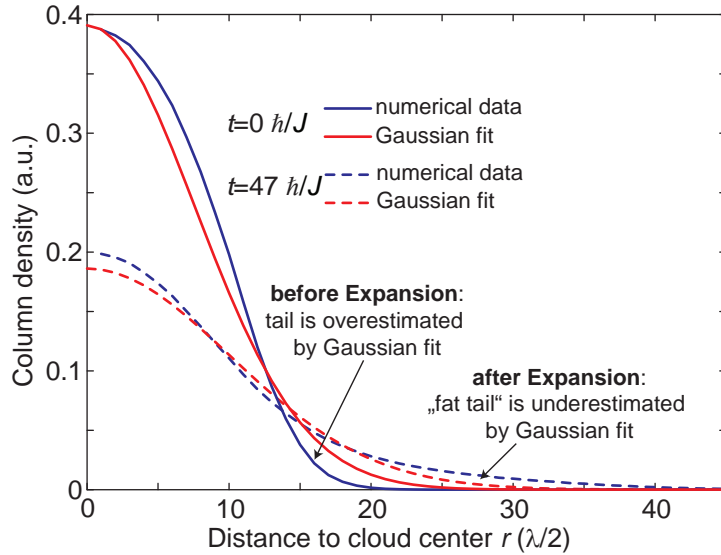


Figure 10.9.: Numerically calculated density distribution for $U/J = 1.2$ together with Gaussian fits. Numerical simulations performed by St. Mandt.

In the case of interacting atoms the shape of the cloud changes considerably during the expansion, evolving from a “compact” Fermi-Dirac like in-trap distribution (cf. sec. 8.3.1) to a “fat tail” distribution, as illustrated in figure 10.9 using fits to numerically simulated data. This leads to considerable systematic errors in the estimation of $\langle \hat{r}_\perp^2 \rangle$ ($\neq R_G^2$) in the interacting case, as no suitable fit function was found. In principle, these systematic errors could be avoided by determining $\langle r^2 \rangle$ via direct integration. In the experiment, however, this is hindered by imaging aberrations and the small signal to noise ratio in the extreme dilute limit (cf. sec. 8.3.1). The change in the shape of the cloud is due to the density dependent dynamics in the interacting case: While the expansion remains ballistic in the low density limit, the expansion velocity decreases for higher densities due to the increasing number of collisions. As a consequence, $\langle \hat{r}_\perp^2 \rangle$ will be dominated by the ballistically expanding outermost atoms for long expansion times.

In order to focus on the dynamics of the high density core, we instead use the core width R_c , which is defined as the half width at half maximum (HWHM) of the column density distribution. It is extracted from phase-contrast images that have been azimuthally averaged and individually normalized. The resulting core widths are shown in figure 10.10 for various interactions and have been fitted by the same fit function as in the non-interacting case (cf. eqn. 10.4).

The resulting core expansion velocities v_c , which are shown in figure 10.11, decrease dramatically already for interactions much smaller than the bandwidth $8J$. This shows the strong impact of moderate interactions on mass transport in defect free systems. It also has important consequences on all dynamic procedures in the lattice, e.g. loading into the lattice or cooling within the lattice (cf. sec. 11.1), as it limits the required adiabaticity timescales.

10. Dynamics in the Fermi-Hubbard model

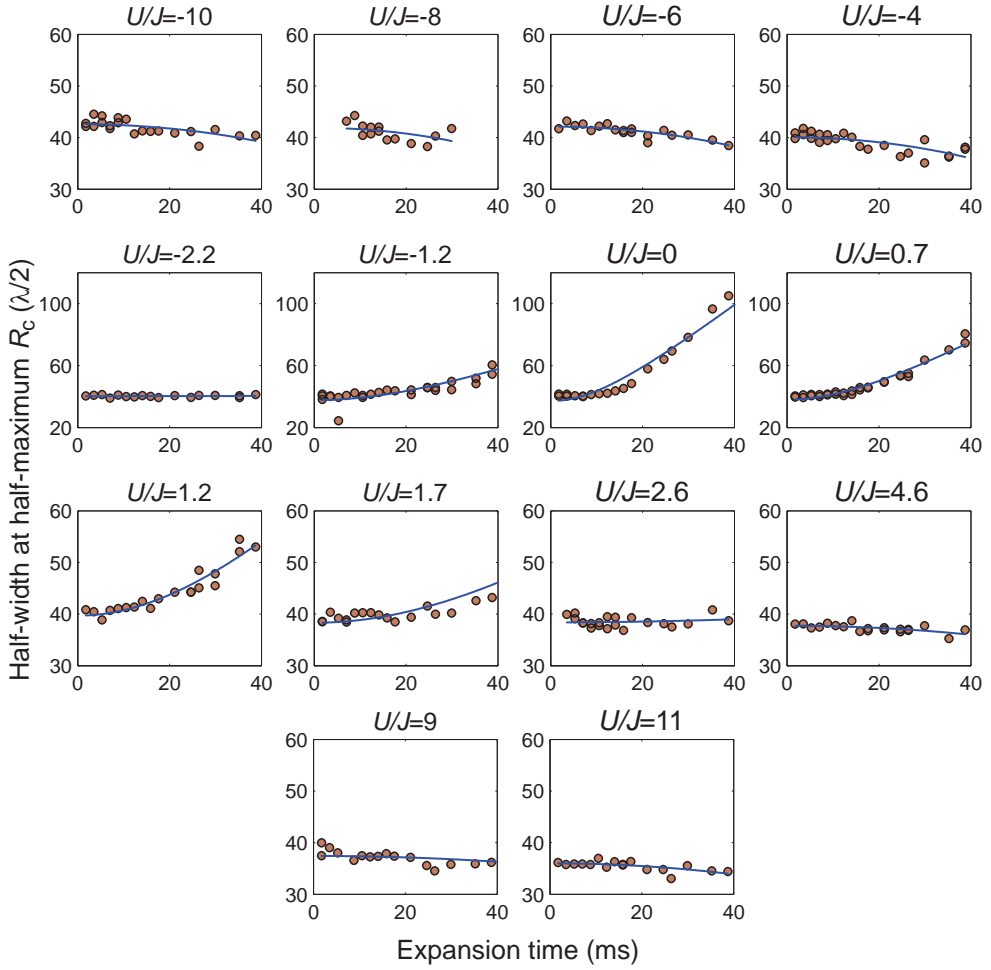


Figure 10.10.: Core widths R_c as a function of expansion time for various interactions in an $8 E_r$ deep lattice in the 2D case. Blue lines denote the fits used to extract the core expansion velocities (Eq. 10.4)

The core expansion velocities v_c even become negative for interactions larger than $|U/J| \gtrsim 3$: In this regime, the diffusive core dissolves by emitting ballistic particles and therefore shrinks in size, as the particle current in the flanks of the core is always higher than in the center of the core, where the density gradient vanishes. The slight asymmetry observed at large interactions can be attributed to interaction dependent losses due to light-assisted collisions during the preparation sequence (cf. sec. 3.4 and fig. 9.7).

All qualitative features seen in the experiment, including the drastic collapse of the expansion velocities and the shrinking of the core width for strong interactions, are well reproduced by the numerical results obtained in the group of Prof. A. Rosch. Quantitative discrepancies between experiment and numerics probably arise because the leading order perturbation theory in U/J , which has been employed in the calculation of the diffusion constant, is not valid for $U \gtrsim J$. Furthermore, the relaxation time approximation breaks down in the crossover re-

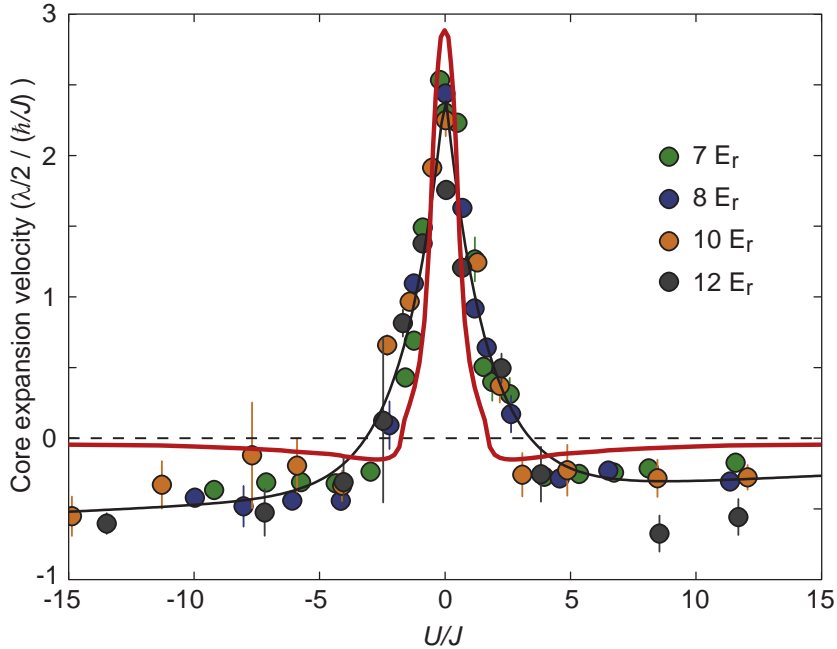


Figure 10.11.: Measured core expansion velocities versus interaction for various lattice depths in a 2D situation. The red line denotes the result of a numerical calculation (see text) and the black line is a guide to the eye.

gion from diffusive to ballistic behaviour, where the colliding atoms are far from thermal equilibrium.

But even though the core expansion velocity can be qualitatively predicted by a diffusive ansatz, the full quantum dynamics is certainly more complex and includes e.g. the formation of entanglement between distant atoms [265, 266]. In the case of a sufficiently high initial doublon density the free expansion itself could possibly be used to locally cool the atoms via quantum distillation processes [248].

10.3.3. Dynamical U vs. $-U$ symmetry of the Hubbard model

In this section, the observed dynamical symmetry between repulsive and attractive interactions in the fermionic Hubbard model is addressed. The presented analysis was performed in collaboration with Prof. A. Rosch, Prof. E. Demler and M. Moreno-Cardoner. First some intuitive argument for the observed symmetry are given before a formal theorem is presented.

In the interacting case elastic collisions between the atoms lead to a diffusive dynamics, whose diffusion constant depends on the scattering cross section σ . Since this cross section is proportional to the square of the interaction strength, $\sigma \propto a^2 \propto U^2$ (cf. eqn. 3.4, 5.2), it is intuitively clear that, for small expansion

10. Dynamics in the Fermi-Hubbard model

times, the dynamics depends only on the absolute value of the interaction, but not on the sign.

For longer expansion times, however, an additional argument is needed, as in the long run all interaction energy will be converted into kinetic energy: In the initial state there is a high number doublons N_D , giving rise to an interaction energy $E_{\text{int}} = N_D U$. During the expansion, the number of doublons decreases and, in the limit of long expansion times, the average density and the number of doublons typically vanish. Consequently, the initial interaction energy will be completely converted into kinetic energy, except for very large interactions, where isolated doublons cannot decay any more [140].

In free space, where the dispersion relation is a parabola ($E \propto p^2$), an increase in kinetic energy will always result in higher group velocities, while a decrease will result in smaller velocities. Therefore the dynamics will not show a U vs. $-U$ symmetry in free space!

The observed symmetry in the lattice now arises from the high symmetry of the tight-binding dispersion relation in the lowest band of a Hubbard model (cf. sec. 4.3.2), which is, for the one dimensional case, plotted in figure 4.14 and 10.12 together with the resulting group velocities (cf. eqn. 4.18).

In contrast to free space, where a higher kinetic energy always results in a higher group velocity, the tight-binding group velocity distribution shows a maximum at a quasi-momentum of $\hbar q = \hbar\pi/(2d)$. This maximum is located in the middle between $q = 0$ and the edge of the first Brillouin zone and corresponds to an energy of $E_{\pi/(2d)} = 0$.

Any force acting on an atom in this Bloch state will slow it down, independent of the sign of the force. Furthermore, the group velocity distribution is completely symmetric with respect to this point.

Due to the specific loading scheme applied in the experiment (cf. sec. 10.1), the many-body state at the beginning of the expansion consists only of localized atoms, since any coherences between different lattice sites dephased during the freeze out period (cf. sec. 10.1). The energy of a Wannier state ($E_W = 0$) lies in the center of the Bloch band and coincides with the energy of the fastest Bloch wave. Furthermore, a Wannier state can be written as an equal superposition of all Bloch waves (cf. fig. 10.12, left), and, as a consequence, its quasi-momentum distribution is flat and symmetric about $\hbar q = \hbar\pi/(2d)$.

During the course of the expansion the average density will decrease and all interaction energy will be converted into kinetic energy.

As both the group velocity distribution and the initial quasi-momentum distribution are symmetric with respect to $\hbar q = \hbar\pi/(2d)$ it follows that the evolution of the total group velocity distribution, and thereby the density distribution, will be independent of the sign of the interaction.

As illustrated in right part of figure 10.12 for the case of a positive interaction, the conversion of interaction energy to kinetic energy will lead to a redistribution

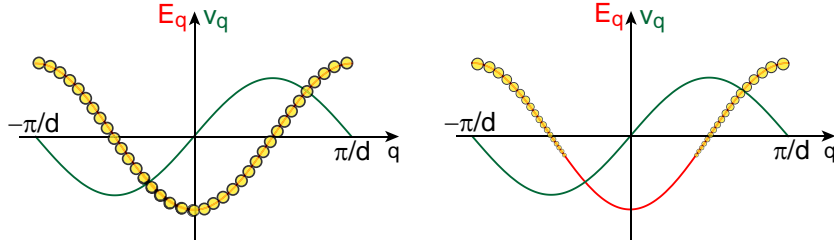


Figure 10.12.: left: Cartoon picture of the initial state in the Bloch basis. Since the initial state consists only of localized particles, its quasi-momentum distribution is flat over the whole Brillouin zone. right: Quasi-momentum distribution after a long expansion time at moderately large positive U . The positive initial interaction energy has been converted into kinetic energy. This results in a non-flat distribution, which can be described by an thermal distribution at negative temperature.

of atoms across the different quasi-momenta. Due to energy conservation, this redistribution will necessarily create a higher occupation of large quasi-momenta, which only have a small group velocity. This explains the observed slowing-down of the expansion in the interacting case on longer timescales. In the case of an attractive interaction, dominantly small quasi-momenta will be occupied in an analogous fashion. Due to the symmetric group velocity distribution for small and large quasi-momenta this will lead to the same slowing-down effect.

Dynamics theorem

The above intuitive argument can be turned into a precise theorem by considering a coherent dynamical evolution arising from two Hubbard-type hamiltonians that differ only in the sign of the interaction term:

$$\hat{\mathcal{H}}_{\pm} = -J \sum_{\langle ij \rangle \sigma} \hat{c}_{i\sigma}^{\dagger} \hat{c}_{j\sigma} \pm U \sum_i \hat{n}_{i\uparrow} \hat{n}_{i\downarrow} \quad (10.11)$$

The desired theorem can be formulated in terms of two operators:

The π -boost operator \hat{B}_Q , which translates all quasi-momenta by $Q = (\pi/d, \pi/d, \pi/d)$, is given in second quantization notation by:

$$\hat{B}_Q \hat{c}_q^{\dagger} \hat{B}_Q = \hat{c}_{q+Q}^{\dagger} \quad (10.12)$$

The effect of the time reversal operator \hat{R}_t on a Bloch wave is to negate the quasi-momentum:

$$\hat{R}_t \hat{c}_q^{\dagger} \hat{R}_t^{\dagger} = \hat{c}_{-q}^{\dagger} \quad (10.13)$$

Using these two operators the observed symmetry can be expressed by the following theorem:

10. Dynamics in the Fermi-Hubbard model

If the experimentally measured quantity \hat{O} is invariant under both time reversal and π -boost, and the initial state $|\Psi_0\rangle$ is time reversal invariant and only acquires a global phase factor under the boost transformation ($\hat{B}_Q |\Psi_0\rangle = e^{i\chi} |\Psi_0\rangle$, $\chi \in \mathbb{R}$), then the observed time evolutions

$$\langle \hat{O}(t) \rangle_{\pm} = \langle \Psi_0 | e^{i\hat{\mathcal{H}}_{\pm} t} \hat{O} e^{-i\hat{\mathcal{H}}_{\pm} t} | \Psi_0 \rangle \quad (10.14)$$

are identical: $\langle \hat{O}(t) \rangle_+ = \langle \hat{O}(t) \rangle_-$.

The proof of this theorem is presented in appendix B.

The experimental observable is the density distribution $\hat{n}(r_j) = \sum_{\sigma} \hat{c}_{j\sigma}^{\dagger} \hat{c}_{j\sigma}$ and the initial state consists of atoms that are completely localized to individual lattice sites (cf. sec. 10.1). Because both the initial state and the measured operator fulfill the requirements of the symmetry theorem (cf. sec. B), the dynamics is guaranteed to show the $U \leftrightarrow -U$ symmetry for all interaction strengths. Since the bi-partite character of the lattice is crucial to the proof of the theorem, this symmetry can be expected to be broken in lattices without the bi-partite structure, such as a triangular lattice.

Temperatures after the expansion

In the interacting case elastic collisions between the atoms will lead to thermalization and the cloud will regain local thermal equilibrium. But to which final temperatures?

As detailed in chapter 5.7.1, the inhomogeneous system can be locally approximated by the homogeneous system by use of the local density approximation. In global equilibrium this results in an inhomogeneous chemical potential and a homogeneous global temperature. During the expansion the system will only regain local thermal equilibrium, i.e. the system can locally again be described by a homogeneous system in equilibrium, but in this case not only the chemical potential but also the temperature becomes position dependent.

If all doublons dissolve during the expansion, the expanding cloud will reach such low densities that interactions between the particles can be neglected. In that case the single particle eigenstates of the homogeneous system are the Bloch waves, whose eigenenergies lie in the interval $\epsilon \in [-4J, 4J]$.

Due to the localized initial states, all Bloch waves are equally occupied and the average kinetic energy per particle is $E = 0$, i.e. it is located exactly in the middle of all possible energies. In the non-interacting case this represents a thermal state of infinite temperature, as only $T = \infty$ describes an even occupation of all single

particle eigenstates:

$$\lim_{T \rightarrow \infty} F(\epsilon) = \lim_{T \rightarrow \infty} \frac{1}{\frac{1}{z} e^{\frac{\epsilon}{k_B T}} + 1} = \frac{1}{\frac{1}{z} e^0 + 1} = \text{const.} \quad (10.15)$$

In the interacting case the initial kinetic energies still follow the same distribution than in the non-interacting case, but on top of that there is the interaction energy, which can range from zero to $U/2$ per particle. During the expansion all interaction energy will be converted into kinetic energy and, for repulsive interactions, raise the average kinetic energy per particle well above the middle of its possible values. In the low density limit this corresponds to a state where high lying single-particle states are more occupied than low lying states. In this limit, the system will consequently equilibrate to negative local temperatures [267–269].

The observed symmetry between repulsively and attractively interacting fermions can again be seen by observing that, for negative interactions the average energy per particle is decreased by the same amount as it is increased in the repulsive case. Therefore the temperatures in the attractive and repulsive case are identical up to the sign.

10.3.4. Doublon dissolution time

Both the qualitative and quantitative analysis of the experimental results assume the relaxation of the system to local equilibrium. For very strong attractive or repulsive interactions $|U| \gg J$, however, doubly occupied sites (doublons) only decay very slowly [140, 169, 228] as the missing or excess energy of order U can only be transferred to other particles in a higher order process [140, 169, 228].

Consequently, an important question for the resulting expansion is whether the rate with which the diffusive core dissolves is determined by the decay time of *individual* doublons or whether the latter is fast compared to the former.

In order to investigate this, the doublon fractions were measured (cf. sec. 6.6) during the expansion and fitted by a simple exponential decay. The resulting doublon dissolution times, which are shown in figure 10.13), are about an order of magnitude larger than the decay time of excess doublons measured recently in a half filled situation [228] in 3D at comparable interactions. In addition, they agree with the timescales for melting of the diffusive core observed in the numerical simulations performed by St. Mandt, although this simulations did not include an explicit doublon dissolution time.

This strongly suggests that, at least in the investigated range of interactions, the doubly occupied sites remain in local equilibrium in the diffusive regime.

10. Dynamics in the Fermi-Hubbard model

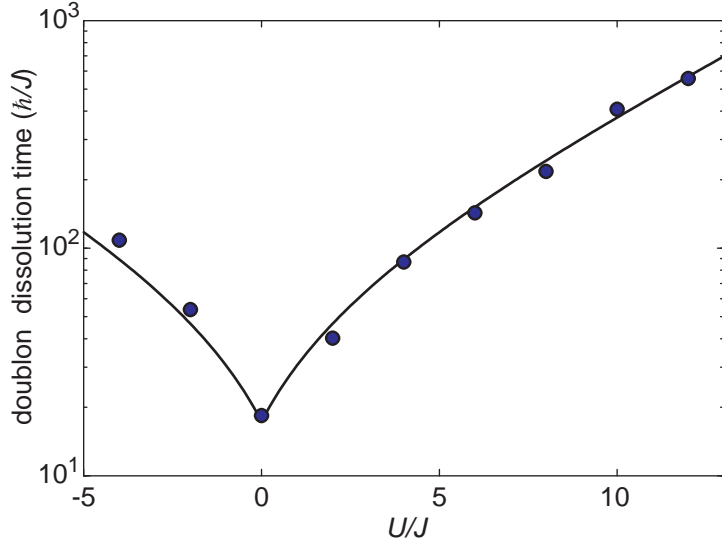


Figure 10.13.: Measured doublon dissolution time during the expansion in a $8 E_r$ deep lattice. The black lines is an exponential fit $\sim c_1 + e^{|U|/c_2}$ ($c_{1,2}$: fit parameters) and serves as a guide to the eye.

10.3.5. Width of Feshbach resonance

Compared to previous dipole trap experiments, the dynamics in the lattice are much more sensitive to small scattering lengths, since the strongly reduced kinetic energy of atoms in a lattice (cf. sec. 4.3.2) enhances the role of interactions. The observed pronounced dependence on small interactions (cf. fig. 10.11) enabled us to remeasure the zero crossing of the scattering length around the Feshbach resonance at $B_0 = 202.1 \text{ G}$ (cf. sec. 3.3.1).

The zero crossing is located at $B(a = 0) = 209.1 \pm 0.2 \text{ G}$ and, using the standard parametrization of the (free space) Feshbach resonances (cf. eqn. 3.6) this zero crossing leads to a new width of

$$w = 7.0 \pm 0.2 \text{ G} \quad (10.16)$$

compared to the previous dipole trap measurement of $w_{\text{dipole}} = 7.8 \pm 0.6 \text{ G}$ [61]. In addition to the pronounced dependence of the slope, only the expansion at the newly assigned zero crossing matches that of a single component Fermi gas under the same conditions and leads to the square shape expected for non-interacting atoms. The uncertainty of the newly assigned zero crossing is dominated by uncertainties in the magnetic field calibrations.

A precise knowledge of the scattering length is of paramount importance for the determination of the interaction parameter U in the Hubbard model and is therefore an important prerequisite for any quantitative analysis of experimental data. Furthermore, precise measurements of the various Feshbach resonances are a valuable input for the global fits of the molecular ground state potentials [40]. Due to

its high sensitivity, this method enables a fast and reliable determination of zero crossings also for other spin combinations and Feshbach resonances.

10.4. Conclusion

In this experiment the non-equilibrium dynamics of interacting and non-interacting fermions in an optical lattice was studied. In particular the possibility of full real-time control of most relevant parameters was used to implement a *quantum quench*, that is a sudden change of the hamiltonian. By monitoring the in-situ density distribution of an expanding cloud of initially localized atoms in a homogeneous Hubbard model, the crossover from a ballistic expansion at small densities or vanishing interactions to diffusive, hydrodynamic expansion in the interacting case could be observed.

Even small interactions lead to a drastic reduction of the expansion velocity of the atomic cloud and change the shape of the expanding cloud from a square in the non-interacting case to the sum of a large spherical symmetric core and a small square background. For strong interactions the core width shrinks instead of expanding.

The feedback between the diffusive and ballistic parts of the cloud controls the expansion: the diffusive core slowly emits ballistic particles which in turn hold the diffusive part of the cloud together and regularize the otherwise singular diffusion in the tails. We observed identical behaviour for both attractive and repulsive interactions, highlighting the high symmetry of the (tight-binding) dispersion relation in the Hubbard model.

The surprisingly large timescales of mass transport in an interacting Hubbard model set lower limits on the timescales needed both to adiabatically load the atoms into the lattice and to cool the system in the lattice [270]. They are therefore of paramount importance for all attempts to create complex, strongly correlated many-body states like Néel-ordered states in these systems.

The method of directly measuring the expansion velocity can be generalized in a straightforward way to more complex quantum states including metallic and Mott-insulating states in the repulsive Hubbard model (cf. sec. 8) or the pseudo-gap regime in the attractive Hubbard model (cf. sec. 9). Furthermore it can be extended to bosonic quantum gases, where the transition from a superfluid to a Mott-insulator can be investigated, and to Bose-Fermi mixtures [271]. In addition, the effects of various disorder potentials on the two-dimensional dynamics can be studied.

11. Challenges

Despite the progress made during the last years in the field, part of which is reported in this thesis, several important challenges remain on the way to the preparation and detection of even lower entropy states in the fermionic Hubbard model: The main challenge is the necessity to prepare states with lower entropy densities, i.e. the need to develop and implement new cooling or entropy management methods.

An important step in this direction is the analysis and suppression of the various technical heating rates.

In addition, a better understanding of the dynamics and characteristic timescales of inhomogeneous Hubbard models is needed. These two points are essential for the development of new preparation and cooling schemes, as any experimental sequence needs to be optimized to minimize the combined effects of non-adiabaticities and technical heating.

Last but not least new detection methods will be required in order to fully characterize the many-body states.

11.1. Cooling and entropy management

In order to approach the ground states of the fermionic Hubbard model, the entropy densities need to be further reduced. The critical entropy densities for antiferromagnetically ordered states in the repulsive Hubbard model, or superfluid states in the attractive case, lie approximately a factor of two (cf. sec. 5.5.2 ff.) below the currently achieved entropy densities of $S/N = \log(2) k_B$ in the fermionic Mott insulator¹ (cf. fig. 8.5). This reduction can in principle be achieved in two ways: Either by cooling, i.e. by reducing the average entropy per particle, or by entropy management, that is by optimizing the entropy distribution among the atoms.

It remains doubtful whether lower entropy samples can be realized by optimizing the evaporative cooling in the dipole trap prior to the loading into the lattice. The collision rate, and thereby the cooling power, decreases and ultimately vanishes for lower temperatures due to the effect of Pauli blocking (cf. sec. 3.2.2). In addition, in the dipole trap setup used so far, a lower trap depth is connected to a lower trap frequency, which leads to a lower density.

¹In the Mott insulator the entropy density, i.e. the entropy per lattice site, and the entropy per atom are identical.

11. Challenges

There have been several proposals on how to utilize the lattice in the cooling process: One idea relies on transferring the entropy onto a second species that is subjected to a different lattice [149, 272, 273]. In the presence of a BEC in a weakly confining lattice, the creation of a highly compressed band-insulator leads to a high net entropy flow from the fermions to the BEC, which could subsequently be evaporated away [273]. In the case of a Rb-K system, however, the needed potentials would result in strong technical heating due to the small detunings necessary to achieve the needed selectivity.

Further ideas include using Raman sideband cooling [274] or implementing filtering operations on states with high initial densities [275].

An alternative possibility is to create lower entropy regions in the lattice by applying *entropy management*: Due to the combination of the optical lattice with an additional trapping potential not only the density distribution, but also the entropy distribution becomes inhomogeneous. As was shown in chapter 5.4.2, the entropy capacity per atom diverges in the low density limit and the entropy is dominantly stored in the outer low density parts of the cloud (cf. sec. 8.2.1).

Using optimized trapping potentials that go beyond a simple harmonic trap, it is possible to further enhance the effect of the low density parts, and thereby to significantly reduce the entropy density in the high density regions [270, 276]. If the potential is tailored such that a large part of the atoms sits in a low density shell, these atoms could carry most of the entropy and thereby enable low temperatures also in the high density part. The reduction in entropy density achievable through this scheme should be sufficient to reach magnetic order in the Mott insulator or superfluid states in the attractive Hubbard model.

This method requires a slow enough loading in order to facilitate the entropy transfer from the high density to the low density regions, but it requires no further change of parameters in the lattice. It is similar to the highly successful “dimple trick” already applied in the loading of dipole traps [45]. Alternatively, the loading procedure could be tailored such that some particles are excited into higher bands, where their average entropy would again be large. In addition the trapping potential could also be changed dynamically in the lattice, thereby providing additional cooling [276] during any further preparation steps.

As the low density (high entropy) areas are located near the edge of the cloud, it would also be possible to evaporatively cool the ensemble in the lattice by selectively removing the outer atoms using either resonant light at moderate spatial resolution or by employing e.g. microwave addressing in the presence of magnetic field gradients [277, 278]. Another possible route would be the introduction of a repulsive barrier between the inner and the outer parts of the cloud. This barrier could then be used to separate the low entropy from the high entropy region [270]. These methods, however, create an intermediate out-of-equilibrium state that subsequently needs to reequilibrate and therefore is affected by technical heating during the sequence and the reequilibration.

While several methods hold the potential for global cooling, i.e. for lowering the

average entropy per particle, they also represent severe additional challenges. Not only do they require additional microwave and light fields, which introduce additional heating sources, they furthermore are based on a reequilibration within the lattice. This includes mass and entropy redistribution and will lead to rather long timescales, which in turn amplify the accumulated heating. Therefore, the best route for the reduction of entropy density needed to achieve superfluidity and magnetic ordering at the moment seems to be the use of entropy management, i.e. optimized potentials.

11.2. Heating rates

The practical limitation of all cooling techniques is given by the various heating processes: These constantly generate entropy and limit the final temperatures to a value set by an equilibrium between heating and cooling.

Relevant heating mechanisms in the dipole trap include fermionic hole heating [279] due to collisions with background gas atoms and three body collisions as well as light assisted collisions and spontaneous photon scattering due to the dipole laser. In addition, all kinds of technical noise on e.g. the magnetic fields or the frequency, power, and pointing of the dipole laser lead to further technical heating.

In the optical lattice, most heating rates will increase due to the increased density of the sample and the presence of the additional lattice light. In the current experiment, the dominant heating process in the lattice seems to be given by pair losses on doubly occupied sites due to light assisted collision (cf. sec. 3.4, 9.6, A).

11.3. Dynamics

All preparation schemes for ultracold atoms, including all cooling methods as well as all loading procedures for the optical lattice, require suitable timescales. They must not only be performed fast compared to the technical heating discussed above, but at the same time they need to be slow enough to ensure adiabaticity and thermalization.

A thorough understanding of the dynamics is therefore required in order to find the optimal sequences. There exists, however, no theoretical tools that can model time-dependent problems in the two or three dimensional fermionic Hubbard model.

Up to now, all experiments rely on the preparation of a low entropy sample in thermal equilibrium in an harmonic trap. The sample is subsequently loaded into the lattice and all comparisons with theoretical calculations assume adiabatic loading, i.e. they assume that the final state in the lattice is a thermal state whose total entropy equals the initial entropy prior to the loading (cf. sec. 2.2.3).

11. Challenges

The amount of heating during the lattice ramp is typically monitored by measuring the total entropy increase after reversing the loading sequence (cf. sec. 8.5, 9.5 and [70, 229]). While this gives an upper bound on technical heating, it is insufficient to determine the many-body state in the lattice, as it is by no means clear whether the final state in the lattice is a thermal state in global equilibrium or not! Recent experiments have in fact shown surprisingly long time scales for mass transport (cf. sec. 10 and [247]) and the relaxation of excess doublons [228]. An additional complication arises due to unwanted reflections of the dipole trap laser from the inside of the glass cell. These lead to a second, incommensurable standing wave that acts as a quasi-disorder potential [242], which could hinder mass transport.

Especially in future experiments aimed at realizing more complex many-body states involving long-range order, e.g. antiferromagnetic order, even longer time scales can be expected due to the lower energy scales.

In addition, a dynamical model is required to analyze experiments on dynamical properties of the Hubbard model, e.g. the expansion experiments presented in the previous chapter. This is a fascinating subject by itself and especially the study of transport properties of mass, spin, and energy or entropy will be a rich field in the future, reaching far beyond being a mere necessity for the preparation of interesting equilibrium states.

11.4. Detection

In addition to the preparation of more complex many-body states in the lattice, the reliable detection of these states presents a challenge as well. In the case of the repulsive Fermi-Hubbard model, many observables have been identified that can be used to detect antiferromagnetic order. These include the use of superlattices to directly measure the staggered magnetization (cf. the PhD thesis of Stefan Trotzky), the use of noise correlation methods to detect the doubling of the unit cell (cf. sec. 6.2), the increase in doublon fraction [280], Bragg scattering [281] and many more [282, 283]. The detection will be complicated by the fact that, in practice, the staggered magnetization will always point in a direction perpendicular to the quantization axis and therefore cannot be detected by a method that can just distinguish the bare hyperfine states [284]. The noise correlation and superlattice methods, however, do not suffer from this problem. A further challenge for the detection stems from the requirement that the measurement must be fast compared to the magnetic dephasing times. In addition, only a fraction of the system will be in the desired quantum state, while the remaining atoms form a metallic shell, thereby diluting the desired signal.

In the case of the attractive Hubbard model on the other hand, much less work has been devoted to finding the best observables in order to observe fermionic superfluidity in the lattice. In dipole traps, the most common method relies on the projection of Cooper pairs onto bound molecules by means of a fast magnetic

11.4. Detection

sweep across the Feshbach resonance [45]. While the center-of-mass momentum of the pair remains unaffected in free space, the vanishing pair hopping in the BEC limit of the attractive Hubbard model ($J_{\text{pair}} \propto J^2/|U|$, cf. sec. 5.5.3) will lead to a localization of these pairs. Superfluid correlations should, however, again show up in noise correlation measurements, especially in the correlations between the different spin components [200].

The ultimate tool will be the use of recently demonstrated imaging techniques with single site resolution [13–19] in combination with single site spin operations and various correlation techniques. Once adapted to the fermionic case, they are in principle capable of measuring the full quantum states of the atoms in the lattice, similar to what is routinely performed for ions [285] and photons [286].

12. Conclusion & Outlook

The main topic of this thesis has been the realization of the Fermi-Hubbard model using spin mixtures of ultracold ^{40}K in optical lattices. By use of a Feshbach resonance and a blue-detuned lattice it was possible to implement the Hubbard model with an independent control over all relevant parameters.

This created the possibility to study several equilibrium phases of both the repulsive and the attractive Hubbard model as well as out-of-equilibrium dynamics in these systems.

To this end, in-situ density measurements, which were implemented using phase-contrast imaging, and measurements of the doublon fraction were performed.

By measuring the global compressibility and the doublon fraction of repulsively interacting fermionic atoms in an optical lattice it was possible to explore different regimes of the repulsive Fermi-Hubbard model and to directly identify compressible metallic states and Mott-/band-insulating states by measuring the cloud size and the global compressibility. This constitutes one of the first realizations of a fermionic Mott insulator using ultracold atoms. By comparing clouds at constant average density, the suppressed doublon fraction at strong interactions directly signaled the entrance into the strongly-correlated regime.

In a second experiment it could be shown how pair formation in a fermionic Hubbard model with attractive interactions gives rise to an anomalous expansion of the gas as the attraction increases. The consequences of pairing in the first band of a lattice potential are fundamentally different from the consequences of pairing in the continuum. The realization of the so-called pseudogap or preformed pair regime, where bound pairs have formed but did not condense, is an important step towards the experimental study of fermionic superfluidity in the attractive Hubbard model. The fact that the observed minimum in cloud size appears for interactions much smaller than the position of the BEC-BCS crossover hints towards a many-body origin of the pairing, as predicted by the Cooper instability.

In a third experiment, the free expansion of a cloud of initially localized atoms in a homogeneous Hubbard model has been studied. This experiment utilized the real-time control over most relevant parameters and demonstrates the possibility to implement quantum quenches and to study the resulting non-equilibrium dynamics in these systems. By monitoring the in-situ density distribution during the expansion, a crossover from a ballistic expansion at small densities or vanishing interactions to a hydrodynamic expansion in the interacting case could be observed. Even small interactions lead to a drastic reduction of the expansion velocity of the atomic cloud and finally, for strong interactions, the core width of the

12. Conclusion & Outlook

atomic cloud shrinks instead of expanding. Surprisingly, only the magnitude but not the sign of the interaction matters: the dynamics is identical for repulsive and attractive interactions, highlighting the high symmetry of the dispersion relation in the Hubbard model.

Although the experiments were performed at entropies per particle on the order of $S/N = (\log(3) - \log(4))k_B$, lower entropy states could be reached in parts of the system, as the combination of lattice and harmonic trap leads to a substantial entropy redistribution.

In addition, the performed studies also revealed the remaining challenges on the way to experimental studies of superfluidity and quantum magnetism in these systems. The dominant heating processes in the lattice seem to be light-assisted collisions, which have been studied extensively (cf. sec. A) and will be further analyzed in the future.

The surprisingly large timescales of mass transport in an interacting Hubbard model set lower limits on the timescales needed both to adiabatically load the atoms into the lattice and to cool the system in the lattice. They are therefore of paramount importance for all attempts to create complex, strongly correlated many-body states like Néel-ordered states in these systems.

12.1. Outlook

In addition to the extension of the current work to lower entropies, there are many important experiments that still remain to be done using already available technology and already demonstrated entropy densities. In the equilibrium case these include a study of the effects of spin imbalance in the various regimes as well as an extension of the developed measurement schemes to the case of a fermionic three component system, i.e. a mixtures of three hyperfine states. In addition these new diagnostics will also be used to study various Bose-Fermi mixtures.

In the repulsive case, the study of the ternary Mott insulator [181] with one atom per lattice site seems especially promising, since in this case three body losses are suppressed. This system approximately realize a Heisenberg spin model with $SU(3)$ symmetry [234] and an enhanced entropy capacity of $S/N = \log(3)k_B$, compared to $S/N = \log(2)k_B$ in the binary case. For a broken $SU(3)$ symmetry, i.e. different interaction strengths between the three components, even more complex states are expected, including color selective and paired Mott insulator states [235, 236].

In the attractive case, we plan to extend our studies to the spin imbalanced case, where even richer ground state phase diagrams with additional phases like the FFLO phase are predicted [148, 171–173].

The method of directly measuring the expansion velocity can be generalized in a straightforward way to more complex quantum states including metallic and

12.1. Outlook

Mott-insulating states in the repulsive Hubbard model (c.f. 8) or the pseudogap regime in the attractive Hubbard model (c.f. 9). Furthermore it can be extended to bosonic quantum gases, where the transition from a superfluid to a Mott-insulator can be investigated, and to Bose-Fermi mixtures [271], where polaronic physics can be studied. In addition, the effects of various disorder potentials on the two-dimensional dynamics can be studied.

Major goals for the future include the observation of superfluidity in the attractive Hubbard model and antiferromagnetic order in the repulsive Hubbard model. To this end, several technical enhancements are currently implemented during the rebuilding of the setup after the move to Munich. They include a new dipole trap setup, better magnetic field control, an improved laser system and an enhanced optical access and should enable the preparation of larger and colder clouds. These can serve as a starting point for analyzing the various heating mechanisms and implementing new entropy management methods.

In a second experimental setup, which is currently under construction, we plan to extend all of the above measurements into the crossover regime between 2D and 3D and to implement superlattice structures.

A. Photo dissociation

In this appendix, photodissociation measurements of $^{40}\text{K}_2$ Feshbach molecules are presented together with a qualitative interpretation. A detailed quantitative analysis, however, is still missing. The photodissociation of Feshbach molecules in the presence of blue-detuned light was studied with two applications in mind:

One important technical goal was to find wavelengths where the photodissociation rate is minimal, as for these wavelengths also heating rates due to light assisted collisions in the lattice are minimal. This is due to the fact that for blue-detuned light photodissociation of a molecule and a light assisted collision of a pair of atoms are essentially the same process. In both cases one of the atoms absorbs a photon and the pair of atoms is excited into a repulsive molecular potential where subsequently a fraction of the photon detuning is converted into kinetic energy (c.f. 3.4).

The typical distance of two atoms on the same lattice site is on the order of the harmonic oscillator length of the on-site wavefunction, which is in the blue detuned case around $55 - 70 \text{ nm} \approx 1100 - 1400 a_0$. This is comparable to the size of a Feshbach molecule close to resonance, which is on the order of half the scattering length $\langle r \rangle \approx a/2 \approx 70 \text{ nm}$ @201.6 G (c.f. 3.3.2). In the range of large detunings $\Delta \gg 10 \text{ nm}$ used for optical lattices, the Condon point lies within the van der Waals potential (c.f. 3.1). At these distances, the wave function is completely governed by the molecular potential, i.e. it is identical for atoms forming a Feshbach molecule and atoms on the same lattice site.

The second motivation for this experiment stems from molecular physics: Provided the repulsive excited state molecular potentials are known precisely, it should be possible to infer the position of the nodes of the Feshbach molecule wavefunction from the dissociation spectra. In the simplest approximation the excitation takes place only at the Condon point, where the energy difference between the molecular potentials equals the photon energy (c.f. 3.4). Consequently, the Franck-Condon factor is proportional to the square of the ground state wave function at this point. In this picture, a minimum in the excitation rate directly corresponds to a node in the molecular wavefunction. In reality, however, there are several further complications:

- There exist in total four excited state molecular potential with dipole allowed transitions to the ground state potentials
- In some of these potentials there exists more than one Condon point

A. Photo dissociation

- For large detunings the above approximation breaks down and the Franck-Condon factor becomes more complex.

In addition, it is not clear at presence whether the excited potentials are known accurately enough for such a direct mapping. In a complete analysis, this photodissociation data should be used together with the position of the Feshbach resonances and the numerous photoassociation data in a global fit for the molecular potentials, similar to the method used in [40, 287].

A.1. Experimental sequence

These measurements were performed in pure dipole trap without a lattice. An equal mixture of the ($|F, m_F\rangle$) $|9/2, -9/2\rangle$ and $|9/2, -7/2\rangle$ hyperfine states was cooled to $T/T_F \approx 0.3$ at a magnetic field of $B \approx 219$ G, which corresponds to weak repulsive interactions above the Feshbach resonance located at $B = 202.1$ G

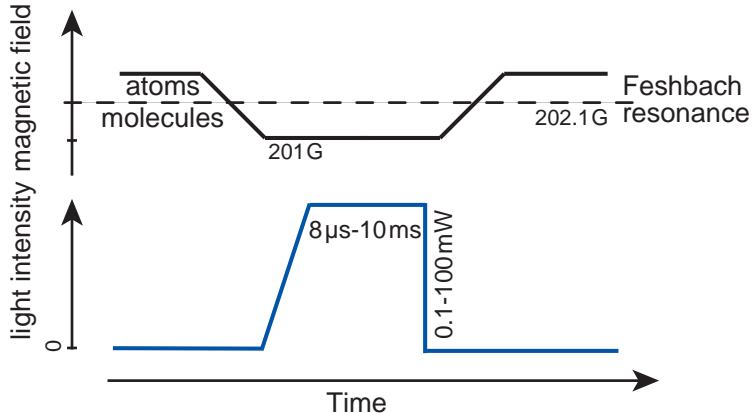


Figure A.1.: Feshbach molecules are produced with an adiabatic magnetic field ramp over the Feshbach resonance at 202.1G and after a hold time get dissociated by a second ramp in the opposite direction. During this (constant) hold time a light pulse of variable wavelength, intensity and duration can photodissociate the molecules.

Then about 60% of the atoms were converted into Feshbach molecules using an adiabatic ramp of the magnetic field down to 201 G. After a short hold time (≤ 10 ms) the molecules were converted back into atoms by a second magnetic field ramp and the atom number was measured using standard time-of-flight imaging. By applying a blue-detuned light pulse during the hold time between the two magnetic field sweeps, a fraction of the molecules was photodissociated.

In this sequence, the detected atom number consists of two parts: Atoms that were not converted into molecules by the first magnetic sweep (atomic background), and molecules that were dissociated by the second magnetic sweep. Due to their

A.2. Experimental results

high kinetic energy, atoms stemming from photodissociated molecules leave the trap immediately and are detected as a reduction of the final atom number. In addition, the atomic background was measured directly by skipping the second magnetic field ramp, since molecules remain invisible on absorption images taken with light resonant on the atomic transition.

A.2. Experimental results

A.2.1. Varying the dissociation wavelength

The main measurement in this experiment is the effect of the wavelength on the dissociation rate. As measuring the dissociation rate for every wavelength would be very time consuming, instead scans of the remaining atom number were taken for constant ramps, timings and intensities: Only the wavelength of the dissociation laser (a cw Ti:Sa) was varied. Every point in the following curves corresponds to an individual run of the experiment.

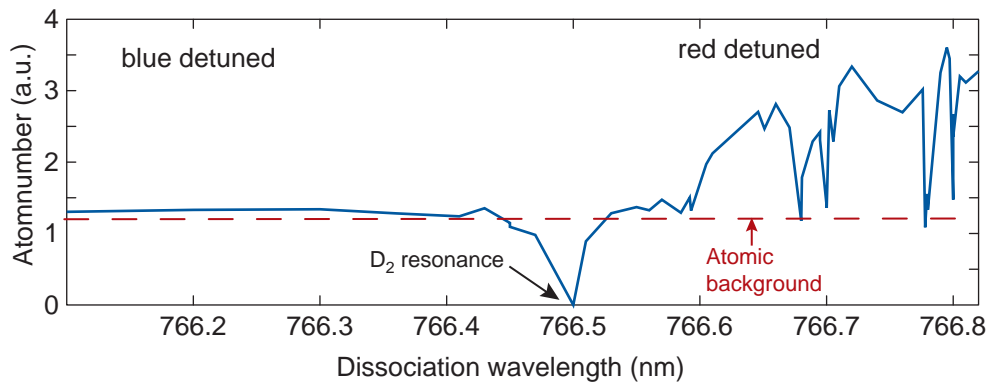


Figure A.2.: Final atom number after the experimental sequence described above. The intensity and duration of the photodissociation pulse were constant; only the wavelength was varied around the atomic D_2 transition at 766.5 nm (766.7 nm vacuum wavelength)

The behaviour of the remaining atom number around the atomic resonance is depicted in Figure A.2 and shows a completely different behaviour for red- and blue-detuned light: On the blue-detuned side ($\lambda < 766.5\text{nm}$) all molecules were photodissociated and only the atomic background was measured. On the atomic D_2 resonance both molecules and atoms leave the trap. In the red-detuned case on the other hand, most molecules survive already for modest detunings of 0.2 nm, except on narrow bound-bound resonances, where the Feshbach molecules are excited into excited molecular states. There should be many more of these narrow resonances, but only a few were hit during this rather coarse scan.

For larger detunings on the blue-detuned side, the photodissociation rate decreases non-monotonically, exhibiting a rather strong oscillating behaviour, as can be seen

A. Photo dissociation

in figure A.3. A maximum in the observed atom number corresponds to a minimum in the photodissociation rate, which is proportional to the Franck-Condon factor. As the photodissociation in the blue detuned case is a bound-free transition into a continuum of states, the Franck-Condon factor will mostly depend on the absolute value of the bound state wavefunction at the Condon point. In this simple picture every maximum corresponds to a node of the Feshbach molecule wavefunction.

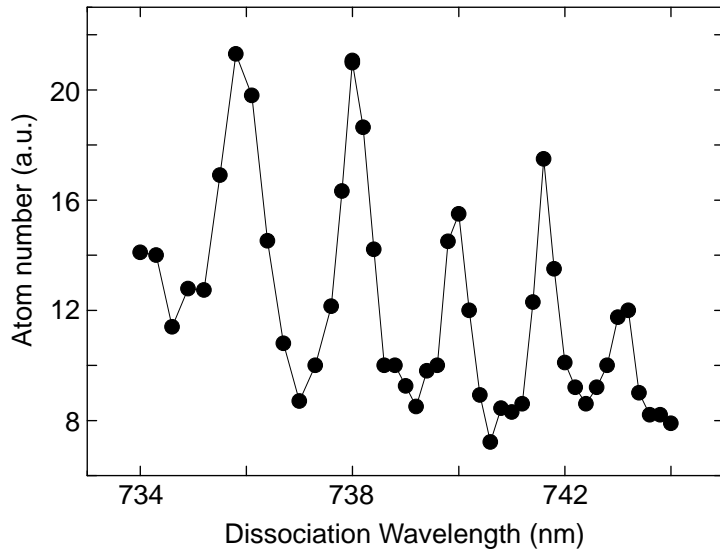


Figure A.3.: A single scan taken on the blue-detuned side of the atomic D_2 resonance at constant magnetic field, intensity and pulse duration, which shows the oscillatory behaviors of the photodissociation rate. Based on this measurement, a wavelength of 738 nm was chosen for the final optical lattice setup.

On top of the oscillatory behaviour the photodissociation rate strongly decreases for increasing detuning. In order to extend the above measurement to a larger wavelength range, several scans were taken with different intensities and pulse duration. The combined results of this measurements are shown in figure A.4, displaying in total almost thirty minima of the photodissociation rate. This would allow in principle the determination of equally many node positions of the Feshbach wavefunction.

A.2.2. Dissociation rate

In order to extract the global scaling of the photodissociation rate Γ_{dis} with detuning, the lifetime τ of the Feshbach molecules in the presence of blue-detuned light with intensity I was measured for several detunings. Since the photodissociation rate is proportional to the intensity of the light, the intensity in every measurement was chosen such that the resulting lifetime ($\tau < 10$ ms) was short compared to the lifetime without any light $\tau_{bg} \approx 26$ ms @ 201 G, which is given

A.2. Experimental results

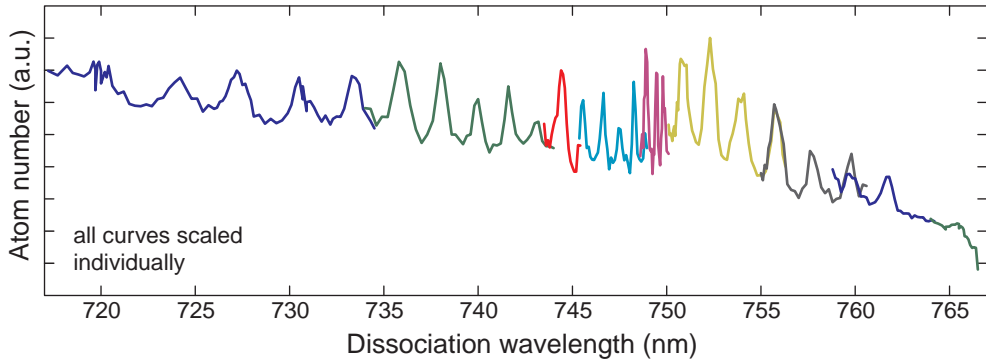


Figure A.4.: Combined data of several scans spanning in total 45 nm on the blue-detuned side of the atomic resonance, taken in steps of 0.05–0.15 nm. Almost 30 maxima were found. The graph is created out of nine individual scans which were taken for different pulse durations and intensities and subsequently were rescaled and displaced vertically in order to produce a continuous curve. The wavelengths were not scaled or shifted!

by collisions. We checked that the number of molecules decays exponentially as a function of pulse duration at constant intensity, and as a function of intensity at constant pulse length.

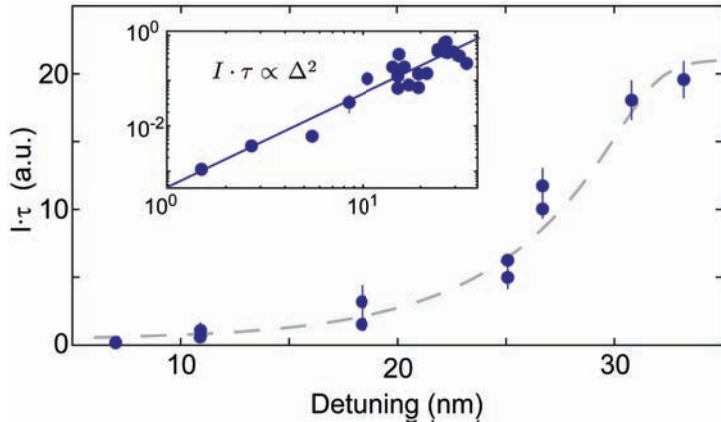


Figure A.5.: The main graph shows the product $I \cdot \tau$ taken at several maxima of figure A.4. This data cannot be fitted by a parabola, a power law fit would suggest $\sim 1/\Delta^3$ and the dashed line is a guide to the eye. The inset shows another measurement of $I \cdot \tau$ for various randomly chosen wavelengths in a log-log plot. This data is compatible with a $1/\Delta^2$ scaling of the photodissociation rate.

In Figure A.5 the resulting product $I \cdot \tau$ is plotted for various measurements. While the data for randomly chosen detunings would be compatible with a $1/\Delta^2$ behaviour, a second measurement performed at several minima of the photodissociation rate displays deviations from the above power for large detunings. Such a deviation is to be expected, since for small distances the molecular potentials deviate from their long distance power-law behaviour and eventually become non-monotonic (c.f. Figure 3.1). This can also be seen in Figure A.6, where the

A. Photo dissociation

distance between subsequent minima in the photodissociation rate is plotted. The pronounced minimum around 750 nm could mean that more than one upper potential is involved or may correspond to a turning point of the upper potential. The measured position at 750 nm would however be inconsistent with the calculated potentials of O. Dulieu, which are shown in figure 3.1.

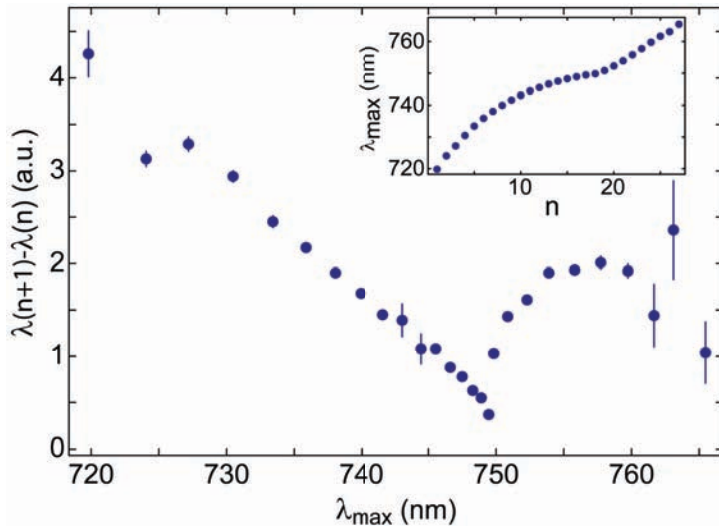


Figure A.6.: The main graph shows the distance from one observed peak to the next, the inset shows the peak positions. The pronounced minimum around 750 nm could mean that more than one upper potential is involved or may correspond to a turning point of the upper potential.

A.2.3. Influence of the magnetic field

In Figure A.7, a detailed scan of the photodissociation rate around the minimum at 738 nm is shown for two different values of the magnetic field and shows that the position of the minimum is independent of the magnetic field, illustrating that the shape of the molecular wavefunction (i.e. the position of the nodes) in the inner part of the molecular potential does not depend on the (kHz scale) variation of the molecular binding energy. Even though the magnetic field has no influence on the positions of the minima, it has a profound effect on the absolute scale of the photodissociation rate. As is shown in Figure A.8, the photodissociation rate decreases by a factor of two upon changing the magnetic field from $B = 201$ G to $B = 201.6$ G.

This decrease in the photodissociation rate with respect to magnetic field can be understood by considering the molecular wavefunction, which is plotted in figure 3.5 in the main text: On approaching the Feshbach resonance, the outermost maximum in the open channel will extend to larger and larger distances, giving rise to the halo character of the molecular wavefunction. Even though the form of the wave function in the inner part does not change, its amplitude will decrease due to normalization. This results in a reduced Frank-Condon factor and leads to a reduced photodissociation rate.

A.2. Experimental results

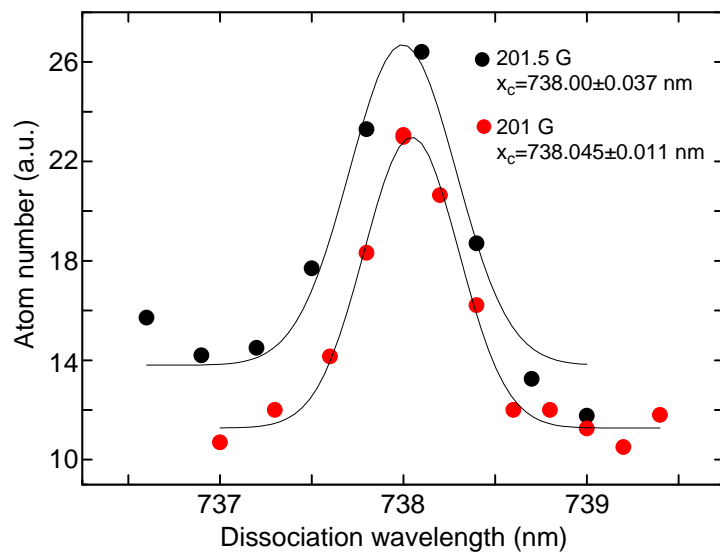


Figure A.7.: Two scans for two different magnetic fields with all other parameters being identical.

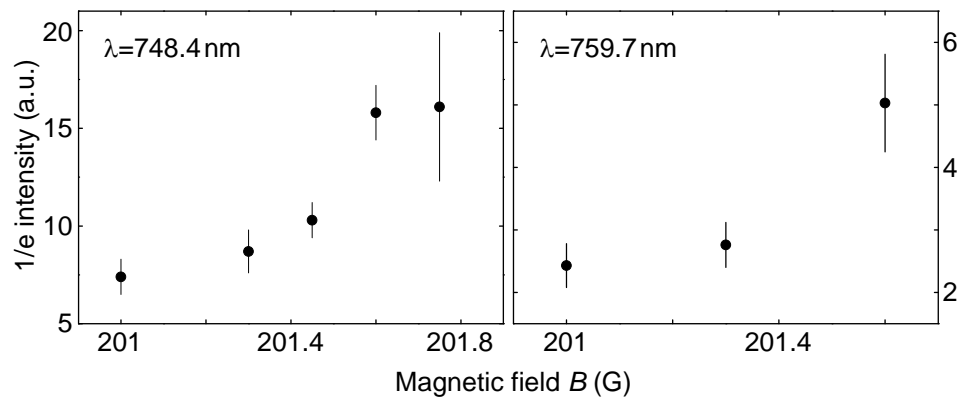


Figure A.8.: Measured $1/e$ -intensities of the number of molecules for a constant pulse duration as a function of the magnetic field. The photodissociation rate decreases for both wavelengths by a factor of two when going from $B = 201$ G to $B = 201.6$ G.

B. Dynamical U vs. -U symmetry

In this appendix the dynamical symmetry theorem, which was found during the analysis of the expansion data shown in chapter 10, is presented in some detail together with an analytical proof. The analysis was performed in collaboration with A.Rosch, E. Demler and M. Moreno-Cardoner.

We consider a coherent dynamical evolution arising from two Hubbard-type hamiltonians that differ only in the sign of the interaction term:

$$\hat{\mathcal{H}}_{\pm} = -J \sum_{\langle ij \rangle \sigma} \hat{c}_{i\sigma}^{\dagger} \hat{c}_{j\sigma} \pm U \sum_i \hat{n}_{i\uparrow} \hat{n}_{i\downarrow} \quad (\text{B.1})$$

In order to state and proof the desired theorem we first introduce two operators, the π -boost operator B_Q and the time reversal operator R_t .

Boost operator The π -boost operator \hat{B}_Q , which translates all quasi-momenta by $Q = (\pi/d, \pi/d, \pi/d)$, is a linear self-adjoint operator ($\hat{B}_Q^2 = 1$) and is given in second quantization notation by:

$$\hat{B}_Q \hat{c}_q^{\dagger} \hat{B}_Q = \hat{c}_{q+Q}^{\dagger} \quad (\text{B.2})$$

Here \hat{c}_q^{\dagger} denotes the creation operator for the Bloch wave with quasi-momentum q . From the definition of a Wannier state (cf. eqn. 4.12)

$$\hat{c}_r^{\dagger} = \frac{1}{\sqrt{N}} \sum_q e^{-iqr} \hat{c}_q^{\dagger} \quad (\text{B.3})$$

we get

$$\begin{aligned} \hat{B}_Q \hat{c}_r^{\dagger} \hat{B}_Q &= \frac{1}{\sqrt{N}} \sum_q e^{-iqr} \hat{B}_Q \hat{c}_q^{\dagger} \hat{B}_Q = \frac{1}{\sqrt{N}} \sum_q e^{-iqr} \hat{c}_{q+Q}^{\dagger} \\ &= \frac{e^{iQr}}{\sqrt{N}} \sum_q e^{-i(q+Q)r} \hat{c}_{q+Q}^{\dagger} = \frac{e^{iQr}}{\sqrt{N}} \sum_{q'} e^{-iq'r} \hat{c}_{q'}^{\dagger} \\ &= e^{iQr} \hat{c}_r^{\dagger} \end{aligned} \quad (\text{B.4})$$

The Boost operator assigns an additional position-dependent phase e^{iQr} to every Wannier state. As a consequence, applying the boost operator to a coherent superposition of Wannier states changes the relative phase between the components:

$$\hat{B}_Q (\hat{c}_r^{\dagger} + \hat{c}_{r'}^{\dagger}) \hat{B}_Q \propto (\hat{c}_r^{\dagger} + e^{iQ(r'-r)} \hat{c}_{r'}^{\dagger}) \quad (\text{B.5})$$

B. Dynamical U vs. $-U$ symmetry

Time reversal operator The time reversal operator \hat{R}_t is an anti-linear operator that obeys $\hat{R}_t z = z^* \hat{R}_t$, $z \in \mathbb{C}$ and $\hat{R}_t \hat{R}_t^\dagger = 1$. Its effect on a Bloch wave is to negate the quasi-momentum:

$$\hat{R}_t \hat{c}_q^\dagger \hat{R}_t^\dagger = \hat{c}_{-q}^\dagger \quad (\text{B.6})$$

This means for a Wannier state:

$$\begin{aligned} \hat{R}_t \hat{c}_r^\dagger \hat{R}_t^\dagger &= \frac{1}{\sqrt{N}} \sum_q \hat{R}_t e^{-iqr} \hat{c}_q^\dagger \hat{R}_t^\dagger = \frac{1}{\sqrt{N}} \sum_q e^{+iqr} \hat{R}_t \hat{c}_q^\dagger \hat{R}_t^\dagger \\ &= \frac{1}{\sqrt{N}} \sum_q e^{+iqr} \hat{c}_{-q}^\dagger = \frac{1}{\sqrt{N}} \sum_{q'} e^{-iq'r} \hat{c}_{q'}^\dagger \\ &= \hat{c}_r^\dagger \end{aligned} \quad (\text{B.7})$$

Note the complex conjugation in the prefactor at the second equal sign, which is due to the anti-linear nature of the operator.

A Wannier state is invariant under time reversal.

Applying the time reversal operator turns the wavefunction into its complex conjugate [288] or, equivalently, modifies the time evolution operator:

$$\hat{R}_t e^{-i\hat{\mathcal{H}}t} \hat{R}_t^\dagger = e^{i\hat{\mathcal{H}}t} \quad (\text{B.8})$$

The theorem

If the experimentally measured quantity \hat{O} is invariant under both time reversal and π -boost, and the initial state $|\Psi_0\rangle$ is time reversal invariant and only acquires a global phase factor under the boost transformation ($\hat{B}_Q |\Psi_0\rangle = e^{i\chi} |\Psi_0\rangle$, $\chi \in \mathbb{R}$), then the observed time evolutions

$$\langle \hat{O}(t) \rangle_\pm = \langle \Psi_0 | e^{i\hat{\mathcal{H}}\pm t} \hat{O} e^{-i\hat{\mathcal{H}}\pm t} | \Psi_0 \rangle \quad (\text{B.9})$$

are identical: $\langle \hat{O}(t) \rangle_+ = \langle \hat{O}(t) \rangle_-$.

In order to proof the above symmetry theorem we first observe that

$$\begin{aligned} \langle \hat{O}(t) \rangle_+ &= \langle \Psi_0 | \hat{R}_t^\dagger \hat{R}_t e^{i\hat{\mathcal{H}}_+ t} \hat{R}_t^\dagger \hat{R}_t \hat{O} \hat{R}_t^\dagger \hat{R}_t e^{-i\hat{\mathcal{H}}_+ t} \hat{R}_t^\dagger \hat{R}_t | \Psi_0 \rangle \\ &= \langle \Psi_0 | e^{-i\hat{\mathcal{H}}_+ t} \hat{O} e^{i\hat{\mathcal{H}}_+ t} | \Psi_0 \rangle \end{aligned} \quad (\text{B.10})$$

The last equation follows from the definition of time reversal invariance, $\hat{R}_t |\Psi_0\rangle = |\Psi_0\rangle$ and $\hat{R}_t \hat{O} \hat{R}_t^\dagger = \hat{O}$, and from the unitarity property $\hat{R}_t^\dagger \hat{R}_t = 1$. Note that equation (B.10) corresponds to the symmetry of time evolutions for $\hat{\mathcal{H}} \rightarrow -\hat{\mathcal{H}}$.

From the definition of the π -boost we get:

$$\begin{aligned}
\hat{B}_Q \hat{\mathcal{H}}_{\pm} \hat{B}_Q &= -J \sum_{\langle ij \rangle \sigma} \hat{B}_Q \hat{c}_{i\sigma}^\dagger \hat{B}_Q^2 \hat{c}_{j\sigma} \hat{B}_Q \pm U \sum_i \hat{B}_Q \hat{n}_{i\uparrow} \hat{B}_Q^2 \hat{n}_{i\downarrow} \hat{B}_Q \\
&= +J \sum_{\langle ij \rangle \sigma} \hat{c}_{i\sigma}^\dagger \hat{c}_{j\sigma} \pm U \sum_i \hat{n}_{i\uparrow} \hat{n}_{i\downarrow} \\
&= -\hat{\mathcal{H}}_{\mp}
\end{aligned} \tag{B.11}$$

Here we used the unitarity of the boost operator $\hat{B}_Q^2 = 1$ and the transformation behaviour of the density operator $\hat{B}_Q \hat{n}_{i\uparrow} \hat{B}_Q = \hat{B}_Q \hat{c}_{i\uparrow}^\dagger \hat{B}_Q^2 \hat{c}_{i\uparrow} \hat{B}_Q = \hat{n}_{i\uparrow}$. With this we can continue equation (B.10):

$$\begin{aligned}
\langle \hat{O}(t) \rangle_+ &= \langle \Psi_0 | \hat{B}_Q^2 e^{-i\hat{\mathcal{H}}_+ t} \hat{B}_Q^2 \hat{O} \hat{B}_Q^2 e^{i\hat{\mathcal{H}}_+ t} \hat{B}_Q^2 | \Psi_0 \rangle \\
&= \langle \Psi_0 | \hat{B}_Q e^{+i\hat{\mathcal{H}}_- t} \hat{O} e^{-i\hat{\mathcal{H}}_- t} \hat{B}_Q | \Psi_0 \rangle \\
&= \langle \Psi_0 | e^{-i\chi} e^{+i\hat{\mathcal{H}}_- t} \hat{O} e^{-i\hat{\mathcal{H}}_- t} e^{i\chi} | \Psi_0 \rangle \\
&= \langle \hat{O}(t) \rangle_- e^{-i\chi} e^{i\chi} \\
&= \langle \hat{O}(t) \rangle_-
\end{aligned} \tag{B.12}$$

In the last equation we used the π -boost invariance of the observable $\hat{B}_Q \hat{O} \hat{B}_Q = \hat{O}$, the required transformation behavior of the initial state $\hat{B}_Q |\Psi_0\rangle = e^{i\chi} |\Psi_0\rangle$, and the unitarity of the boost operator $\hat{B}_Q^2 = 1$.

Initial state

The many-body state given in the experiment can be written as an incoherent mixture of states of the form:

$$|\Psi_{mb}\rangle = \prod_{i=1}^n \hat{c}_{r_i}^\dagger |vac\rangle \tag{B.13}$$

This state describes n particles localized at the positions r_i and transforms under \hat{B}_Q according to:

$$\begin{aligned}
\hat{B}_Q |\Psi_{mb}\rangle &= \hat{B}_Q \prod_{i=1}^n \hat{c}_{r_i}^\dagger |vac\rangle \\
&= \hat{B}_Q \hat{c}_{r_1}^\dagger \hat{B}_Q^2 \hat{c}_{r_2}^\dagger \hat{B}_Q^2 \hat{c}_{r_3}^\dagger \hat{B}_Q^2 \cdots \hat{c}_{r_n}^\dagger \hat{B}_Q^2 |vac\rangle \\
&= e^{iQr_1} \hat{c}_{r_1}^\dagger e^{iQr_2} \hat{c}_{r_2}^\dagger e^{iQr_3} \hat{c}_{r_3}^\dagger \cdots e^{iQr_n} \hat{c}_{r_n}^\dagger |vac\rangle \\
&= \prod_i e^{iQr_i} |\Psi_{mb}\rangle \\
&= e^{iQ \sum_i r_i} |\Psi_{mb}\rangle
\end{aligned} \tag{B.14}$$

B. Dynamical U vs. $-U$ symmetry

On the second line we used $\hat{B}_Q^2 = 1$ and on the third line we used $\hat{B}_Q |\text{vac}\rangle = |\text{vac}\rangle$.

An according calculation with \hat{R}_t results in $\hat{R}_t |\Psi\rangle = |\Psi\rangle$. This shows that a many-body state of the form of eqn. B.13 fulfills the requirements of the above symmetry theorem. The extension to the mixed state used in the experiment is straightforward. Due to the definition of a general density matrix $\rho = \sum_j p_j |\Psi_j\rangle\langle\Psi_j|$ we get:

$$\langle \hat{O} \rangle_\rho = \text{tr}[\rho \hat{O}] = \sum_j p_j \langle \Psi_j | \hat{O} | \Psi_j \rangle \quad (\text{B.15})$$

and see that the theorem also holds for mixed states, as it holds for every term in the sum.

The experimental observable is the density distribution $\hat{n}(r_j) = \sum_\sigma \hat{c}_{j\sigma}^\dagger \hat{c}_{j\sigma}$ and the initial state consists of atoms that are completely localized to individual lattice sites (cf. sec. 10.1). Because both the initial state and the measured operator fulfill the requirements of the symmetry theorem, we are guaranteed to find the described $U \leftrightarrow -U$ symmetry in the dynamics for all interaction strengths.

Since the bi-partite character of the lattice is crucial to the proof of the theorem, this symmetry can be expected to be broken in lattices without the bi-partite structure, such as a triangular lattice.

C. Poly-logarithmic functions

A class of useful functions are the poly-logarithmic functions which appear in the analytic solution of the following common integrals:

$$\int_0^\infty \epsilon^n F(\epsilon) d\epsilon = -(k_b T)^{1+n} \Gamma(1+n) \text{Li}_{1+n}(-Z) \quad (\text{C.1})$$

Here $\text{Li}_n(z)$ denotes the poly-logarithm of order n and Γ is the Euler gamma function. The poly-logarithms can be calculated using the following power series

$$\text{Li}_n(-z) = \sum_{k=1}^{\infty} \frac{(-z)^k}{k^n} \quad (\text{C.2})$$

which converges for all complex numbers with $|z| \leq 1$.

In the case of the dilogarithm an arbitrary argument can be mapped into the unit circle using the following reflection identity [289]:

$$\text{Li}_2(x) = -\text{Li}_2\left(\frac{1}{x}\right) - \frac{\pi^2}{6} - \frac{1}{2}(\log(-x))^2 \quad (\text{C.3})$$

Bibliography

- [1] M. H. Anderson, J. R. Ensher, M. R. Matthews, C. E. Wieman, and E. A. Cornell. *Observation of Bose-Einstein Condensation in a Dilute Atomic Vapor*. *Science* **269**, 198–201 (1995).
- [2] K. B. Davis, M. O. Mewes, M. R. Andrews, N. J. van Druten, D. S. Durfee, D. M. Kurn, and W. Ketterle. *Bose-Einstein Condensation in a Gas of Sodium Atoms*. *Phys. Rev. Lett.* **75**, 3969–3973 (1995).
- [3] B. DeMarco and D. S. Jin. *Onset of Fermi Degeneracy in a Trapped Atomic Gas*. *Science* **285**, 1703–1706 (1999).
- [4] M. Greiner, O. Mandel, T. Esslinger, T. W. Hansch, and I. Bloch. *Quantum phase transition from a superfluid to a Mott insulator in a gas of ultracold atoms*. *Nature* **415**, 39–44 (2002).
- [5] M. P. A. Fisher, P. B. Weichman, G. Grinstein, and D. S. Fisher. *Boson localization and the superfluid-insulator transition*. *Phys. Rev. B* **40**, 546–570 (1989).
- [6] D. Jaksch, C. Bruder, J. I. Cirac, C. W. Gardiner, and P. Zoller. *Cold Bosonic Atoms in Optical Lattices*. *Phys. Rev. Lett.* **81**, 3108–3111 (1998).
- [7] I. Bloch, J. Dalibard, and W. Zwerger. *Many-body physics with ultracold gases*. *Rev. Mod. Phys.* **80**, 885 (2008).
- [8] R. P. Feynman. *Simulating physics with computers*. *International Journal of Theoretical Physics* **21**, 467–488 (1982).
- [9] S. Yamada, T. Imamura, and M. Machida. *16.447 TFlops and 159-Billion-dimensional Exact-diagonalization for Trapped Fermion-Hubbard Model on the Earth Simulator*. Proceedings of Supercomputing 2005 (2005). <http://sc05.supercomputing.org/schedule/pdf/pap188.pdf>.
- [10] T. Rom, T. Best, O. Mandel, A. Widera, M. Greiner, T. W. Hänsch, and I. Bloch. *State Selective Production of Molecules in Optical Lattices*. *Phys. Rev. Lett.* **93**, 73002 (2004).
- [11] K.-K. Ni, S. Ospelkaus, M. H. G. de Miranda, A. Pe'er, B. Neyenhuis, J. J. Zirbel, S. Kotochigova, P. S. Julienne, D. S. Jin, and J. Ye. *A High Phase-Space-Density Gas of Polar Molecules*. *Science* **322**, 231–235 (2008).

Bibliography

- [12] J. G. Danzl, E. Haller, M. Gustavsson, M. J. Mark, R. Hart, N. Bouloufa, O. Dulieu, H. Ritsch, and H.-C. Nagerl. *Quantum Gas of Deeply Bound Ground State Molecules*. *Science* **321**, 1062–1066 (2008).
- [13] K. D. Nelson, X. Li, and D. S. Weiss. *Imaging single atoms in a three-dimensional array*. *Nature Physics* **3**, 556–560 (2007).
- [14] T. Gericke, P. Wuertz, D. Reitz, T. Langen, and H. Ott. *High-resolution scanning electron microscopy of an ultracold quantum gas*. *Nature Physics* **4**, 949–953 (2008).
- [15] M. Karski, L. Förster, J. Choi, W. Alt, A. Widera, and D. Meschede. *Nearest-Neighbor Detection of Atoms in a 1D Optical Lattice by Fluorescence Imaging*. *Phys. Rev. Lett.* **102**, 53001 (2009).
- [16] W. S. Bakr, J. I. Gillen, A. Peng, S. Foelling, and M. Greiner. *A quantum gas microscope for detecting single atoms in a Hubbard-regime optical lattice*. *Nature* **462**, 74–77 (2009).
- [17] P. Würtz, T. Langen, T. Gericke, A. Koglbauer, and H. Ott. *Experimental Demonstration of Single-Site Addressability in a Two-Dimensional Optical Lattice*. *Phys. Rev. Lett.* **103**, 80404 (2009).
- [18] W. S. Bakr, A. Peng, M. E. Tai, R. Ma, J. Simon, J. I. Gillen, S. Fölling, L. Pollet, and M. Greiner. *Probing the Superfluid-to-Mott-Insulator Transition at the Single-Atom Level*. *Science* **329**, 547–550 (2010).
- [19] J. F. Sherson, C. Weitenberg, M. Endres, M. Cheneau, I. Bloch, and S. Kuhr. *Single-atom-resolved fluorescence imaging of an atomic Mott insulator*. *Nature* **467**, 68–72 (2010).
- [20] J. M. Leinaas and J. Myrheim. *On the theory of identical particles*. *Il Nuovo Cimento B* **37**, 1–23 (1977).
- [21] F. Wilczek. *Quantum Mechanics of Fractional-Spin Particles*. *Phys. Rev. Lett.* **49**, 957–959 (1982).
- [22] C. Hermann. *Statistical Physics*. Springer, New York (2005).
- [23] W. Pauli. *The Connection Between Spin and Statistics*. *Phys. Rev.* **58**, 716–722 (1940).
- [24] A. J. Leggett. *Quantum Liquid*. Oxford University Press (2006).
- [25] A. Einstein. *Quantentheorie des einatomigen idealen Gases*. Sitzungsber. Preuss. Akad. Wiss. **23**, 1–14 (1925).
- [26] S. N. Bose. *Plancks Gesetz und Lichtquantenhypothese*. *Zeitschrift für Physik* **26**, 178–181 (1924).

Bibliography

- [27] M. Gustavsson, E. Haller, M. J. Mark, J. G. Danzl, G. Rojas-Kopeinig, and H.-C. Nägerl. *Control of Interaction-Induced Dephasing of Bloch Oscillations*. *Phys. Rev. Lett.* **100**, 80404 (2008).
- [28] M. Fattori, C. D'Errico, G. Roati, M. Zaccanti, M. Jona-Lasinio, M. Modugno, M. Inguscio, and G. Modugno. *Atom Interferometry with a Weakly Interacting Bose-Einstein Condensate*. *Phys. Rev. Lett.* **100**, 80405 (2008).
- [29] H. Ibach and H. Lüth. *Festkörperphysik*. Springer, Berlin (2002).
- [30] K. Huang. *Statistical mechanics*. Wiley, New York (1987).
- [31] M. Köhl. *Thermometry of fermionic atoms in an optical lattice*. *Phys. Rev. A* **73**, 31601 (2006).
- [32] D. A. Butts and D. S. Rokhsar. *Trapped Fermi gases*. *Phys. Rev. A* **55**, 4346–4350 (1997).
- [33] B. Demarco. *Quantum Behavior of an Atomic Fermi Gas*. University of Colorado (2001).
- [34] G. Bruun and C. Clark. *Ideal gases in time-dependent traps*. *Phys. Rev. A* **61**, 61601 (2000).
- [35] W. Ketterle, D. S. Durfee, and D. M. Stamper-Kurn. *Making, probing and understanding Bose-Einstein condensates*. arXiv:cond-mat/9904034v2 (1999). <http://arxiv.org/abs/cond-mat/9904034>.
- [36] K. Levenberg. *A Method for the Solution of Certain Problems in Least Squares*. *Quart. Appl. Math.* **2**, 164–168 (1944).
- [37] D. Marquardt. *An Algorithm for Least-Squares Estimation of Nonlinear Parameters*. *SIAM J. Appl. Math.* **11**, 431–441 (1963).
- [38] L. P. Pitaevskii and S. Stringari. *Bose-Einstein Condensation*. Oxford University Press (2003).
- [39] W. Demtröder. *Atoms, Molecules and Photons*. Springer, Berlin (2006).
- [40] S. Falke, H. Knöckel, J. Friebel, M. Riedmann, E. Tiemann, and C. Lisdat. *Potassium ground-state scattering parameters and Born-Oppenheimer potentials from molecular spectroscopy*. *Phys. Rev. A* **78**, 12503 (2008).
- [41] K. M. Jones, E. Tiesinga, P. D. Lett, and P. S. Julienne. *Ultracold photoassociation spectroscopy: Long-range molecules and atomic scattering*. *Rev. Mod. Phys.* **78**, 483 (2006).
- [42] C. Chin, R. Grimm, P. Julienne, and E. Tiesinga. *Feshbach resonances in ultracold gases*. *Rev. Mod. Phys.* **82**, 1225–1286 (2010).
- [43] J. Weiner, V. S. Bagnato, S. Zilio, and P. S. Julienne. *Experiments and theory in cold and ultracold collisions*. *Rev. Mod. Phys.* **71**, 1–85 (1999).

Bibliography

- [44] J. Stuhler, A. Griesmaier, T. Koch, M. Fattori, T. Pfau, S. Giovanazzi, P. Pedri, and L. Santos. *Observation of Dipole-Dipole Interaction in a Degenerate Quantum Gas*. *Phys. Rev. Lett.* **95**, 150406 (2005).
- [45] M. Inguscio, W. Ketterle, and C. Salomon, editors. *Ultra-cold Fermi Gases, Proceedings of the International School Of Physics Enrico Fermi*. IOS Press, Amsterdam (2007).
- [46] B. DeMarco, S. B. Papp, and D. S. Jin. *Pauli Blocking of Collisions in a Quantum Degenerate Atomic Fermi Gas*. *Phys. Rev. Lett.* **86**, 5409–5412 (2001).
- [47] B. DeMarco, J. L. Bohn, J. P. Burke, M. Holland, and D. S. Jin. *Measurement of p-Wave Threshold Law Using Evaporatively Cooled Fermionic Atoms*. *Phys. Rev. Lett.* **82**, 4208–4211 (1999).
- [48] T. Köhler, K. Góral, and P. S. Julienne. *Production of cold molecules via magnetically tunable Feshbach resonances*. *Rev. Mod. Phys.* **78**, 1311 (2006).
- [49] U. Fano. *Effects of Configuration Interaction on Intensities and Phase Shifts*. *Phys. Rev.* **124**, 1866–1878 (1961).
- [50] H. Feshbach. *Unified theory of nuclear reactions*. *Annals of Physics* **5**, 357–390 (1958).
- [51] W. C. Stwalley. *Stability of Spin-Aligned Hydrogen at Low Temperatures and High Magnetic Fields: New Field-Dependent Scattering Resonances and Predissociations*. *Phys. Rev. Lett.* **37**, 1628–1631 (1976).
- [52] E. Tiesinga, B. J. Verhaar, and H. T. C. Stoof. *Threshold and resonance phenomena in ultracold ground-state collisions*. *Phys. Rev. A* **47**, 4114–4122 (1993).
- [53] K. Góral, T. Köhler, S. A. Gardiner, E. Tiesinga, and P. S. Julienne. *Adiabatic association of ultracold molecules via magnetic-field tunable interactions*. *J. Phys. B: At. Mol. Opt. Phys.* **37**, 3457–3500 (2004).
- [54] A. J. Moerdijk, B. J. Verhaar, and A. Axelsson. *Resonances in ultracold collisions of Li₆, Li₇, and Na₂₃*. *Phys. Rev. A* **51**, 4852–4861 (1995).
- [55] S. Inouye, M. R. Andrews, J. Stenger, H.-J. Miesner, D. M. Stamper-Kurn, and W. Ketterle. *Stability of Spin-Aligned Hydrogen at Low Temperatures and High Magnetic Fields: New Field-Dependent Scattering Resonances and Predissociations*. *Nature* **392**, 151–154 (1998).
- [56] P. Courteille, R. S. Freeland, D. J. Heinzen, F. A. van Abeelen, and B. J. Verhaar. *Observation of a Feshbach Resonance in Cold Atom Scattering*. *Phys. Rev. Lett.* **81**, 69–72 (1998).

Bibliography

- [57] J. L. Roberts, N. R. Claussen, J. P. Burke, C. H. Greene, E. A. Cornell, and C. E. Wieman. *Resonant Magnetic Field Control of Elastic Scattering in Cold R85b*. *Phys. Rev. Lett.* **81**, 5109–5112 (1998).
- [58] V. Vuletić, A. J. Kerman, C. Chin, and S. Chu. *Observation of Low-Field Feshbach Resonances in Collisions of Cesium Atoms*. *Phys. Rev. Lett.* **82**, 1406–1409 (1999).
- [59] J. L. Bohn. *Cooper pairing in ultracold 40K using Feshbach resonances*. *Phys. Rev. A* **61**, 53409 (2000).
- [60] T. Loftus, C. A. Regal, C. Ticknor, J. L. Bohn, and D. S. Jin. *Resonant Control of Elastic Collisions in an Optically Trapped Fermi Gas of Atoms*. *Phys. Rev. Lett.* **88**, 173201 (2002).
- [61] C. Regal. *Experimental realization of BCS-BEC crossover physics with a Fermi gas of atoms*. PhD-Thesis, University of Colorado (2006).
- [62] M. Köhl, H. Moritz, T. Stöferle, K. Günter, and T. Esslinger. *Fermionic Atoms in a Three Dimensional Optical Lattice: Observing Fermi Surfaces, Dynamics, and Interactions*. *Phys. Rev. Lett.* **94**, 80403 (2005).
- [63] K. Günter, T. Stöferle, H. Moritz, M. Köhl, and T. Esslinger. *p-Wave Interactions in Low-Dimensional Fermionic Gases*. *Phys. Rev. Lett.* **95**, 230401 (2005).
- [64] C. A. Regal, C. Ticknor, J. L. Bohn, and D. S. Jin. *Tuning p-Wave Interactions in an Ultracold Fermi Gas of Atoms*. *Phys. Rev. Lett.* **90**, 53201 (2003).
- [65] C. A. Regal, M. Greiner, and D. S. Jin. *Observation of Resonance Condensation of Fermionic Atom Pairs*. *Phys. Rev. Lett.* **92**, 40403 (2004).
- [66] T. Stöferle, H. Moritz, K. Günter, M. Köhl, and T. Esslinger. *Molecules of Fermionic Atoms in an Optical Lattice*. *Phys. Rev. Lett.* **96**, 30401 (2006).
- [67] H. Moritz, T. Stöferle, K. Günter, M. Köhl, and T. Esslinger. *Confinement Induced Molecules in a 1D Fermi Gas*. *Phys. Rev. Lett.* **94**, 210401 (2005).
- [68] N. Strohmaier, Y. Takasu, K. Günter, R. Jordens, M. Köhl, H. Moritz, and T. Esslinger. *Interaction-Controlled Transport of an Ultracold Fermi Gas*. *Phys. Rev. Lett.* **99**, 220601 (2007).
- [69] C. A. Regal and D. S. Jin. *Measurement of Positive and Negative Scattering Lengths in a Fermi Gas of Atoms*. *Phys. Rev. Lett.* **90**, 230404 (2003).
- [70] R. Jordens, N. Strohmaier, K. Gunter, H. Moritz, and T. Esslinger. *A Mott insulator of fermionic atoms in an optical lattice*. *Nature* **455**, 204–207 (2008).
- [71] C. Ticknor, C. A. Regal, D. S. Jin, and J. L. Bohn. *Multiplet structure of Feshbach resonances in nonzero partial waves*. *Phys. Rev. A* **69**, 42712 (2004).

Bibliography

- [72] T. Köhler, T. Gasenzer, P. S. Julienne, and K. Burnett. *Long-Range Nature of Feshbach Molecules in Bose-Einstein Condensates*. *Phys. Rev. Lett.* **91**, 230401 (2003).
- [73] C. A. Regal, C. Ticknor, J. L. Bohn, and D. S. Jin. *Creation of ultracold molecules from a Fermi gas of atoms*. *Nature* **424**, 47–50 (2003).
- [74] K. E. Strecker, G. B. Partridge, and R. G. Hulet. *Conversion of an Atomic Fermi Gas to a Long-Lived Molecular Bose Gas*. *Phys. Rev. Lett.* **91**, 80406 (2003).
- [75] J. Cubizolles, T. Bourdel, S. J. J. M. F. Kokkelmans, G. V. Shlyapnikov, and C. Salomon. *Production of Long-Lived Ultracold Li₂ Molecules from a Fermi Gas*. *Phys. Rev. Lett.* **91**, 240401 (2003).
- [76] E. Hodby, S. T. Thompson, C. A. Regal, M. Greiner, A. C. Wilson, D. S. Jin, E. A. Cornell, and C. E. Wieman. *Production Efficiency of Ultracold Feshbach Molecules in Bosonic and Fermionic Systems*. *Phys. Rev. Lett.* **94**, 120402 (2005).
- [77] S. Jochim, M. Bartenstein, A. Altmeyer, G. Hendl, C. Chin, J. H. Denschlag, and R. Grimm. *Pure Gas of Optically Trapped Molecules Created from Fermionic Atoms*. *Phys. Rev. Lett.* **91**, 240402 (2003).
- [78] J. Stenger, S. Inouye, M. R. Andrews, H.-J. Miesner, D. M. Stamper-Kurn, and W. Ketterle. *Strongly Enhanced Inelastic Collisions in a Bose-Einstein Condensate near Feshbach Resonances*. *Phys. Rev. Lett.* **82**, 2422–2425 (1999).
- [79] S. L. Cornish, N. R. Claussen, J. L. Roberts, E. A. Cornell, and C. E. Wieman. *Stable 85Rb Bose-Einstein Condensates with Widely Tunable Interactions*. *Phys. Rev. Lett.* **85**, 1795–1798 (2000).
- [80] S. Dürr, T. Volz, A. Marte, and G. Rempe. *Observation of Molecules Produced from a Bose-Einstein Condensate*. *Phys. Rev. Lett.* **92**, 20406 (2004).
- [81] D. S. Petrov. *Three-body problem in Fermi gases with short-range interparticle interaction*. *Phys. Rev. A* **67**, 10703 (2003).
- [82] D. S. Petrov, C. Salomon, and G. V. Shlyapnikov. *Weakly Bound Dimers of Fermionic Atoms*. *Phys. Rev. Lett.* **93**, 90404 (2004).
- [83] C. A. Regal, M. Greiner, and D. S. Jin. *Lifetime of Molecule-Atom Mixtures near a Feshbach Resonance in K40*. *Phys. Rev. Lett.* **92**, 83201 (2004).
- [84] G. Thalhammer, K. Winkler, F. Lang, S. Schmid, R. Grimm, and J. H. Denschlag. *Long-Lived Feshbach Molecules in a Three-Dimensional Optical Lattice*. *Phys. Rev. Lett.* **96**, 50402 (2006).
- [85] J. Bardeen, L. N. Cooper, and J. R. Schrieffer. *Microscopic Theory of Superconductivity*. *Phys. Rev.* **106**, 162–164 (1957).

Bibliography

- [86] J. Bardeen, L. N. Cooper, and J. R. Schrieffer. *Theory of Superconductivity*. *Phys. Rev.* **108**, 1175–1204 (1957).
- [87] M. Greiner, C. A. Regal, and D. S. Jin. *Emergence of a molecular Bose-Einstein condensate from a Fermi gas*. *Nature* **426**, 537–540 (2003).
- [88] M. W. Zwierlein, A. Schirotzek, C. H. Schunck, and W. Ketterle. *Fermionic Superfluidity with Imbalanced Spin Populations*. *Science* **311**, 492–496 (2006).
- [89] M. W. Zwierlein, C. A. Stan, C. H. Schunck, S. M. F. Raupach, S. Gupta, Z. Hadzibabic, and W. Ketterle. *Observation of Bose-Einstein Condensation of Molecules*. *Phys. Rev. Lett.* **91**, 250401 (2003).
- [90] J. Kinast, S. L. Hemmer, M. E. Gehm, A. Turlapov, and J. E. Thomas. *Evidence for Superfluidity in a Resonantly Interacting Fermi Gas*. *Phys. Rev. Lett.* **92**, 150402 (2004).
- [91] K. M. O’Hara, S. L. Hemmer, M. E. Gehm, S. R. Granade, and J. E. Thomas. *Observation of a Strongly Interacting Degenerate Fermi Gas of Atoms*. *Science* **298**, 2179–2182 (2002).
- [92] S. Jochim, M. Bartenstein, A. Altmeyer, G. Hendl, S. Riedl, C. Chin, J. Hecker Denschlag, and R. Grimm. *Bose-Einstein Condensation of Molecules*. *Science* **302**, 2101–2103 (2003).
- [93] C. Chin, M. Bartenstein, A. Altmeyer, S. Riedl, S. Jochim, J. H. Denschlag, and R. Grimm. *Observation of the Pairing Gap in a Strongly Interacting Fermi Gas*. *Science* **305**, 1128–1130 (2004).
- [94] T. Bourdel, L. Khaykovich, J. Cubizolles, J. Zhang, F. Chevy, M. Teichmann, L. Tarruell, S. J. J. M. F. Kokkelmans, and C. Salomon. *Experimental Study of the BEC-BCS Crossover Region in Lithium 6*. *Phys. Rev. Lett.* **93**, 50401 (2004).
- [95] A. Schirotzek, C.-H. Wu, A. Sommer, and M. W. Zwierlein. *Observation of Fermi Polarons in a Tunable Fermi Liquid of Ultracold Atoms*. *Phys. Rev. Lett.* **102**, 230402 (2009).
- [96] S. Nascimbène, N. Navon, K. J. Jiang, L. Tarruell, M. Teichmann, J. McKeever, F. Chevy, and C. Salomon. *Collective Oscillations of an Imbalanced Fermi Gas: Axial Compression Modes and Polaron Effective Mass*. *Phys. Rev. Lett.* **103**, 170402 (2009).
- [97] P. S. Julienne. *Cold Binary Atomic Collisions in a Light Field*. *J. Res. Natl. Inst. Stand. Technol.* **101**, 487 (1996).
- [98] K. Burnett, P. S. Julienne, and K.-A. Suominen. *Laser-Driven Collisions between Atoms in a Bose-Einstein Condensed Gas*. *Phys. Rev. Lett.* **77**, 1416–1419 (1996).

Bibliography

- [99] V. Vuletić, C. Chin, A. J. Kerman, and S. Chu. *Suppression of Atomic Radiative Collisions by Tuning the Ground State Scattering Length*. *Phys. Rev. Lett.* **83**, 943–946 (1999).
- [100] W. Ketterle, K. B. Davis, M. A. Joffe, A. Martin, and D. E. Pritchard. *High densities of cold atoms in a dark spontaneous-force optical trap*. *Phys. Rev. Lett.* **70**, 2253–2256 (1993).
- [101] M. H. Anderson, W. Petrich, J. R. Ensher, and E. A. Cornell. *Reduction of light-assisted collisional loss rate from a low-pressure vapor-cell trap*. *Phys. Rev. A* **50**, R3597–R3600 (1994).
- [102] H. J. Metcalf and P. van der Straten. *Laser Cooling and Trapping*. Springer, Berlin (2002).
- [103] R. Grimm, M. Weidemuller, and Y. B. Ovchinnikov. *Optical dipole traps for neutral atoms*. *Advances in Atomic, Molecular, and Optical Physics* **42**, 95 (2000).
- [104] H. Pichler, A. J. Daley, and Z. P. *Non-equilibrium dynamics of bosonic atoms in optical lattices: Decoherence of many-body states due to spontaneous emission*. arXiv:1009.0194v1 [cond-mat.quant-gas] (2010). <http://de.arxiv.org/abs/1009.0194>.
- [105] O. Morsch and M. Oberthaler. *Dynamics of Bose-Einstein condensates in optical lattices*. *Rev. Mod. Phys.* **78**, 179 (2006).
- [106] M. Greiner. *Ultracold quantum gases in three-dimensional optical lattice potentials*. Ludwig-Maximilians-Universität, München (2003).
- [107] C. Kittel. *Introduction to Solid State Physics*. Wiley, Hoboken (2005).
- [108] N. W. Ashcroft and N. D. Mermin. *Solid State Physics*. Cengage Learning Services (1976).
- [109] T. Müller, S. Fölling, A. Widera, and I. Bloch. *State Preparation and Dynamics of Ultracold Atoms in Higher Lattice Orbitals*. *Phys. Rev. Lett.* **99**, 200405 (2007).
- [110] L. Viverit, C. Menotti, T. Calarco, and A. Smerzi. *Efficient and Robust Initialization of a Qubit Register with Fermionic Atoms*. *Phys. Rev. Lett.* **93**, 110401 (2004).
- [111] P. B. Blakie, A. Bezett, and P. Buonsante. *Degenerate Fermi gas in a combined harmonic-lattice potential*. *Phys. Rev. A* **75**, 63609 (2007).
- [112] C. Hooley and J. Quintanilla. *Single-Atom Density of States of an Optical Lattice*. *Phys. Rev. Lett.* **93**, 80404 (2004).
- [113] T. Hartmann, F. Keck, H. J. Korsch, and S. Mossmann. *Dynamics of Bloch oscillations*. *New J. Phys.* **6**, 2 (2004).

Bibliography

- [114] M. Ben Dahan, E. Peik, J. Reichel, Y. Castin, and C. Salomon. *Bloch Oscillations of Atoms in an Optical Potential*. *Phys. Rev. Lett.* **76**, 4508–4511 (1996).
- [115] H. Ott, E. de Mirandes, F. Ferlaino, G. Roati, G. Modugno, and M. Inguscio. *Collisionally Induced Transport in Periodic Potentials*. *Phys. Rev. Lett.* **92**, 160601 (2004).
- [116] W. Heisenberg. *Zur Theorie des Ferromagnetismus*. *Z. Phys.* **49**, 619–636 (1928).
- [117] J. H. de Boer and E. J. W. Verwey. *Semi-conductors with partially and with completely filled 3d-lattice bands*. *Proc. Phys. Soc.* **49**, 59–71 (1937).
- [118] N. F. Mott and R. Peierls. *Discussion of the paper by de Boer and Verwey*. *Proc. Phys. Soc.* **49**, 72–73 (1937).
- [119] N. Mott. *The Basis of the Electron Theory of Metals, with Special Reference to the Transition Metals*. *Proc. Phys. Soc. A* **62**, 416–422 (1949).
- [120] I. G. Austin and N. F. Mott. *Metallic and Nonmetallic Behavior in Transition Metal Oxides*. *Science* **168**, 71–77 (1970).
- [121] M. Imada, A. Fujimori, and Y. Tokura. *Metal-insulator transitions*. *Rev. Mod. Phys.* **70**, 1039–1263 (1998).
- [122] J. Hubbard. *Electron Correlations in Narrow Energy Bands*. *Proc. R. Soc. A.* **276**, 238–257 (1963). <http://www.jstor.org/stable/2414761>.
- [123] J. Hubbard. *Electron correlations in narrow energy-bands*. Current Contents, Citation Classics **22**, 16 (1980). <http://garfield.library.upenn.edu/classics1980/A1980JS76400001.pdf>.
- [124] J. Spalek and A. M. Oles. *No Title*. *Physica B* **375**, 86–88 (1977).
- [125] J. Spalek. *t-J model then and now: A personal perspective from the pioneering times*. *ACTA PHYSICA POLONICA A* **111**, 409 (2007). <http://arxiv.org/abs/0706.4236>.
- [126] J. G. Bednorz and K. A. Müller. *Possible highTc superconductivity in the Ba-La-Cu-O system*. *Z. Phys. B Condensed Matter* **64**, 189–193 (2001).
- [127] D. N. Basov and T. Timusk. *Electrodynamics of high- Tc superconductors*. *Rev. Mod. Phys.* **77**, 721–779 (2005).
- [128] V. Z. Kresin and S. A. Wolf. *Colloquium: Electron-lattice interaction and its impact on high T_c superconductivity*. *Rev. Mod. Phys.* **81**, 481 (2009).
- [129] P. A. Lee, N. Nagaosa, and X.-G. Wen. *Doping a Mott insulator: Physics of high-temperature superconductivity*. *Rev. Mod. Phys.* **78**, 17 (2006).

Bibliography

- [130] M. Rigol, A. Muramatsu, G. G. Batrouni, and R. T. Scalettar. *Local Quantum Criticality in Confined Fermions on Optical Lattices*. *Phys. Rev. Lett.* **91**, 130403 (2003).
- [131] U. Schneider, L. Hackermuller, S. Will, T. Best, I. Bloch, T. A. Costi, R. W. Helmes, D. Rasch, and A. Rosch. *Supporting online material for: Metallic and Insulating Phases of Repulsively Interacting Fermions in a 3D Optical Lattice*. *Science* **322**, 1520–1525 (2008).
- [132] D. Pines and P. Nozieres. *The Theory of Quantum Liquids*. Benjamin, New York (1966).
- [133] G. D. Mahan. *Many Particle Physics*, 3rd ed. Plenum, New York (2000).
- [134] M. C. Gutzwiller. *Correlation of Electrons in a Narrow s Band*. *Phys. Rev.* **137**, A1726–A1735 (1965).
- [135] P. Zanardi. *Quantum entanglement in fermionic lattices*. *Phys. Rev. A* **65**, 42101 (2002).
- [136] A. Kantian, A. J. Daley, P. Torma, and P. Zoller. *Atomic lattice excitons: from condensates to crystals*. *New J. Phys.* **9**, 407 (2007).
- [137] M. Valiente and D. Petrosyan. *Two-particle states in the Hubbard model*. *J. Phys. B: At. Mol. Opt. Phys.* **41**, 161002 (2008).
- [138] M. Wouters and G. Orso. *Two-body problem in periodic potentials*. *Phys. Rev. A* **73**, 12707 (2006).
- [139] P. Fedichev, M. Bijlsma, and P. Zoller. *Extended Molecules and Geometric Scattering Resonances in Optical Lattices*. *Phys. Rev. Lett.* **92**, 80401 (2004).
- [140] K. Winkler, G. Thalhammer, F. Lang, R. Grimm, J. Hecker Denschlag, A. J. Daley, A. Kantian, H. P. Büchler, and P. Zoller. *Repulsively bound atom pairs in an optical lattice*. *Nature* **441**, 853–856 (2006).
- [141] L. Belkhir and M. Randeria. *Collective excitations and the crossover from Cooper pairs to composite bosons in the attractive Hubbard model*. *Phys. Rev. B* **45**, 5087–5090 (1992).
- [142] J. P. Sethna, editor. *Entropy, Order Parameters, and Complexity*. Oxford University Press, New York (2006).
- [143] A. Sewer, X. Zotos, and H. Beck. *Quantum Monte Carlo study of the three-dimensional attractive Hubbard model*. *Phys. Rev. B* **66**, 140504 (2002).
- [144] M. Keller, W. Metzner, and U. Schollwöck. *Dynamical Mean-Field Theory for Pairing and Spin Gap in the Attractive Hubbard Model*. *Phys. Rev. Lett.* **86**, 4612–4615 (2001).

Bibliography

- [145] A. Toschi, P. Barone, M. Capone, and C. Castellani. *Pairing and superconductivity from weak to strong coupling in the attractive Hubbard model.* *New J. Phys.* **7**, 7 (2005).
- [146] C.-C. Chien, Q. Chen, and K. Levin. *Fermions with attractive interactions on optical lattices and implications for correlated systems.* *Phys. Rev. A* **78**, 43612 (2008).
- [147] M. Hinczewski and A. N. Berker. *Two superconducting phases in the $d=3$ Hubbard model.* *Eur. Phys. J. B* **48**, 1–17 (2005).
- [148] M. Iskin and C. A. R. S. de Melo. *Superfluid and Insulating Phases of Fermion Mixtures in Optical Lattices.* *Phys. Rev. Lett.* **99**, 80403 (2007).
- [149] W. Hofstetter, J. I. Cirac, P. Zoller, E. Demler, and M. D. Lukin. *High-Temperature Superfluidity of Fermionic Atoms in Optical Lattices.* *Phys. Rev. Lett.* **89**, 220407 (2002).
- [150] R. W. Helmes, T. A. Costi, and A. Rosch. *Mott Transition of Fermionic Atoms in a Three-Dimensional Optical Trap.* *Phys. Rev. Lett.* **100**, 56403 (2008).
- [151] M. J. Rozenberg, R. Chitra, and G. Kotliar. *Finite Temperature Mott Transition in the Hubbard Model in Infinite Dimensions.* *Phys. Rev. Lett.* **83**, 3498–3501 (1999).
- [152] R. Staudt, M. Dzierzawa, and A. Muramatsu. *Phase diagram of the three-dimensional Hubbard model at half filling.* *Eur. Phys. J. B* **17**, 411–415 (2000).
- [153] P. G. J. van Dongen. *Thermodynamics of the extended Hubbard model in high dimensions.* *Phys. Rev. Lett.* **67**, 757–760 (1991).
- [154] E. Stoner. *No Title.* *Philos. Mag.* **15**, 1018 (1933).
- [155] B. Wunsch, L. Fritz, N. T. Zinner, E. Manousakis, and E. Demler. *Magnetic structure of an imbalanced Fermi gas in an optical lattice.* *Phys. Rev. A* **81**, 13616 (2010).
- [156] S. Trotzky, P. Cheinet, S. Folling, M. Feld, U. Schnorrberger, A. M. Rey, A. Polkovnikov, E. A. Demler, M. D. Lukin, and I. Bloch. *Time-Resolved Observation and Control of Superexchange Interactions with Ultracold Atoms in Optical Lattices.* *Science* **319**, 295–299 (2008).
- [157] S. Wessel. *Critical entropy of quantum Heisenberg magnets on simple-cubic lattices.* *Phys. Rev. B* **81**, 52405 (2010).
- [158] R. Jördens, L. Tarruell, D. Greif, T. Uehlinger, N. Strohmaier, H. Moritz, T. Esslinger, L. De Leo, C. Kollath, A. Georges, V. Scarola, L. Pollet, E. Burovski, E. Kozik, and M. Troyer. *Quantitative Determination of Temperature in the Approach to Magnetic Order of Ultracold Fermions in an Optical Lattice.* *Phys. Rev. Lett.* **104**, 180401 (2010).

Bibliography

- [159] A. B. Kuklov and B. V. Svistunov. *Counterflow Superfluidity of Two-Species Ultracold Atoms in a Commensurate Optical Lattice*. *Phys. Rev. Lett.* **90**, 100401 (2003).
- [160] K. G. Wilson. *The renormalization group: Critical phenomena and the Kondo problem*. *Rev. Mod. Phys.* **47**, 773–840 (1975).
- [161] C. J. Halboth and W. Metzner. *Renormalization-group analysis of the two-dimensional Hubbard model*. *Phys. Rev. B* **61**, 7364–7377 (2000).
- [162] H. Heiselberg. *Hubbard-model calculations of phase separation in optical lattices*. *Phys. Rev. A* **79**, 63611 (2009).
- [163] F. C. Zhang. *Gossamer Superconductor, Mott Insulator, and Resonating Valence Bond State in Correlated Electron Systems*. *Phys. Rev. Lett.* **90**, 207002 (2003).
- [164] S. Onari, H. Yokoyama, and Y. Tanaka. *Phase diagram of half-filled square lattice for frustrated Hubbard model*. *Physica C* **463–465**, 120–122 (2007).
- [165] P. W. Anderson, P. A. Lee, M. Randeria, T. M. Rice, N. Trivedi, and F. C. Zhang. *The physics behind high-temperature superconducting cuprates: the ‘plain vanilla’ version of RVB*. *J. Phys.: Condens. Matter* **16**, R755–R769 (2004).
- [166] S. Trebst, U. Schollwöck, M. Troyer, and P. Zoller. *d-Wave Resonating Valence Bond States of Fermionic Atoms in Optical Lattices*. *Phys. Rev. Lett.* **96**, 250402 (2006).
- [167] S. Raghu, S. A. Kivelson, and D. J. Scalapino. *Superconductivity in the repulsive Hubbard model: An asymptotically exact weak-coupling solution*. *Phys. Rev. B* **81**, 224505 (2010).
- [168] P. Nozières and S. Schmitt-Rink. *Bose condensation in an attractive fermion gas: From weak to strong coupling superconductivity*. *Journal of Low Temperature Physics* **59**, 195–211 (1985).
- [169] A. Rosch, D. Rasch, B. Binz, and M. Vojta. *Metastable Superfluidity of Repulsive Fermionic Atoms in Optical Lattices*. *Phys. Rev. Lett.* **101**, 265301 (2008).
- [170] T. Paiva, R. Scalettar, M. Randeria, and N. Trivedi. *Fermions in 2D Optical Lattices: Temperature and Entropy Scales for Observing Antiferromagnetism and Superfluidity*. *Phys. Rev. Lett.* **104**, 66406 (2010).
- [171] T. Gottwald and P. G. J. van Dongen. *Ground state properties of an asymmetric Hubbard model for unbalanced ultracold fermionic quantum gases*. *Eur. Phys. J. B* **61**, 277–285 (2008).
- [172] M. Iskin and C. A. R. S. de Melo. *Quantum phases of Fermi-Fermi mixtures in optical lattices*. *Phys. Rev. A* **78**, 13607 (2008).

Bibliography

- [173] Y. Loh and N. Trivedi. *Large Range of Stability of Larkin-Ovchinnikov States for Imbalanced Fermi Gases in Optical Lattices.* arXiv:0907.0679v1 [cond-mat.quant-gas] (2009). <http://arxiv.org/abs/0907.0679>.
- [174] R. Micnas, J. Ranninger, and S. Robaszkiewicz. *Superconductivity in narrow-band systems with local nonretarded attractive interactions.* *Rev. Mod. Phys.* **62**, 113–171 (1990).
- [175] M. Randeria, N. Trivedi, A. Moreo, and R. T. Scalettar. *Pairing and spin gap in the normal state of short coherence length superconductors.* *Phys. Rev. Lett.* **69**, 2001–2004 (1992).
- [176] O. Fischer, M. Kugler, I. Maggio-Aprile, C. Berthod, and C. Renner. *Scanning tunneling spectroscopy of high-temperature superconductors.* *Rev. Mod. Phys.* **79**, 353–419 (2007).
- [177] J. L. Tallon and J. W. Loram. *The doping dependence of T^* - what is the real high- T_c phase diagram?* *Physica C* **349**, 53–68 (2001).
- [178] A. F. Ho, M. A. Cazalilla, and T. Giamarchi. *Quantum simulation of the Hubbard model: The attractive route.* *Phys. Rev. A* **79**, 33620 (2009).
- [179] E. H. Lieb and F. Y. Wu. *Absence of Mott Transition in an Exact Solution of the Short-Range, One-Band Model in One Dimension.* *Phys. Rev. Lett.* **20**, 1445–1448 (1968).
- [180] A. Georges, G. Kotliar, W. Krauth, and M. Rozenberg. *Dynamical mean-field theory of strongly correlated fermion systems and the limit of infinite dimensions.* *Rev. Mod. Phys.* **68**, 13 (1996).
- [181] E. V. Gorelik and N. Blümer. *Mott transitions in ternary flavor mixtures of ultracold fermions on optical lattices.* *Phys. Rev. A* **80**, 51602 (2009).
- [182] U. Schollwöck. *The density-matrix renormalization group.* *Rev. Mod. Phys.* **77**, 259–315 (2005).
- [183] M. Troyer and U.-J. Wiese. *Computational Complexity and Fundamental Limitations to Fermionic Quantum Monte Carlo Simulations.* *Phys. Rev. Lett.* **94**, 170201 (2005).
- [184] P. R. C. Kent, M. Jarrell, T. A. Maier, and T. Pruschke. *Efficient calculation of the antiferromagnetic phase diagram of the three-dimensional Hubbard model.* *Phys. Rev. B* **72**, 60411 (2005).
- [185] R. W. Helmes, T. A. Costi, and A. Rosch. *Kondo Proximity Effect: How Does a Metal Penetrate into a Mott Insulator?* *Phys. Rev. Lett.* **101**, 66802 (2008).
- [186] T. Best, S. Will, U. Schneider, L. Hackermüller, D. van Oosten, I. Bloch, and D.-S. Lühmann. *Role of Interactions in ^{87}Rb - ^{40}K Bose-Fermi Mixtures in a 3D Optical Lattice.* *Phys. Rev. Lett.* **102**, 30408 (2009).

Bibliography

- [187] D.-S. Lühmann, K. Bongs, K. Sengstock, and D. Pfannkuche. *Self-Trapping of Bosons and Fermions in Optical Lattices*. *Phys. Rev. Lett.* **101**, 50402 (2008).
- [188] S. Will, T. Best, U. Schneider, L. Hackermüller, D.-S. Lühmann, and I. Bloch. *Time-resolved observation of coherent multi-body interactions in quantum phase revivals*. *Nature* **465**, 197 (2010).
- [189] F. Werner, O. Parcollet, A. Georges, and S. R. Hassan. *Interaction-Induced Adiabatic Cooling and Antiferromagnetism of Cold Fermions in Optical Lattices*. *Phys. Rev. Lett.* **95**, 56401 (2005).
- [190] F. Gerbier, A. Widera, S. Fölling, O. Mandel, T. Gericke, and I. Bloch. *Interference pattern and visibility of a Mott insulator*. *Phys. Rev. A* **72**, 53606 (2005).
- [191] Y. Kato, Q. Zhou, N. Kawashima, and N. Trivedi. *Exploring Phase Coherence in a 2D Lattice of Bose-Einstein Condensates*. *Nat. Phys.* **4**, 617 (2008).
- [192] S. Trotzky, L. Pollet, F. Gerbier, U. Schnorrberger, I. Bloch, N. Prokof'ev, B. Svistunov, and M. Troyer. *Suppression of the critical temperature for superfluidity near the Mott transition: validating a quantum simulator*. arXiv:0905.4882v1 [cond-mat.quant-gas] (2009).
- [193] S. Fölling, F. Gerbier, A. Widera, O. Mandel, T. Gericke, and I. Bloch. *Spatial quantum noise interferometry in expanding ultracold atom clouds*. *Nature* **434**, 481–484 (2005).
- [194] T. Rom, T. Best, D. van Oosten, U. Schneider, S. Fölling, B. Paredes, and I. Bloch. *Free fermion antibunching in a degenerate atomic Fermi gas released from an optical lattice*. *Nature* **444**, 733–736 (2006).
- [195] E. Altman, E. Demler, and M. D. Lukin. *Probing many-body states of ultracold atoms via noise correlations*. *Phys. Rev. A* **70**, 13603 (2004).
- [196] G. M. Bruun, O. F. Syljuåsen, K. G. L. Pedersen, B. M. Andersen, E. Demler, and A. S. Sørensen. *Antiferromagnetic noise correlations in optical lattices*. *Phys. Rev. A* **80**, 33622 (2009).
- [197] S. Fölling. *Probing Strongly Correlated States of Ultracold Atoms in Optical Lattices*. Johannes Gutenberg-Universität, Mainz (2008).
- [198] V. W. Scarola, E. Demler, and S. D. Sarma. *Searching for a supersolid in cold-atom optical lattices*. *Phys. Rev. A* **73**, 51601 (2006).
- [199] M. Greiner, C. A. Regal, J. T. Stewart, and D. S. Jin. *Probing Pair-Correlated Fermionic Atoms through Correlations in Atom Shot Noise*. *Phys. Rev. Lett.* **94**, 110401 (2005).
- [200] T. Paananen, T. K. Koponen, P. Törmä, and J.-P. Martikainen. *Noise correlations of the ultracold Fermi gas in an optical lattice*. *Phys. Rev. A* **77**, 53602 (2008).

Bibliography

- [201] A. Turlapov, J. Kinast, B. Clancy, L. Luo, J. Joseph, and J. Thomas. *Is a Gas of Strongly Interacting Atomic Fermions a Nearly Perfect Fluid?* *J. Low. Temp. Phys.* **150**, 567–576 (2008).
- [202] A. Altmeyer, S. Riedl, C. Kohstall, M. J. Wright, R. Geursen, M. Bartenstein, C. Chin, J. H. Denschlag, and R. Grimm. *Precision Measurements of Collective Oscillations in the BEC-BCS Crossover.* *Phys. Rev. Lett.* **98**, 40401 (2007).
- [203] X.-J. Liu, P. D. Drummond, and H. Hu. *Signature of Mott-Insulator Transition with Ultracold Fermions in a One-Dimensional Optical Lattice.* *Phys. Rev. Lett.* **94**, 136406 (2005).
- [204] A. Kastberg, W. D. Phillips, S. L. Rolston, R. J. C. Spreeuw, and P. S. Jessen. *Adiabatic Cooling of Cesium to 700 nK in an Optical Lattice.* *Phys. Rev. Lett.* **74**, 1542–1545 (1995).
- [205] M. Greiner, I. Bloch, O. Mandel, T. W. Hänsch, and T. Esslinger. *Exploring Phase Coherence in a 2D Lattice of Bose-Einstein Condensates.* *Phys. Rev. Lett.* **87**, 160405 (2001).
- [206] Y. Shin, M. W. Zwierlein, C. H. Schunck, A. Schirotzek, and W. Ketterle. *Observation of Phase Separation in a Strongly Interacting Imbalanced Fermi Gas.* *Phys. Rev. Lett.* **97**, 30401 (2006).
- [207] G. Reinaudi, T. Lahaye, Z. Wang, and D. Guéry-Odelin. *Strong saturation absorption imaging of dense clouds of ultracold atoms.* *Opt. Lett.* **32**, 3143–3145 (2007).
- [208] M. T. DePue, S. L. Winoto, D. J. Han, and D. S. Weiss. *Transient compression of a MOT and high intensity fluorescent imaging of optically thick clouds of atoms.* *Opti. Commun.* **180**, 73–79 (2000).
- [209] E. Hecht. *Optics, fourth edition.* Addison Wesley, San Francisco (2002).
- [210] C. C. Bradley, C. A. Sackett, and R. G. Hulet. *Bose-Einstein Condensation of Lithium: Observation of Limited Condensate Number.* *Phys. Rev. Lett.* **78**, 985–989 (1997).
- [211] M. R. Andrews, D. M. Kurn, H.-J. Miesner, D. S. Durfee, C. G. Townsend, S. Inouye, and W. Ketterle. *Propagation of Sound in a Bose-Einstein Condensate.* *Phys. Rev. Lett.* **79**, 553–556 (1997).
- [212] C. Maurer, A. Jesacher, S. Bernet, and M. Ritsch-Marte. *Phase contrast microscopy with full numerical aperture illumination.* *Opt. Express* **16**, 19821–19829 (2008).
- [213] A. Damascelli. *Probing the Electronic Structure of Complex Systems by ARPES.* *Physica Scripta* **T109**, 61–74 (2004).

Bibliography

- [214] A. Damascelli, Z. Hussain, and Z.-X. Shen. *Angle-resolved photoemission studies of the cuprate superconductors*. *Rev. Mod. Phys.* **75**, 473–541 (2003).
- [215] C. H. Schunck, Y.-i. Shin, A. Schirotzek, and W. Ketterle. *Determination of the fermion pair size in a resonantly interacting superfluid*. *Nature* **454**, 739–743 (2008).
- [216] K. R. A. Hazzard and E. J. Mueller. *Many-body physics in the radio-frequency spectrum of lattice bosons*. *Physical Review A* **81** (2010).
- [217] G. K. Campbell, J. Mun, M. Boyd, P. Medley, A. E. Leanhardt, L. G. Marcassa, D. E. Pritchard, and W. Ketterle. *Imaging the Mott Insulator Shells by Using Atomic Clock Shifts*. *Science* **313**, 649–652 (2006).
- [218] J. T. Stewart, J. P. Gaebler, and D. S. Jin. *Using photoemission spectroscopy to probe a strongly interacting Fermi gas*. *Nature* **7205**, 744 (2008).
- [219] A. Schirotzek, Y.-i. Shin, C. H. Schunck, and W. Ketterle. *Determination of the Superfluid Gap in Atomic Fermi Gases by Quasiparticle Spectroscopy*. *Phys. Rev. Lett.* **101**, 140403 (2008).
- [220] F. Zambelli, L. Pitaevskii, D. M. Stamper-Kurn, and S. Stringari. *Dynamic structure factor and momentum distribution of a trapped Bose gas*. *Phys. Rev. A* **61**, 63608 (2000).
- [221] J. Stenger, S. Inouye, A. P. Chikkatur, D. M. Stamper-Kurn, D. E. Pritchard, and W. Ketterle. *Bragg Spectroscopy of a Bose-Einstein Condensate*. *Phys. Rev. Lett.* **82**, 4569–4573 (1999).
- [222] P. T. Ernst, S. Götze, J. S. Krauser, K. Pyka, D.-S. Lühmann, D. Pfannkuche, and K. Sengstock. *Probing superfluids in optical lattices by momentum-resolved Bragg spectroscopy*. *Nature Physics* **6**, 56–61 (2009).
- [223] T. Stöferle, H. Moritz, C. Schori, M. Köhl, and T. Esslinger. *Transition from a Strongly Interacting 1D Superfluid to a Mott Insulator*. *Phys. Rev. Lett.* **92**, 130403 (2004).
- [224] C. Kollath, A. Iucci, I. P. McCulloch, and T. Giamarchi. *Modulation spectroscopy with ultracold fermions in an optical lattice*. *Phys. Rev. A* **74**, 41604 (2006).
- [225] H. J. Metcalf and P. van der Straten. *Laser Cooling and Trapping*. Springer, Berlin (2001).
- [226] M. Greiner, I. Bloch, T. W. Hänsch, and T. Esslinger. *Magnetic transport of trapped cold atoms over a large distance*. *Phys. Rev. A* **63**, 31401 (2001).
- [227] S. Gupta, Z. Hadzibabic, M. W. Zwierlein, C. A. Stan, K. Dieckmann, C. H. Schunck, E. G. M. van Kempen, B. J. Verhaar, and W. Ketterle. *Radio-Frequency Spectroscopy of Ultracold Fermions*. *Science* **300**, 1723–1726 (2003).

Bibliography

- [228] N. Strohmaier, D. Greif, R. Jördens, L. Tarruell, H. Moritz, T. Esslinger, R. Sensarma, D. Pekker, E. Altman, and E. Demler. *Observation of Elastic Doublon Decay in the Fermi-Hubbard Model*. *Phys. Rev. Lett.* **104**, 80401 (2010).
- [229] U. Schneider, L. Hackermüller, S. Will, T. Best, I. Bloch, T. Costi, R. Helmes, D. Rasch, and A. Rosch. *Metallic and Insulating Phases of Repulsively Interacting Fermions in a 3D Optical Lattice*. *Science* **322**, 1520–1525 (2008).
- [230] I. Pomeranchuk. *On the theory of liquid He3*. *Zh. Eksp. Teor. Fiz.* **20**, 919 (1950).
- [231] R. C. Richardson. *The Pomeranchuk effect*. *Rev. Mod. Phys.* **69**, 683–690 (1997).
- [232] R. Sensarma, D. Pekker, E. Altman, E. Demler, N. Strohmaier, D. Greif, R. Jordens, L. Tarruell, H. Moritz, and T. Esslinger. *Lifetime of double occupancies in the Fermi-Hubbard model*. arXiv:1001.3881v1 [cond-mat.quant-gas] (2010). <http://arxiv.org/abs/1001.3881>.
- [233] A. Koetsier, R. A. Duine, I. Bloch, and H. T. C. Stoof. *Achieving the Néel state in an optical lattice*. *Phys. Rev. A* **77**, 23623 (2008).
- [234] M. Hermele, V. Gurarie, and A. M. Rey. *Mott Insulators of Ultracold Fermionic Alkaline Earth Atoms: Underconstrained Magnetism and Chiral Spin Liquid*. *Phys. Rev. Lett.* **103**, 135301 (2009).
- [235] S.-y. Miyatake, K. Inaba, and S.-i. Suga. *Three-component fermionic atoms with repulsive interaction in optical lattices*. *Phys. Rev. A* **81**, 21603 (2010).
- [236] K. Inaba, S.-y. Miyatake, and S.-i. Suga. *Mott Transitions of Three-Component Fermionic Atoms with Repulsive Interaction in Optical Lattices*. arXiv:1006.1685v1 [cond-mat.quant-gas] (2010). <http://arxiv.org/abs/1006.1685>.
- [237] L. Hackermüller, U. Schneider, M. Moreno-Cardoner, T. Kitagawa, T. Best, S. Will, E. Demler, E. Altman, I. Bloch, and B. Paredes. *Anomalous Expansion of Attractively Interacting Fermionic Atoms in an Optical Lattice*. *Science* **327**, 1621–1624 (2010).
- [238] W. Metzner. *Linked-cluster expansion around the atomic limit of the Hubbard model*. *Phys. Rev. B* **43**, 8549–8563 (1991).
- [239] J. A. Henderson, J. Oitmaa, and M. C. B. Ashley. *High-temperature expansion for the single-band Hubbard model*. *Phys. Rev. B* **46**, 6328–6337 (1992).
- [240] V. W. Scarola, L. Pollet, J. Oitmaa, and M. Troyer. *Discerning Incompressible and Compressible Phases of Cold Atoms in Optical Lattices*. *Phys. Rev. Lett.* **102**, 135302 (2009).

Bibliography

- [241] R. Jördens, L. Tarruell, D. Greif, T. Uehlinger, N. Strohmaier, H. Moritz, T. Esslinger, L. De Leo, C. Kollath, A. Georges, V. Scarola, L. Pollet, E. Burovski, E. Kozik, and M. Troyer. *Quantitative Determination of Temperature in the Approach to Magnetic Order of Ultracold Fermions in an Optical Lattice*. *Phys. Rev. Lett.* **104**, 180401 (2010).
- [242] G. Roati, C. D’Errico, L. Fallani, M. Fattori, C. Fort, M. Zaccanti, G. Modugno, M. Modugno, and M. Inguscio. *Anderson localization of a non-interacting Bose-Einstein condensate*. *Nature* **453**, 895 (2008).
- [243] A. W. Rost, R. S. Perry, J.-F. Mercure, A. P. Mackenzie, and S. A. Grigera. *Entropy Landscape of Phase Formation Associated with Quantum Criticality in Sr₃Ru₂O₇*. *Science* **325**, 1360–1363 (2009).
- [244] G. Moos. *Dynamics of photoexcited electrons in metals and semimetals*. Freie Universität Berlin (2003). http://www.diss.fu-berlin.de/diss/receive/FUDISS_thesis_00000000894.
- [245] T. Gericke, F. Gerbier, A. Widera, S. Foelling, O. Mandel, and I. Bloch. *Adiabatic loading of a Bose-Einstein condensate in a 3D optical lattice*. *J. Mod. Opt.* **54**, 735–743 (2007).
- [246] J. Wernsdorfer, M. Snoek, and W. Hofstetter. *Lattice-ramp-induced dynamics in an interacting Bose-Bose mixture*. *Phys. Rev. A* **81**, 43620 (2010).
- [247] C.-L. Hung, X. Zhang, N. Gemelke, and C. Chin. *Slow Mass Transport and Statistical Evolution of an Atomic Gas across the Superfluid–Mott-Insulator Transition*. *Phys. Rev. Lett.* **104**, 160403 (2010).
- [248] F. Heidrich-Meisner, S. R. Manmana, M. Rigol, A. Muramatsu, A. E. Feiguin, and E. Dagotto. *Quantum distillation: Dynamical generation of low-entropy states of strongly correlated fermions in an optical lattice*. *Phys. Rev. A* **80**, 41603 (2009).
- [249] F. Heidrich-Meisner, M. Rigol, A. Muramatsu, A. E. Feiguin, and E. Dagotto. *Ground-state reference systems for expanding correlated fermions in one dimension*. *Phys. Rev. A* **78**, 013620 (2008).
- [250] H. Lignier, C. Sias, D. Ciampini, Y. Singh, A. Zenesini, O. Morsch, and E. Arimondo. *Dynamical Control of Matter-Wave Tunneling in Periodic Potentials*. *Phys. Rev. Lett.* **99**, 220403 (2007).
- [251] C. D. Fertig, K. M. O’Hara, J. H. Huckans, S. L. Rolston, W. D. Phillips, and J. V. Porto. *Strongly Inhibited Transport of a Degenerate 1D Bose Gas in a Lattice*. *Phys. Rev. Lett.* **94**, 120403 (2005).
- [252] L. Pezzè, L. Pitaevskii, A. Smerzi, S. Stringari, G. Modugno, E. de Mirandes, F. Ferlaino, H. Ott, G. Roati, and M. Inguscio. *Insulating Behavior of a Trapped Ideal Fermi Gas*. *Phys. Rev. Lett.* **93**, 120401 (2004).

Bibliography

- [253] Y. Aharonov, L. Davidovich, and N. Zagury. *Quantum random walks*. *Phys. Rev. A* **48**, 1687–1690 (1993).
- [254] E. Farhi and S. Gutmann. *Quantum computation and decision trees*. *Phys. Rev. A* **58**, 915–928 (1998).
- [255] M. Karski, L. Forster, J.-M. Choi, A. Steffen, W. Alt, D. Meschede, and A. Widera. *Quantum Walk in Position Space with Single Optically Trapped Atoms*. *Science* **325**, 174–177 (2009).
- [256] A. Childs, R. Cleve, E. Deotto, E. Farhi, S. Gutmann, and D. Spielman. *Exponential algorithmic speedup by a quantum walk*. In *STOC ’03: Proceedings of the thirty-fifth annual ACM symposium on Theory of computing*, pages 59–68, New York, NY, USA (2003). ACM. ISBN 1-58113-674-9.
- [257] M. Rigol, V. Dunjko, and M. Olshanii. *Thermalization and its mechanism for generic isolated quantum systems*. *Nature* **452**, 854 (2008).
- [258] M. Eckstein, M. Kollar, and P. Werner. *Thermalization after an Interaction Quench in the Hubbard Model*. *Phys. Rev. Lett.* **103**, 56403 (2009).
- [259] J. L. Vázquez. *Smoothing and Decay Estimates for Nonlinear Diffusion Equations*. Oxford University Press, Oxford (2006).
- [260] U. Schneider, L. Hackermüller, J. Ronzheimer, S. Will, S. Braun, T. Best, I. Bloch, E. Demler, S. Mandt, D. Rasch, and A. Rosch. *Breakdown of diffusion: From collisional hydrodynamics to a continuous quantum walk in a homogeneous Hubbard model*. arXiv:1005.3545v1 [cond-mat.quant-gas] (2010). <http://arxiv.org/abs/1005.3545>.
- [261] U. Schneider, L. Hackermüller, J. Ronzheimer, S. Will, S. Braun, T. Best, I. Bloch, E. Demler, S. Mandt, D. Rasch, and A. Rosch. *Supplementary material for: Breakdown of diffusion: From collisional hydrodynamics to a continuous quantum walk in a homogeneous Hubbard model*. arXiv:1005.3545v1 [cond-mat.quant-gas] (2010). <http://arxiv.org/abs/1005.3545>.
- [262] P. Daskalopoulos and M. A. Del Pino. *On a singular diffusion equation*. *Comm. Analysis and Geometry* **3**, 523 (1995).
- [263] R. S. Hamilton. *The Ricci Flow on Surface*. *Contemporary Math.* **71**, 237 (1988).
- [264] G. Perelman. *Finite extinction time for the solutions to the Ricci flow on certain three-manifolds*. arXiv:math/0307245 (2003). <http://arxiv.org/abs/math/0307245>.
- [265] O. Romero-Isart, K. Eckert, C. Rodo, and A. Sanpera. *Transport and entanglement generation in the Bose-Hubbard model*. *J. Phys. A: Math. Theor.* **40**, 8019–8031 (2007). <http://stacks.iop.org/1751-8121/40/8019>.

Bibliography

- [266] M. Moeckel and S. Kehrein. *Interaction Quench in the Hubbard Model*. *Phys. Rev. Lett.* **100**, 175702 (2008).
- [267] E. M. Purcell and R. V. Pound. *A Nuclear Spin System at Negative Temperature*. *Phys. Rev.* **81**, 279–280 (1951).
- [268] A. P. Mosk. *Atomic Gases at Negative Kinetic Temperature*. *Phys. Rev. Lett.* **95**, 40403 (2005).
- [269] A. Rapp, S. Mandt, and A. Rosch. *Equilibration rates and negative absolute temperatures for ultracold atoms in optical lattices*. arXiv:1008.0468v1 [cond-mat.quant-gas] (2010). <http://arxiv.org/abs/1008.0468>.
- [270] J.-S. Bernier, C. Kollath, A. Georges, L. De Leo, F. Gerbier, C. Salomon, and M. Köhl. *Cooling fermionic atoms in optical lattices by shaping the confinement*. *Phys. Rev. A* **79**, 61601 (2009).
- [271] A. Ponomarev, J. Madroñero, A. Kolovsky, and A. Buchleitner. *Atomic Current across an Optical Lattice*. *Phys. Rev. Lett.* **96**, 50404 (2006).
- [272] A. J. Daley, P. O. Fedichev, and P. Zoller. *Single-atom cooling by superfluid immersion: A nondestructive method for qubits*. *Phys. Rev. A* **69**, 22306 (2004).
- [273] T.-L. Ho and Q. Zhou. *Squeezing out the entropy of fermions in optical lattices*. *PNAS* **106**, 6916–6920 (2009).
- [274] A. J. Kerman, V. Vuletić, C. Chin, and S. Chu. *Beyond Optical Molasses: 3D Raman Sideband Cooling of Atomic Cesium to High Phase-Space Density*. *Phys. Rev. Lett.* **84**, 439–442 (2000).
- [275] M. Popp, J.-J. Garcia-Ripoll, K. G. Vollbrecht, and J. I. Cirac. *Ground-state cooling of atoms in optical lattices*. *Phys. Rev. A* **74**, 13622 (2006).
- [276] T.-L. Ho and Q. Zhou. *Universal Cooling Scheme for Quantum Simulation*. arXiv:0911.5506v1 [cond-mat.quant-gas] (2009). <http://arxiv.org/abs/0911.5506>.
- [277] H. Ott, E. de Mirandes, F. Ferlaino, G. Roati, V. Türck, G. Modugno, and M. Inguscio. *Radio Frequency Selective Addressing of Localized Atoms in a Periodic Potential*. *Phys. Rev. Lett.* **93**, 120407 (2004).
- [278] S. Fölling, A. Widera, T. Müller, F. Gerbier, and I. Bloch. *Formation of Spatial Shell Structure in the Superfluid to Mott Insulator Transition*. *Phys. Rev. Lett.* **97**, 60403 (2006).
- [279] E. Timmermans. *Degenerate Fermion Gas Heating by Hole Creation*. *Phys. Rev. Lett.* **87**, 240403 (2001).
- [280] E. V. Gorelik, I. Titvinidze, W. Hofstetter, M. Snoek, and N. Blümer. *Néel Transition of Lattice Fermions in a Harmonic Trap: A Real-Space Dynamic Mean-Field Study*. *Phys. Rev. Lett.* **105**, 65301 (2010).

Bibliography

- [281] T. A. Corcovilos, S. K. Baur, J. M. Hitchcock, E. J. Mueller, and R. G. Hulet. *Detecting antiferromagnetism of atoms in an optical lattice via optical Bragg scattering*. *Phys. Rev. A* **81**, 13415 (2010).
- [282] A. M. Rey, V. Gritsev, I. Bloch, E. Demler, and M. D. Lukin. *Preparation and Detection of Magnetic Quantum Phases in Optical Superlattices*. *Phys. Rev. Lett.* **99**, 140601 (2007).
- [283] K. Eckert, O. Romero-Isart, M. Rodriguez, M. Lewenstein, E. S. Polzik, and A. Sanpera. *Quantum non-demolition detection of strongly correlated systems*. *Nature Physics* **4**, 50–54 (2007).
- [284] T. Gottwald and P. G. J. van Dongen. *Antiferromagnetic order of repulsively interacting fermions on optical lattices*. *Phys. Rev. A* **80**, 33603 (2009).
- [285] C. F. Roos, M. Riebe, H. Haffner, W. Hansel, J. Benhelm, G. P. T. Lancaster, C. Becher, F. Schmidt-Kaler, and R. Blatt. *Control and Measurement of Three-Qubit Entangled States*. *Science* **304**, 1478–1480 (2004).
- [286] A. I. Lvovsky and M. G. Raymer. *Continuous-variable optical quantum-state tomography*. *Rev. Mod. Phys.* **81**, 299–332 (2009).
- [287] A. Pashov, P. Popov, H. Knöckel, and E. Tiemann. *Spectroscopy of the $a^3\Sigma_u^+$ state and the coupling to the $X^1\Sigma_g^+$ state of K_2* . *Eur. Phys. J. D* **46**, 241–249 (2007).
- [288] S. K. Kim. *Group theoretical methods*. Cambridge University Press, Cambridge (1999).
- [289] J. Vollinga and S. Weinzierl. *Numerical evaluation of multiple polylogarithms*. *Computer Physics Communications* **167**, 177–194 (2005).